

CONTENTS

	Page
INTRODUCTION	1
PREVOST SOIL MODEL AND TEST DATA	3
BOUNDARY VALUE PROBLEMS	6
Multi-Element Simulation	6
Consolidation Analysis	8
Anisotropic Consolidation Analysis	11
SOIL-STRUCTURE PROBLEM	13
Static Analysis	13
Dynamic Analysis	14
PILE AND PIER FOUNDATIONS	17
Load Capacity	17
Cyclic Behavior of Piles	21
Friction Between Calcareous Sand and Building Materials	23
Piles in Calcareous Sands	25
CONCLUSION	28
REFERENCES	29

INTRODUCTION

The characterization of the behavior of soil under loading is a complex task. The finite element method has in recent years been a useful tool in analyzing structures, structures on soil, and soil-structures. An emphasis has been placed on use of nonlinear plasticity soil models to more accurately capture the soil response. Recent work has focused on effective stress analysis - the ability to not only calculate the soil stress but also to calculate the pore fluid pressure.

The use of an effective stress model has application in analysis of ocean floor soils, nearshore and offshore structures, and in seismic analysis. Oscillations in loading, whether from wave action or seismic shaking, produce a dynamic loading that can induce significant increases in pore pressure. The increase in pore pressure can reduce allowable soil capacities and increase deformations from a reduction in effective confining stress. Under extreme conditions flow slides and liquefaction occur. Although liquefaction has been identified as a phenomenon for 20 years, soil mechanics is just beginning to understand the interaction of stress confinement and drainage path, which occurs in the field such as under a foundation or around a pile. For example, common engineering practice in the evaluation of seismically induced soil liquefaction considers level ground conditions away from the structure. Shear stresses from the structure are not considered. Present design guidelines for pile foundations are based on static load considerations.

Recent earthquakes, particularly those in Alaska, Japan, and Chile, have emphasized the high damage threat the soil liquefaction phenomenon poses to waterfront structures. In the 1960 Chilean earthquake (magnitude 7) quaywalls, sheet piles, and sea walls were damaged by liquefaction of loose, fine, sandy soils. In the 1964 Alaskan earthquake (magnitude 8.4) severe damage to Anchorage, Cordova, and Valdez occurred, including large-scale land slides, as a result of liquefaction. Japanese

earthquakes (Niigata, 1964, magnitude 7.3; Miyagi-Ken-Oki, 1978, magnitude 7.4) caused severe waterfront damage to wharfs, bulkheads, quaywalls, piers, and conventional structures. The majority of the damage sustained in waterfront areas was primarily from liquefaction of loose, cohesionless sands.

A study conducted by the Office of Naval Research (Ref 1) recognized a major liquefaction hazard existing at West Coast Naval stations. A more recent investigation at the Naval Air Station (NAS) North Island, Calif. (Ref 2), concluded that liquefaction under design earthquake levels could result in destruction of such critical structures as aircraft carrier berths, aviation fuel tank farms, and underground utility service lines. Unfortunately, almost all previous studies of the liquefaction problem have been concerned with either conventional building foundations or with analyses of dams, and procedures for analysis are not available for specialized Navy structures.

The effective stress model is of major significance since the Navy must locate in areas where the water table is high. Even if liquefaction (a loss of shear strength from a loss of effective confining stress) does not occur, a buildup of pore pressure is probable both in sands and clays. This pore pressure buildup can be of major significance to structural behavior.

The Navy has a drydock certification program in progress. These structures are examples of situations where a structure is surrounded by soil, often with a high water table. Soil loading causes wall deflections which, in turn, alter the soil load. Note that even though drydocks are critical Navy structures, the present analytical techniques reflect the state-of-the-art as of 1950. Basically, static structural analysis procedures are used with estimates of the soil pressure. The drydock is only one of many types of structures at the waterfront that illustrates the significance of soil-structure interaction.

The effective stress soil model is a critical tool for use on waterfront structures. Dynamic analysis techniques are essential for a realistic assessment of drydock safety. Drydocks are only one application; others include quaywalls, bulkheads, retaining walls, ocean floor structures, etc.

Effective stress techniques are also of interest in understanding pile behavior. Pore pressure builds up during the cyclic loading process and then deformations increase.

This report documents work performed during FY83 investigating use of the effective stress soil model. Funding for this task was obtained jointly from the Navy and the Department of the Interior.

PREVOST SOIL MODEL AND TEST DATA

In order to evaluate the behavior of the Prevost soil model a series of tests was performed for the Naval Civil Engineering Laboratory (NCEL) by Professor Lade, University of California at Los Angeles. Prevost developed an automated procedure to compute the parameters required to use his soil model. This procedure was used to fit the silica sand from Lade's test data. Triaxial compression and extension test results were studied. Two cases were investigated:

(1) 11 surfaces model using:

compression test results: 12 points

extension test results: 15 points

(2) 29 surfaces model using:

compression test results: 34 points

extension test results: 34 points

Case (2) uses the same set of test results as case (1) with additional data points for improved definition. For case (2) the additional extension points were obtained by interpolation of reported test data points.

To evaluate the material models for cases (1) and (2) above, the computer codes DYNA-FLO and TESTA, developed by Prevost, were used to perform triaxial simulations. DYNA-FLO is a nonlinear transient finite element analysis code, and TESTA, the subroutine PCONST from DYNA-FLO,

is used as a driver for the soil model under prescribed strain paths. DYNA-FLO was used to run drained and undrained triaxial simulations, and TESTA was used to run undrained cyclic simulations.

The stress-strain data curve for Lade's silica sand is shown in Figure 1. These data were used to produce the resulting yield surfaces shown in Figures 2 and 3 for cases (1) and (2) above. In each case, 100 yield surfaces were requested; the program produced 11 surfaces for case (1) and 29 surfaces for case (2). Some of the yield surfaces touch; this is permitted, however, as long as they do not overlap.

The one-element three-dimensional runs using the DYNA-FLO program used the following control options:

- (1) a symmetric stiffness matrix
- (2) an elliptic case (a static problem)
- (3) implicit-explicit treatment
- (4) 100 time steps
- (5) 10 iterations

The single-element model is confined at nodal points by horizontal nodal forces and is loaded vertically by a displacement function. A variation of initial modulus, G_1 and B_1 , parameter study for the 11-surface model is shown in Figures 4, 5, and 6. Run 1 uses the original B_1 and G_1 ($G_1 = 253$ and $B_1 = 675$). Run 6, with $G_1 = 66$ and $B_1 = 338$, appears to fit the test data the best. Similar results for the 29-surface model are shown in Figures 7, 8, and 9. These results show the sensitivity of model behavior to the values of initial modulus. The initial modulus serves as the reference line for the computation of the nonassociativity parameters, which relate stress-strain space. Thus, the initial modulus has a significant effect on volume strain as can be seen in Figures 6 and 9. The selection of B_1 and G_1 had an effect on (the lack of) convergence of the equilibrium iteration.

For drained behavior, both the 11- and 29-yield-surface models produced similar and satisfactory agreement with the test data.

Figure 10a shows the undrained stress path for case (1) with 11 yield surfaces. Note that the test data exhibit a greater drop in mean stress, indicating higher pore pressure generation than would be exhibited by the computed results. Figure 6 does indicate some difference in drained volumetric behavior, which would translate into undrained behavior differences. Part of the problem was thought to be the lack of definition in the yield surfaces as shown in Figure 10b. Figures 11a and 11b show the stress path for case (2) with 29 yield surfaces. It can be seen that the improvement in results is only slight. Figure 12 shows the pore pressure, comparing computed results with test data.

In an attempt to improve the volumetric behavior, the nonassociativity parameters were varied in compression. Figure 13 shows the effect on volume strain, and Figure 14 shows the effect on pore pressure. The approximate magnitude of pore pressure is correctly predicted; however, the pore pressure drops off too early.

It is important to note that the actual sand is a very uniform sand at a relative density of about 30%. This relative density was chosen such that liquefaction would occur in five cycles. The material exhibits an initial low level region in which a definite yielding or straining without additional stress occurs. This is attributed to the "seating" of the grains with perhaps some segregation. The very low density of the test sample must be constructed in the laboratory and would not occur in nature. Perhaps the material goes through a transition in which its continuum representation breaks down. The model does predict the level of pore pressure expected but not the full strain state.

The 11-yield-surface model was examined under cyclic undrained loading. The level of load oscillated at 20% of the initial confining stress. At this low loading level, the model behaved elastically since all loadings were within the first surface. The 29-yield-surface model was then examined under the same cyclic loading. Figure 15 shows the effective stress path of the computed results along with the test data. Liquefaction is noted in four cycles for both. Figure 16 shows stress-strain behavior. The first loading cycle of the model behaves elastically.

The model experiences greater strain in extension than the data on the first unloading cycle. Figure 17 shows the pore pressure with vertical strain. The model behaves qualitatively correctly, although vertical strain in extension appears to be larger than indicated. It is important to remember that the model undrained cyclic predictions are based on drained tests. This again demonstrates the sensitivity of the results to extension test data.

To better understand the undrained model behavior, one cycle of loading was applied to the 29-yield-surface model. Figure 18 shows the stress path and load steps. Figure 19 shows the position of the surfaces of each load step. The "x" shows the location of the load step in stress space. It is important to note the number of surfaces actually involved in the computation. Although the 29-surface model has a large number of surfaces, most of these are in higher ranges not used in this case. The definition in the low ranges is still coarse. This is limited by the number of data points available. Future experimental tests will focus on obtaining more data in the low range.

The level at which stress stabilizes and flow yielding occurs is controlled by the size of the last surface. Values of the plastic bulk and shear modulus are set to zero on the last surface to produce the yield condition. The effect of doubling the size of the last yield surface, increasing stress levels, is shown in Figure 20.

BOUNDARY VALUE PROBLEMS

Multi-Element Simulation

To develop a better understanding of the model behavior it was decided to try a simple multi-element case. The 11-yield-surface soil data were used in a drained environment. Two studies were done: the first had 60 elements, the second 120. The analysis was two-dimensional plane strain with two degrees-of-freedom per node using the hyperbolic solver. Figure 21 shows the undeformed mesh with node numbers for the 60- and 120-element runs. Confining pressures of 2.0 kg/cm^2 were

applied to both vertical faces, and the analysis was performed using a displacement-time function applied vertically. The center node on the base, node 44 for the 60-element run and node 77 for the 120-element run, was constrained horizontally and vertically. The other nodes on the base were constrained in only the vertical direction.

For the 60-element mesh, Figure 22 shows that the velocity vector starts as initially uniform and then shows a computational instability occurring at step 50. Also shown is the deformed mesh at step 60 to exaggerated scale. Stress results were determined for the analysis and are shown in Figure 23. Values of stress were the same in all elements as long as the solution remained stable. At step 50 an instability occurred with a value of vertical stress of 5.40 kg/cm^2 .

The problem was repeated with the 120-element mesh; Figure 24 shows the velocity vector of step 80. The finer mesh eliminated the premature numerical instability experienced above. All elements maintained the same stress, showing uniform behavior as would be expected from a "perfectly balanced" system without initial imperfection. Had an "imperfection" been introduced, a typical bifurcation failure would have occurred. Figure 25 shows vertical stress; the horizontal confining stress remained at 2.0 kg/cm^2 . The failure shear stress ($6.8 - 2.0 = 4.8$) agrees well with expected test results. Use of the implicit-explicit element produced similar results.

The problem was repeated using the parabolic solver. Results are similar (Figure 26), producing the same deformation pattern until about step 60, at which time a localized deformation occurs. By step 70, however, the deformation returns to a generalized deformation pattern. Figure 27 presents the stress plots showing an instability at about step 60. The problem was repeated with the parabolic solver with three degrees-of-freedom per node. Results were very similar to the 2 degree-of-freedom solution.

The problem was again repeated using the elliptic solver. Results are similar to those of the parabolic solver, with an instability occurring around step 60.

The same problem was repeated using the hyperbolic explicit formulation. In this formulation a mass matrix is formed and a dynamic solution occurs. The explicit formulation has a strict time step requirement that the time step be less than the transit time through an element. Figure 28 summarizes the process. The solution is a wave propagation problem in which the top surface is loaded and a wave propagates through the soil and reflects on the fixed base. Figure 29 shows the velocity vector plots showing the travel of the wave.

Consolidation Analysis

One of the applications of an effective stress soil model is the analysis of consolidation of soil under loading. A foundation typical of a strip footing was investigated to evaluate the buildup and dissipation of pore pressure with loading.

A 100-element mesh (Figure 30) was used to represent a two-dimensional foundation. A parabolic analysis option was required to permit flow of fluid between elements; thus three degrees-of-freedom (one for pore fluid pressure) were used. Implicit-explicit formulation was utilized with 10 equilibrium iterations. Fifteen time steps were used.

For material having pore pressure, a material type, an NTYPE of 4, specifying the two-dimensional element with porous media formulation must be used. The following values were recommended for Gaussian quadrature:

1 point	Initial stress stiffness integration
1 point	Volumetric stiffness integration
2 x 2	Deviatoric stiffness integration

When incompatible modes are included to improve an element in bending and in application to incompressible materials, two-by-two Gaussian quadrature in both volumetric and deviatoric terms should be employed.

The water table was at the top surface of the mesh, and drainage was permitted there. Two cases were studied: an elastic soil model and the

Prevost soil model. In both cases 10 element groups were used to represent the soil layers. The buoyant weight of the soil is used in conjunction with the weight of the water:

$$\gamma_{\text{buoyant}} = \gamma_{\text{soil}} - \gamma_{\text{water}}$$

$$\gamma_{\text{soil}} = \gamma_{\text{solid}} \cdot (1-\eta) + \gamma_{\text{water}} (\eta)$$

where η is the porosity.

This convention maintains the initial effective soil stress and the initial pore fluid pressure from gravity acting in the usual downward direction. The gravity stresses offset the initial stresses in the Prevost soil model prescribed for each layer.

The permeability matrix at the element level requires K_{12} and K_{21} to be set to values different from K_{11} and K_{22} , or a singularity will develop. Values of K_{12} and K_{21} of 0.0 have been used specifying only K_{11} and K_{22} . The horizontal permeability is normally substantially greater than the vertical permeability (10 to 1 in stratified materials).

In the elastic case $\mu = 0.41$ was used for all 10 groups, and E ranged from 16.5 to 133.5 kg/cm² from top to bottom layers. The variation in E was calculated using the values of G_1 and B_1 , the elastic shear and bulk modulus for each layer, from the Prevost model. In the Prevost model, the Lade silica sand, with confining stress of 2.0 kg/cm² discussed above, was scaled according to confining stress in the soil field for the 10 layers. The initial effective (confining) stresses in the 10 layers ranged from 0.0158 to 1.034 kg/cm², top to bottom. Displacement and stress histories and contour plots are compared.

The soil field was loaded with a pressure of 0.05 kg/cm² at the upper right corner as shown in Figure 30. Figure 31 shows the load-time function used in the analysis and the velocity vector field at step 3 ($t = 0.000975$ seconds). This velocity field was at the time the load-time function attains its maximum value of 1.0, and it was typical of both the elastic and Prevost model cases. Figure 32 shows the deformed mesh plots at step = 15 ($t = 62.1$ seconds). The deformed mesh plot for the

Prevost model case shows the three elements under the pressure load folded over; this results from the exaggerated deformation scale used in the automated plotting.

Figures 33 and 34 show pore pressure contour plots for the elastic and Prevost material model cases. The plots show the buildup and dissipation of pore pressure; at step = 4 the maximum buildup of pore pressure is shown. The hydrostatic fluid pressures from the water table are not shown in the plots. Comparison of Figures 33 and 34 indicates the numerical values and spatial variation of pore pressure are very similar during both buildup and dissipation as would be expected from the low level of loading.

Figure 35 shows the vertical displacement time histories of nodes 121, 117, 97, and 73. The solid line indicates displacement for the elastic model, while the dashed line is for the Prevost model. For nodes 97 and 73, which are away from the applied 0.05 kg/cm^2 , the elastic and Prevost model solutions are very similar. However, for node 121 for $t \geq 10^{-2}$ seconds, the displacements become increasingly greater for the Prevost model. The displacements for node 117 indicate upward movement.

Figures 36 and 37 show stress histories for elements 89 and 100 (see Figure 30 for these two elements). Gravity stresses are not included. These figures indicate that up to time $t = 10^{-2}$ seconds, the elastic and Prevost model solutions are similar. For $t > 10^{-2}$ seconds, the effective stresses for the elastic case are greater than those of the Prevost model. However, the pore fluid pressures for the elastic case are less than those of the Prevost model case. The effective stresses are greater and the displacements are lower for the elastic model as compared to the Prevost model.

The above problem was repeated, this time comparing the behavior of the Prevost model using the parabolic (diffusion) and hyperbolic (dynamic) options. The parabolic (diffusion) option has a third degree-of-freedom representing pore pressure. Defining the pore pressure at a boundary such as a free surface is accomplished by setting the nodal boundary condition to 1. This sets the pore pressure value, given no other input, to a value of 0.0. Drainage is permitted. In the hyperbolic case

four degrees-of-freedom are used. The third degree-of-freedom is x direction fluid velocity, and the fourth degree-of-freedom is y-direction fluid velocity. To prevent fluid flow at a boundary such as the sides or bottom of a mesh, which should represent equilibrium no-flow conditions, it is necessary to set the nodal boundary conditions to 1. A free surface is left at 0. This is opposite to the parabolic condition and can cause considerable confusion if not fully appreciated. The hyperbolic option can be used in a quasi-static mode by selection of α and β to 1.5 and 1.0, respectively. This results in a heavily damped solution and, when coupled with large time steps, will produce a solution similar to the parabolic solution.

The results for the parabolic and hyperbolic solutions did agree within 5% when larger (10-second) time steps were used. The results did not agree closely at early time steps when small time steps were used, showing the influence of the inertial terms.

Anisotropic Consolidation Analysis

The Prevost soil model utilizes stress surfaces whose position is based on the initial confining stress. Thus, to analyze a soil field it is necessary to divide it into layers with each layer having different properties. Triaxial test data are not available for all layers, so it is necessary to scale the data available to different confining stresses. Based on limited data, it has been found reasonable to scale by the ratio of average confining stress levels. The elastic shear modulus, the initial elastoplastic shear modulus, and the elastic bulk modulus are scaled by the square root of the stress ratio. The bulk exponent is not scaled. Initial stress components are scaled by the ratio. The size of the yield surface is scaled by the stress ratio. The elastoplastic shear and plastic bulk moduli are scaled by the square root of the stress ratio; the degree of nonassociativity is not scaled.

Anisotropic consolidation can also be treated by shifting the ellipses. If it is assumed that isotropic data are used and the J_1 value is maintained constant, then

$$J_1 = \sigma_v + 2 \sigma_H$$

$$J_1 = (1 + 2 k_o) \sigma_v$$

$$\text{Shift } \sqrt{J_2} = \frac{\sigma_v - \sigma_H}{\sqrt{3}}$$

$$\text{Shift } \sqrt{J_2} = \frac{(1 - k_o)}{\sqrt{3}} \sigma_v$$

$$\text{Shift } \sqrt{J_2} = \left[\frac{1 - K_o}{\sqrt{3}} \right] \left[\frac{J_1}{1 + 2 k_o} \right]$$

The new values for σ_v are

$$\sigma_v = \frac{J_1}{1 + 2 k_o}$$

$$F(\sigma', \eta) = 0$$

where J_1 is the isotropic test.

Figure 38 shows results of scaling data from a confining stress of 2 to 5 kg/cm². Also shown is actual test data from tests performed by Lade. The results are satisfactory for use.

Figure 39 illustrates conversion to anisotropic conditions. Figure 39a shows the original soil surfaces based directly upon the test data. Figure 39b shows the shift to the appropriate isotropic confining stress desired. Figure 39c shows the imposition of a k_o condition of 0.5 maintaining the vertical stress level.

It was of interest to compare the isotropic soil for the previously discussed problem of the foundation compression. Figure 40 shows the pore pressure contour plot at step = 14 for the two-dimensional consolidation problem using an anisotropic Prevost soil model. The pore pressure plots for steps 2, 4, and 10 are not shown because they are similar to the isotropic model results. Comparison of Figures 34 and 40 at step 14 shows that the pore pressure dissipates at a faster rate for the isotropic soil model.

Figures 41 to 43 show vertical displacement and stress histories for selected nodes and elements. These results are similar to those of the isotropic elastic and Prevost model results. The anisotropic Prevost model results show greater displacements, as would be expected since the initial horizontal confining pressures are one-half of those in the isotropic case.

SOIL-STRUCTURE PROBLEM

Static Analysis

To illustrate a typical soil-structure problem, beam elements were used to represent a structural frame on a soil foundation. Figure 44 shows the mesh. The structure was embedded in the soil resting on the top of the fourth soil layer. Figure 45 illustrates the coupling of the beam elements to the soil field using contact elements. Contact elements were used at the base to permit change from the third degree-of-freedom in the quadrilateral elements (pore pressure) to the third degree-of-freedom in the beam (rotation). Vertical and horizontal contact elements were used along the side of structure, vertical to allow for frictional forces and horizontal to permit contact/separation with deformation. Figures 46 and 47 show the deformed mesh at steps 5 and 15 of loading. Figures 48 and 49 show the vector velocity at steps 5 and 15. Figure 50 shows the stress path in the element beneath the corner of the structure. Note that as the load is applied the stress builds up gradually, most of load being carried by pore pressure. As the pore pressure dissipates (Figure 51) the effective stress in the soil increases and deformation increases (Figure 52). The high loading produces localized yielding. This is evident in the deformed mesh plots and vector velocity plots, which show (to an exaggerated scale) the failure of the soil near the structure. Figure 53 shows the pore pressure contours. The pore pressure contours are similar to those in the previous consolidation problem. Pore pressure is a maximum near the lower left corner of the structure, since drainage is permitted only at the surface.

Dynamic Analysis

It was of interest to analyze a two-dimensional model of a structure on soil subject to horizontal shaking motion. The model used (Figure 54) is similar to the previous model composed of half the structure (Figure 44). This time the full mesh is utilized to capture asymmetric effects such as building rocking. The model is composed of 182 quadrilateral elements, 28 beam elements, and 21 nodal contact elements. As done above, 10 soil layers were used, each composed of an 11-surface model scaled to the layer's depth. The Prevost model incorporates an initial stress as a model parameter; gravity was applied from time = 0 to offset the initial material stress. The building weight was applied slowly in five steps, and pore pressures from this load were allowed to dissipate to produce an equilibrium static condition as the starting point for dynamic excitation. This solution was performed using the hyperbolic option with integration parameters $\alpha = 1.5$ and $\beta = 1.0$ to produce a highly damped "static" condition. Thus, the first 10 steps were a static analysis. The solution utilized four degrees-of-freedom per node. The vertical side boundaries were free boundaries for translation, having static gravity pressure loads applied horizontally to maintain equilibrium and having nodal dampers to simulate nonreflecting boundaries. Flow was not permitted through the boundary. The water table was at the top surface, where drainage was permitted. Figure 55 shows the deformed mesh and displacement vectors at the end of the static solution (10th step).

At the 11th step the time increment was changed to a short dynamic increment (0.0125 seconds) and the integration parameters α and β were changed to 0.65 and 0.33, respectively, for dynamic damped response. The loading chosen for this case was a sine wave horizontally applied at the base as a displacement function. Since the solution was a continuing solution at the 11th step, initial conditions corresponding to an initial base velocity could not be input during the solution. An initial transient is noted in the solution.

Figures 56 and 57 show the deformed mesh and velocity vectors at one point in the solution. Figures 58a to 58d show time histories at key points in the mesh. Note the initial transients at the base (Figure 58a).

Figure 59 shows the pore pressure contours in the mesh at various points in the dynamic loading. As can be seen, as the mesh moves to the right, fluid pressure builds up along the left boundary, which does not permit flow, and as the direction reverses fluid pressure builds up on the opposite side. The solution for 210 time steps took 100,000 CPU seconds on a Prime 550-II with about 60 clock hours.

The problem of initial conditions was examined through analysis of a vertical column of soil elements 1 element wide, 10 elements high. Figure 60a illustrates base response for a condition of sinusoidal base excitation with initial conditions at the base and with integration parameters α and β equal to 0.50 and 0.25 to produce minimum damping. Note the increasing acceleration transients. Figure 60b shows the use of α and β of 0.65 and 0.33, respectively, with initial conditions. This response is as expected. However, if, as in Figure 60c, initial conditions are omitted, the response is markedly different, having high initial acceleration transients. One approximate technique to eliminate the effect of the initial condition is to merge the desired sinusoidal excitation loading with an X^3 function such that derivatives of the function at times = 0 are 0.0. Figure 60d illustrates use of that technique. The previous problem of the building on soil was repeated using the displacement function of Figure 60d. The high initial transient was significantly reduced as expected.

To eliminate the fluid pressure buildup at the boundaries, the boundaries were defined to permit flow across them. Fluid forces were computed based on the depth to the center of each element and applied to the nodal points acting on the third degree-of-freedom as follows:

$$F = (\gamma_w h p) \times \text{element height}$$

where: F = total force applied half to each of two boundary nodes' third degree-of-freedom with sign corresponding to direction

γ_w = fluid unit weight

h = depth to center of element

p = porosity

The forces active to restrain the vertical boundary from the soil weight were computed and applied to the first degree-of-freedom as follows:

$$F = [\gamma_s h (1-p)] \times \text{element height}$$

where: F = total force applied half to each of the two boundary nodes' first degree-of-freedom with sign corresponding to direction

γ_s = unit weight of dry phase

h = depth to center of element

p = porosity

Figure 61 presents the deformed mesh, showing the soil field and structure displacement to an exaggerated scale. Figure 62 shows velocity vector plots, and Figure 63 shows pore pressure contours. The loose soil subjected to the 0.5-cm horizontal displacement (about 0.1g) liquefies in the region beneath the corners of the structure after two and one-half cycles. The pore pressure continues to build up until a computational instability occurs.

The solution technique is able to provide a satisfactory static and dynamic analysis. Problems arising from this study are summarized as:

- Lengthy computational time
- Need for static solution as a prerequisite for dynamic solution
- Inability to input initial dynamic conditions once solution started
- Lack of full restart option

The above problems can be reduced by future modification to the code and improvement of the element formulation.

PILE AND PIER FOUNDATIONS

Load Capacity

Piles and piers are used to transmit foundation loads to strata of adequate bearing capacity and to eliminate settlements. Piles also are often used to resist lateral loads or uplift forces. Figure 64 shows the variety of typical pile types used. Timber piles are well suited for use as friction piles in granular materials. Steel piles are best for endbearing on rock. Concrete cast-in-place piles are economical to use. Concrete-filled steel piles offer high bending resistance. Depending on type of pile used, piles are either driven or cast-in-place. Deep foundations utilize piers that resemble large cast-in-place piles to transmit the loading.

This discussion will consider only straight piles driven into homogeneous deposits of cohesionless materials. Experience has shown that when piles are driven into sand, the soil near the pile is compacted to a distance of a few pile diameters. In a homogeneous sand the point resistance and average skin friction increase with depth of penetration up to a critical depth. Beyond the critical depth the point resistance and skin friction remain almost constant; generally, this is caused by soil compressibility, crushing, and arching. The empirical approach to predicting pile behavior has proven more satisfactory than analytical bearing capacity predictions.

The load transfer mechanism between the pile and the surrounding soil governs the behavior of the pile. The design of a pile requires determination of the proportion of load transferred to the soil by adhesion and friction between the pile and the soil and that transferred by end bearing. This is influenced by the flexibility of the pile, the stiffness of the soil, and the nature of the transfer mechanisms between pile surface and soil.

Through use of instrumented field and model studies an understanding of the design of piles and piers has been improved. Figure 65 illustrates use of pile driving resistance formulas to estimate individual allowable pile loads. Figure 66 illustrates the calculation of

ultimate load capacity of piles in cohesive soils, and Figures 67 and 68 illustrate the calculation of load capacity of piles for cohesionless soils. However, these conventional ultimate design approaches assume the simultaneous and full mobilization of pile shear resistance and base bearing which is not well founded. Studies have shown that movement of a pile must be present to mobilize its load-carrying capacity.

Reese and O'Neill (Ref 1) show the division of load between pier and base for a pier on stiff clay (Figure 69). The first two load increments show that almost all the load is carried by friction; as the loading increases more is carried by end bearing. Above 80 tons any additional load is taken by end bearing. Note how curve C simply translates to form curve D, indicating additional load is taken by end bearing. Using the information in Figure 69 a typical load transfer relationship can be obtained showing side friction (Figure 70). From the slope in Figure 69 it is evident that frictional effects are greatest in the middle (depth) of the pile, and a reduction in the rate of load transfer occurs in the lower part, particularly just above the base. The distribution of frictional forces depends upon the soil type. Modifications to ultimate strength formulations have been suggested by Reese and O'Neill (Ref 1). Factors include an effective depth concept in lateral earth pressure calculation for granular soils and a friction reduction factor for ultimate resistance in cohesive soils.

A theoretical solution of the load transfer phenomenon can provide considerable insight. Such a problem would be a soil-structure problem in which the nature and mechanism of load transfer is of considerable importance. Solution of this problem must focus on the stress-strain characteristics of the soil and the behavior of the interface between pile and soil. Use of a linear-elastic constitutive model would be a gross simplification of the real material properties. The Prevost soil model offers an opportunity to explore nonlinear relationships.

Several approaches have been used to model the contact problem. Peterson (Ref 2) treats the two contacting surfaces as distinct and joins them mathematically by use of Lagrange multipliers. However, this does not allow pre-slip deformation. Herrman (Ref 3,4,5) defines three behavior modes: nonslip, slip, and separation. A compatibility model

combining compatibility and equilibrium is used. The compatibility model involves linking the two surfaces with fictitious bond springs, and the frictional forces are applied as surface tractions. This allows a pre-slip deformation that would not otherwise be computed.

Another approach simply links two nodes initially overlapping with nonlinear springs. The procedure has the advantage of simplicity of operation, but unfortunately may produce undesirable numerical characteristics when distinct rapid changes occur in stiffness.

Prevost has formulated a contact element in the DYNA-FLO code. The contact element may be used to impose inequality constraints between nodes. Either perfect friction (i.e., "stick") or frictionless (i.e., "slip") conditions may be achieved.

A contact element is defined by two nodes: a spring constant, or "penalty parameter," k ; and a fixed direction vector, \underline{n} . The present location of node A ($a = 1, 2$) is given by $\underline{x}_A + \underline{d}_A$, where \underline{x}_A is the initial position vector and \underline{d}_A is the displacement vector. The contact plane passes through the point $\underline{x}_A + \underline{d}_A$ and is perpendicular to \underline{n} (Figure 71).

The contact/release condition is defined as follows:

$$\sigma > 0 \quad \text{release}$$

$$\sigma \leq 0 \quad \text{contact}$$

$$\text{where: } \sigma = \underline{\ell} \cdot \underline{n}$$

$$\underline{\ell} = \underline{x}_B + \underline{d}_B - \underline{x}_A - \underline{d}_A$$

The quantity σ is a measure of the distance between $\underline{x}_B + \underline{d}_B$ and the contact plane. When contact is noted, a contact element stiffness and out-of-balance force are added to the global equations.

If $k > 0$ is sufficiently large, the point $\underline{x}_B + \underline{d}_B$ will be forced to lie (approximately) on the contact plane. In subsequent steps, only the stiffness is assembled, and the decision to remain in contact, or release, is made on the basis of the sign of σ , as above.

For purposes of interpreting output, the contact element "displacement" is defined to be σ , and the "force" is given by:

$$k\sigma \quad \text{if } \sigma < 0$$

$$0 \quad \text{if } \sigma \geq 0$$

In addition to the contact element, Prevost has defined a slide element. The slide-line element may be used to impose inequality constraints between nodes. Either perfect friction (i.e., "stick") or frictionless (i.e., "slip") conditions may be achieved.

A slide-line element is defined by three nodes and a spring constant or "penalty parameter," k . The connection from node A to node B defines the "slide-line" direction, and node C is the contact node (Figure 72).

The projected distance of node C to node A onto the slide-line direction is denoted by α and is given by:

$$\alpha = \vec{AB} \cdot \vec{AC} / \left| \vec{AB} \right|^2 \quad 0 \leq \alpha \leq 1$$

where " \cdot " denotes the dot product of two vectors. The direction of the unit vector \vec{n} to the slide-line direction is given by:

(a) in two dimensions by rotating \vec{AB} as an angle $+\pi/2$

(b) in three-dimensions:

$$\vec{n} = (\vec{AB} \times \vec{AC}) \times \vec{AB} / \left| (\vec{AB} \times \vec{AC}) \times \vec{AB} \right|$$

where " \times " denotes the cross product of two vectors. The local contact stiffness matrix \underline{k} is given by:

$$k = k \begin{bmatrix} (1 - \alpha)^2 & \alpha(1 - \alpha) & -(1 - \alpha) \\ \alpha(1 - \alpha) & \alpha^2 & -\alpha \\ -(1 - \alpha) & -\alpha & 1 \end{bmatrix}$$

where the rows and columns are arranged such that the first, second and third rows (columns) correspond to nodes A, B, and C, respectively. The contact/release condition is defined as follows:

(a) in two-dimensions:

$0 \leq \alpha \leq 1$ and $\vec{AB} \cdot \vec{n} \leq 0$: contact

otherwise, release

(b) in three-dimensions:

$0 \leq \alpha \leq 1$ contact

otherwise, release

If $k > 0$ is sufficiently large, the point C will be forced to lie (approximately) on the slide-line AB. In subsequent steps, only the contact stiffness is assembled, and the decision to remain in contact, or not, is made as described above.

Cyclic Behavior of Piles

Poulos (Ref 6) concludes that the ultimate load capacity and cyclic stiffness decrease with increasing number of cycles and increasing cycle load level. This becomes more significant when the cyclic load approaches half the static ultimate load. The cyclic degradation appears to begin at the top of the pile and progresses downward, resulting in a gradual transfer of load to the lower position of the pile. The crucial factor in determining the amount of cyclic degradation is the shear strain for skin friction.

Poulos (Ref 7) has investigated an effective stress approach to determine pore pressure increases with cyclic loading and the resulting modulus degradation factors. Possibly a lack of data prevented further development. Figure 73 shows a compilation of observations (Ref 6) showing degradation as a function of strain ratio, where:

$$\gamma_{ss} = (0.10 \text{ to } 0.25) (\gamma_s)$$

and γ_s = static shear strain to failure

Poulos (Ref 6) reports that "one-way" cyclic loading (i.e., cyclic loading between zero minimum load and a specified maximum) produces significantly less degradation of pile capacity than would occur with "two-way" loading (loading alternating between tension and compression with zero as a mean value). He points out that degradation will occur at different rates along the pile depending on local stress level. Even in initially homogeneous soil, a nonuniform distribution of soil modulus and skin friction will result from cyclic loading because nonuniformity of stress distribution occurs along the pile. Degradation occurs in the ultimate skin friction along the length of the pile and also in the ultimate base resistance. The major problem in a cyclic response is determining how the degradation factors vary with strain and number of cycles.

The cyclic shear strain in the soil adjacent to the pile, γ_c , can be estimated as:

$$\gamma_c = \frac{2 P_c}{\zeta d}$$

where: P_c = cyclic displacement of pile at a point on the pile shaft

d = pile diameter

ζ = $\ln [5\Psi (1-\mu_s) L/d]$

Ψ = 1.0 homogeneous infinitely deep soil
0.5 modulus increases with depth

μ_s = Poisson's ratio

L = embedded pile length

The cyclic base strain can be estimated from the above assuming $U_s = 0.5$, $L/d = 100$.

$$\gamma_c = \frac{0.4 P_{bc}}{d_b}$$

where: P_{bc} is the cyclic displacement of pile base and
 d_b is the diameter pile base.

It is important to note that the above is based on the assumptions of elastic behavior. Typical predictions for pile settlement take the form of Figure 73b. Also shown in Figure 73c is the ultimate cyclic load as a function of number of cycles. The settlement problem is the major concern for piles in cohesionless materials.

Friction Between Calcareous Sand and Building Materials

Calcareous sediments have proven troublesome to offshore facilities. Piles driven into calcareous sands have been noted to penetrate and to be extracted with much less effort than predicted by conventional techniques. A research program was previously conducted at NCEL (Ref 8) in which calcareous sediments were collected from three environments: a deep-ocean site, a shallow-ocean site, and a coralline sand from an atoll beach. The coefficients of friction of these sands and of a quartz sand used as a standard were measured against surfaces of rough and smooth steel and mortar. Volume changes were measured as a function of sliding displacement.

Experience has caused engineers to reduce pile capacities in calcareous materials. This usually results in load capacity reductions to one fourth that of piles in normal materials. It was not clearly understood why calcareous materials exhibit inferior pile support. Measured angles of internal friction, a measure of strength, are high, 34 degrees or greater. Part of the problem was the low increase in soil effective stress during

pile driving, which is thought to result from a crushing or collapse of a cemented soil structure or from the breakup of individual carbonate grains. This lack of increase in effective stress results in a relatively lower shear strength in the soil mass surrounding the pile. Further, it was thought that the coefficients of friction might be substantially less between calcareous materials and piles. Valent (Ref 8) conducted a test program using a modified direct shear test machine in which the lower half of the apparatus contained the building material and the upper half the soil sample. Table 1 summarizes his results.

In general, the results show that the low friction forces in calcareous sediments are not the result of low achievable coefficients of friction between calcareous sediments. Since the coefficients of friction of calcareous sands are comparable to other sands, low friction, then, must be attributable to low normal force. The deep-ocean sand (foraminiferal sand-silt) exhibits one possible cause for low developed normal force. The volume change during testing indicates a considerable volume decrease during development of resisting friction force, probably due to crushing of the skeletal structures and shell fragments. Penetration of a pile in such a material would crush the hollow shell material with only a minimal increase in effective stress of the surrounding material.

Quoting from Valent (Ref 8):

1. The calcareous sediments tested, and presumably calcareous sediments in general, develop coefficients of friction against steel and concrete building materials that are comparable to those developed by quartz-type sands. Thus, the possibility of low coefficients of friction being responsible for the observed low friction forces on driven piling and other penetrators in calcareous materials is ruled out.
2. The observed large volume decreases during shear of the foraminiferal sand-silt are probably responsible for the low developed friction forces in these hollow-shelled materials. Such large volume decreases at nonincreasing normal load imply densification in the field without accompanying increases in normal stress on the penetrator surface.

3. Low developed friction forces in other calcareous materials may arise from a similar mechanism involving a hypothesized loose, but cemented, structure for the soil material. The application of shear stresses during penetration would cause collapse of this structure to a denser, but still loose, arrangement.

Piles in Calcareous Sands

The calcareous sands as discussed above are noted for loose arrangement of particles lightly cemented to form a structure to support other layers without compacting. However, upon shearing the structure is destroyed, breaking the cement bonds, and the loose-grained structure compacts and densifies. The sand discussed above (Lade sand) is a very loose sand (30% relative density) and, as such, is a "manufactured" sand that would not occur in nature. The properties of this material might qualitatively be expected to represent the constitutive behavior of a calcareous sand.

To analyze a pile's load capacity using the effective stress soil model, the mesh in Figure 74 was used. This mesh simulates a pile already in place, (i.e., not the driving of the pile). Horizontal and vertical springs were used to join the pile to the soil field to simulate the interface and allow for pile movement. Unfortunately, DYNA-FLO permits only elastic springs at this time.

The soil properties used were those of Lade sand, discussed above. The material properties simulate the condition of the soil after placement of the pile. No densification occurs, since the pile is in place at the start of the analysis. A prediction of pile capacity was made using conventional techniques in Figures 67 and 68 adjusted to the problem conditions not counting densification. Results indicated a pile resistance in normal average cohesionless sand of at least 1,500 kg with about 150 kg of that in side friction and the remainder in end bearing.

Figure 75 shows the load settlement of the pile. Several values were tried for the spring constants. Results show the pile experiences large settlements between 300 and 400 kg. Figure 76 shows the distribution of force within the pile for three load levels. Note that most of the

increase in load is due to skin friction. Figure 77 shows the distribution of force along the pile at a point in the loading having a force of 300 kg applied at the top of the pile. The results in Figure 77 show about one-half to two-thirds of the load is taken in skin friction. The skin friction portion of the load agrees with the predicted values; however, the end bearing is substantially less. It is important to note that the sand used had a relative density of only 30% which is so loose as not to occur in nature but is "manufactured" in the laboratory. The level of loading is about one-fourth that of a pile on normal sand, which is the level expected from experience in calcareous sands. Figure 78 shows contours of principal stress around the pile at a typical load step. These show typical patterns as would be expected. The level of stress below the pile tip would be on the last surface at yield.

The results show that the order of magnitude of the pile capacity in calcareous materials is predicted correctly. Further, the friction developed on the sides of the pile is at the expected level, not substantially reduced from normal sands. The amount of end bearing is slightly dependent on the vertical spring constant. Use of nonlinear springs would have allowed slip to occur, transferring more load into end bearing when exceeding some local slip level.

Next, pile behavior under cyclic loading was examined. The applied loading consisted of cyclic variation of the vertical load on the pile. In one case the loading was cycled in "one-way" loading (zero minimum and specified maximum) and in "two-way" loading (alternating compression and tension). The first example was at a relatively low level of loading for the model pile (about one-seventh of yield). Figure 79 shows the stress beneath the pile tip for one-way loading. Figure 80 shows the shear stress around the pile. Figure 81 shows the stress beneath the pile tip for two-way loading; the shear stress plot is similar. Note that the tip force reduces with loading, transferring more to friction to maintain load levels. Figure 82 shows the typical contact element force, a measure of friction between the soil and pile. Note the gradual buildup in the two-way loading case.

The loading was increased to about 40% of yield. Figure 83 shows the distribution of force within the pile for both one-way and two-way loading for the first and fifth cycles. Note the increase in friction loading in the pile with two-way loading, showing the degradation with cyclic loading. Note also that for both cases the friction increases more in the lower half of the pile. Figure 84 composes the typical contact element force, again showing the increase in friction with each cycle. Figures 85 and 86 show the stress beneath the pile tip. Both drop off with each cycle; however, the two-way loading does so at a faster rate. Figure 87 shows the pile settlements for both cases. Note the change in settlement between the first and fifth cycle is over 4 times greater for the two-way loading. Figure 88 shows the deformed mesh for the one-way loading; the mesh would be similar for the two-way loading.

The loading was increased to 80% of pile capacity, and the one-way loading case was tried. This load exceeds the friction capacity by itself, so two-way loading could not be used. Figure 89 shows the stress beneath the pile tip, and Figure 90 shows the deformed mesh. Failure occurs between steps 70 and 80. Figure 91 shows the shear stresses around the pile at steps 10 and 70. More stress is transferred from tip end bearing to side friction.

The cyclic results clearly show the degradation of the pile under cyclic loading. Results show the two-way loading to cause more degradation as expected. The model appears to be performing well in predicting the qualitative pile behavior, particularly the settlements (Figures 73 and 87).

The pile problems were repeated for the undrained case in which the water table was at the surface. Figure 92 shows the load settlement curve. The original load increment used in the drained problem above was too coarse for the undrained problem and produced an instability at yielding. The load step was reduced and the solution proceeded in a satisfactory manner. The pile capacity was about 250 kg, lower than the 350 kg in the drained case. The loading was cycled in one-way and two-way conditions. Figure 93 presents the distribution of force within the pile, showing the increase in friction with cycling as with the drained case. The friction is slightly greater in this case. Figures 94

and 95 show the soil stress beneath the pile. The end bearing stress drops off with cycling showing the shift to friction. The "two-way" loading has a faster degradation. This is clearly shown in Figure 96, which shows the settlement. The two-way loading produces a more permanent settlement differential after the fifth cycle. Figure 97 shows the pore pressure in the soil beneath the pile tip. The pore pressure rises to about three-quarters of the continuing stress and then drops off as the load is shifted to friction on the sides. Figure 98 shows the friction force. Note the degradation effects with cycling as load drops off with each cycle.

CONCLUSION

The work accomplished focused on evaluation of the Prevost soil model by itself, comparing laboratory test data to predicted data, and in a boundary value context. The model can accurately predict drained behavior using material properties from triaxial compression and extension tests under an arbitrary loading. This is a significant improvement over tangent modulus and yield line models, which simply represented compression data based on one test condition.

The Prevost soil model can predict qualitatively the correct level of pore pressure under undrained conditions based on drained material properties. However, agreement of stress-strain predictions with test data under undrained conditions is not good. However, this may be a result of "seating" problems in the test data. The model did perform well under cyclic loading, indicating liquefaction in the same number of cycles as expected, although the stress path varied somewhat.

The soil model was evaluated under a series of static, cyclic, and dynamic boundary value problems. Generally, static problems performed well with no difficulties. Cyclic loading performed well, indicating soil degradation as expected. The material model also performed well under dynamic loading; however, there were difficulties in the utilization of the model.

The model requires specification of the initial stress; this requires specification of the starting gravity stresses in a dynamic analysis. When static dead load (structure) stresses are present in addition to gravity stresses, a static analysis must precede the dynamic analysis such that the correct static stress distribution is used as the starting point for the dynamic analysis. This is difficult since a true restart option does not presently exist. Definition of proper dynamic initial conditions is also complicated by lack of a restart option. However, these problems are soluble by future modification to the coding.

Analysis of piles in calcareous sands indicated qualitatively the correct level of pile capacity. Cyclic behavior exhibited degradation with loading showing that two-way loading is more severe than one-way loading.

REFERENCES

1. L.C. Reese and M.W. O'Neill. "Field tests of bored piles in beaumont clay," American Society of Civil Engineers Annual Meeting, Chicago, 1969. (Preprint 1008)
2. H. Peterson. "Application of finite element method in the analysis of contact problems," in Proceedings of the International Conference on Finite Elements in Nonlinear Solids and Structural Mechanics, Geilo, Norway, vol 2, Aug 1977.
3. L.R. Herrmann. "Nonlinear finite element analysis of frictional systems," in Proceedings of the International Conference on Finite Elements in Nonlinear Solids and Structural Mechanics, Geilo, Norway, vol 2, Aug 1977.
4. L.R. Hermann and Z. Al-Yassin. "Numerical analysis of reinforced soil systems," American Society of Civil Engineers National Spring Convention and Continuing Education Program, Pittsburgh, Pa., Apr 24-28, 1978. (Preprint 3125)

5. L.R. Herrmann. "Finite element analysis of contact problems," Journal of Engineering Mechanical Division of ASCE, vol 104, no. EM5, Oct 1978.
6. H.G. Poulos. "Cyclic axial response of single pile," Journal of the Geotechnical Division ASCE, vol 107, GT1, Jan 1981.
7. H.G. Poulos. "Development of an analysis for cyclic axial loading of piles," Third International Conference on Numerical Methods in Geomechanics, Aachen, Germany, vol 4, Rotterdam, 1979, A. A. Bolkema.
8. P. J. Valent. Coefficient of friction between calcareous sands and some building materials, and their significance, Civil Engineering Laboratory, Technical Note N-1541. Port Hueneme, Calif., Jan 1979.

Table 1. Summary of Friction Test Results (Ref 8)

Test No.	Base Material ^a	Soil Material	μ_{peak} ^b	μ_{residual} ^b
1	Sand ^c	Quartz sand	0.67 ^d	0.54
2	Sand	Coralline sand	0.66	0.56
3	Sand	Coralline sand	0.68	0.57
4	Sand	Oolitic sand	0.77 ^d	0.61
5	Sand	Oolitic sand	0.81	0.62
6	Sand	Foram sand-silt	0.64 ^d	0.58
7	Smooth steel	Quartz sand	0.27 ^d	0.19
8	Smooth steel	Coralline sand	0.20	0.17
9	Smooth steel	Coralline sand	0.20	0.18 ^e
10	Smooth steel	Coralline sand	0.21	0.17
11	Smooth steel	Oolitic sand	0.15 ^d	0.13
12	Smooth steel	Oolitic sand	0.32	0.31
13	Smooth steel	Foram sand-silt	0.40	0.37
14	Rough steel	Quartz sand	0.60	0.54
15	Rough steel	Coralline sand	0.63	0.55
16	Rough steel	Oolitic sand	0.54	0.51
17	Rough steel	Oolitic sand	0.58	0.50
18	Rough steel	Foram sand-silt	---- ^f	0.66
19	Smooth concrete	Quartz sand	0.60	0.54
20	Smooth concrete	Coralline sand	0.63	0.56
21	Smooth concrete	Oolitic sand	0.59	0.52
22	Smooth concrete	Oolitic sand	0.58	0.54
23	Smooth concrete	Foram sand-silt	---- ^f	0.67
24	Rough concrete	Quartz sand	0.69	0.57
25	Rough concrete	Coralline sand	0.66	0.59
26	Rough concrete	Oolitic sand	0.74	0.57

^aSoil in bottom shear ring for direct shear tests, or building material in friction tests.

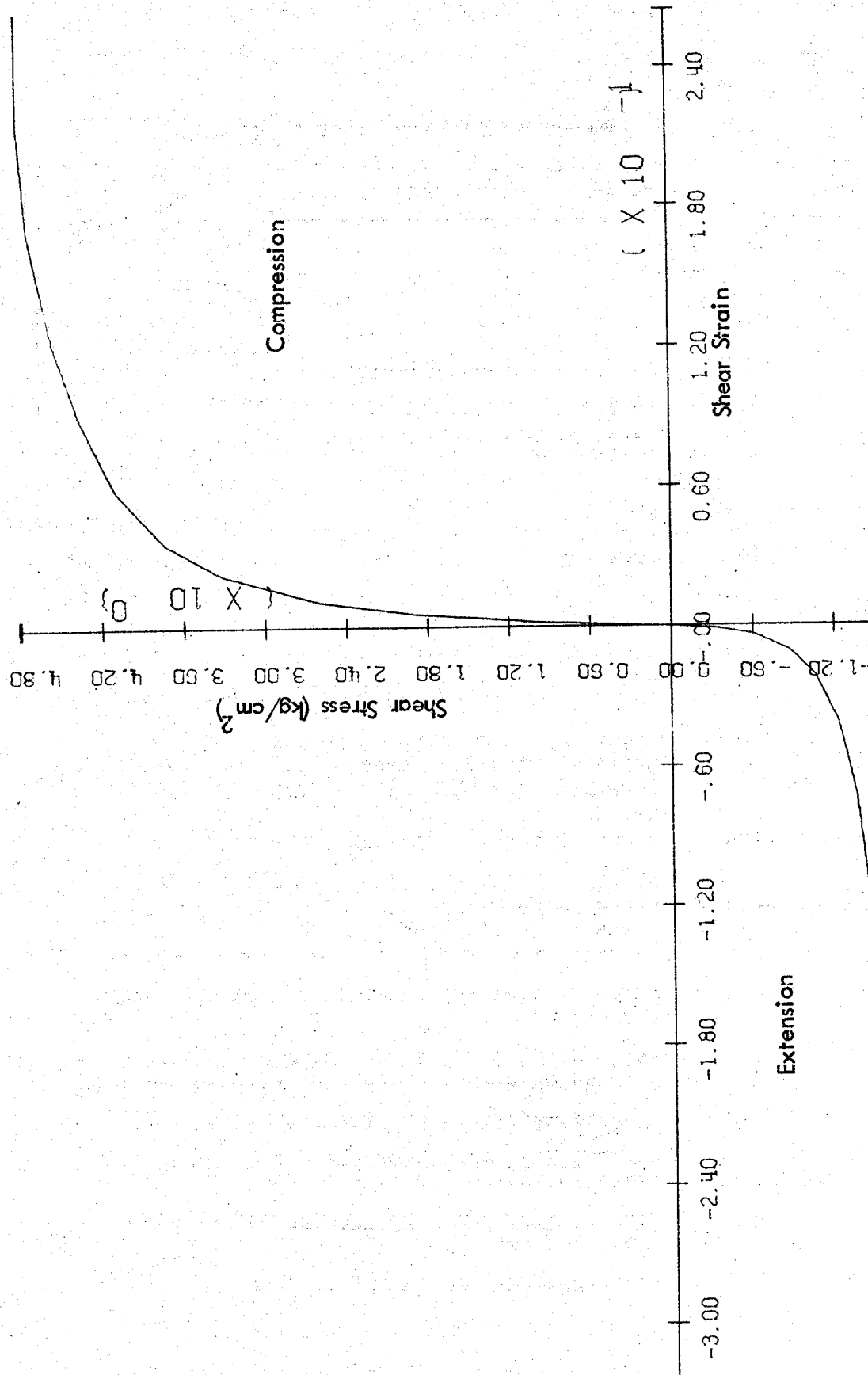
^bFor direct shear tests $\mu = \tan \phi$ where ϕ = angle of internal friction; for friction tests $\mu = \tan \delta$ where δ = angle of sliding friction.

^cBase material same as soil material for direct shear tests.

^dThese tests run with mechanical measurement system; i.e., proving ring and manual recording of data.

^eLow value for μ reached shortly after μ_{peak} , thereafter μ increased with displacement to end of test.

^fNo peak μ reached, μ increasing through end of test.



AXIAL TESTS DATA

S11 - S22 VS E11 - E22

Figure 1 . Stress-Strain for Lade Silica Sand

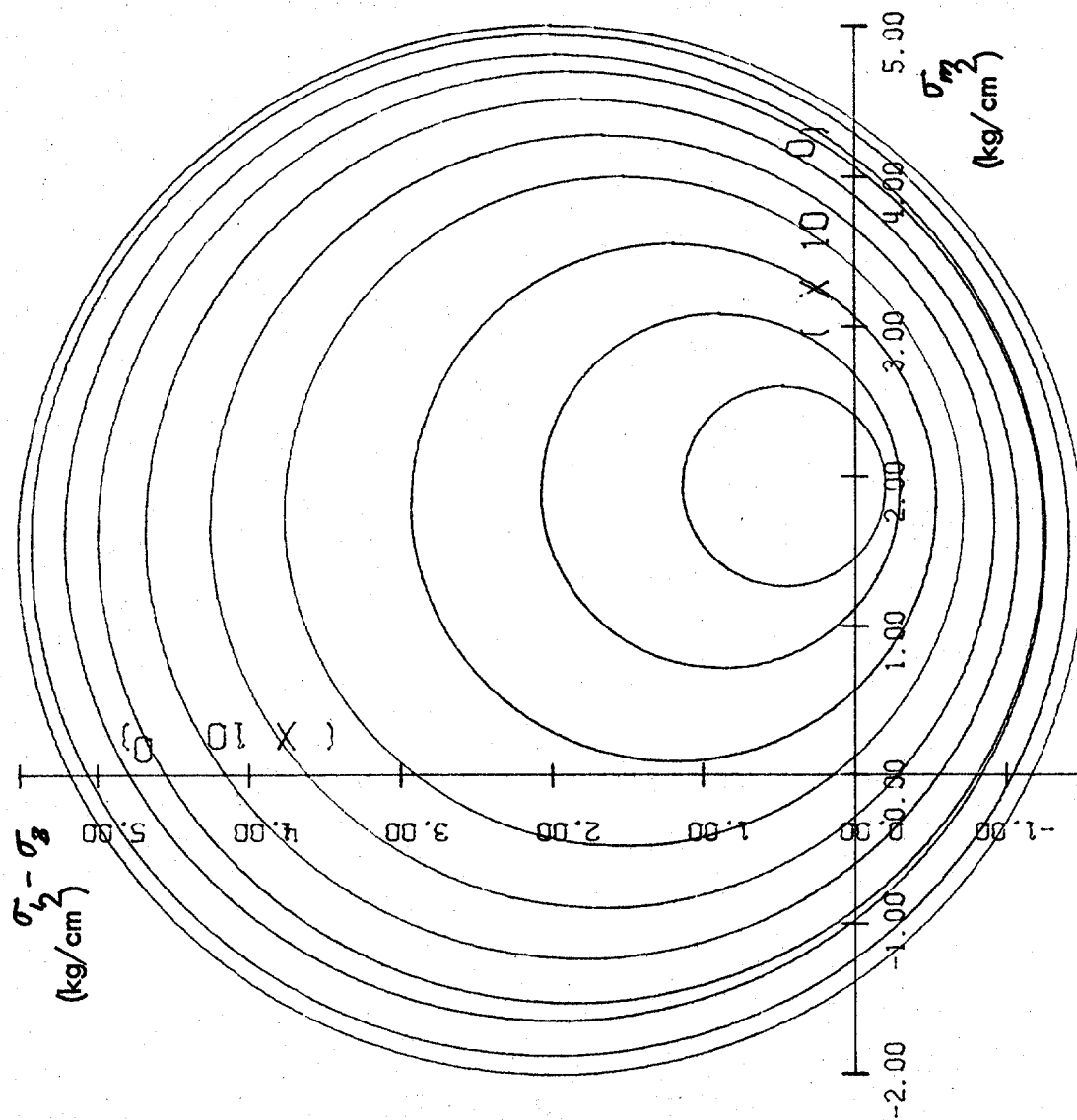
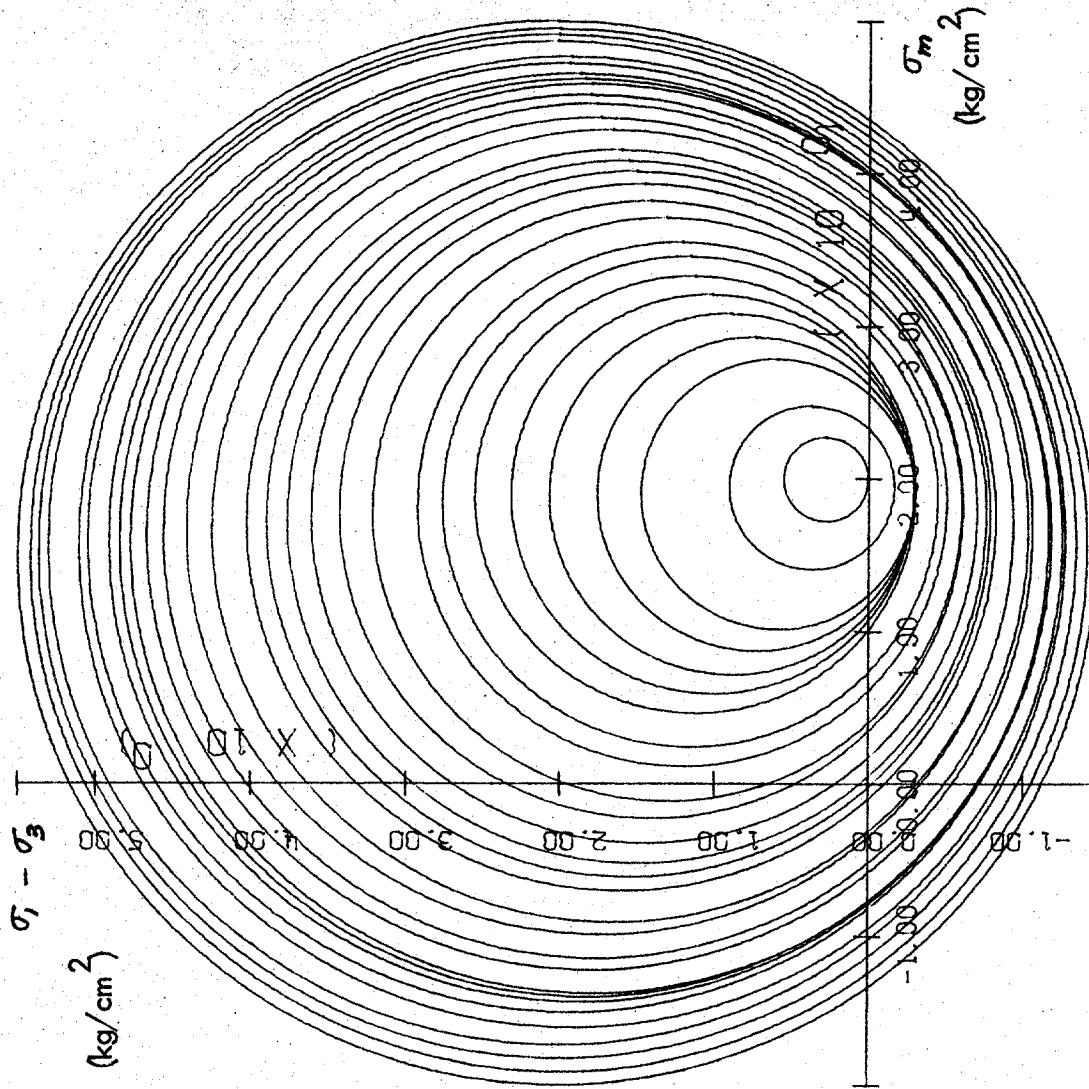


Figure 2. Yield Surfaces for case (I): 12 pts CD, 15 pts CDE



YIELD SURFACES

Figure 3 . Yield Surfaces for case (2): 34 pts CD, 34 pts CDE

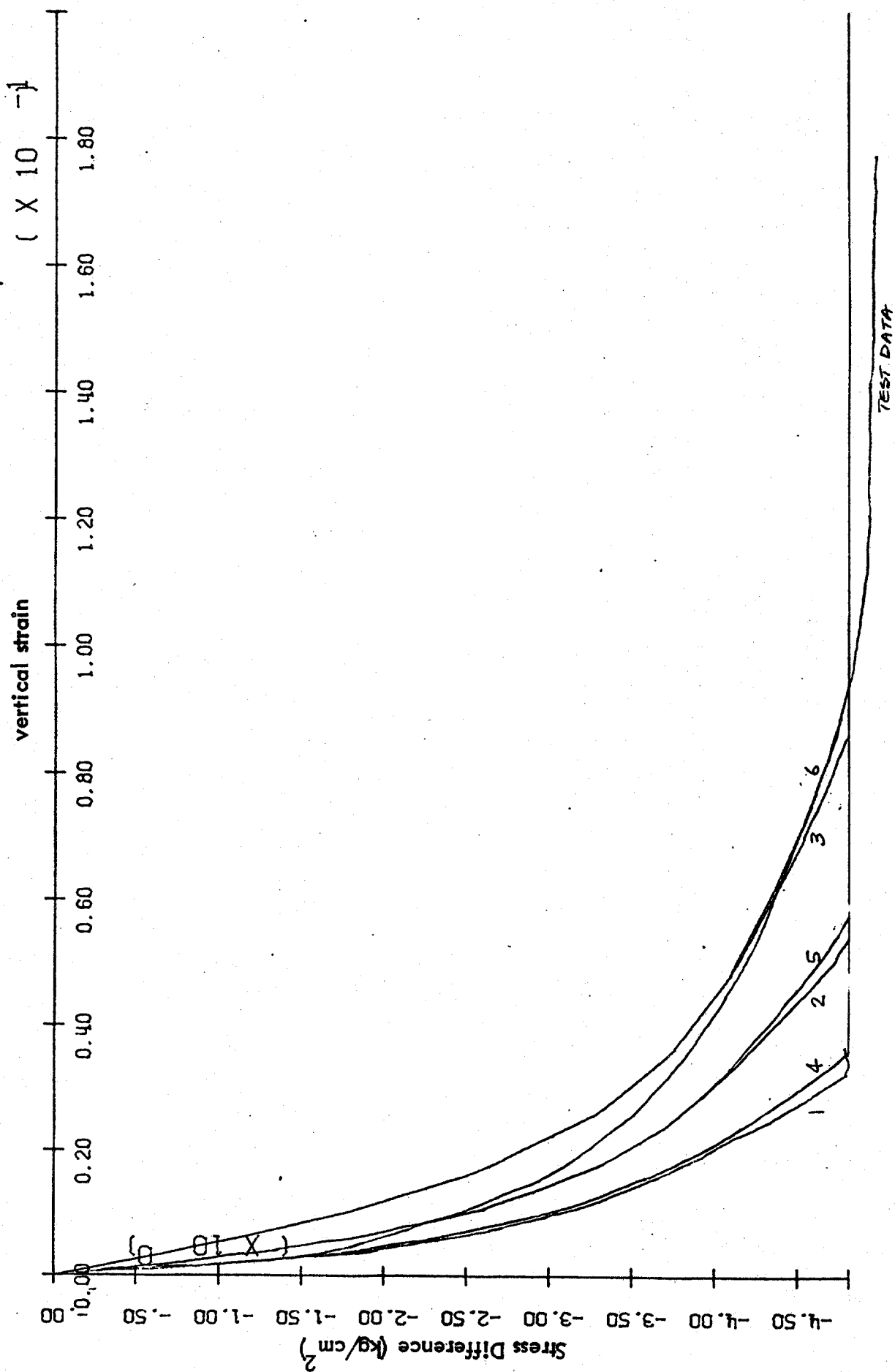


Figure 4 . Stress Difference-Vertical strain, compression test, case (1)

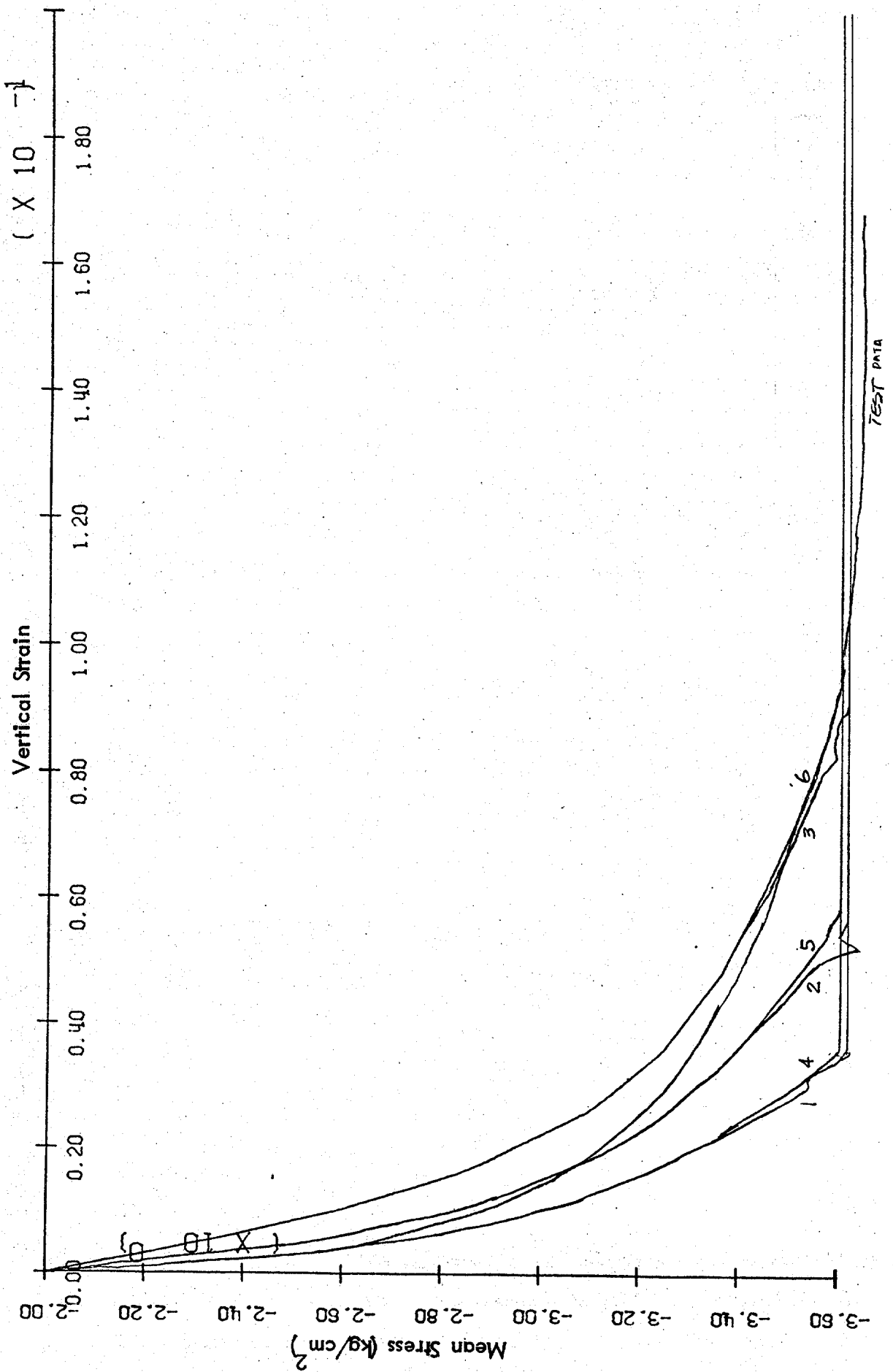


Figure 5 . Mean Stress-Vertical Strain, compression test, case (I)

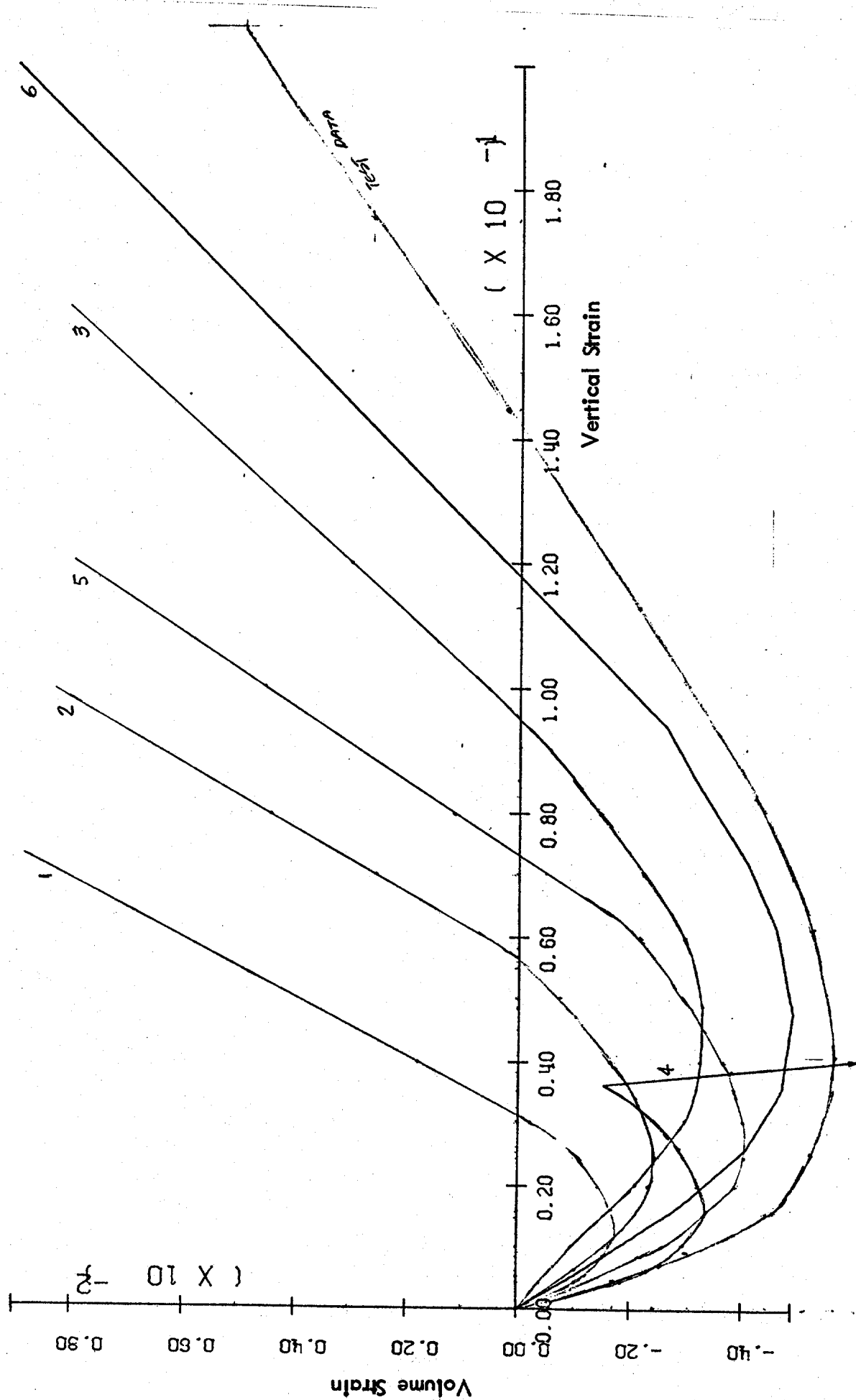


Figure 6 . Volume strain-Vertical strain, case (I)

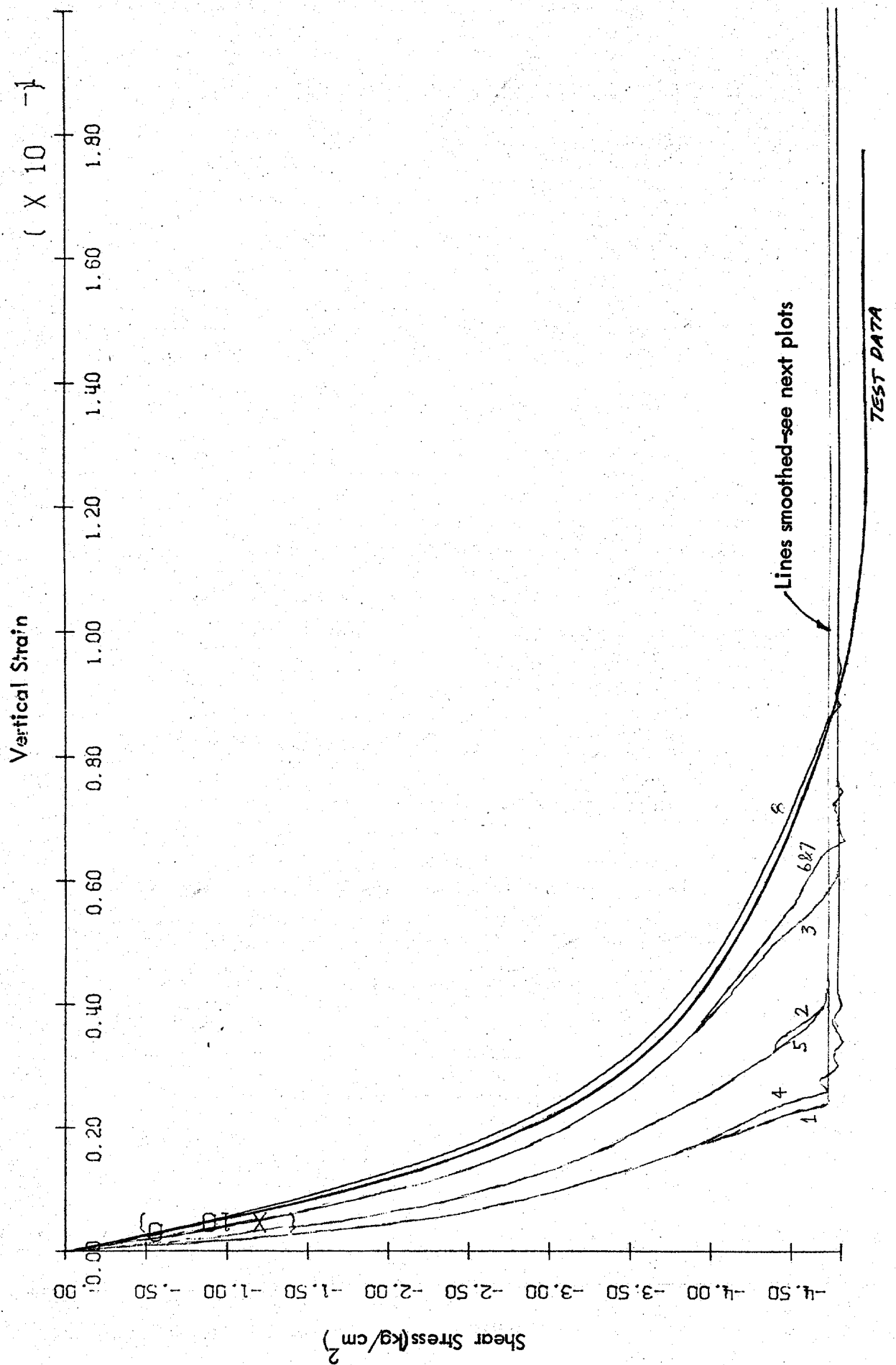


Figure 7 . Shear stress - Vertical strain compression test, case (2)

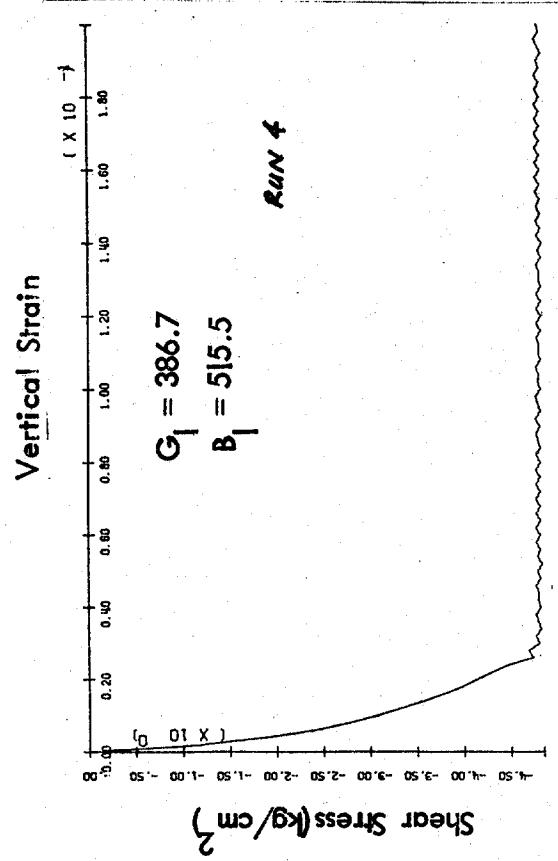
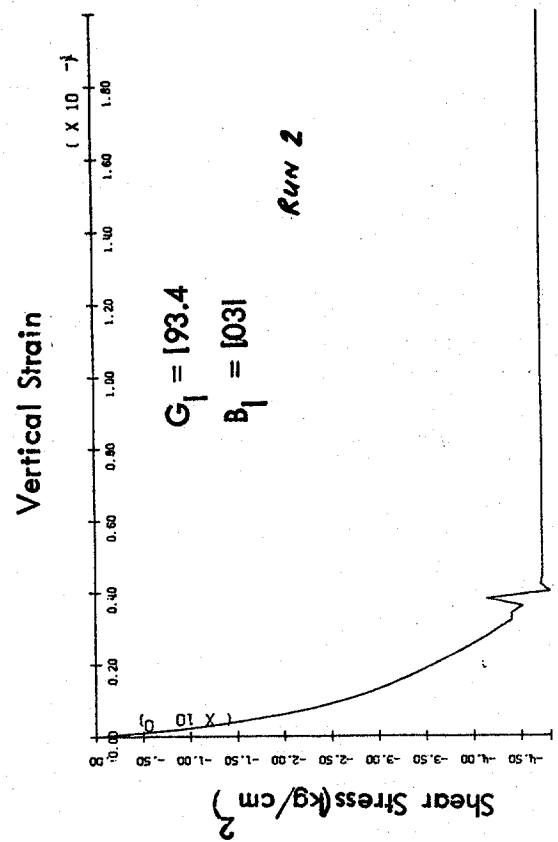
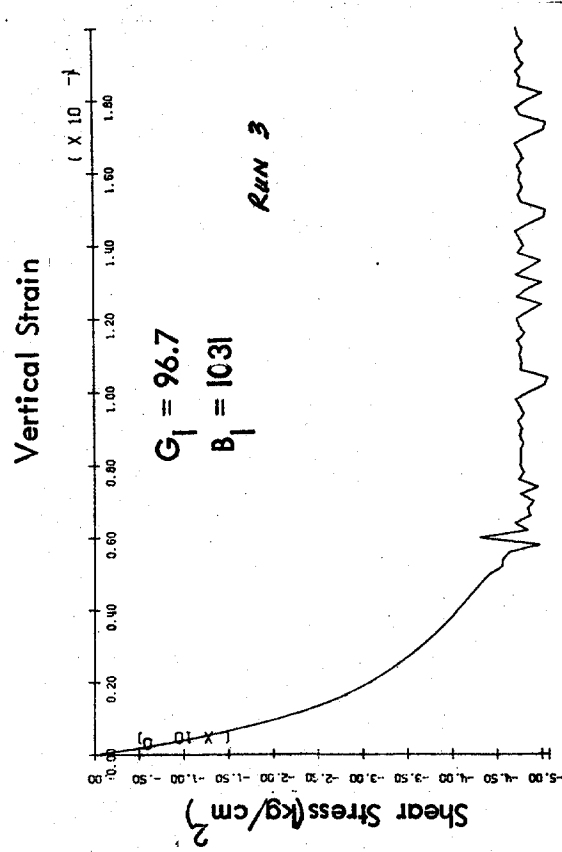
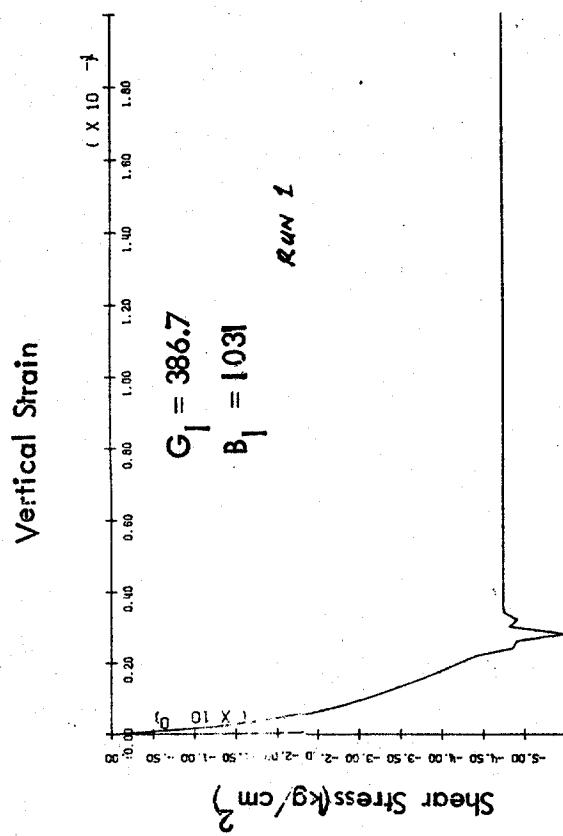


Figure 7 . (cont'd)

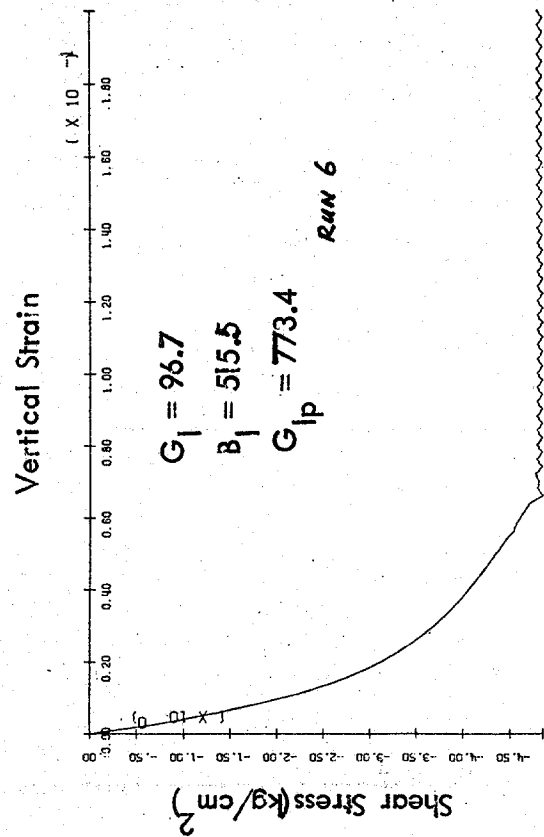
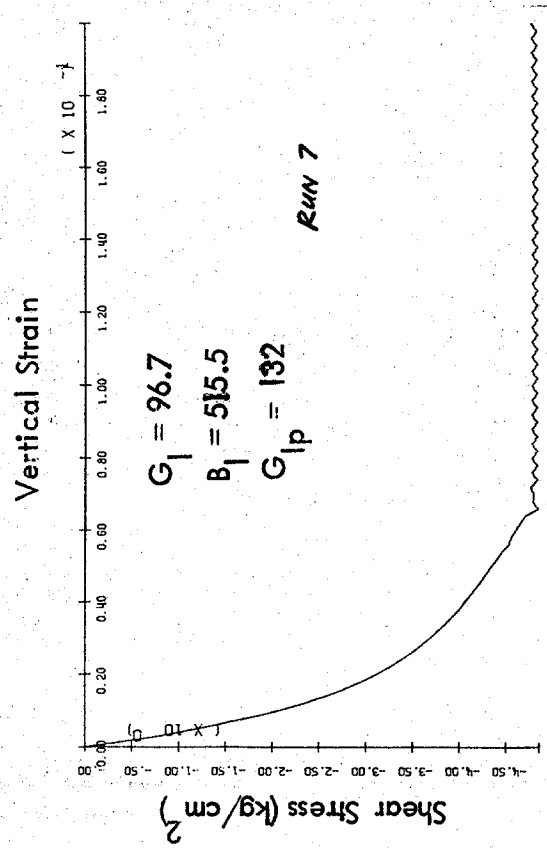
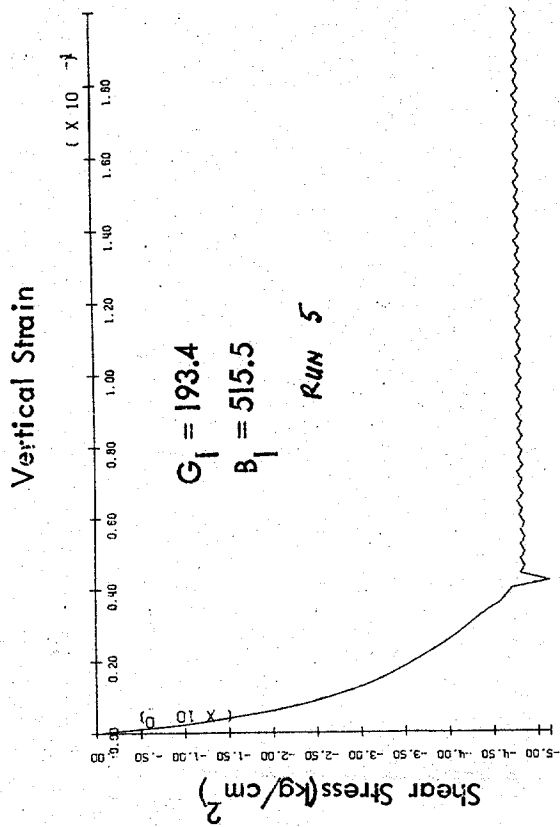


Figure 7 . (cont'd)

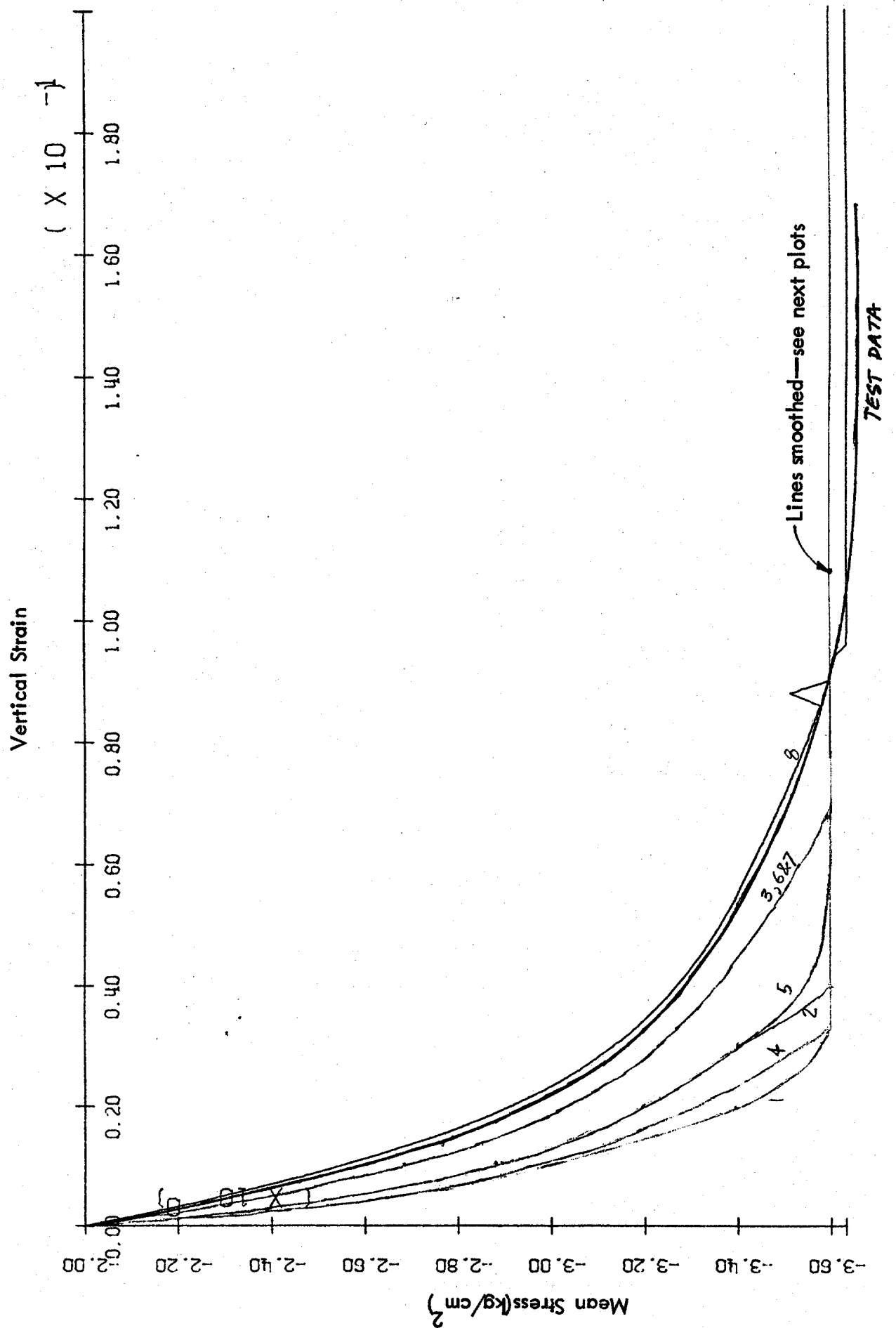


Figure 8 . Mean stress - Vertical strain compression test, case (2)

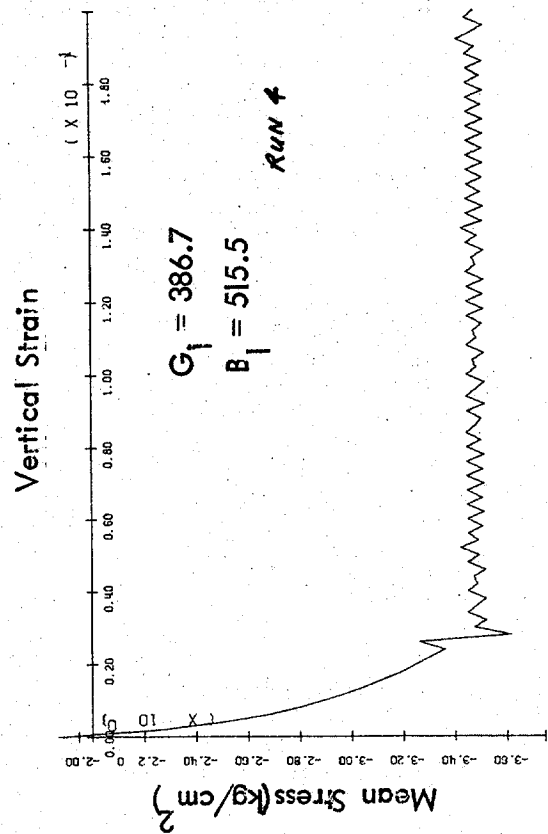
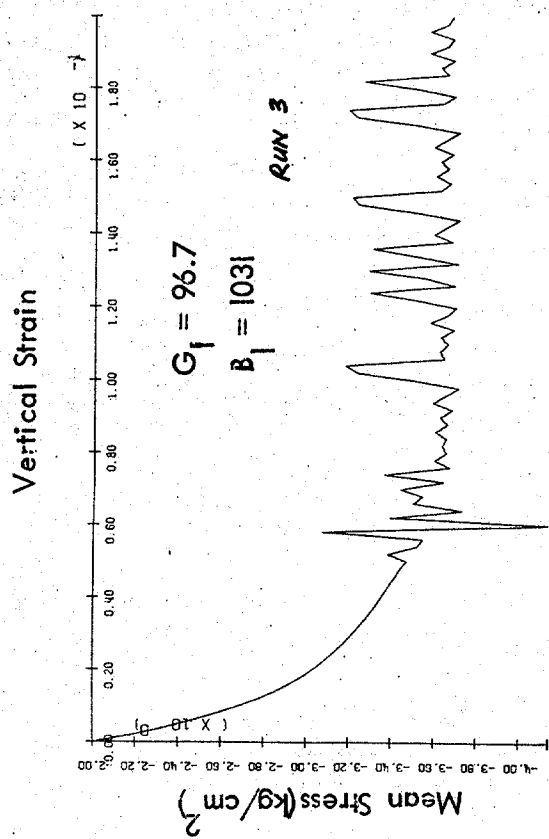
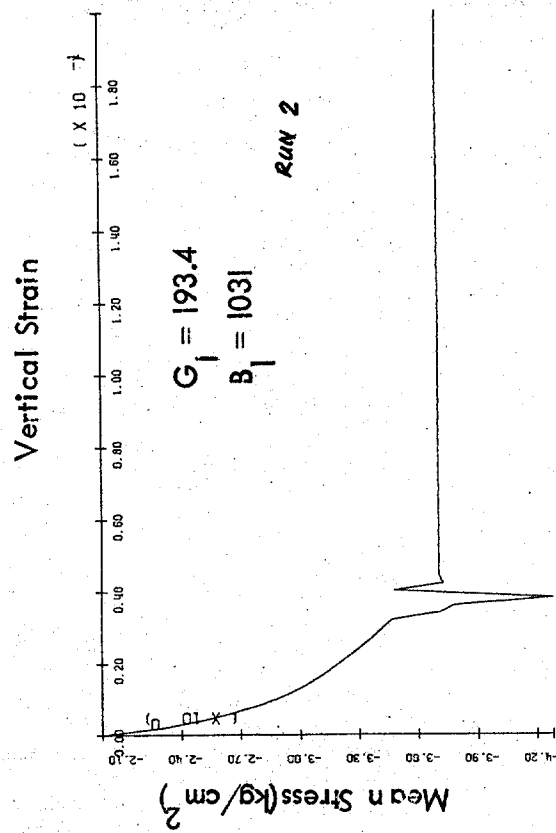
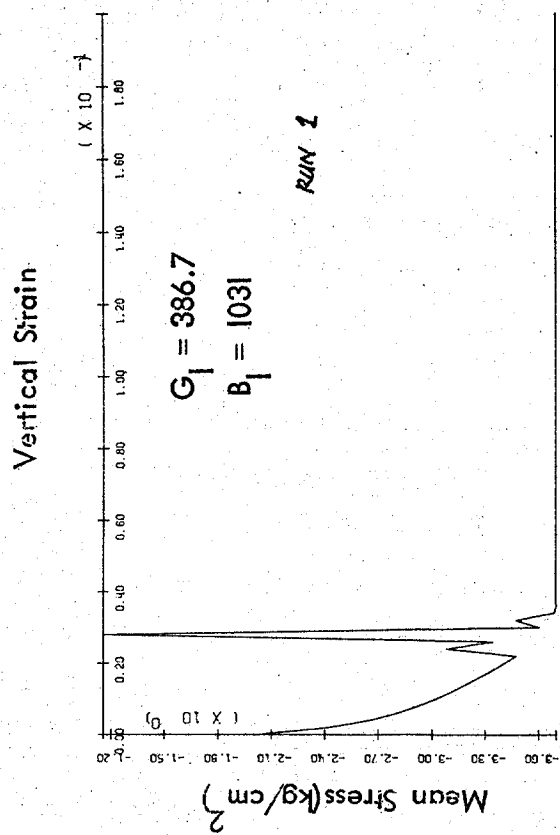


Figure 8. (cont'd)

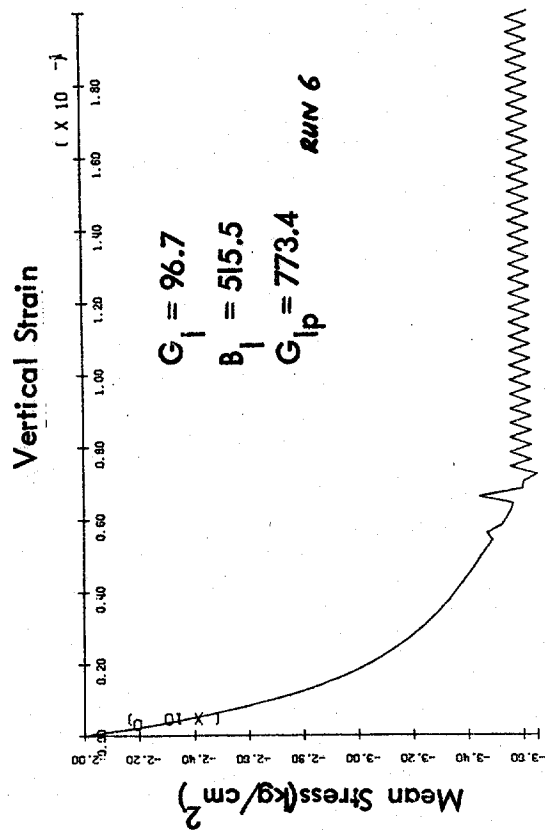
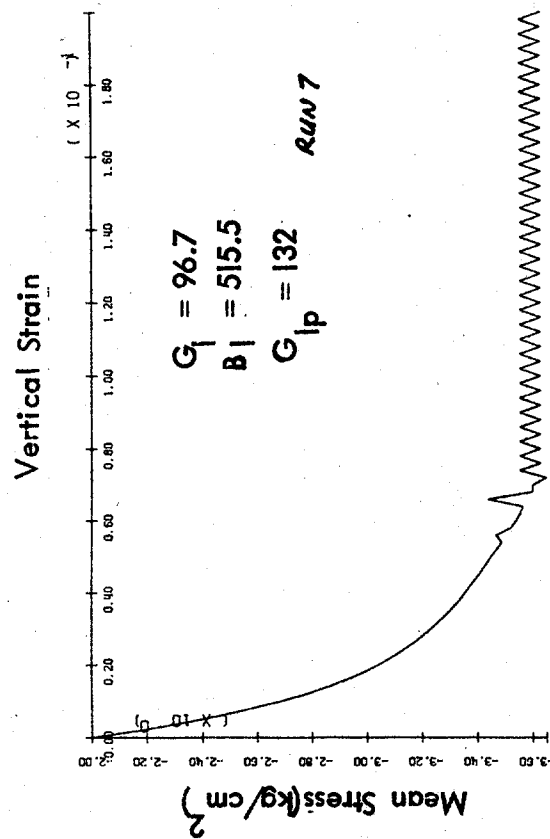
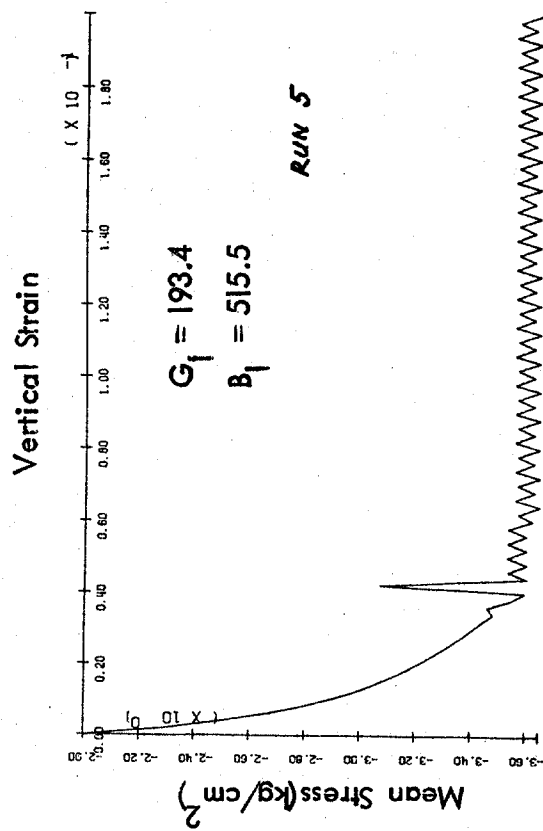


Figure 8. (cont'd)

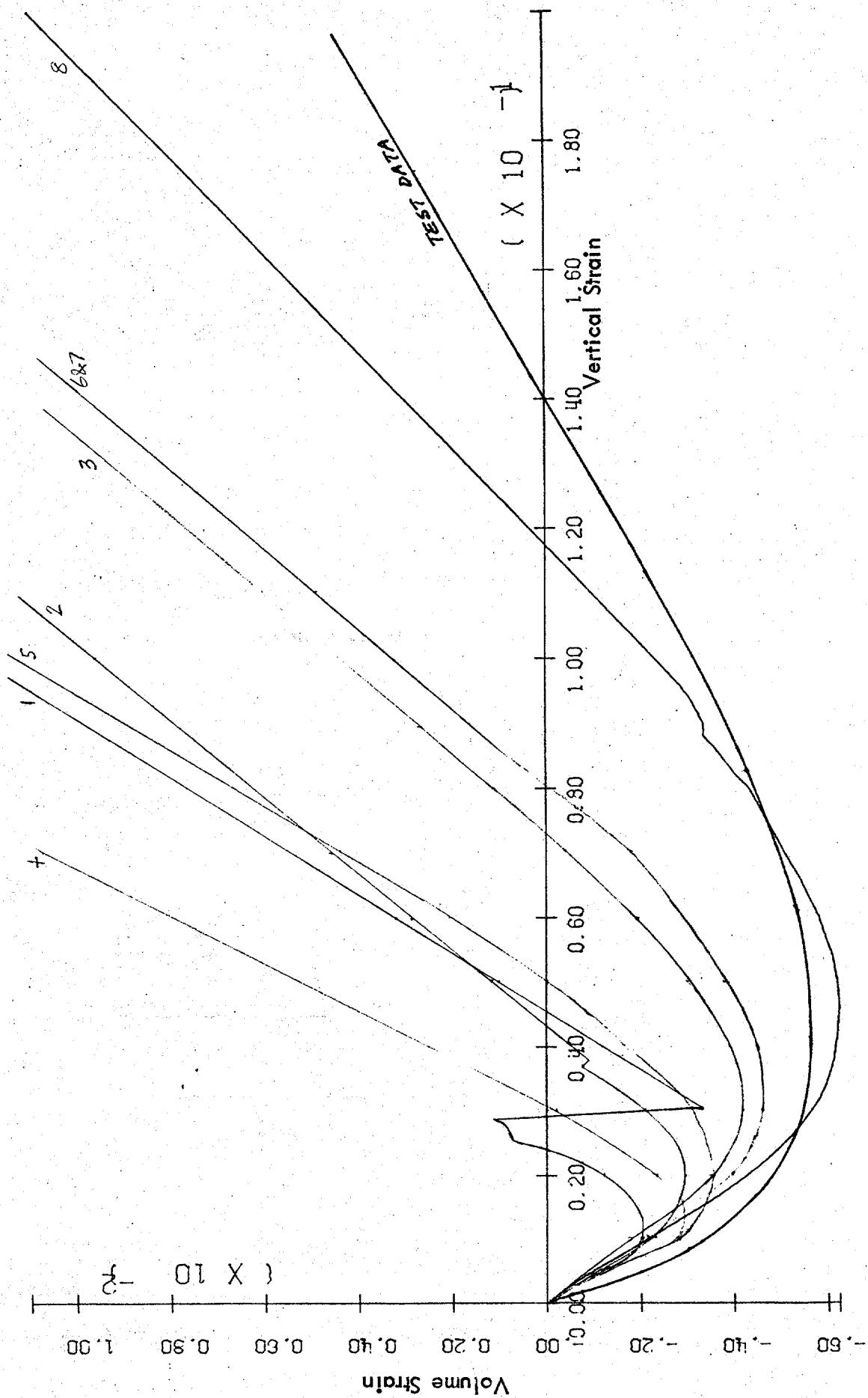


Figure 9. Volume strain - Vertical strain compression test, case (2)

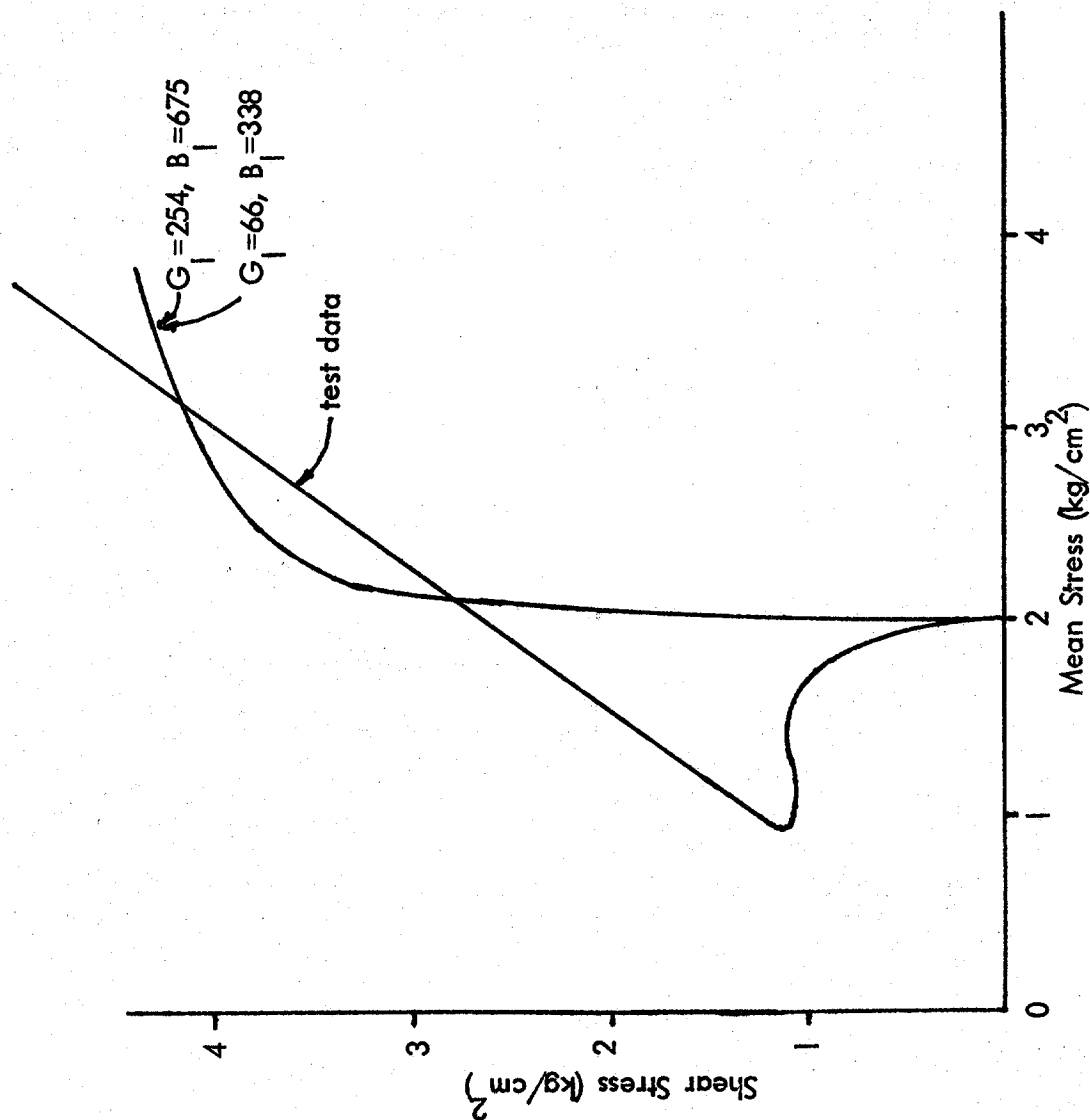


Figure 10a. Undrained Stress Path (II yield surfaces)

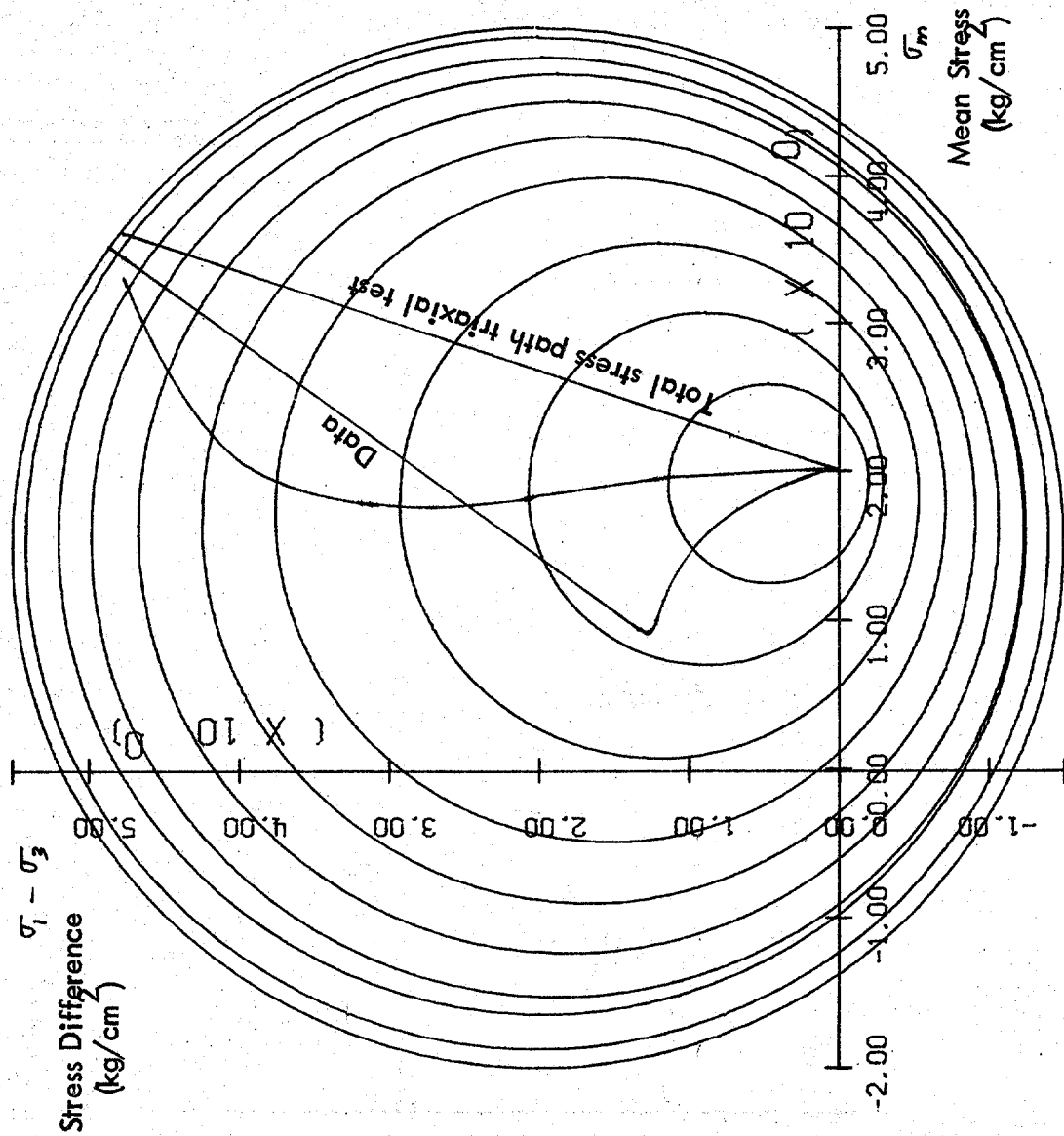


Figure 10b. Yield surfaces and stress path, case (1)

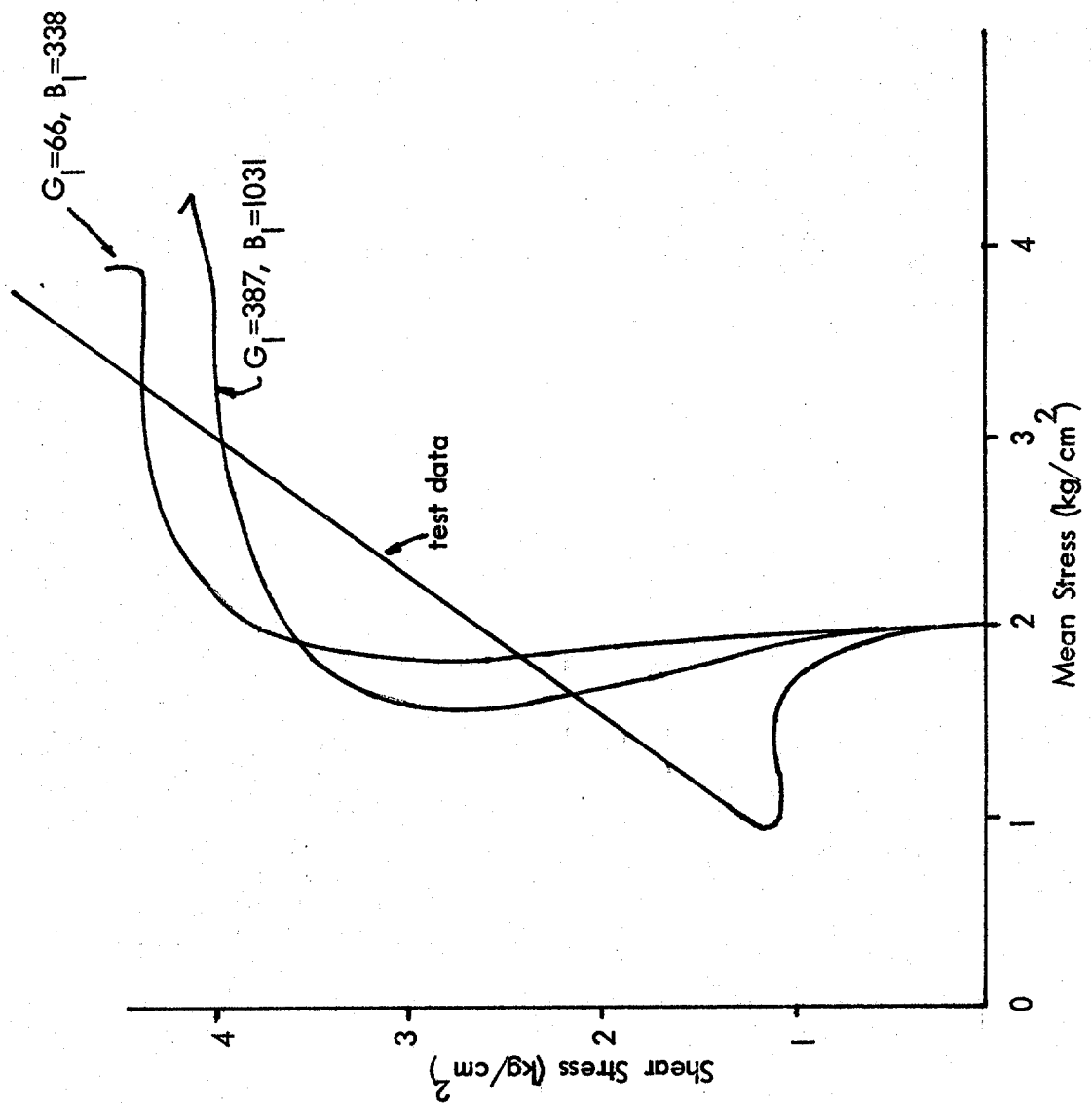
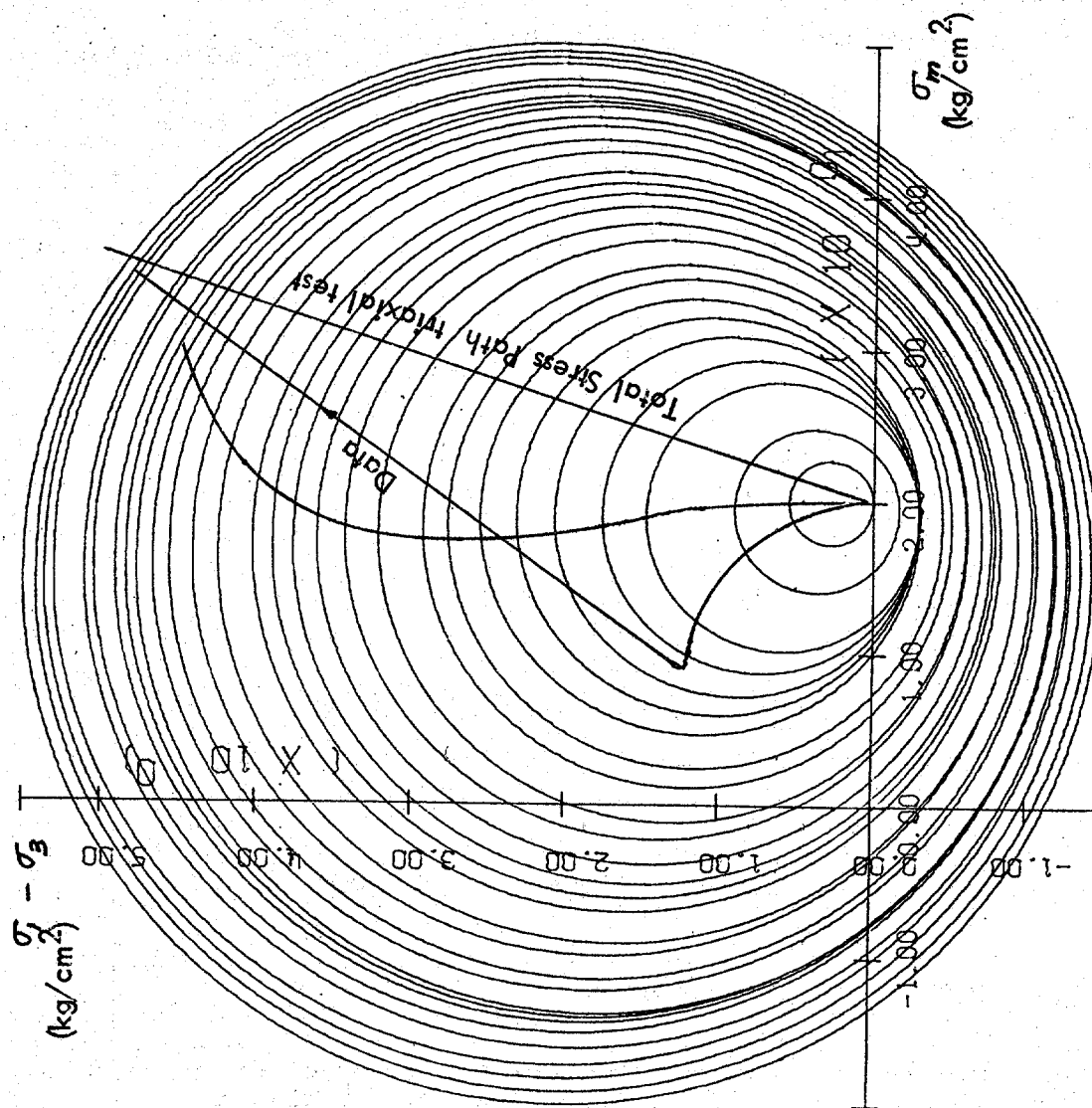


Figure 11a. Undrained Stress Path (29 yield surfaces)



YIELD SURFACES

AXIAL TESTS DATA

Figure 11b. Yield Surfaces and Stress Path, case (2)

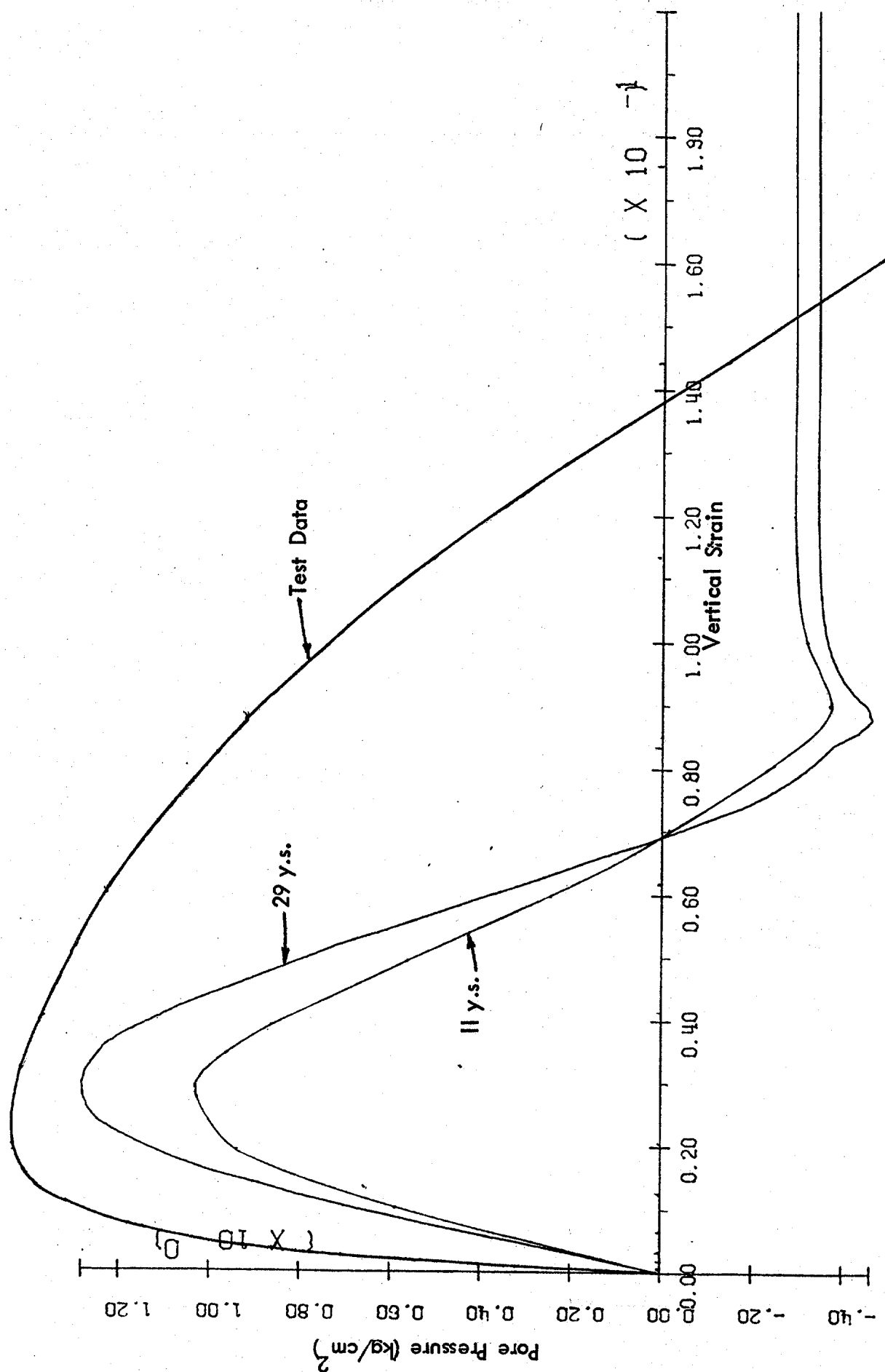


Figure 12. Pore Pressure - Vertical Strain, $G_1=66$, $B_1=338$.

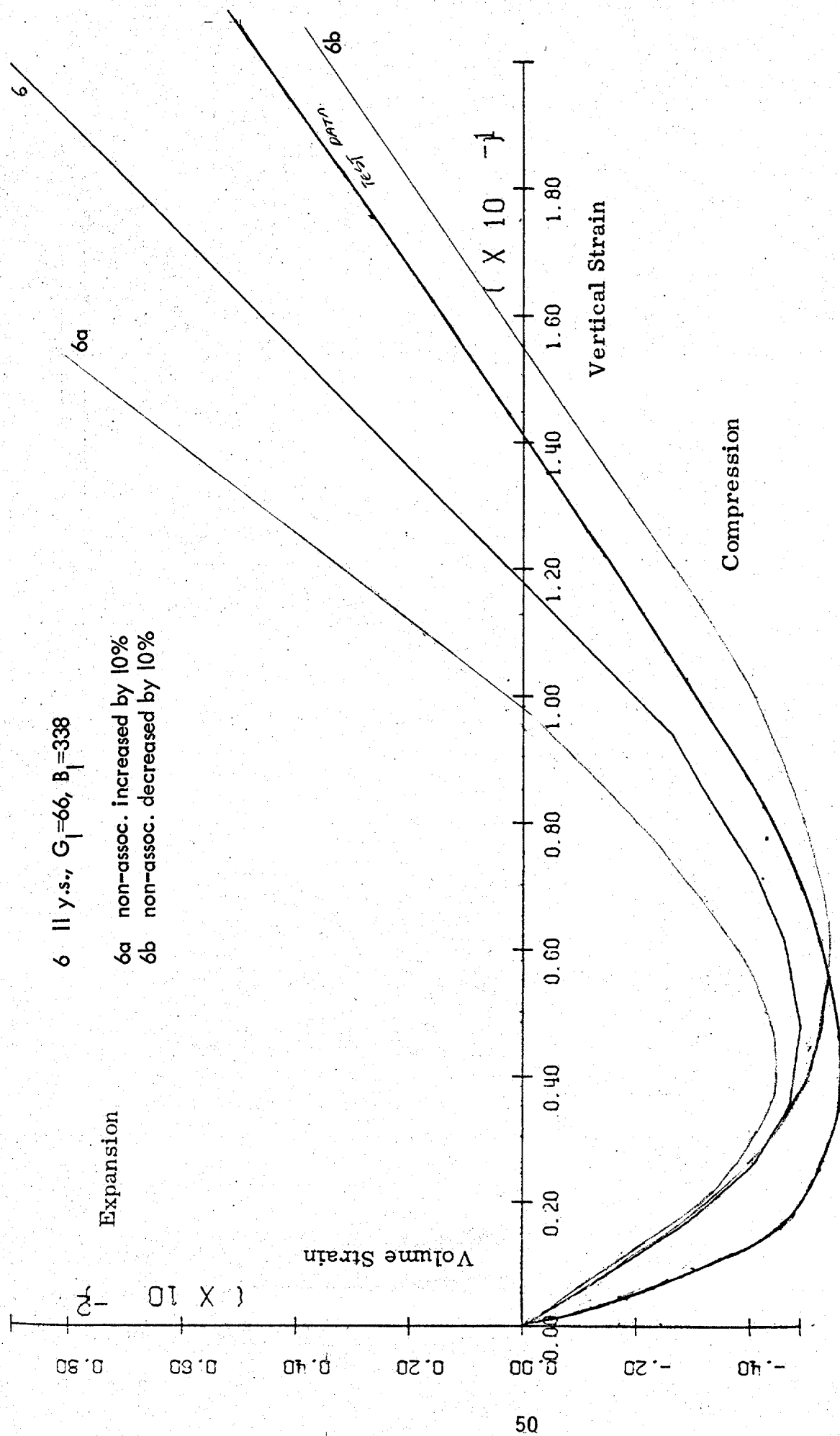


Figure 13 . Effect of non-associativity on Volume Strain.

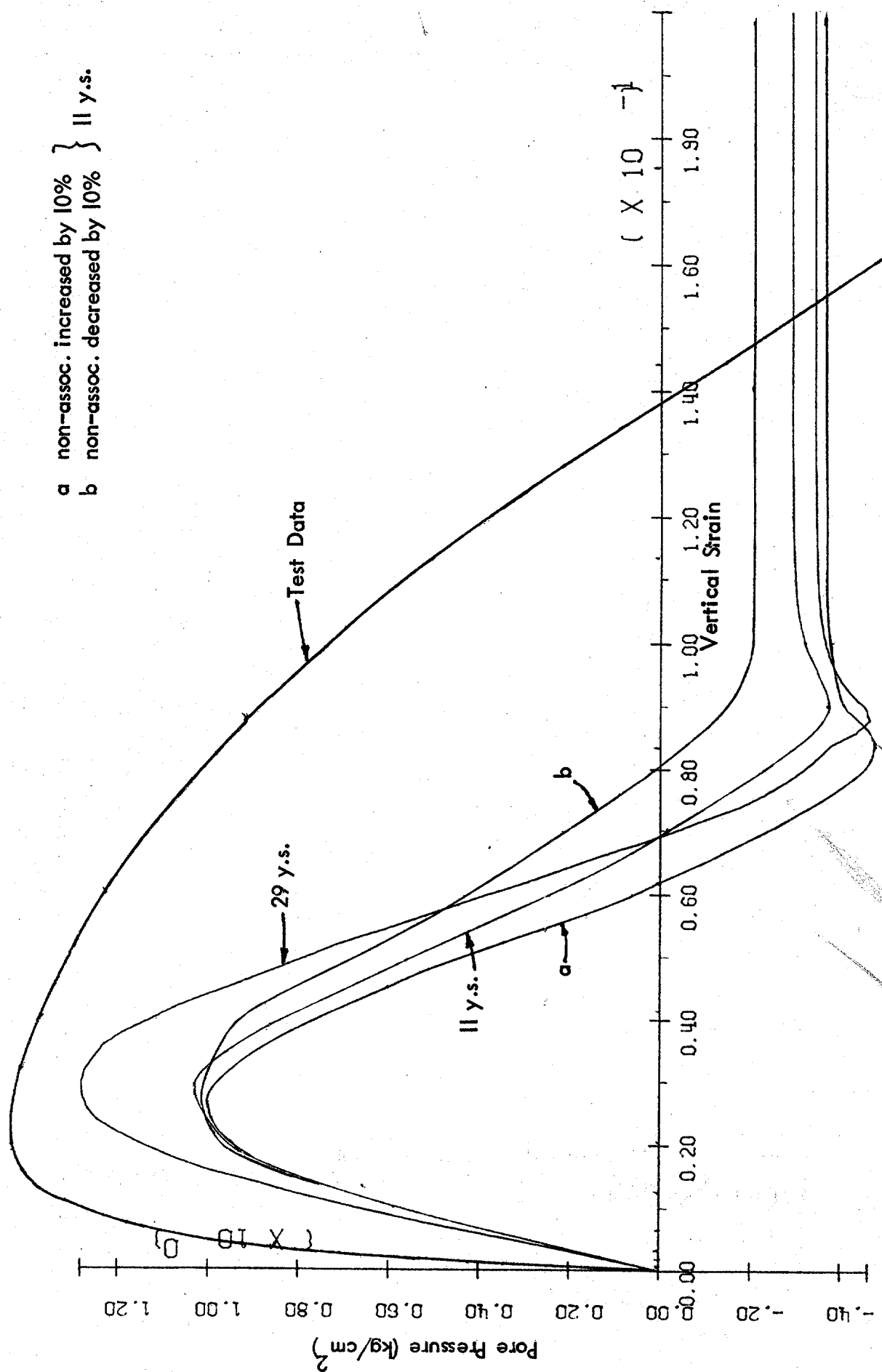


Figure 14. Pore Pressure - Vertical Strain, $G_1=66$, $B_1=338$.

$$B_1 = 387 \text{ kg/cm}^2, G_1 = 1031 \text{ kg/cm}^2$$

Test No. Cyc-2.0-3

$$e = 0.760; D_r = 30.0\%$$

$$\sigma'_{3c} = 2.00 \text{ kg/cm}^2$$

$$q = \frac{\sigma_1 - \sigma_3}{2} \quad (\text{kg/cm}^2)$$

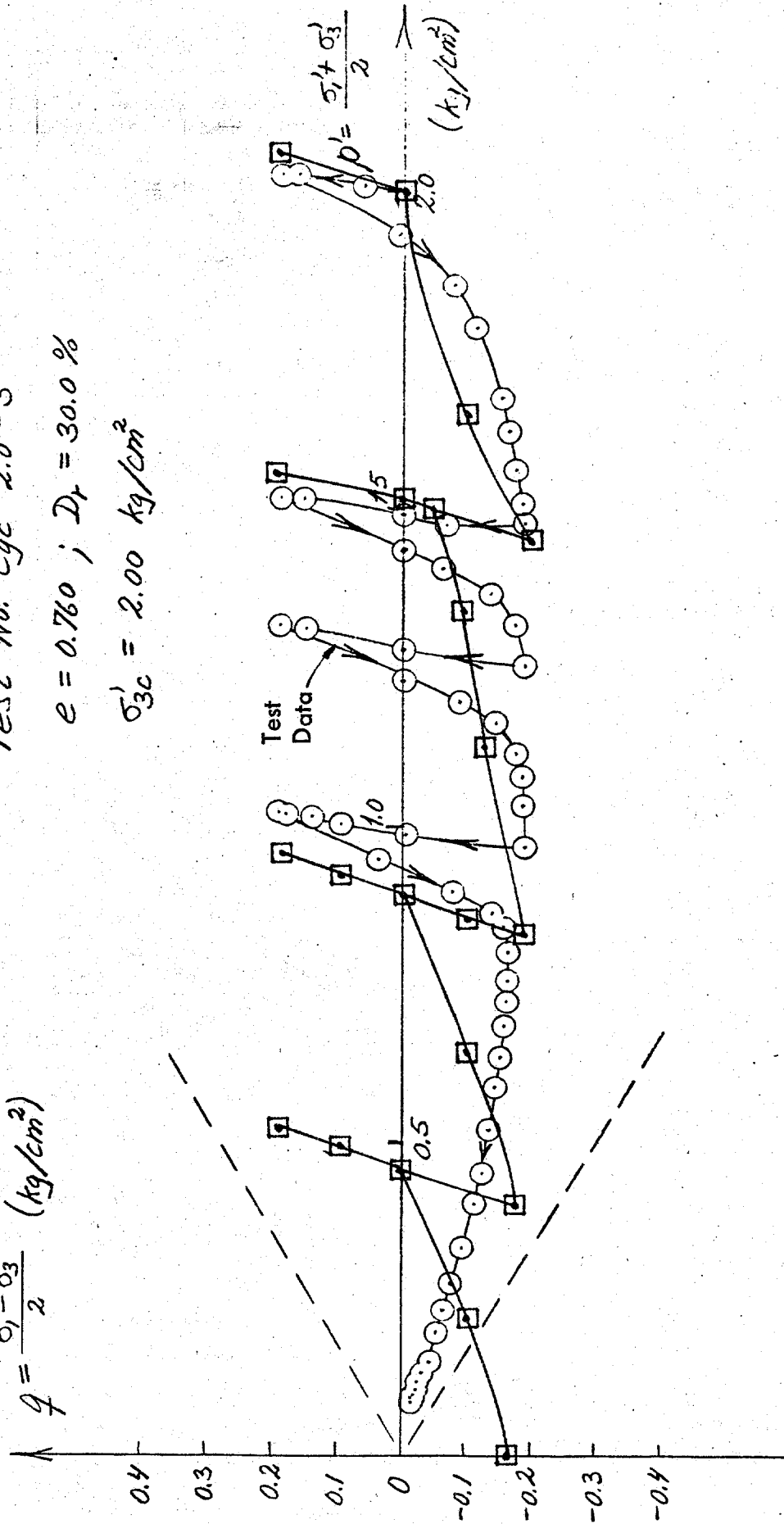


Figure 15 . Effective stress path, undrained cyclic test, case (2)

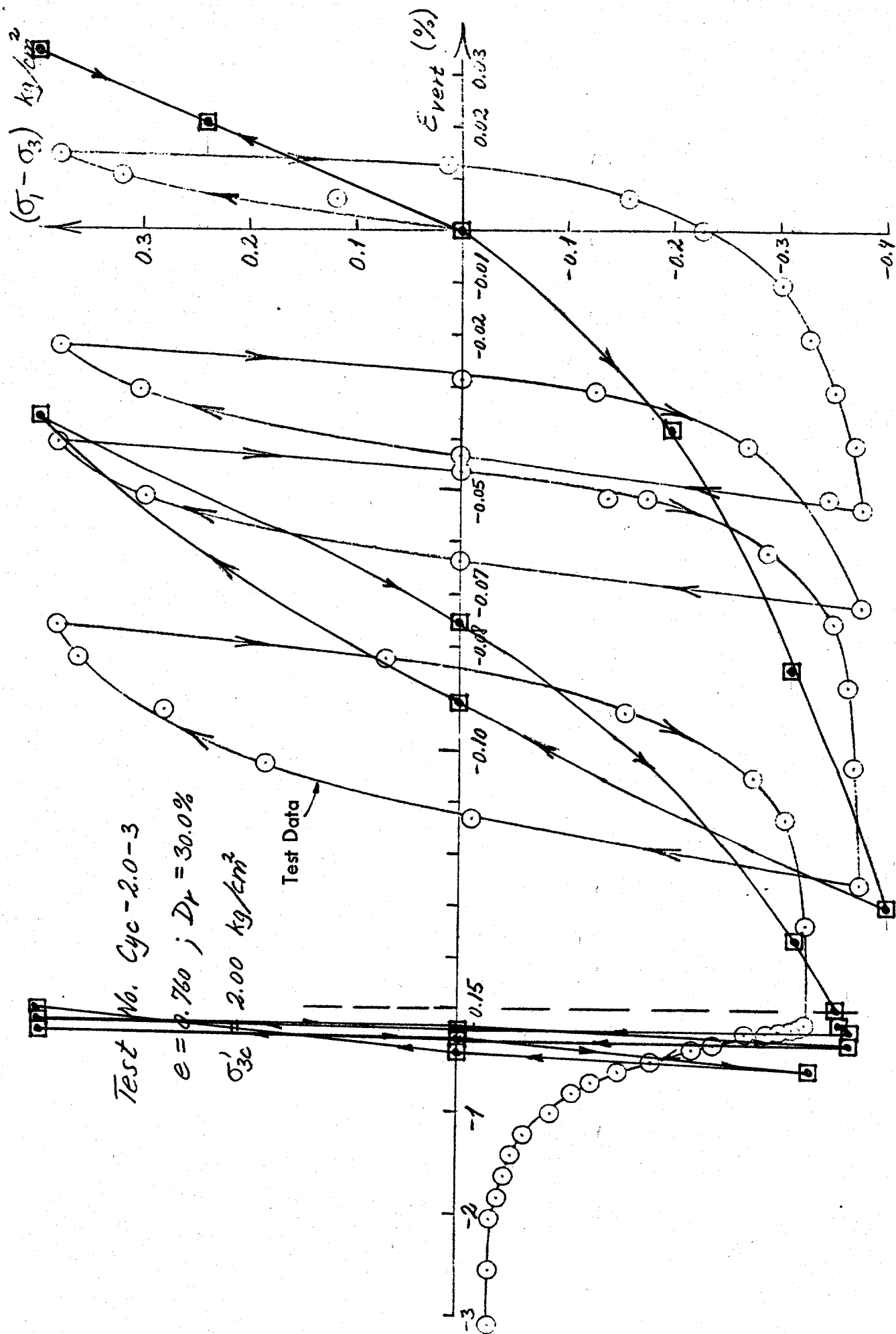


Figure 16 . Stress difference - Vertical strain, undrained cyclic test

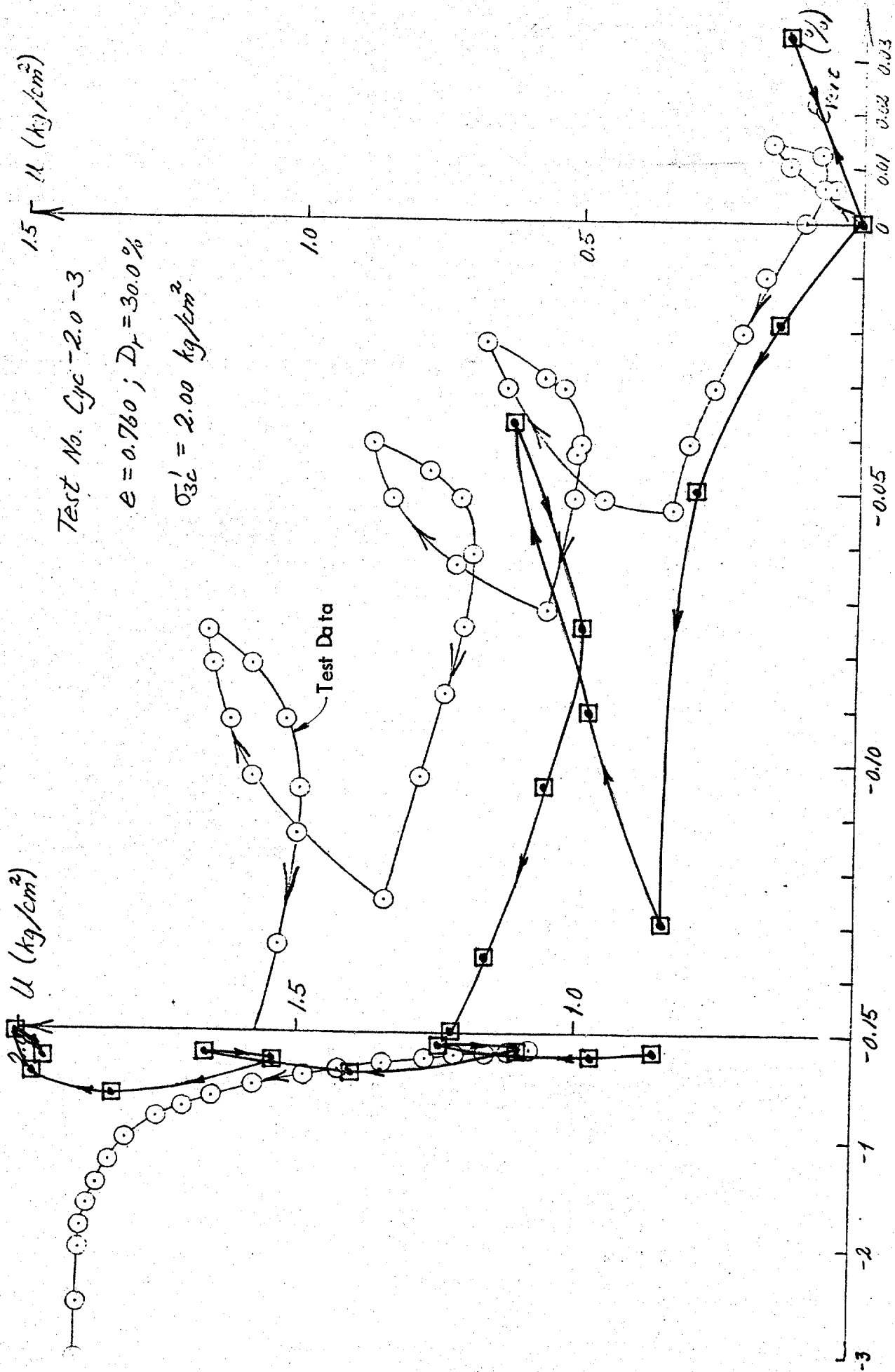


Figure 17. Pore water pressure - Vertical strain, undrained cyclic test

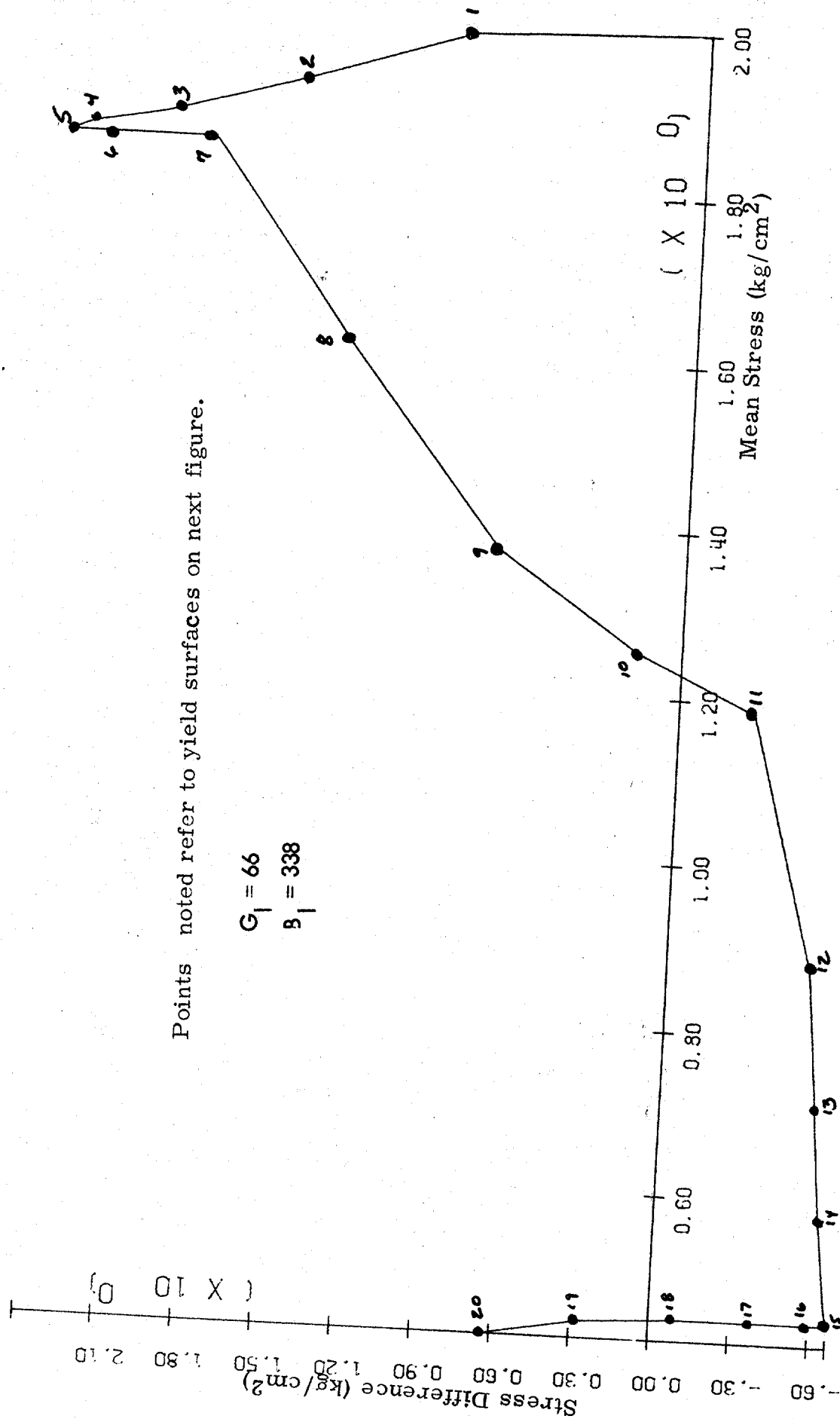


Figure 18. Stress path 1 cycle case2.

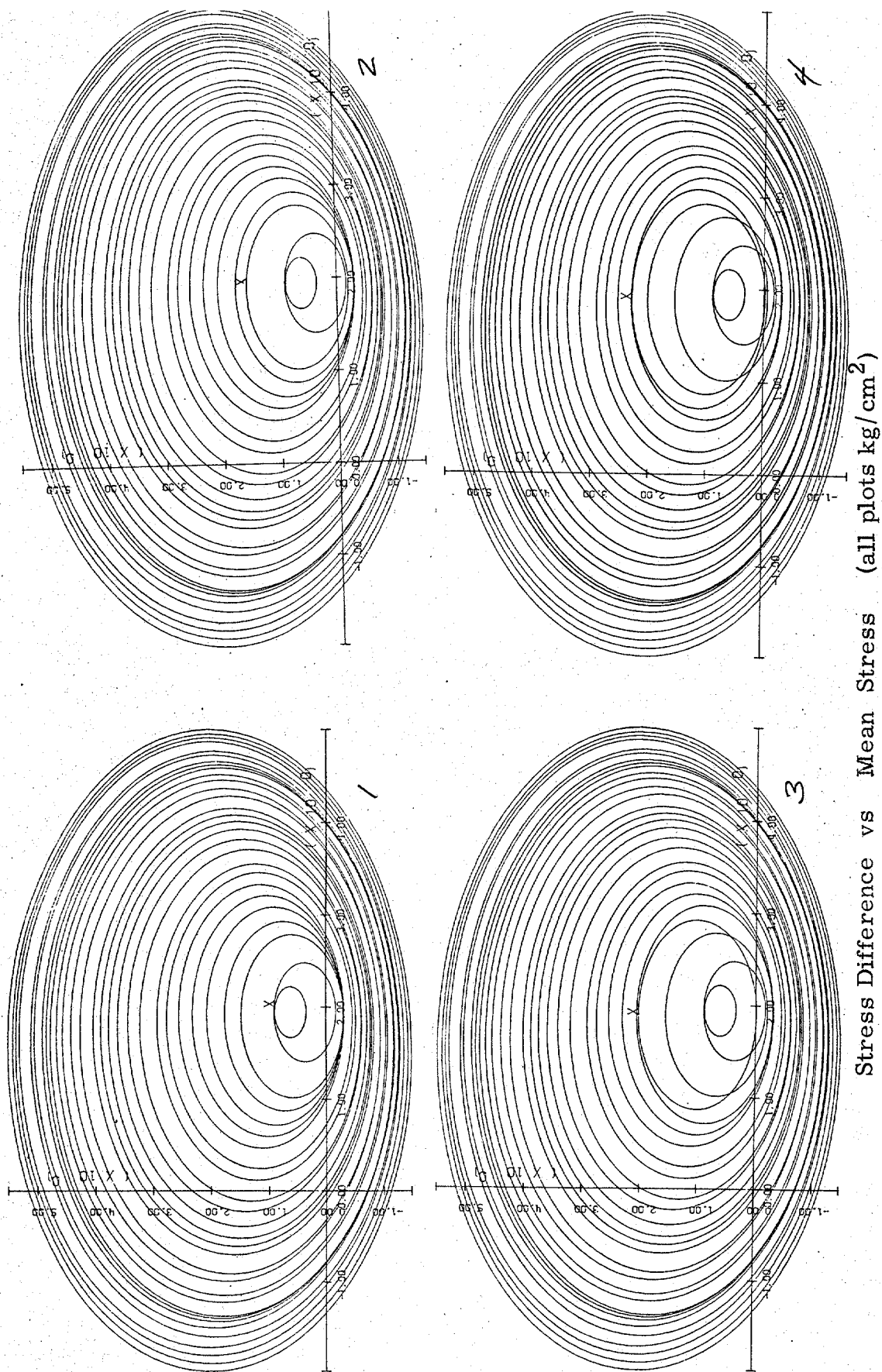


Figure 19. Yield surfaces at different loading points, refer to previous figure.

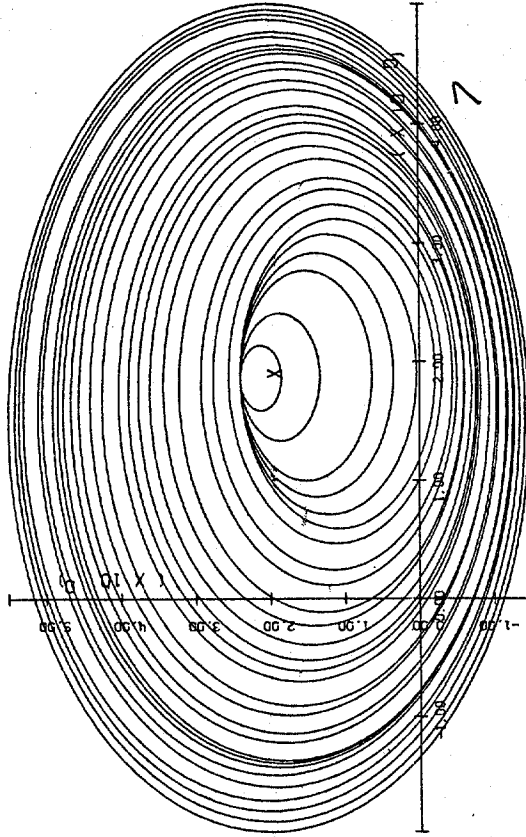
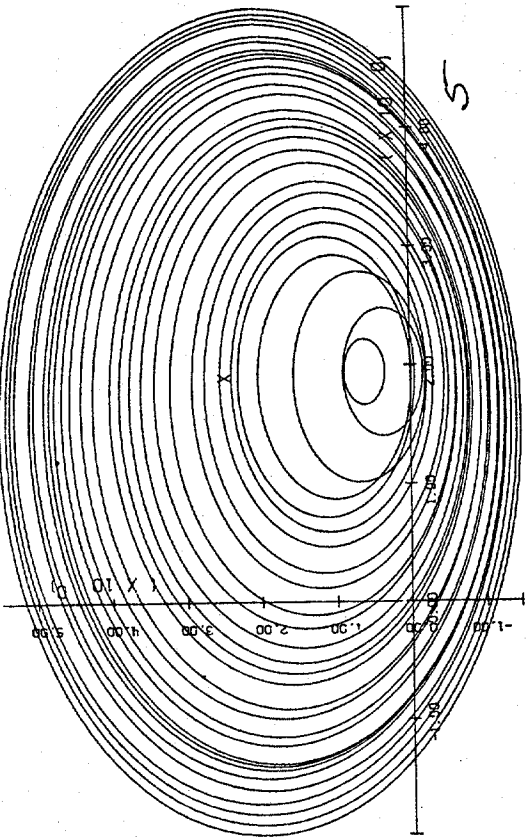
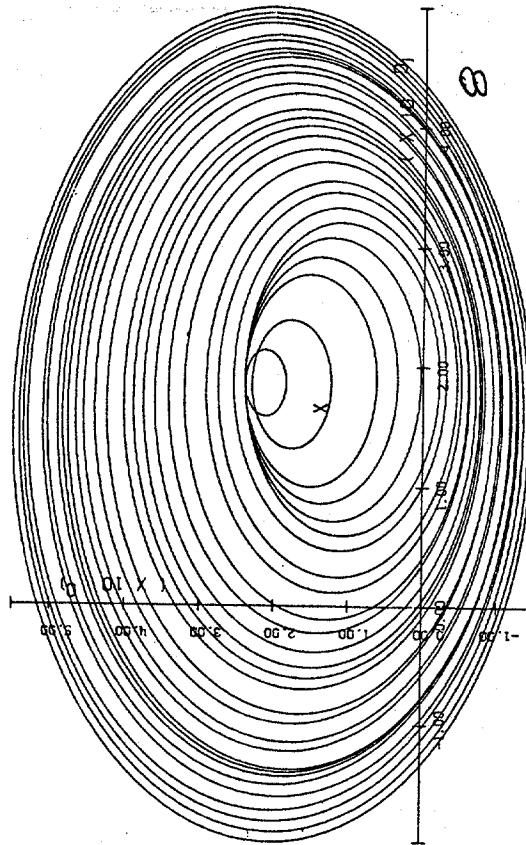
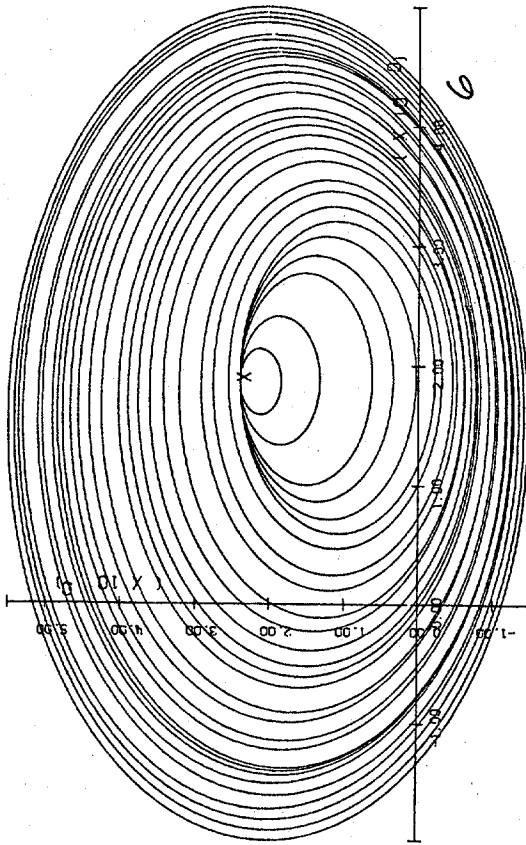


Figure 19. Continued.

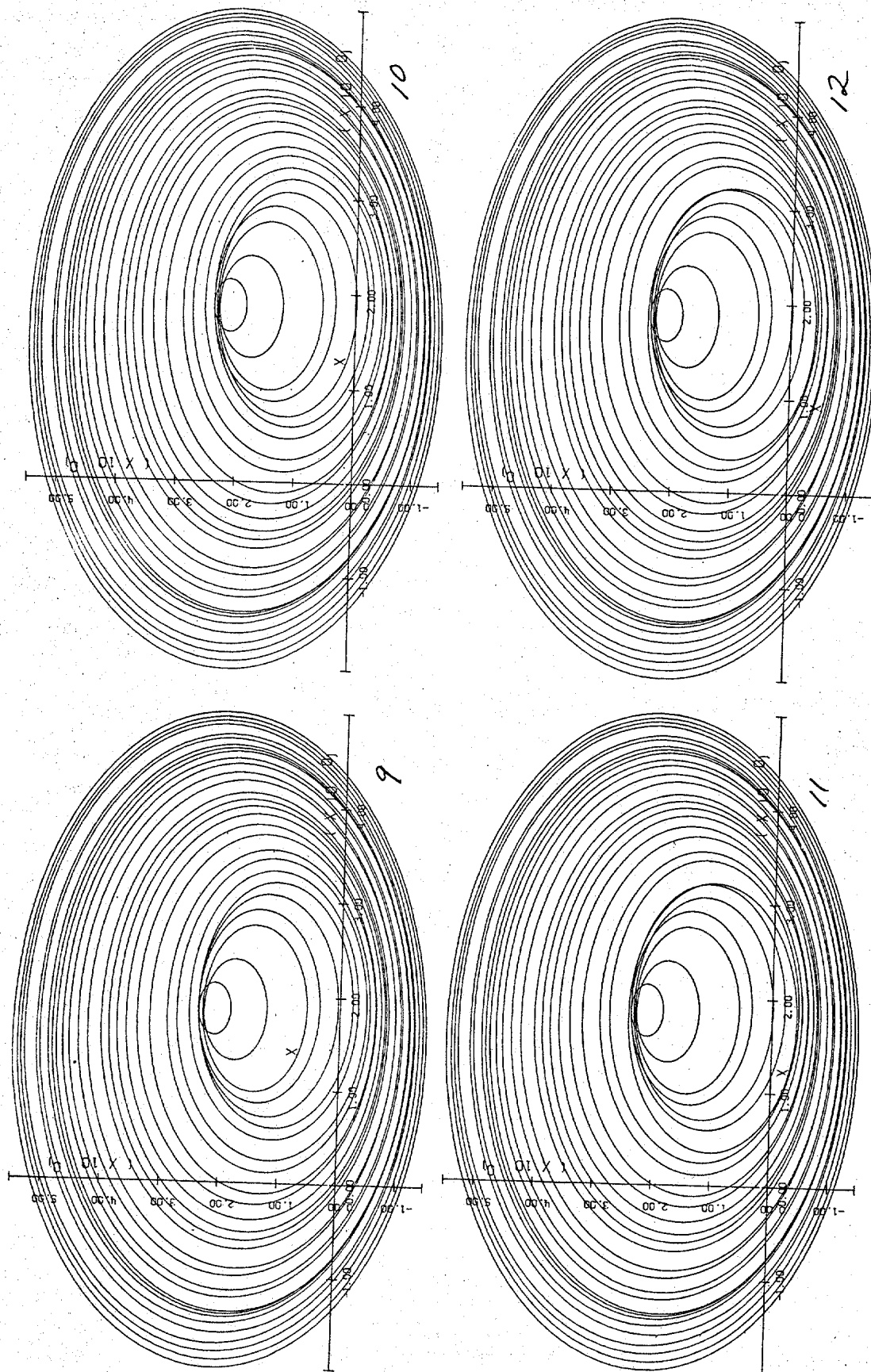


Figure 19. Continued.

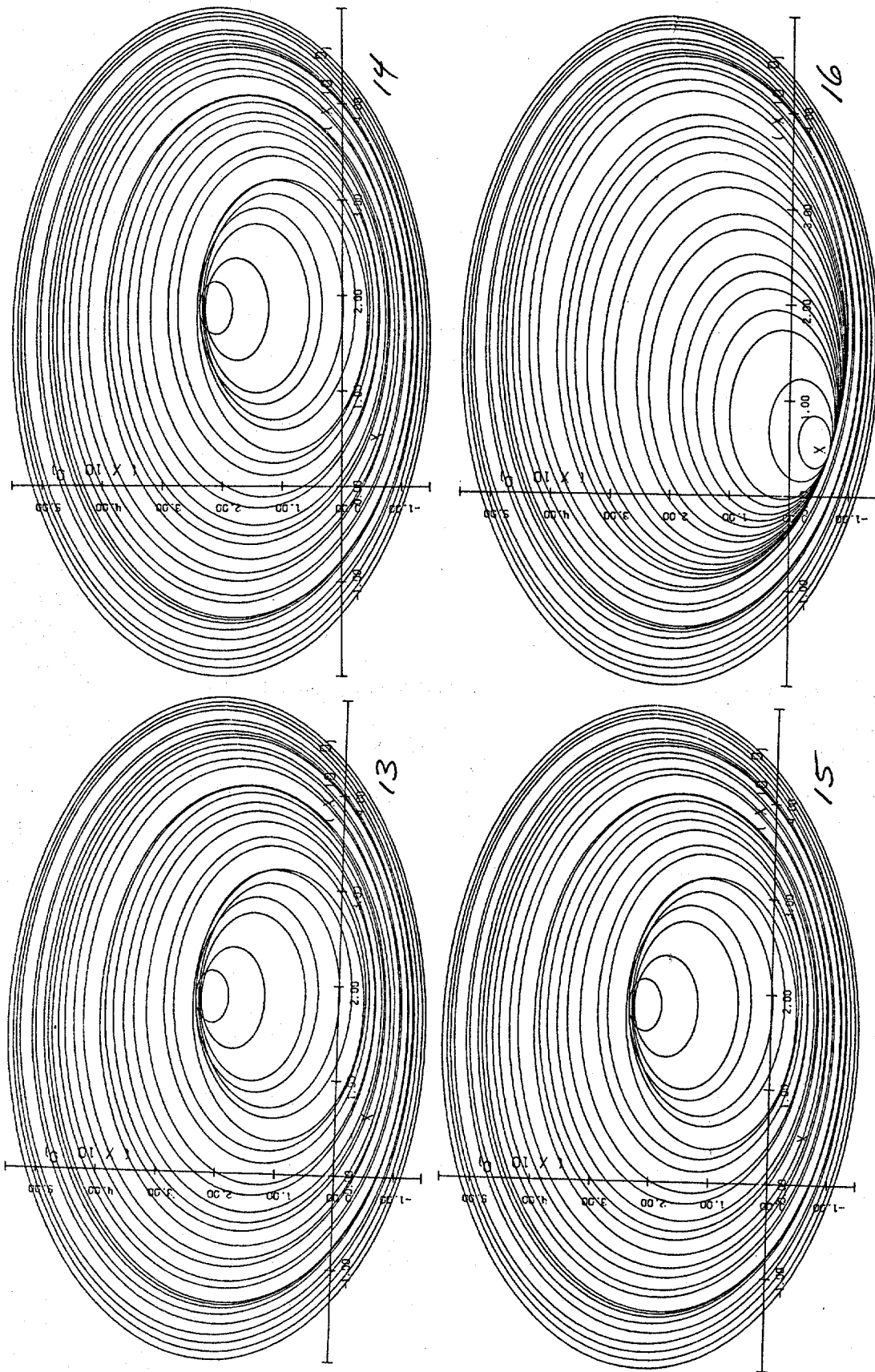


Figure 19. Continued.

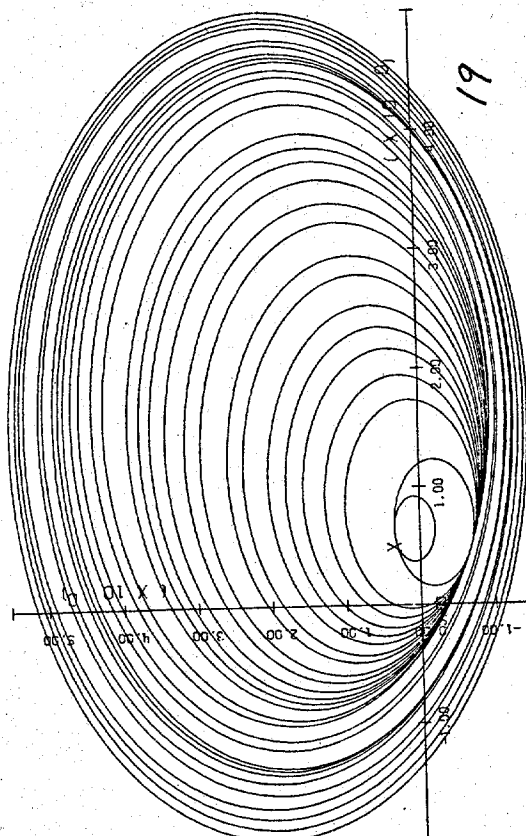
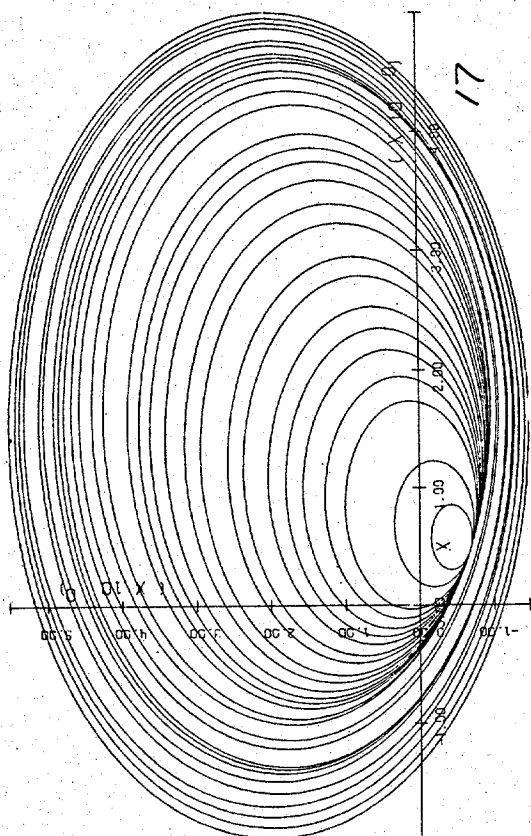
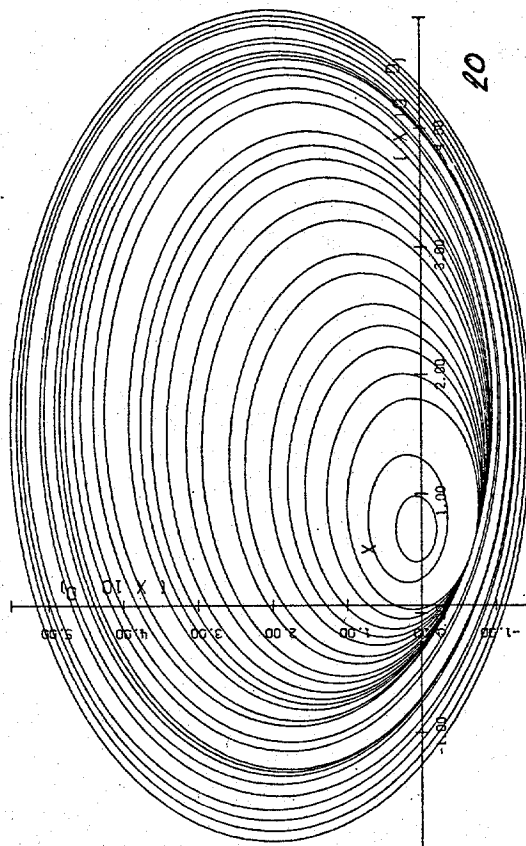
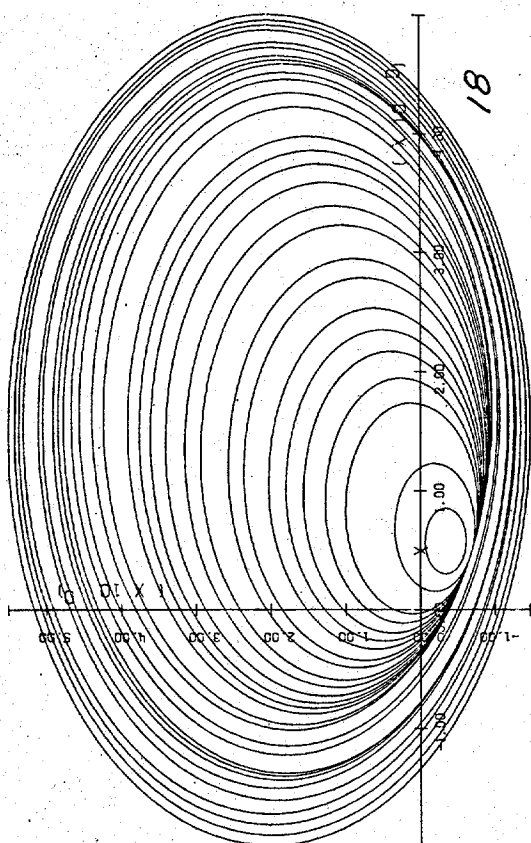


Figure 19. Continued.

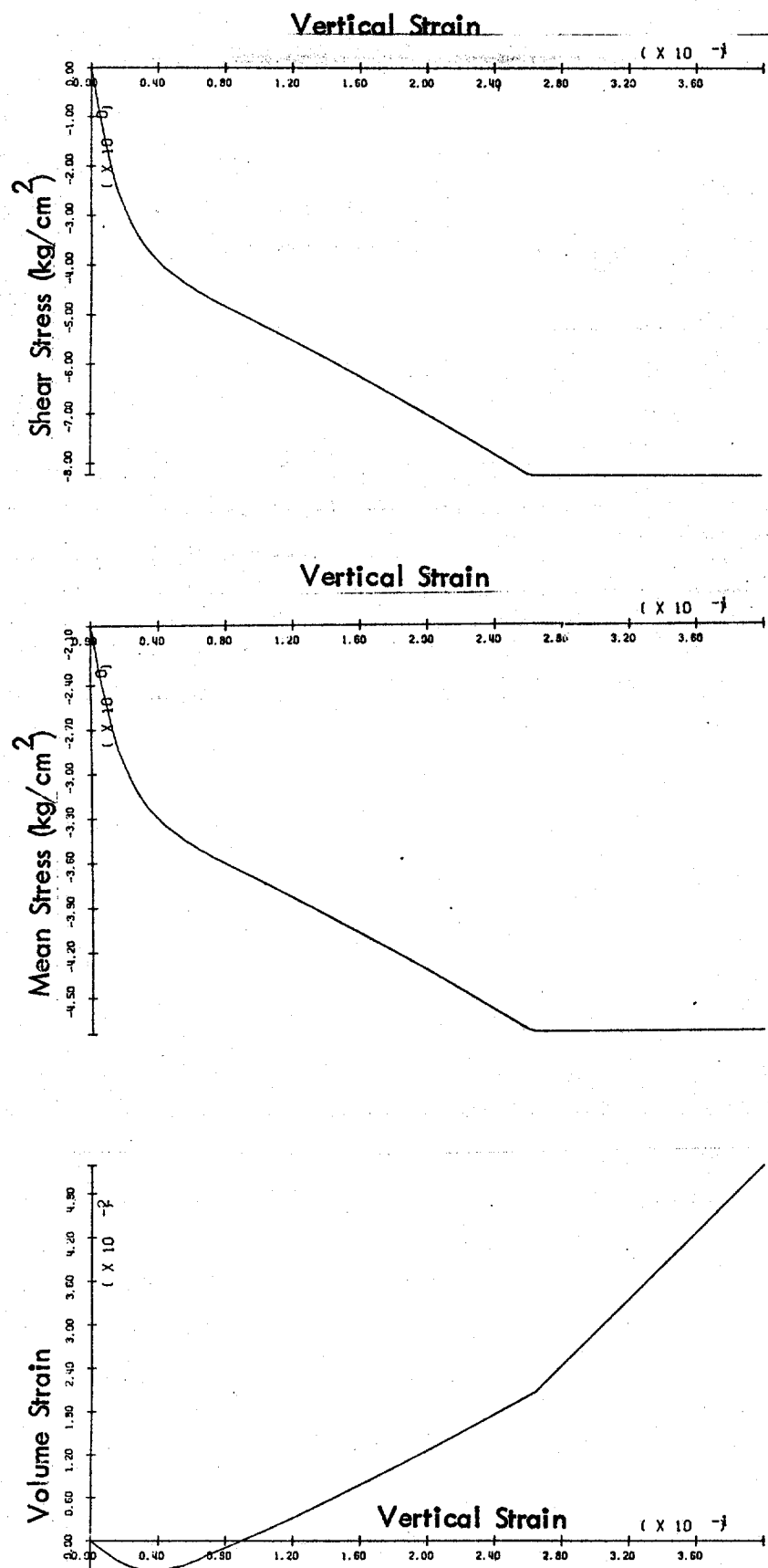


Figure 20. Effect of doubling the size of the 11th yield surface, model case (I).

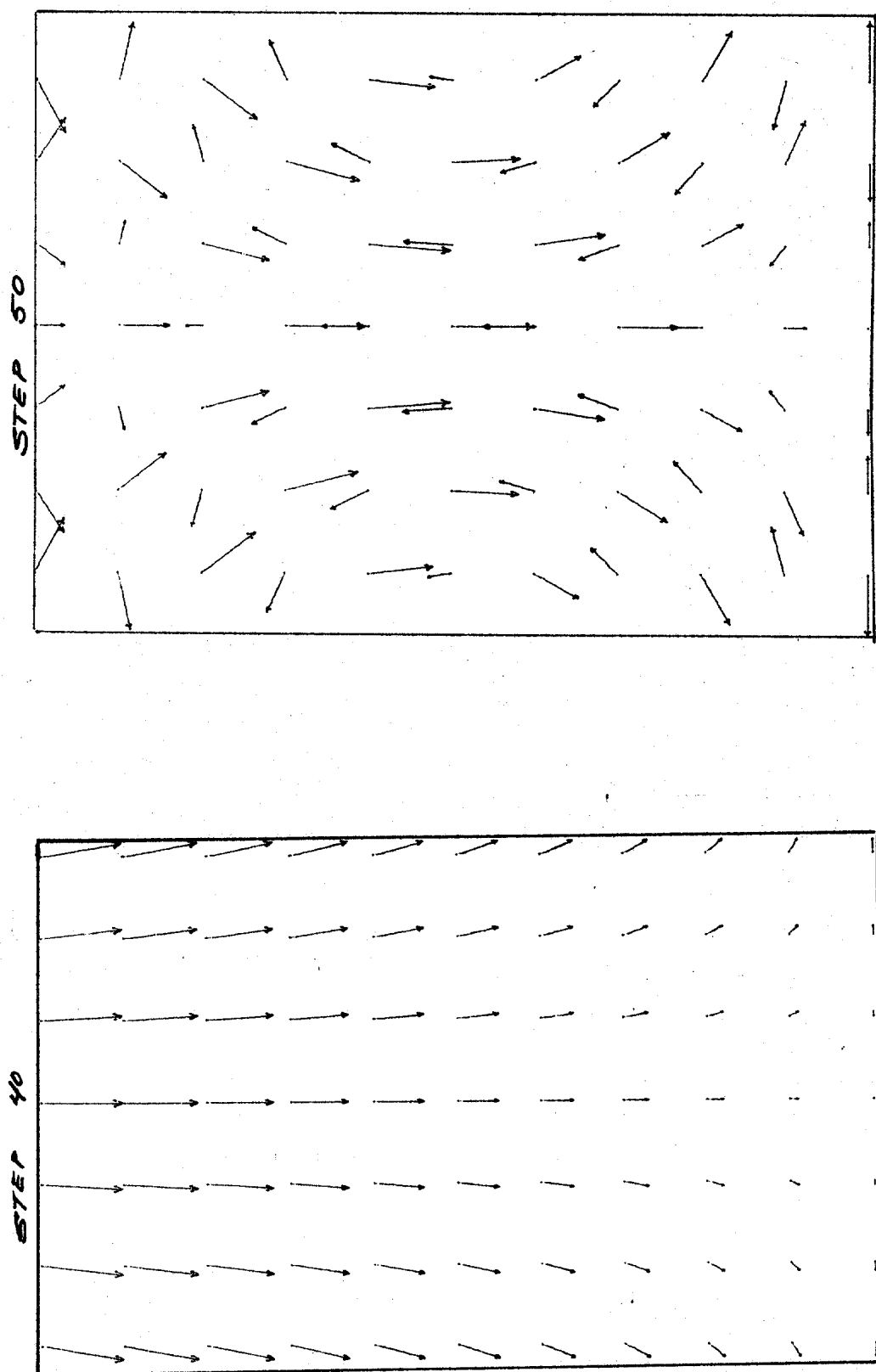
1	12	23	34	45	56	67
2	13	24	35	46	57	68
3	14	25	36	47	58	69
4	15	26	37	48	59	70
5	16	27	38	49	60	71
6	17	28	39	50	61	72
7	18	29	40	51	62	73
8	19	30	41	52	63	74
9	20	31	42	53	64	75
10	21	32	43	54	65	76
11	22	33	44	55	66	77

60 Element Mesh

1	12	23	34	45	56	67	78	89	100	111	122	133
2	13	24	35	46	57	68	79	90	101	112	123	134
3	14	25	36	47	58	69	80	91	102	113	124	135
4	15	26	37	48	59	70	81	92	103	114	125	136
5	16	27	38	49	60	71	82	93	104	115	126	137
6	17	28	39	50	61	72	83	94	105	116	127	138
7	18	29	40	51	62	73	84	95	106	117	128	139
8	19	30	41	52	63	74	85	96	107	118	129	140
9	20	31	42	53	64	75	86	97	108	119	130	141
10	21	32	43	54	65	76	87	98	109	120	131	142
11	22	33	44	55	66	77	88	99	110	121	132	143

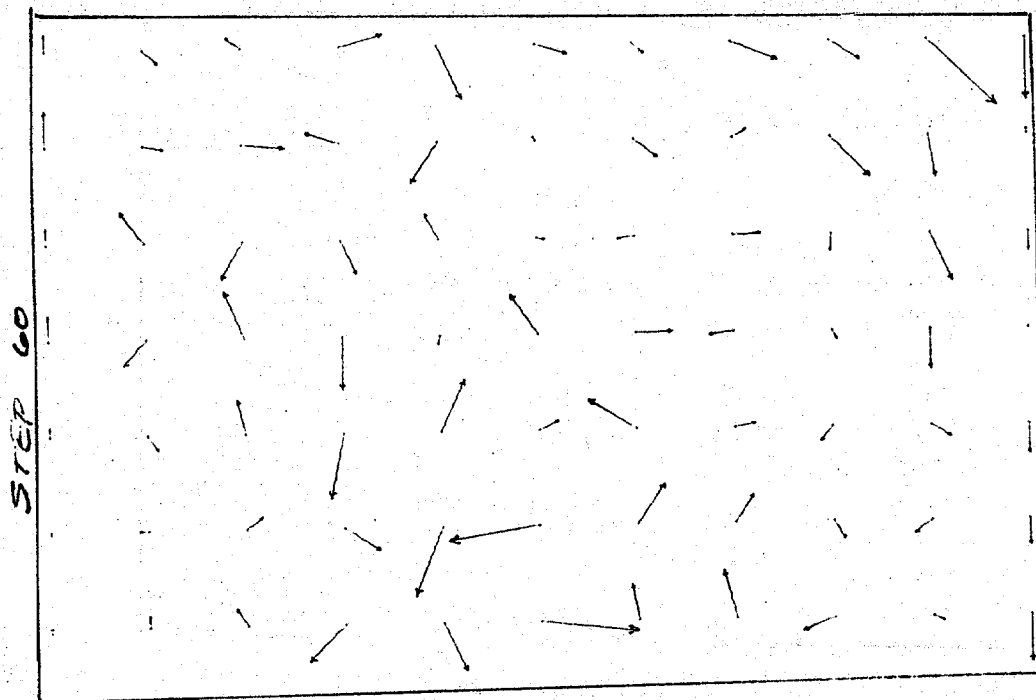
120 Element Mesh

Figure 21. Finite element meshes.

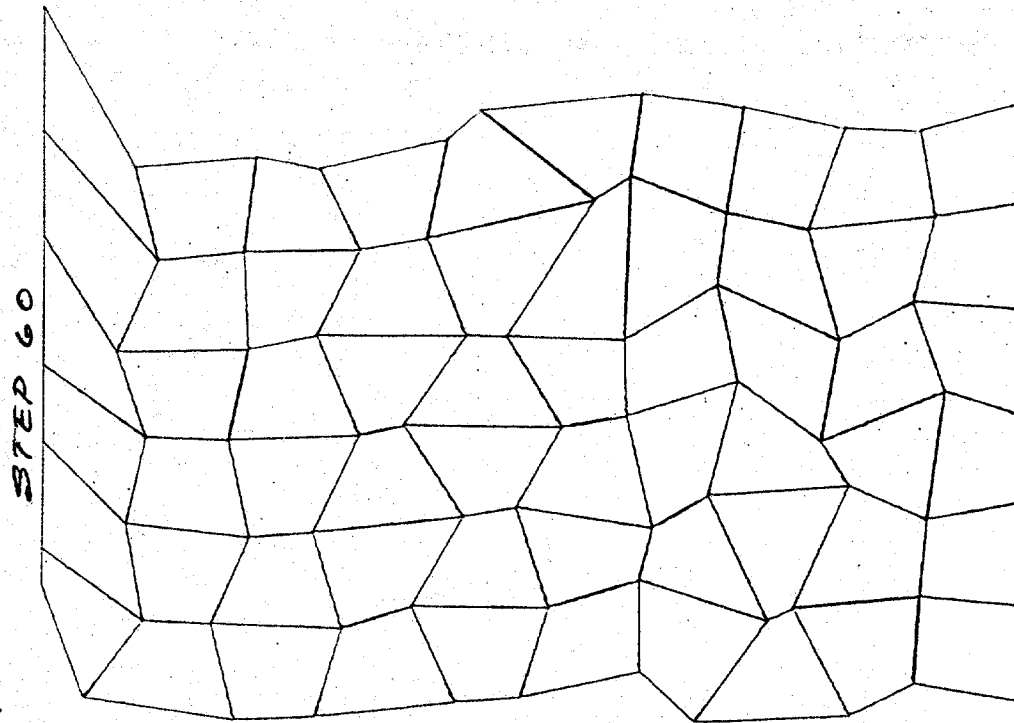


Velocity Vectors

Figure 22. 60 - element mesh.



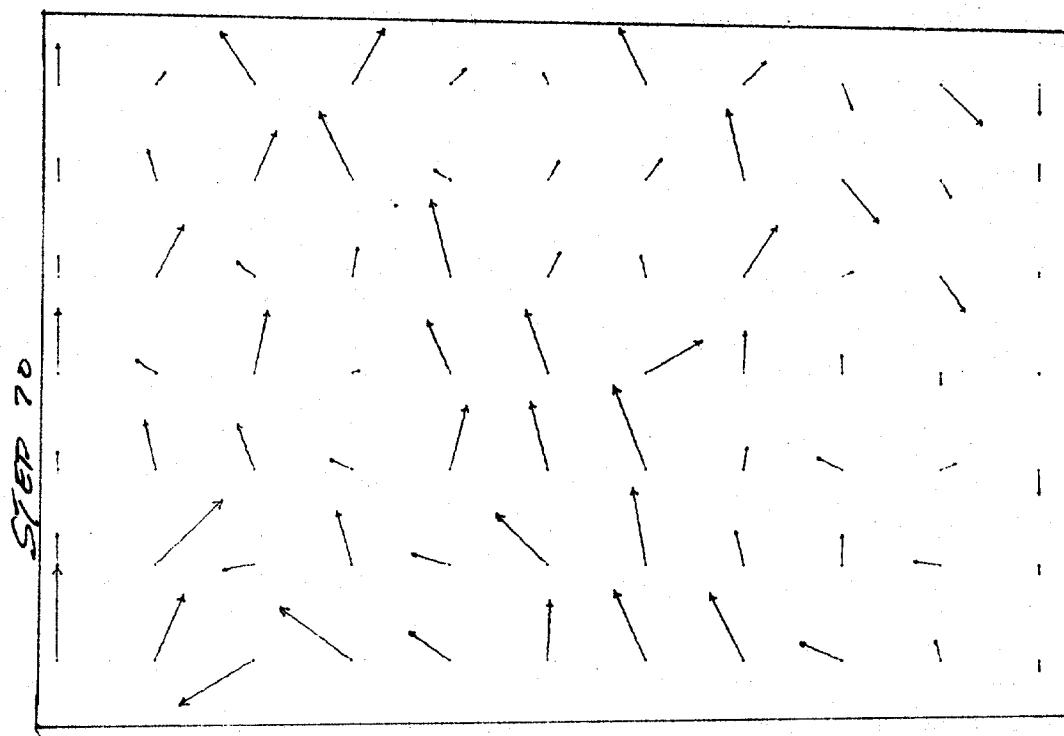
Velocity Vectors



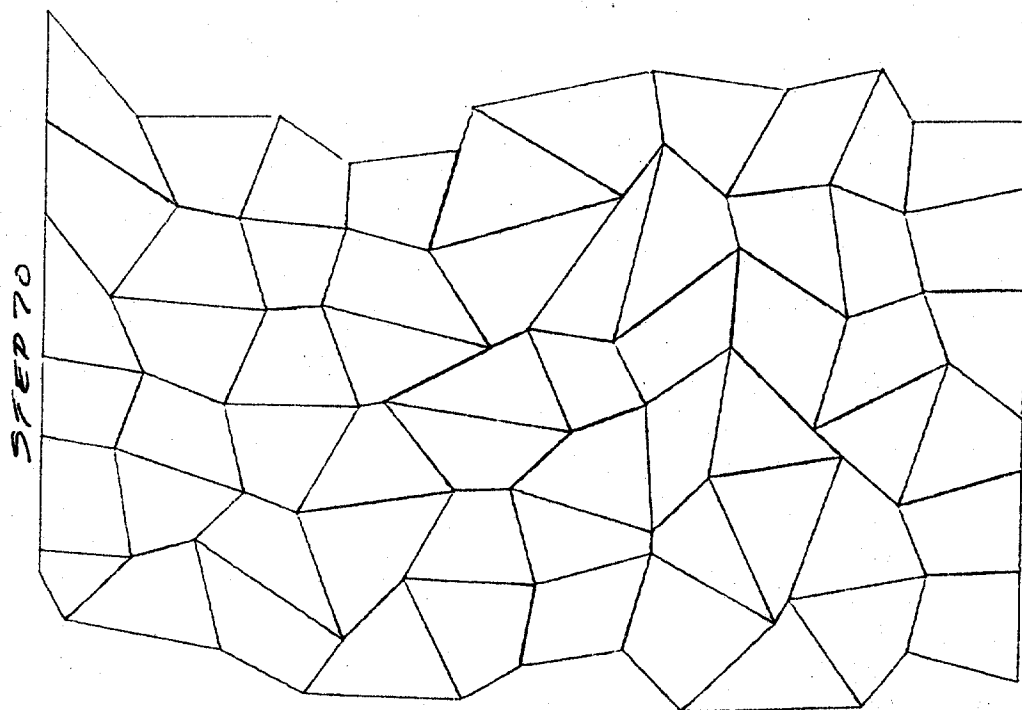
DEFORMATION SCALE FACTOR = 269.433

Deformed Mesh

Figure 22. Continued.



Velocity Vector



DEFORMATION SCALE FACTOR = 520.336

Deformed Mesh

Figure 22. Continued.

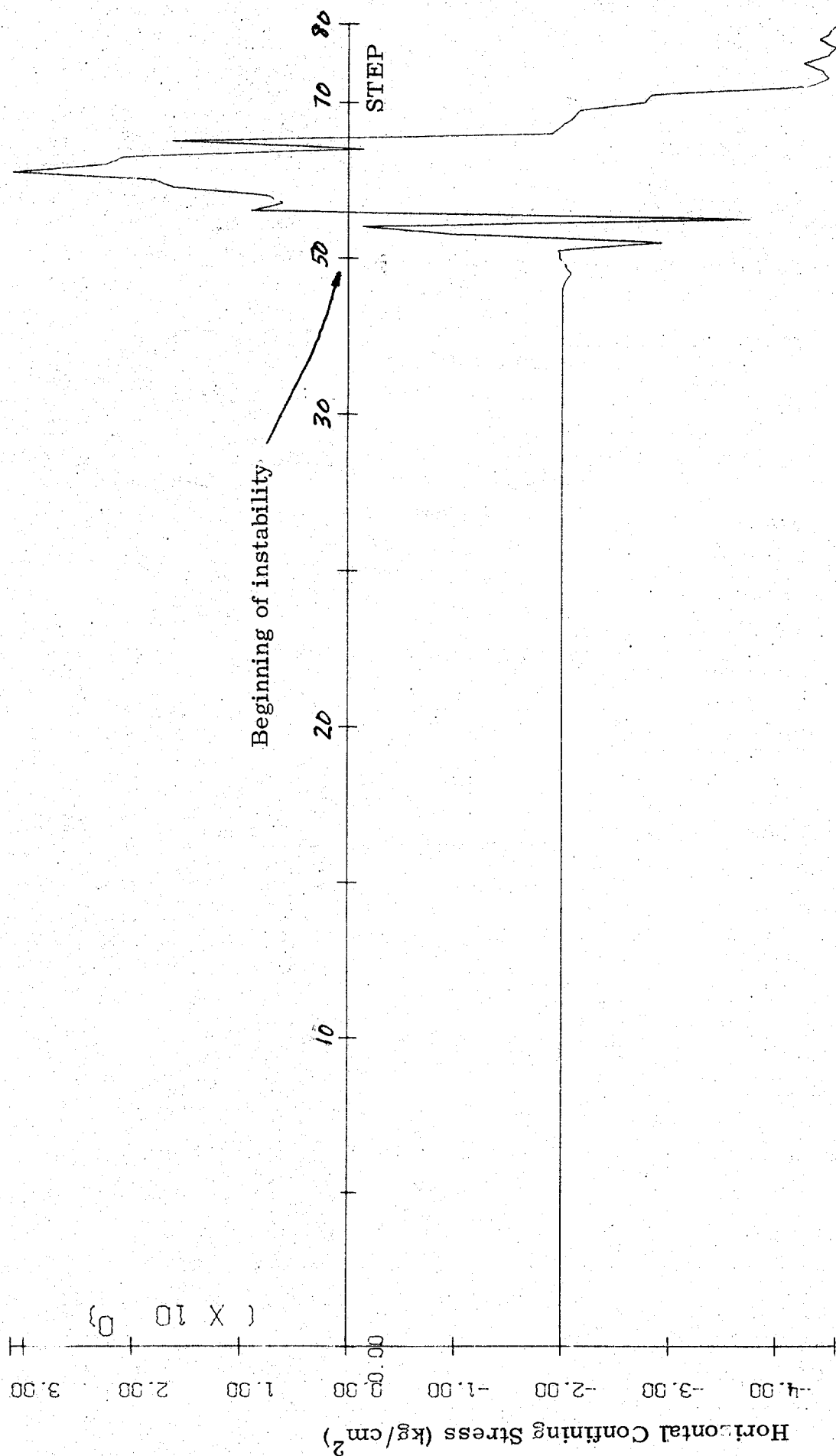


Figure 23. Stress plots 60 element mesh.

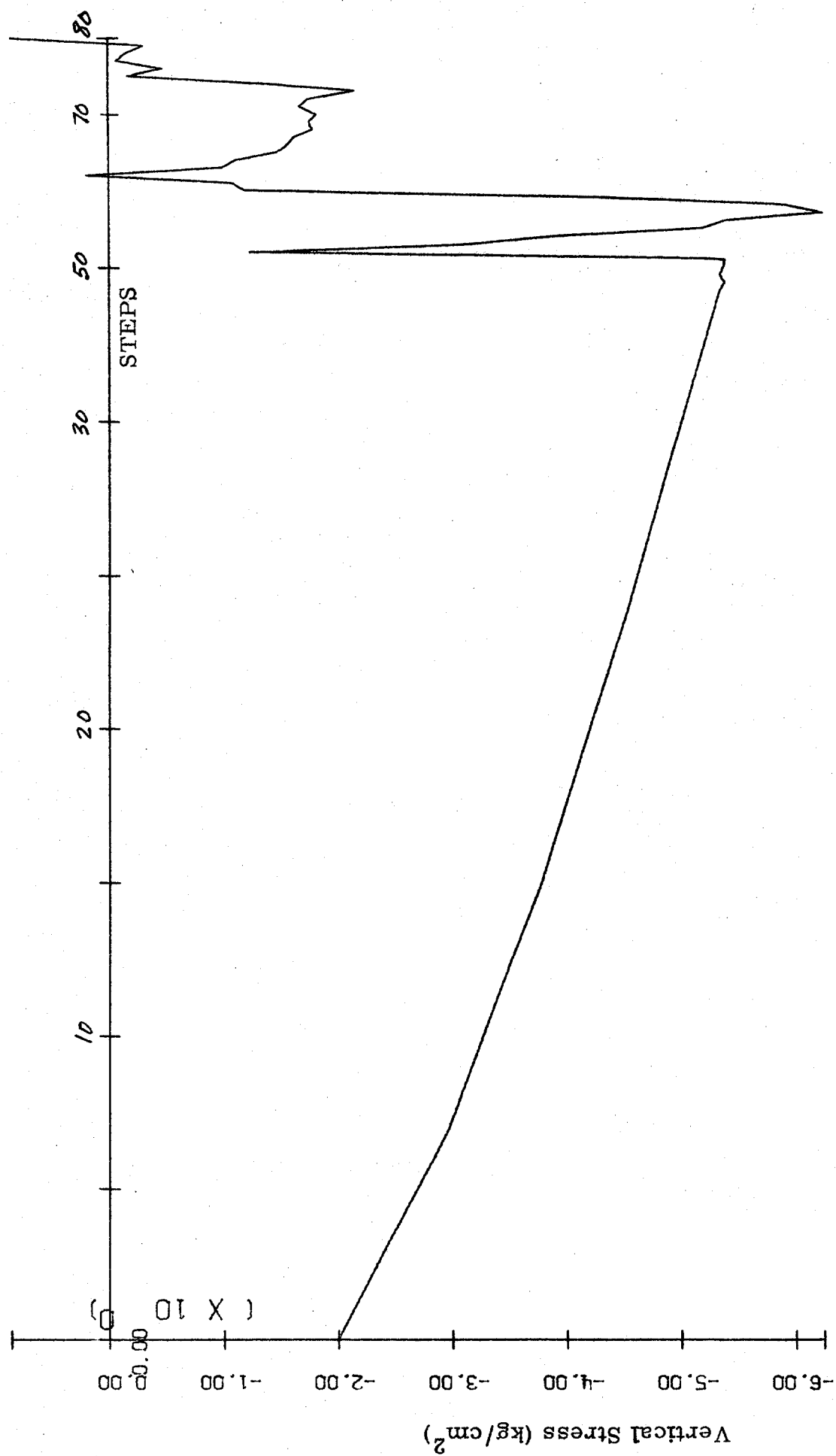


Figure 23. Contin ued.

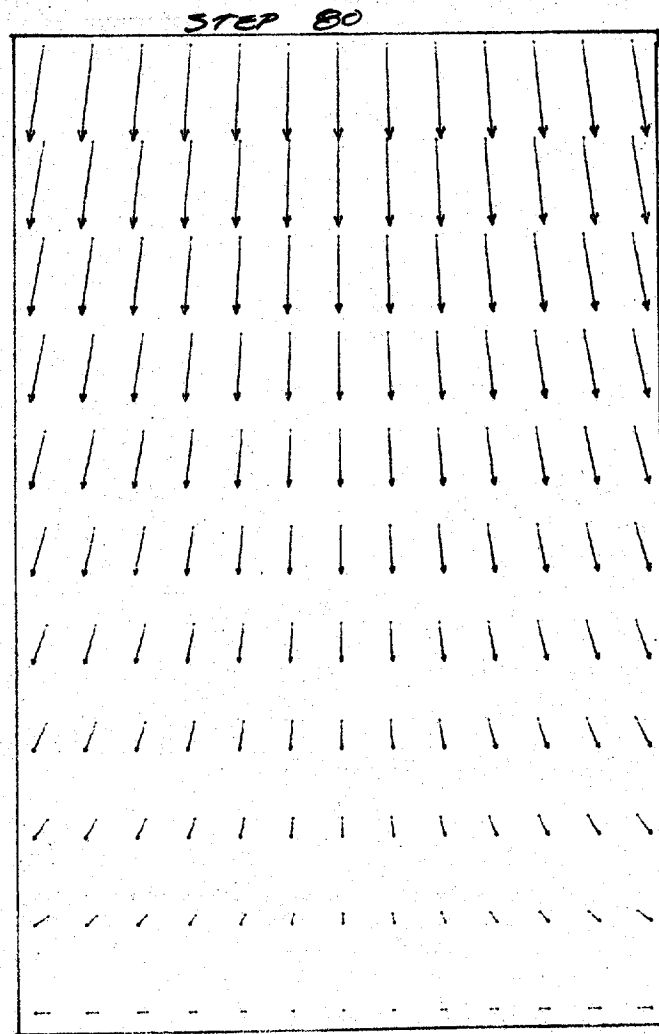


Figure 24. Velocity vector plot 120 - element mesh.

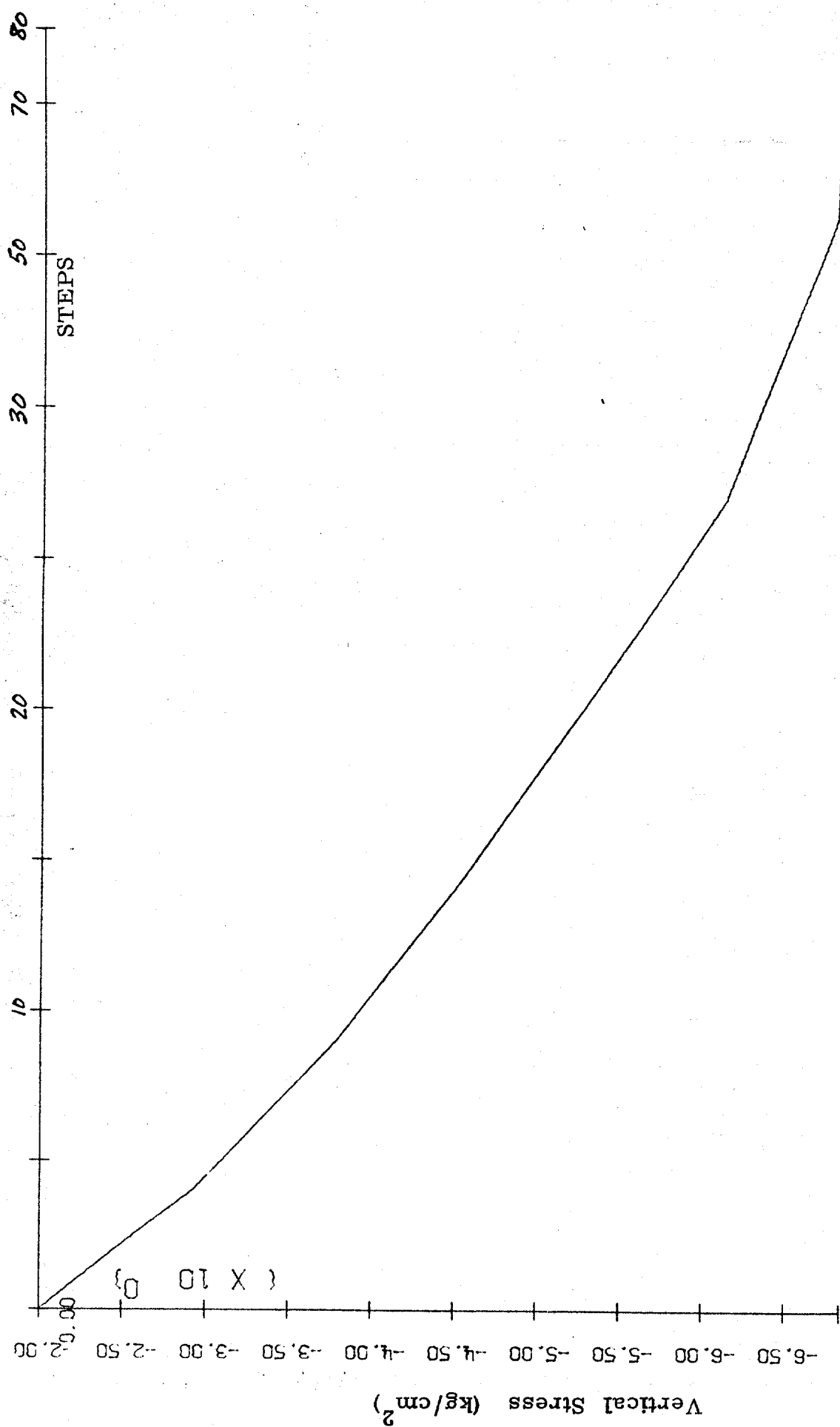
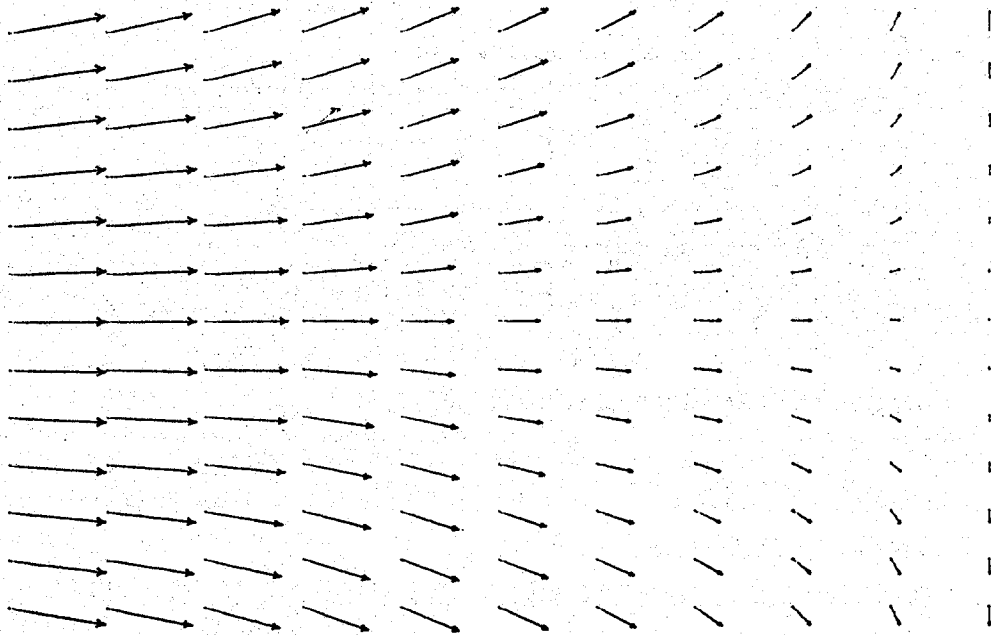


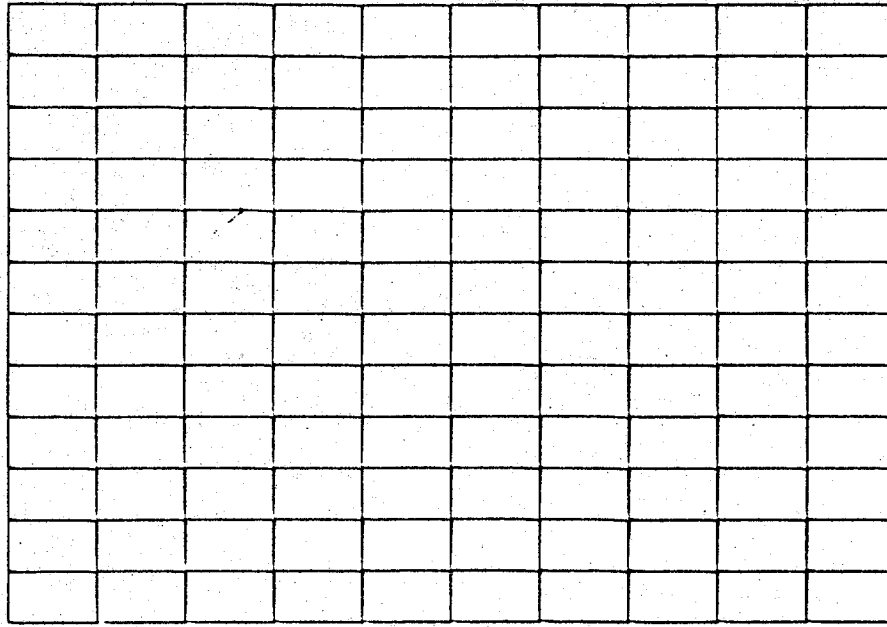
Figure 25. Stress plot 120-element mesh.

Step 50



Velocity Vector

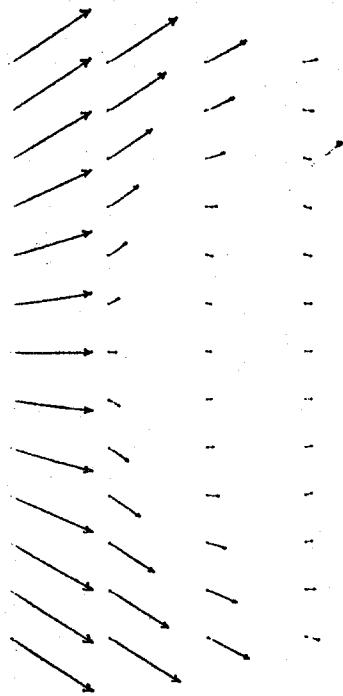
Step 50



Deformed Mesh

Figure 26. 120-element mesh, Parabolic solution, 2 DOF.

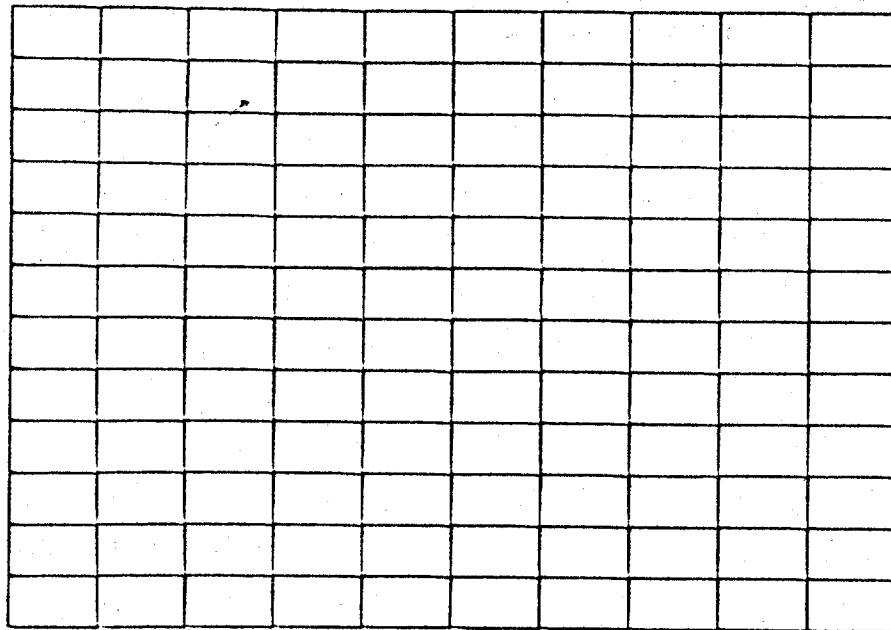
Step 60



Velocity Vector

Step 60

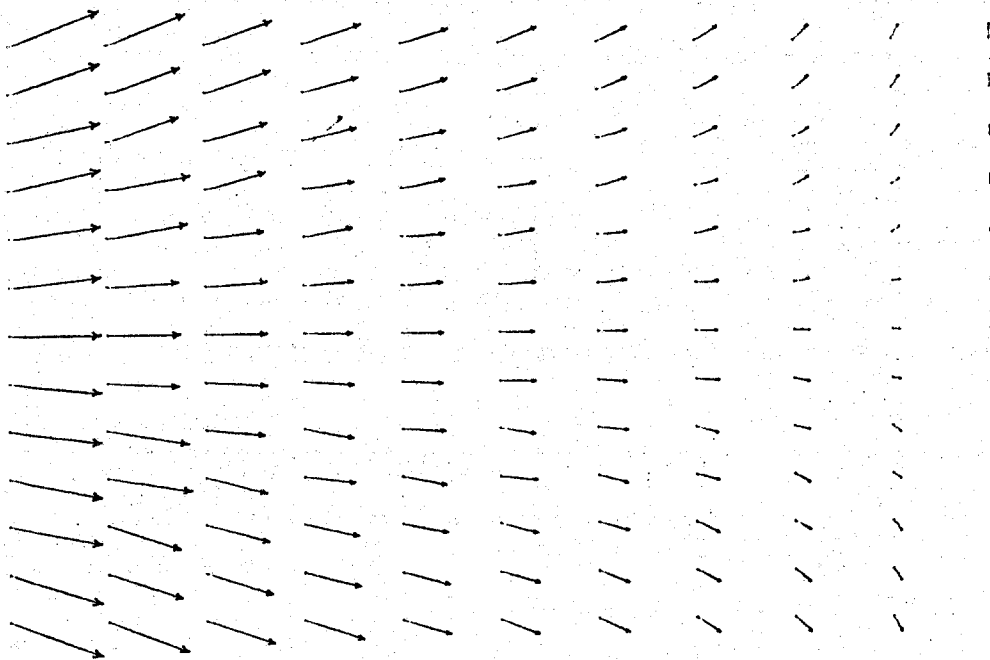
DEFORMATION SCALE FACTOR = 0.168



Deformed Mesh

Figure 26 . Continued

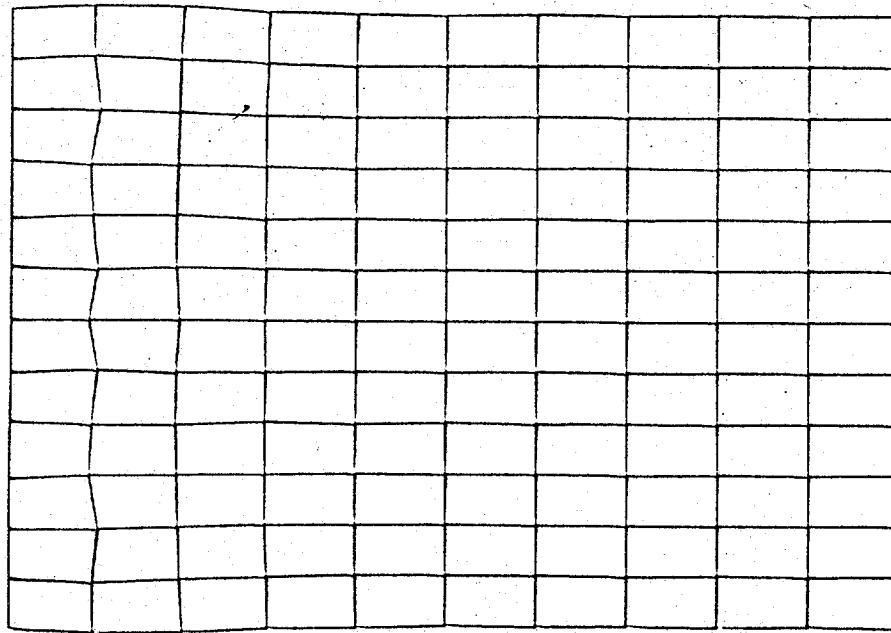
Step 70



Velocity Vector

Step 70

DEFORMATION SCALE FACTOR = 0.917



Deformed Mesh

Figure 26 . Continued

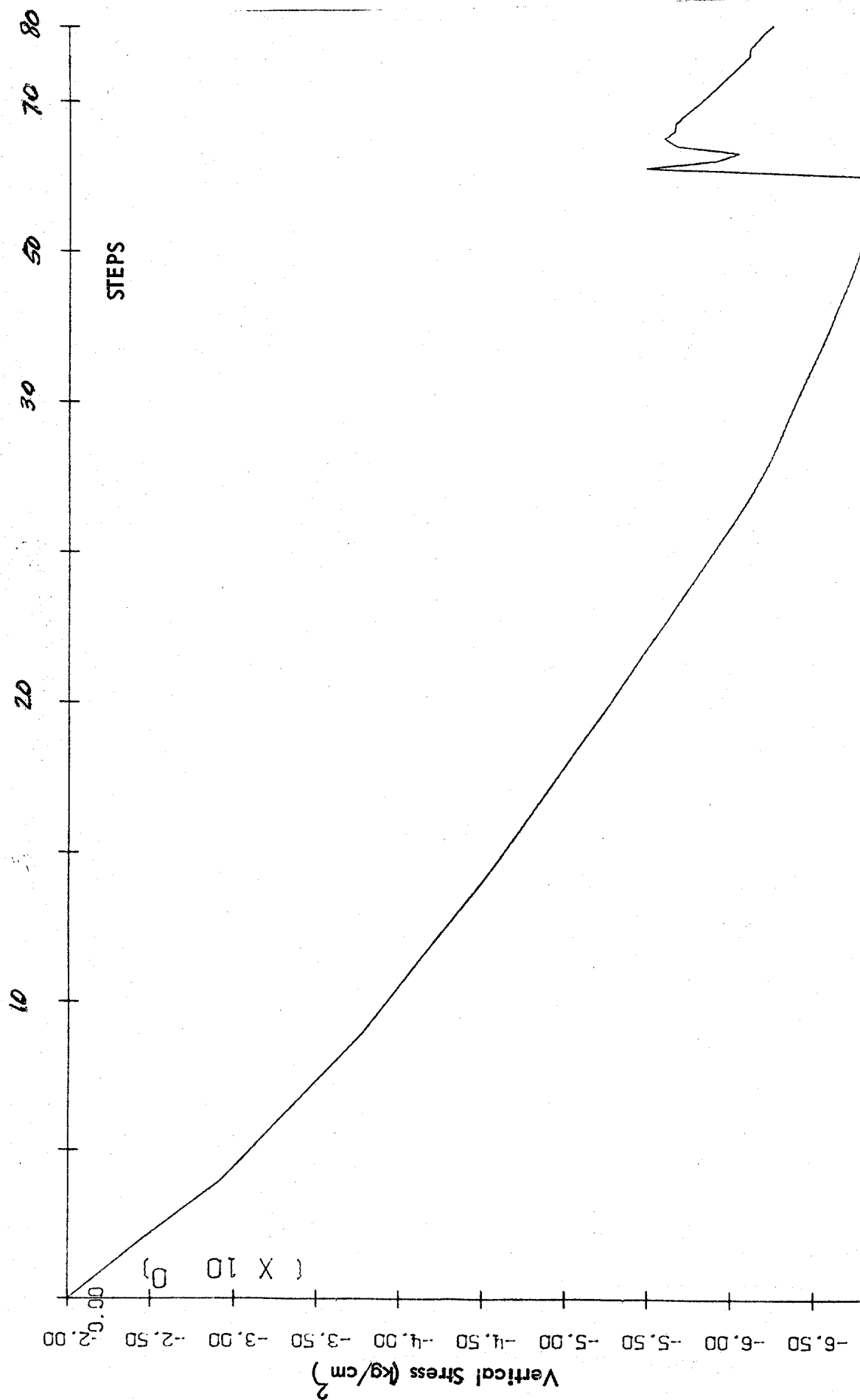


Figure 27. Stress plots, Parabolic solution, 2 DOF.

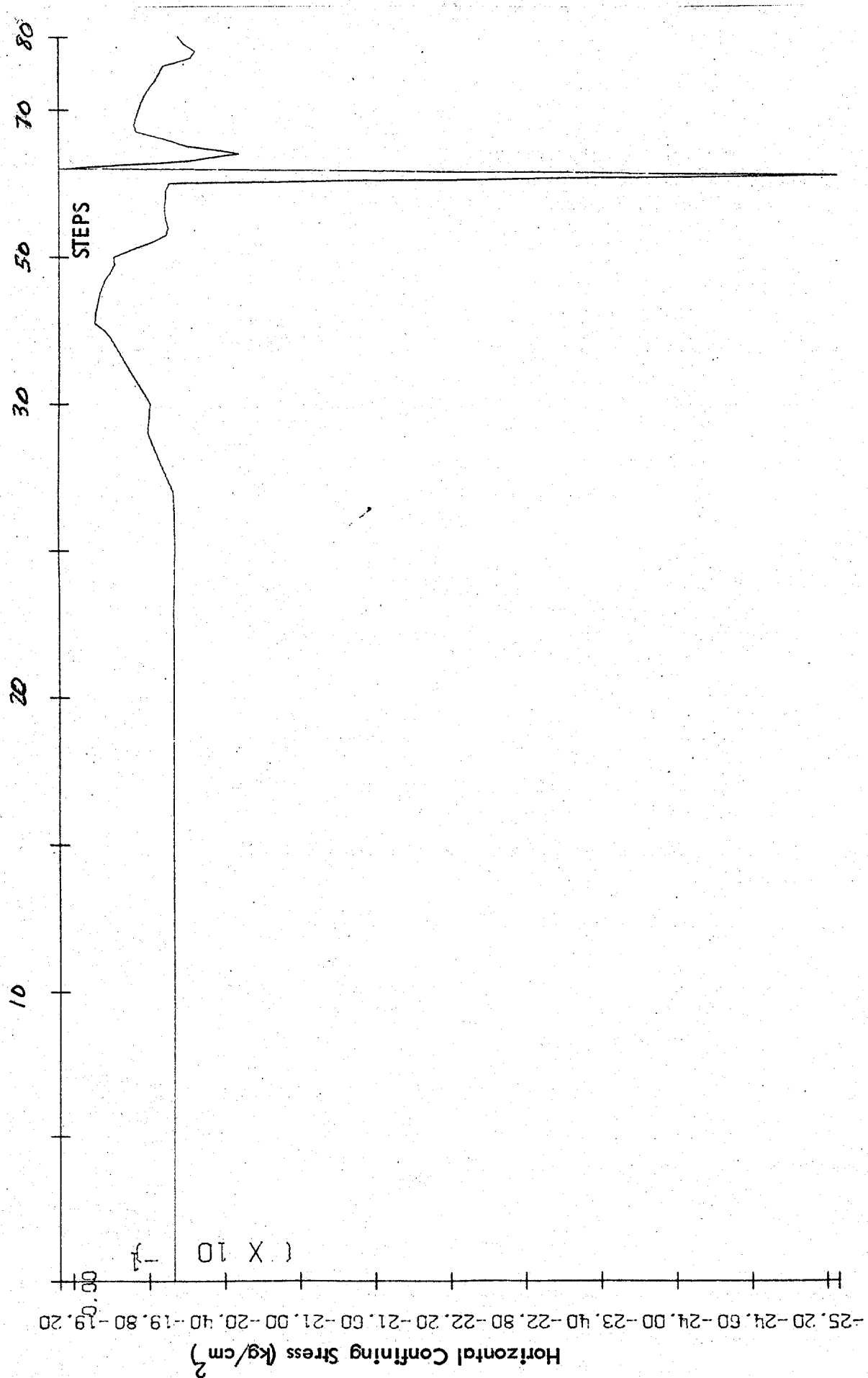


Figure 27. Continued.

Figure 28. Computation of Explicit Time Step

$K = 675.4 \text{ kg/cm}^2$ = Elastic bulk modulus
 $G = 253.3 \text{ kg/cm}^2$ = Elastic shear modulus
 $L = 1 \text{ cm}$ = Length of an element (propagation direction)
 $\rho = (1.943 \times 10^{-3} / 980) \text{ kg-sec/cm}^4$ = mass density

$$D = \frac{E(1-\mu)}{(1+\mu)(1-2\mu)}$$

$$K = \frac{E}{3(1-2\mu)}$$

$$G = \frac{E}{2(1+\mu)}$$

$$C_D = \sqrt{\frac{D}{\rho}}$$

From K and E above, $\mu = \frac{3K - 2G}{6K + 2G}$ $E = 2G(1+\mu)$

$$\mu = \frac{3(675.4) - 2(253.3)}{6(675.4) + 2(253.3)} = 0.333$$

$$E = 2(253.3)(1+0.333) = 675.4 \text{ kg/cm}^2$$

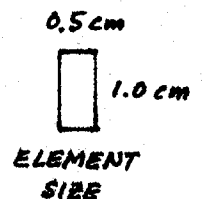
$$D = \frac{675.4(1-0.333)}{(1+0.333)(1-2(0.333))} = 1012 \text{ kg/cm}^2$$

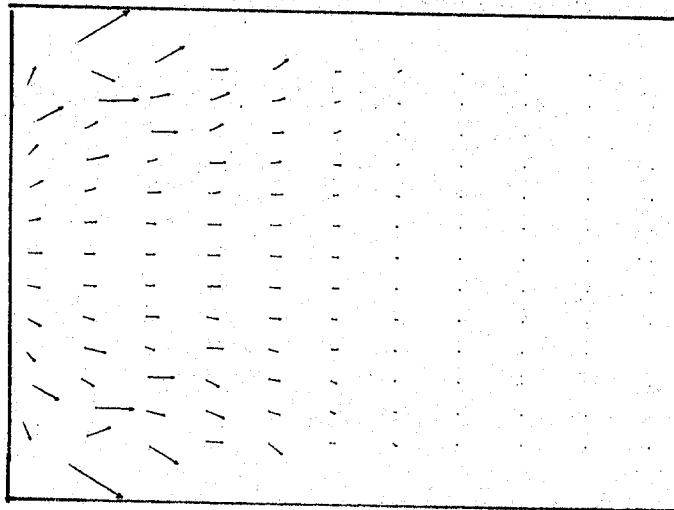
$$C_D = \sqrt{\frac{1012(980)}{1.943 \times 10^{-3}}} = 22600 \text{ cm/sec}$$

T = Time for wave to travel through an element

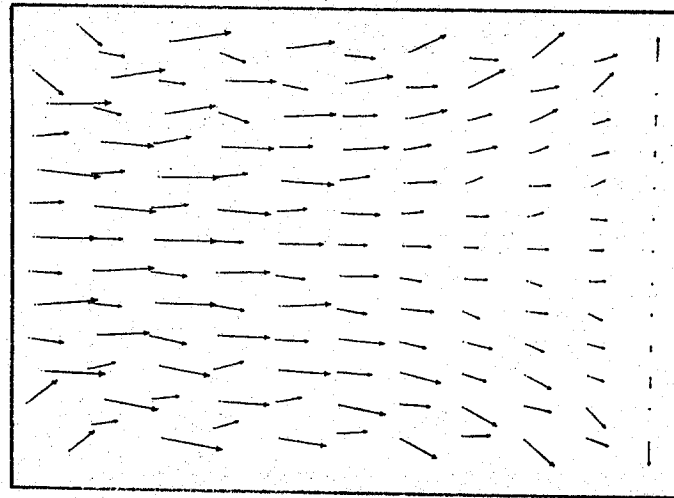
$$T = L/C_D = 1/22600 = 4.4 \times 10^{-5} \text{ sec}$$

In DYNA-FLOW: $\Delta t = T/4 = 1.2 \times 10^{-5} \text{ sec}$

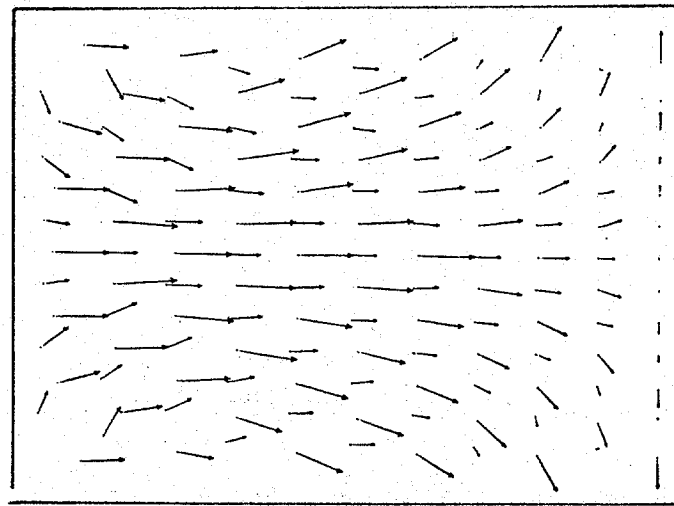




Step 20

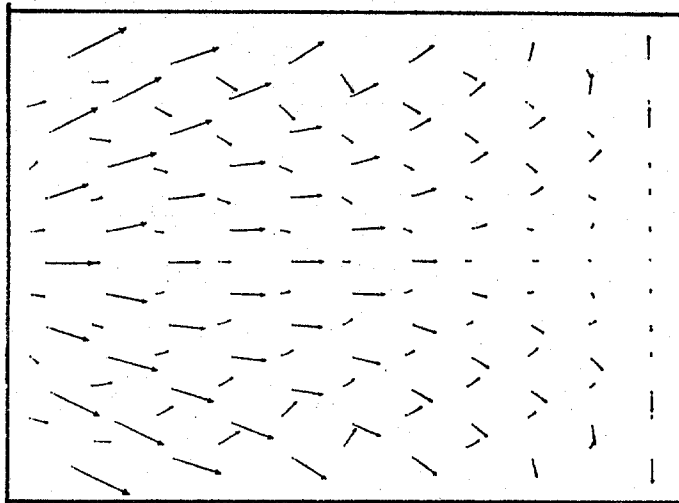


Step 40

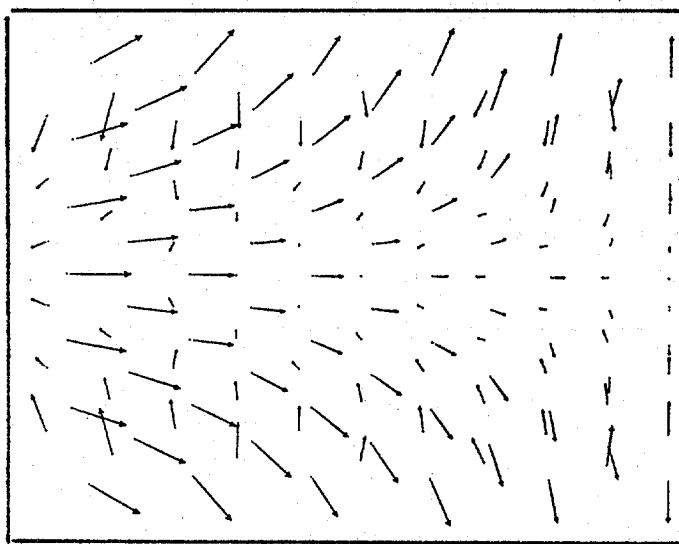


Step 60

Figure 29 . Explicit Solution: Wave Propagation



Step 80



Step 100

Figure 29. Continued.

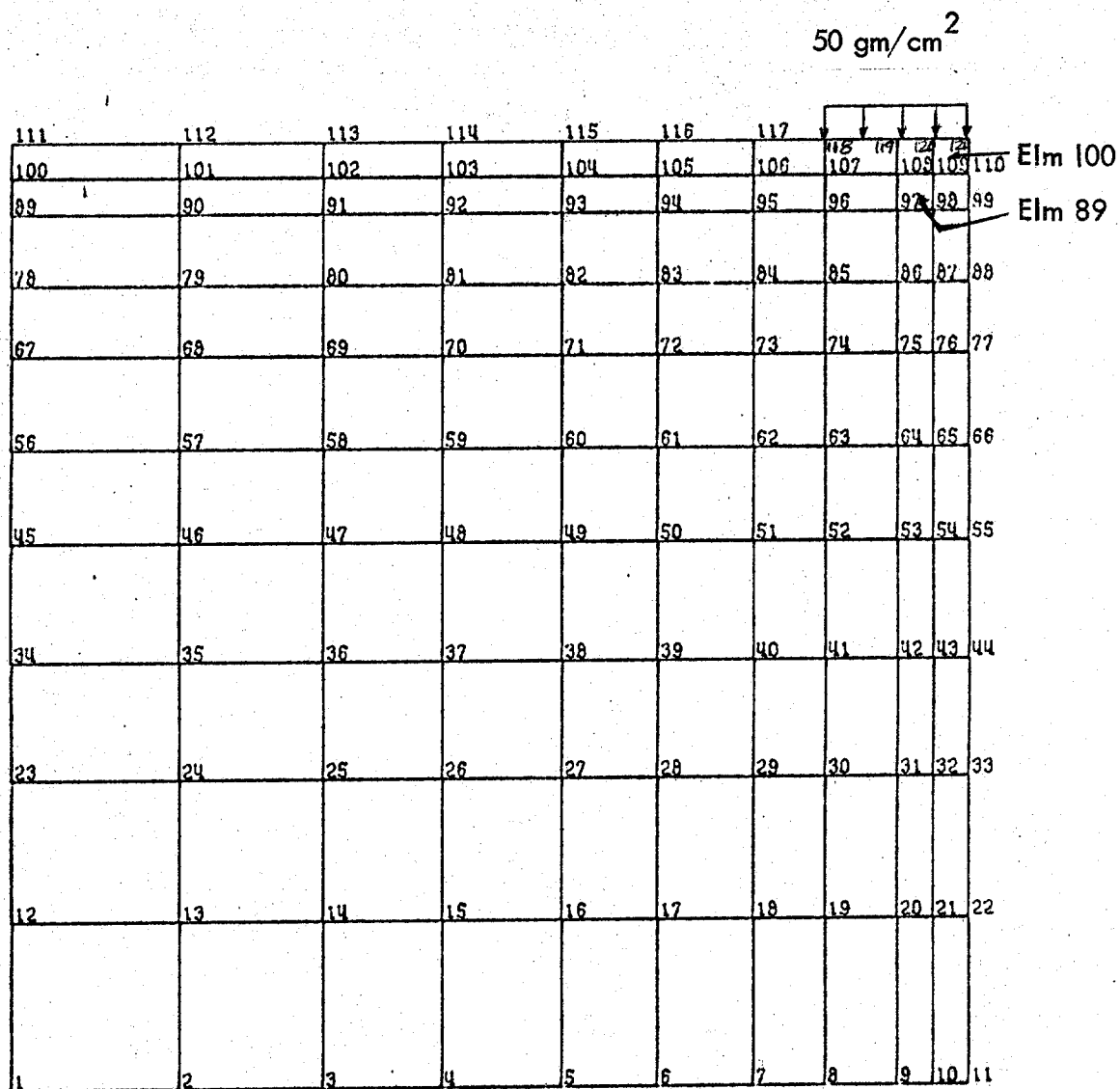


Figure 30. Undeformed mesh — 2D consolidation

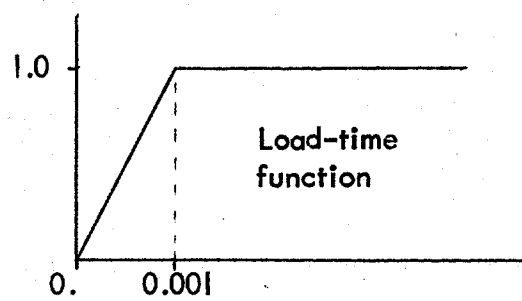
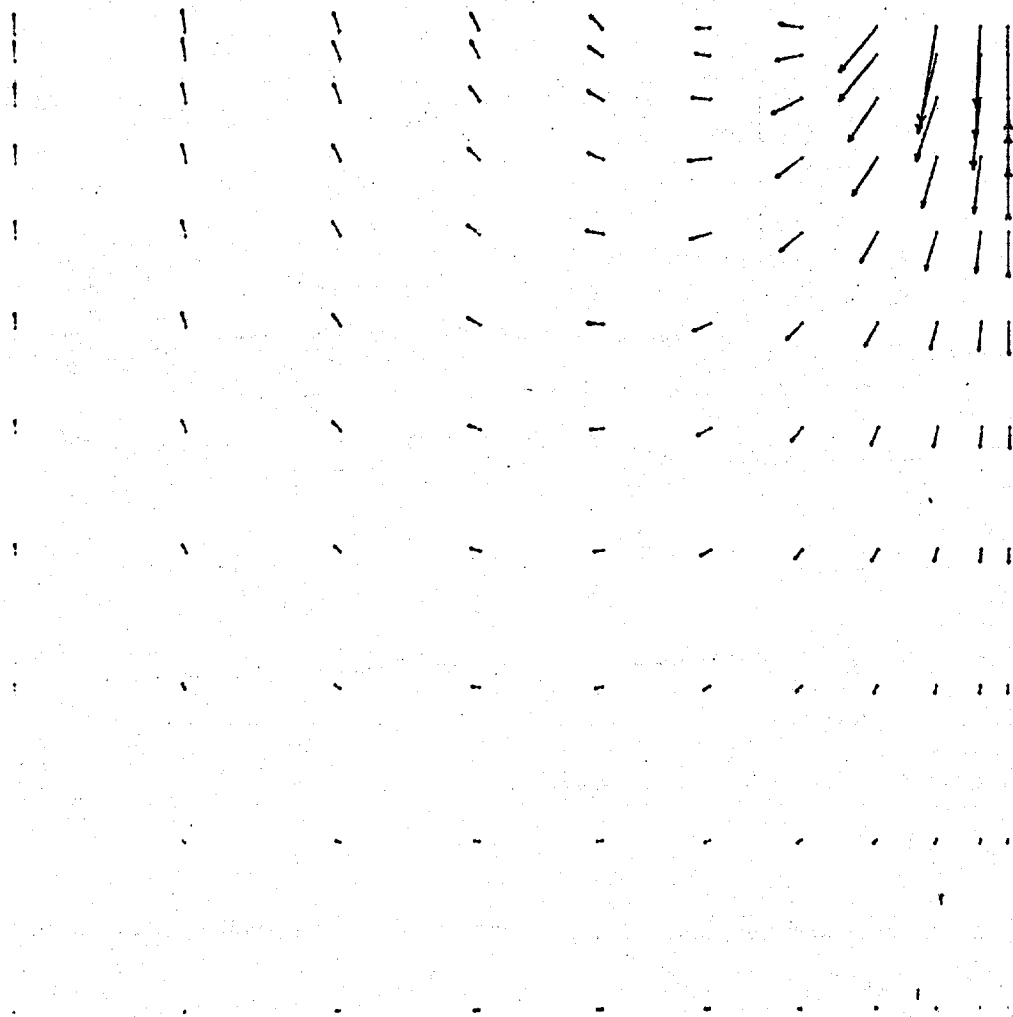


Figure 31. Velocity vector field — 2D consolidation

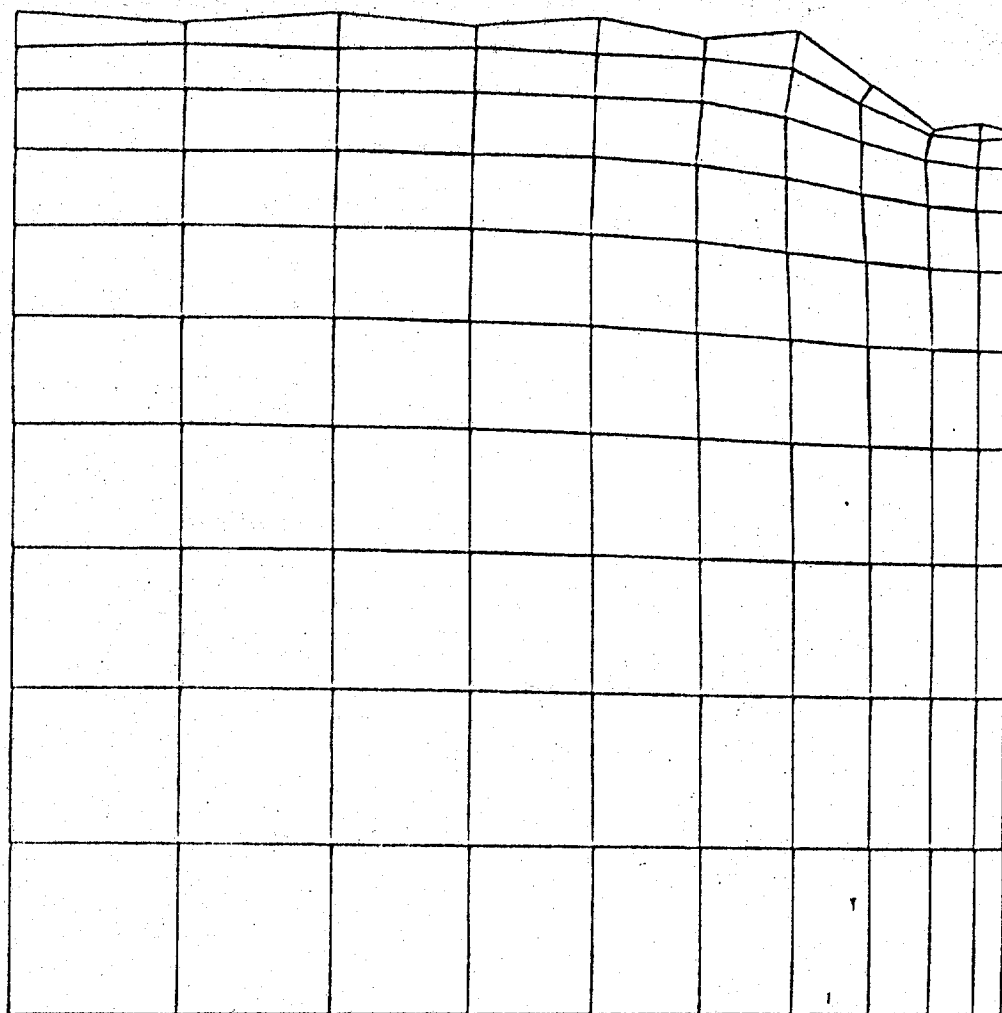


Figure 32. Deformed mesh — Elastic soil model

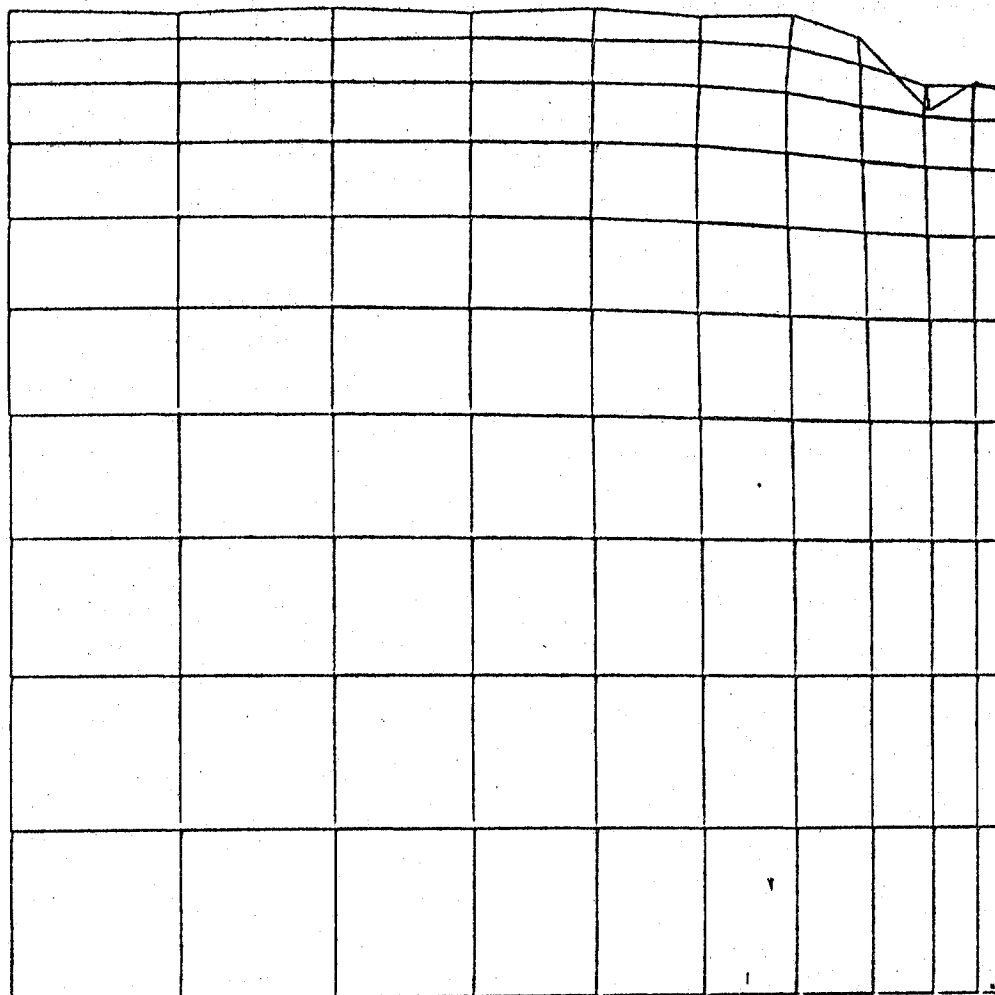


Figure 32 . (Continued)
Deformed mesh — Prevost soil model

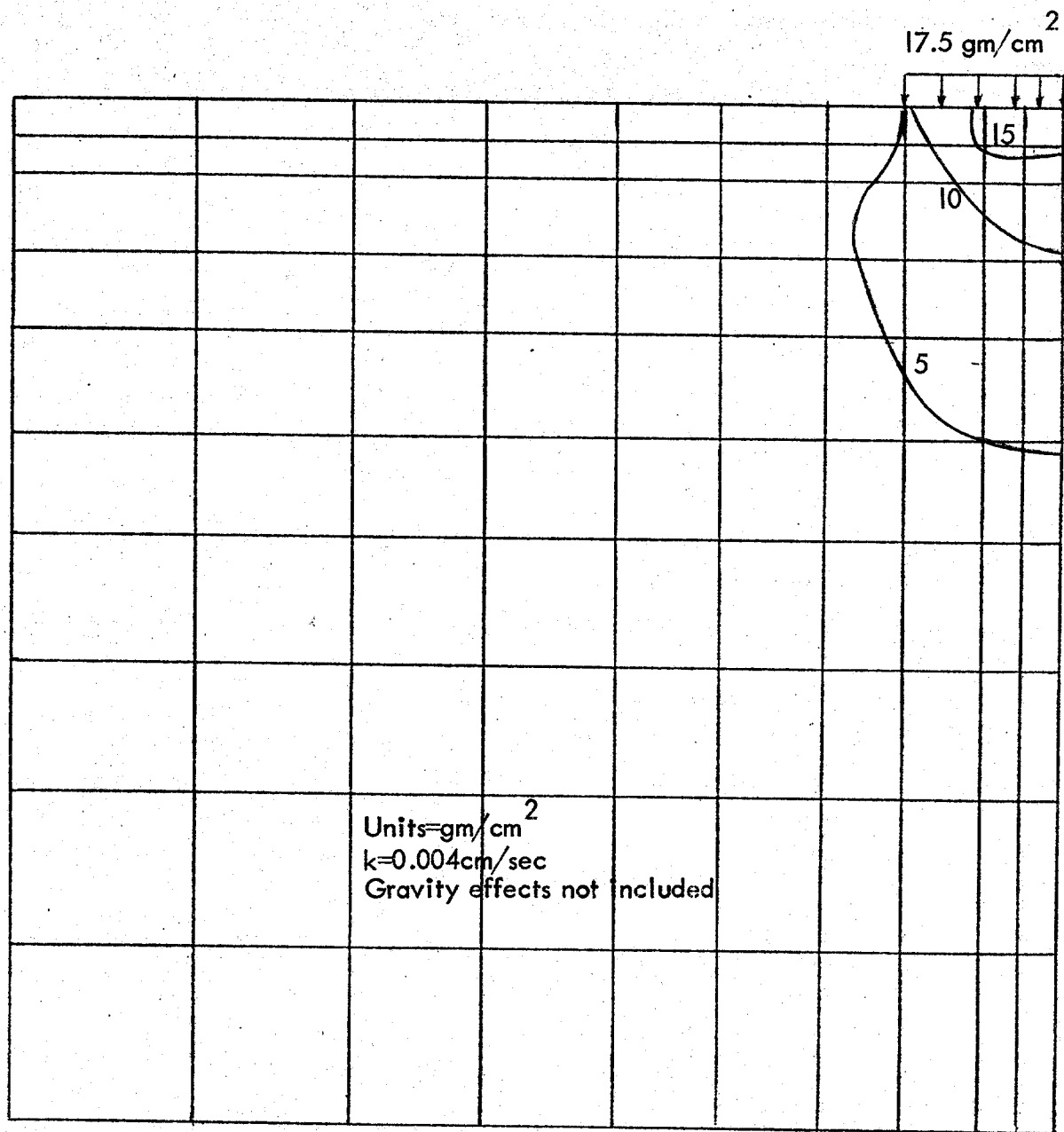


Figure 33. Pore pressure contours — Elastic soil model
 Step=2, time=0.00035 sec

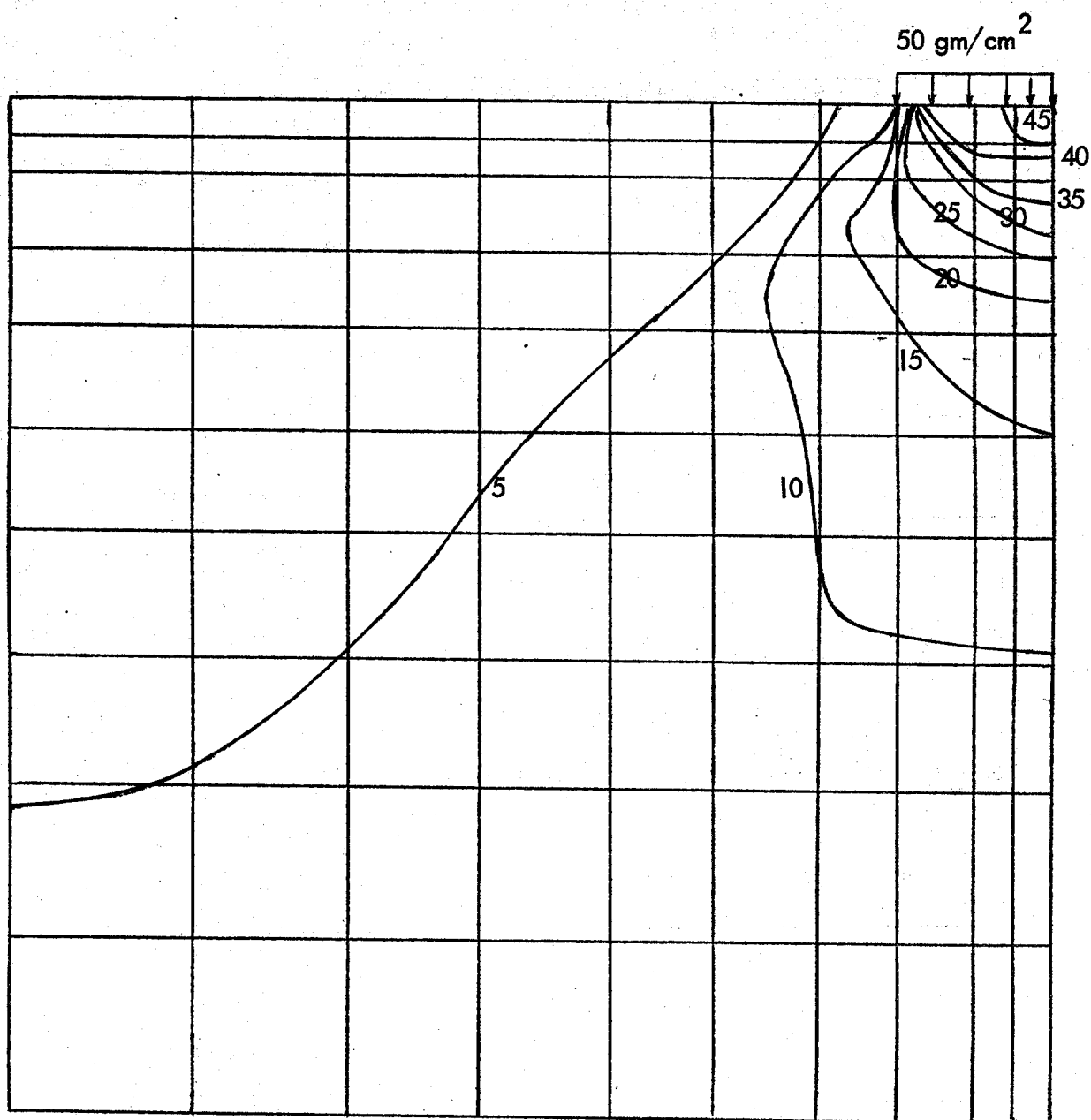


Figure 33. (Continued) Step=4, time=0.0025 sec

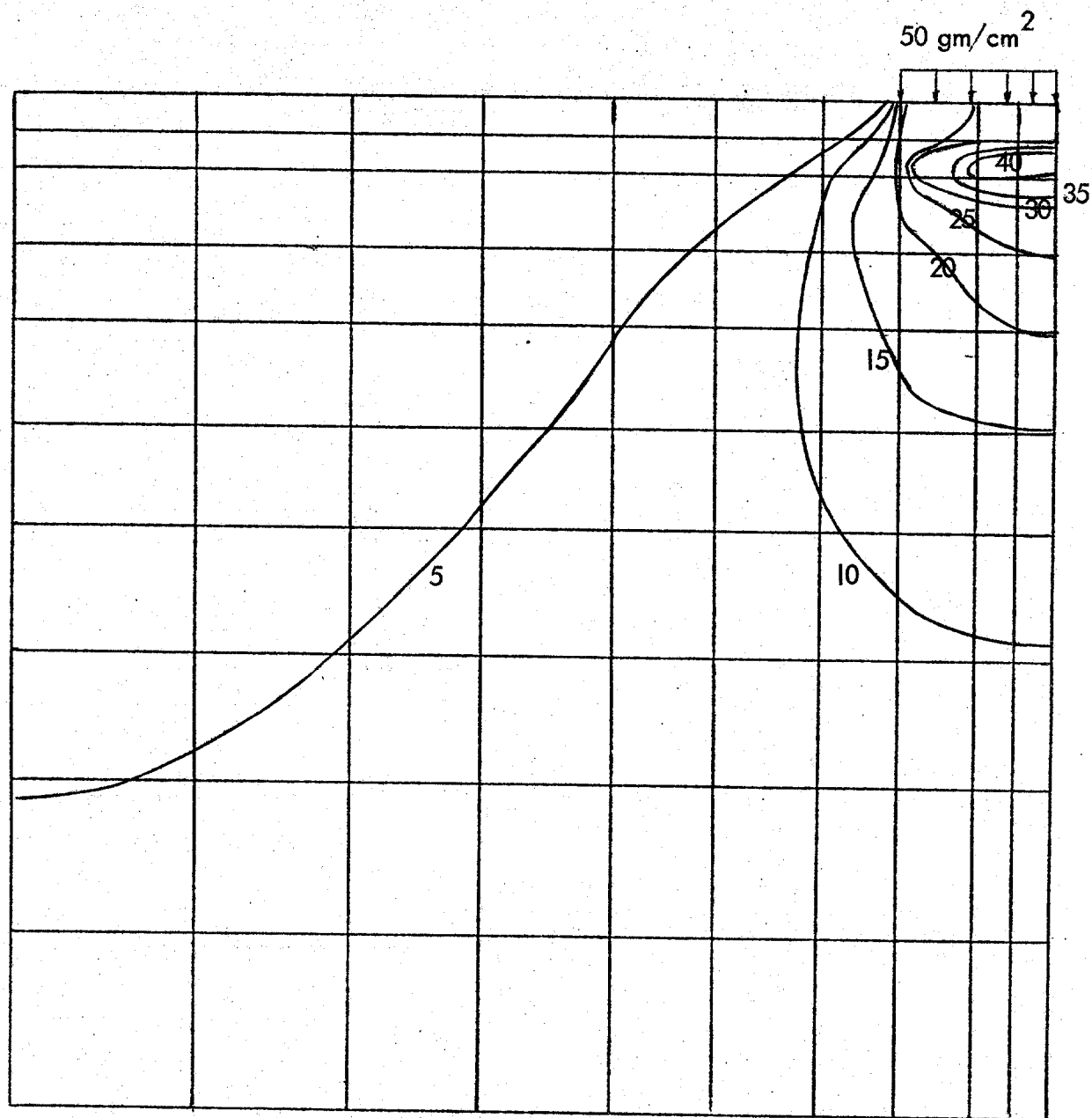


Figure 33. (Continued) Step=10, time=0.64 sec

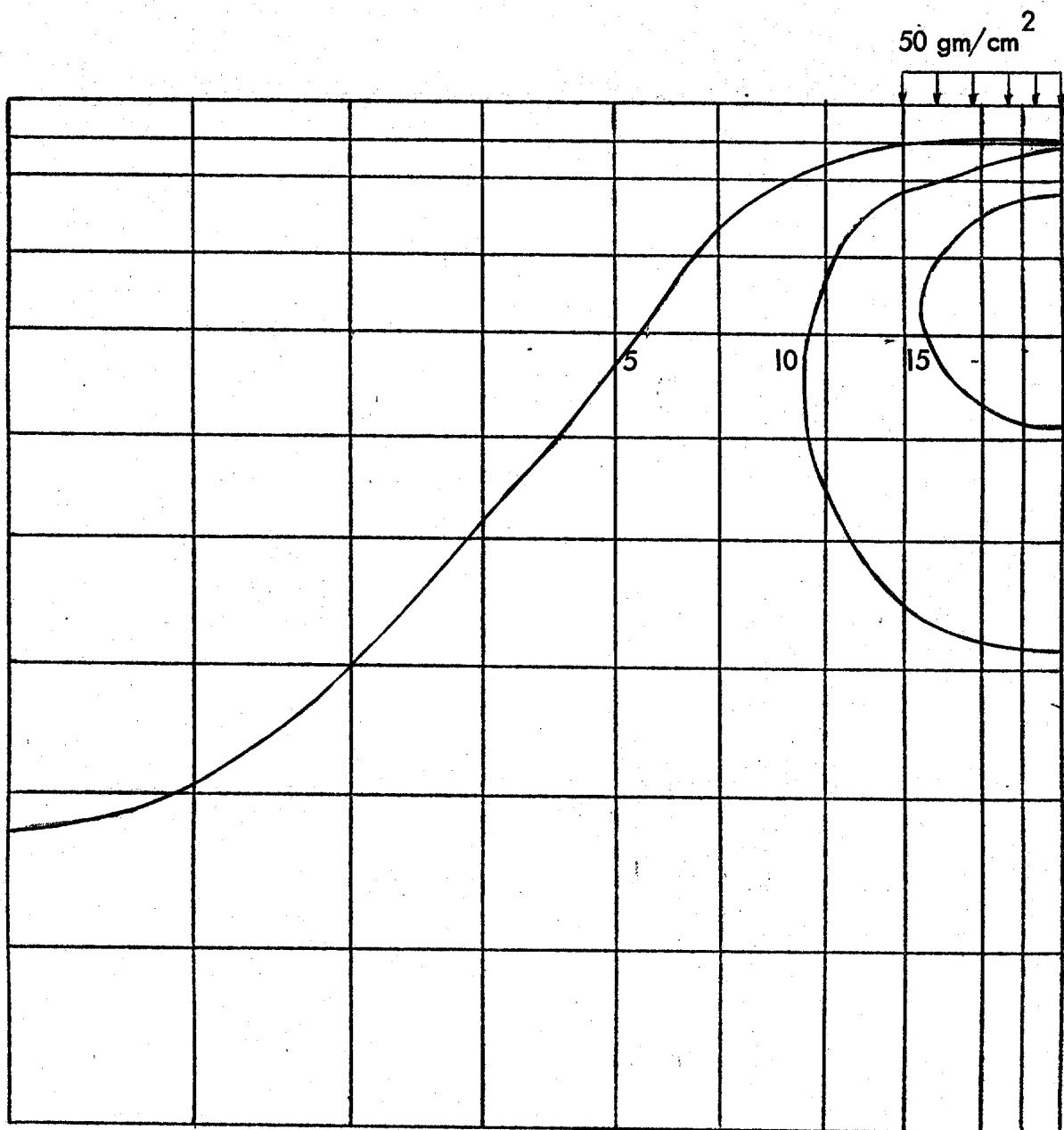


Figure 33. (Continued) Step=14, time=24.8 sec

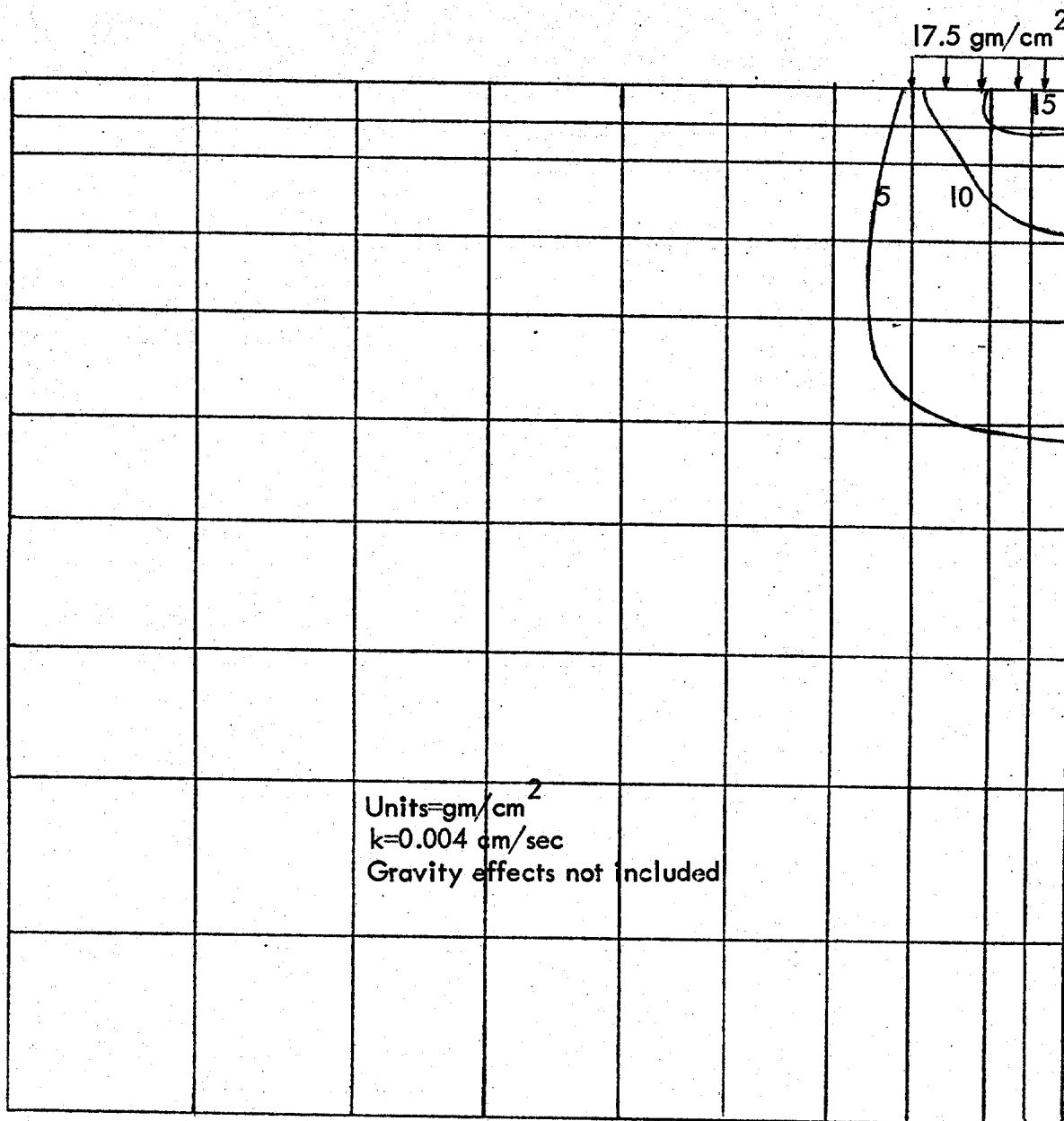


Figure 34. Pore pressure contours — Prevost soil model
 Step=2, time=0.00035 sec

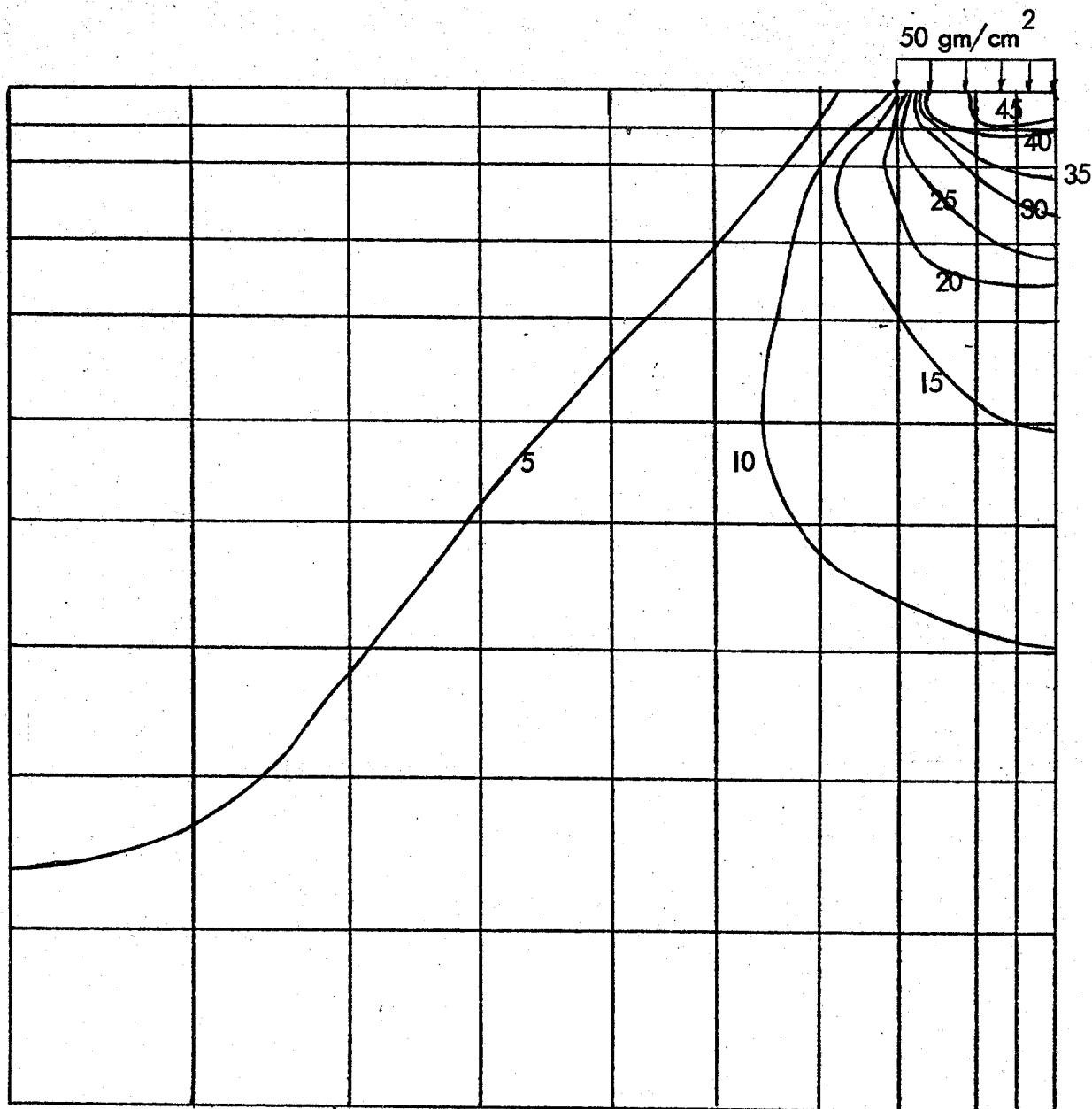


Figure 34. (Continued) Step=4, time=0.0025 sec

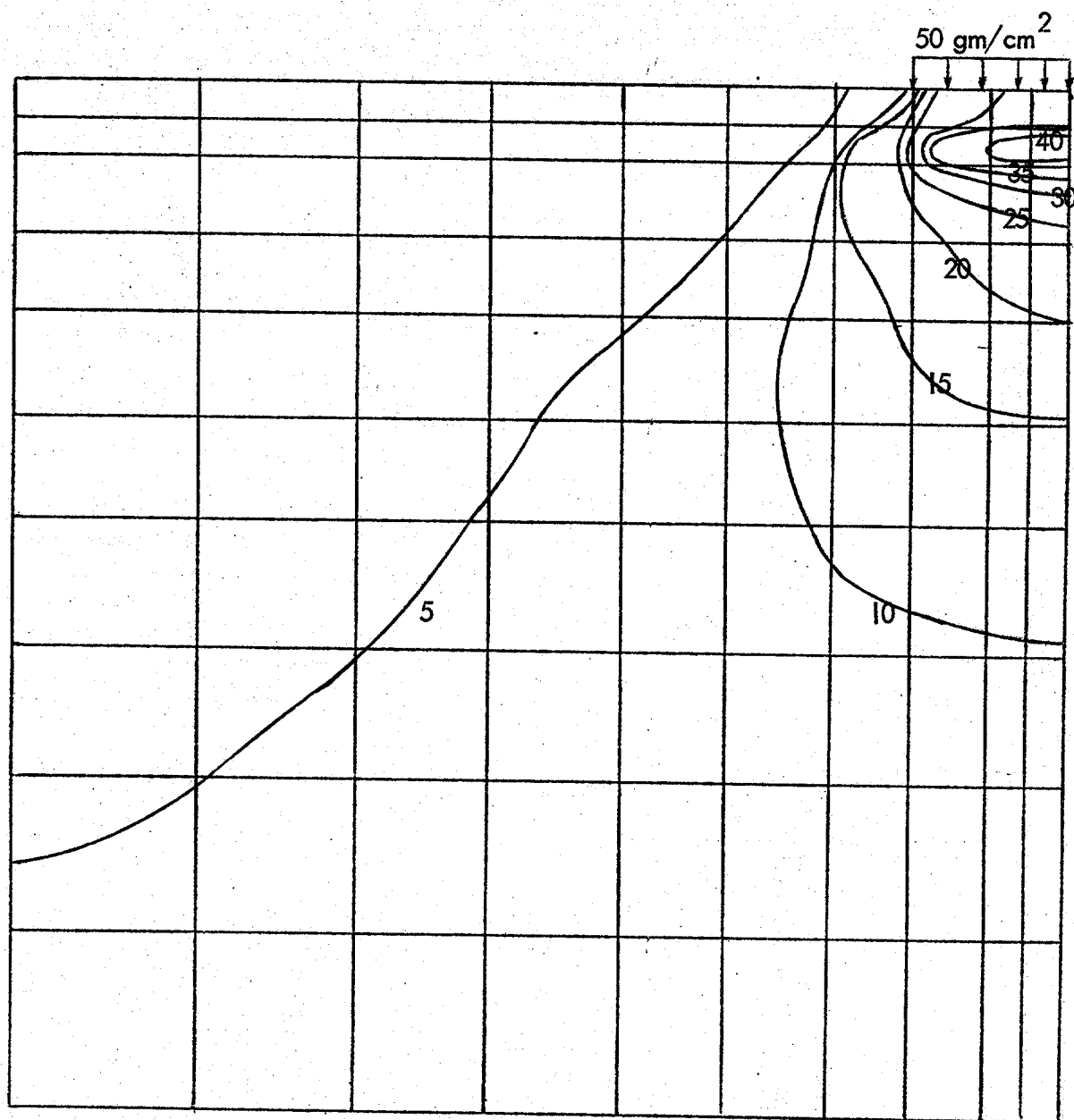


Figure 34. (Continued) Step=10, time=0.64 sec

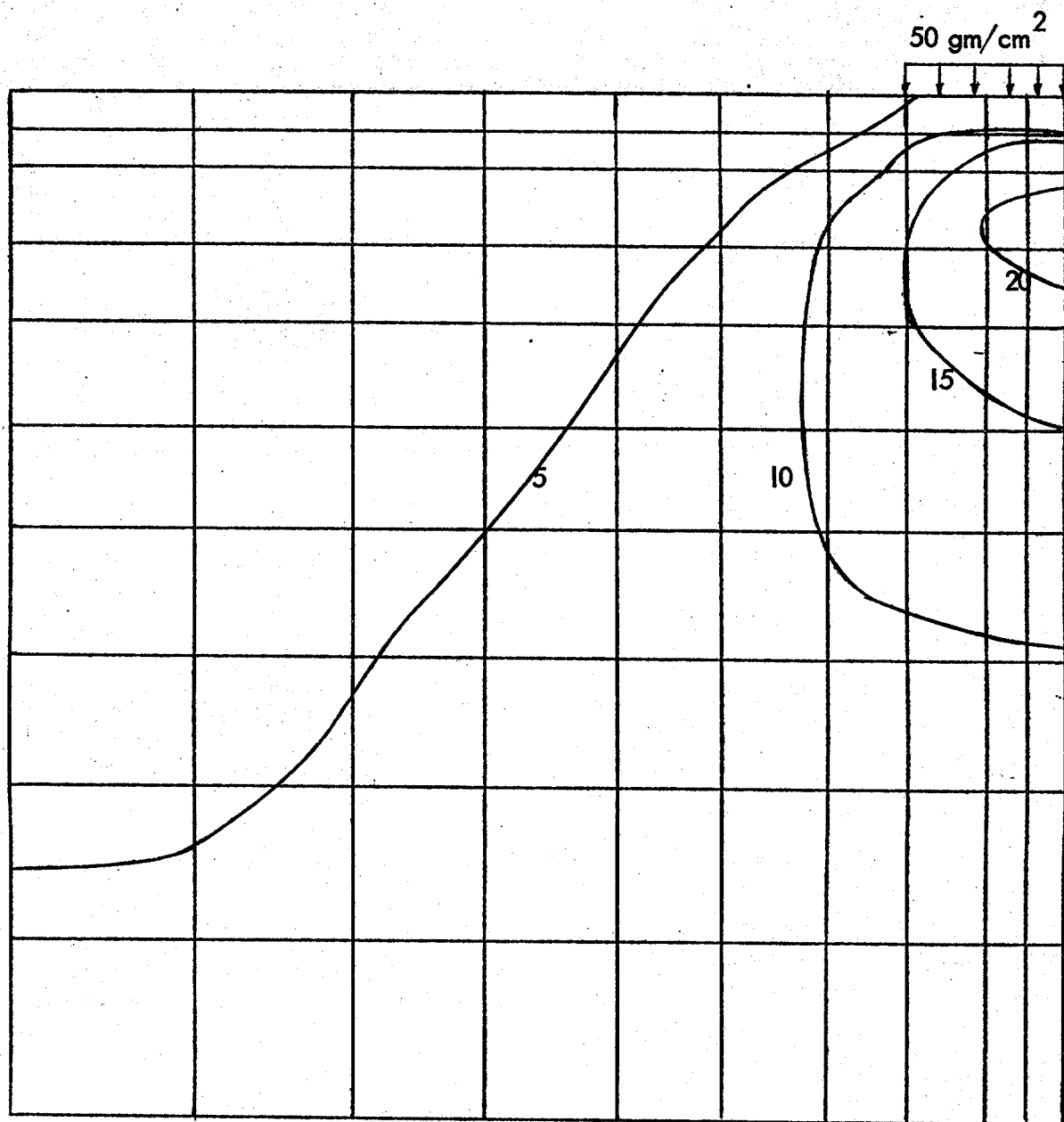


Figure 34. (Continued) Step=14, time=24.8 sec

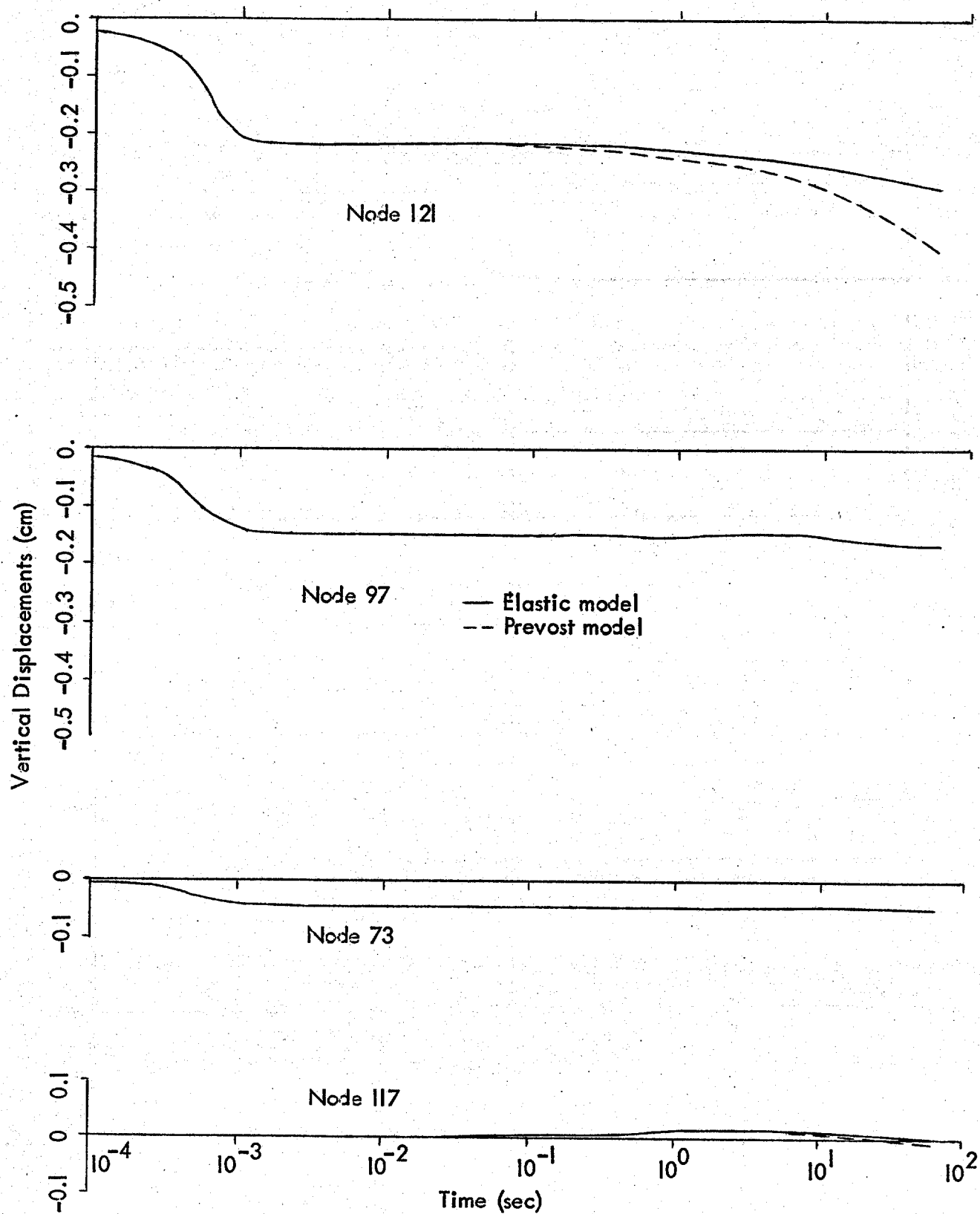


Figure 35 . Vertical nodal displacements — 2D consolidation

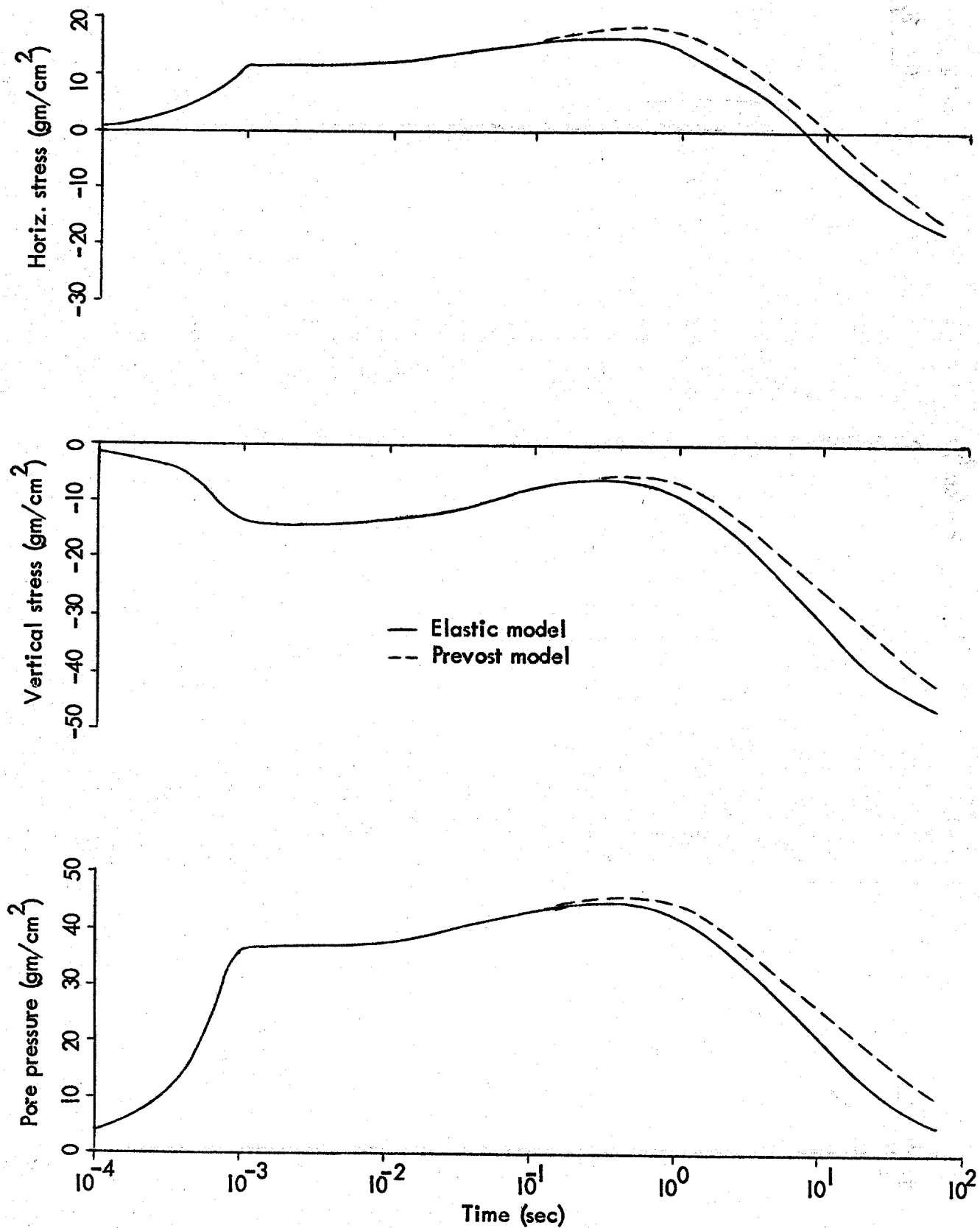


Figure 36 . Stress time histories — 2D consolidation
(Element 89)

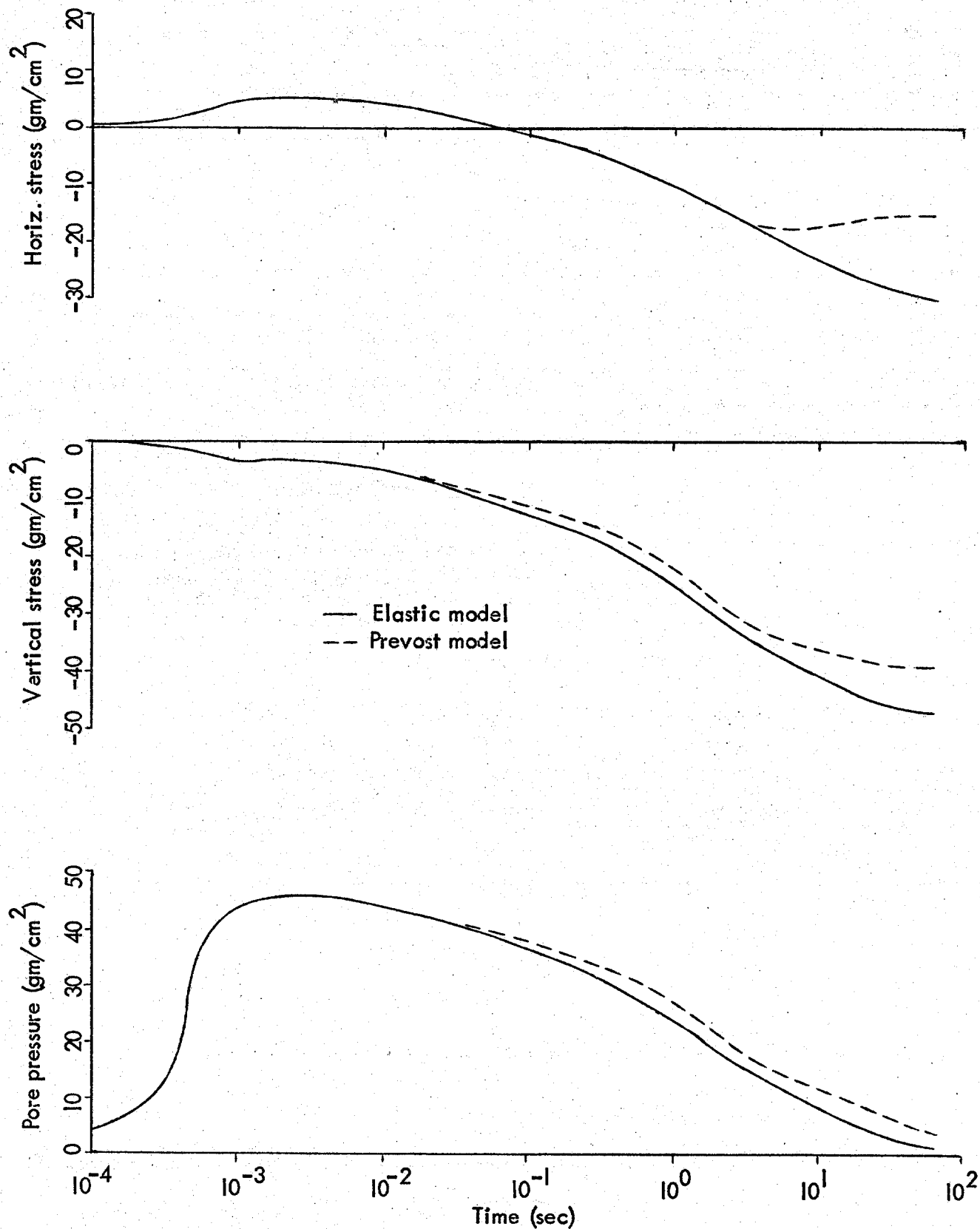


Figure 37. Stress time histories — 2D consolidation (Element 100)

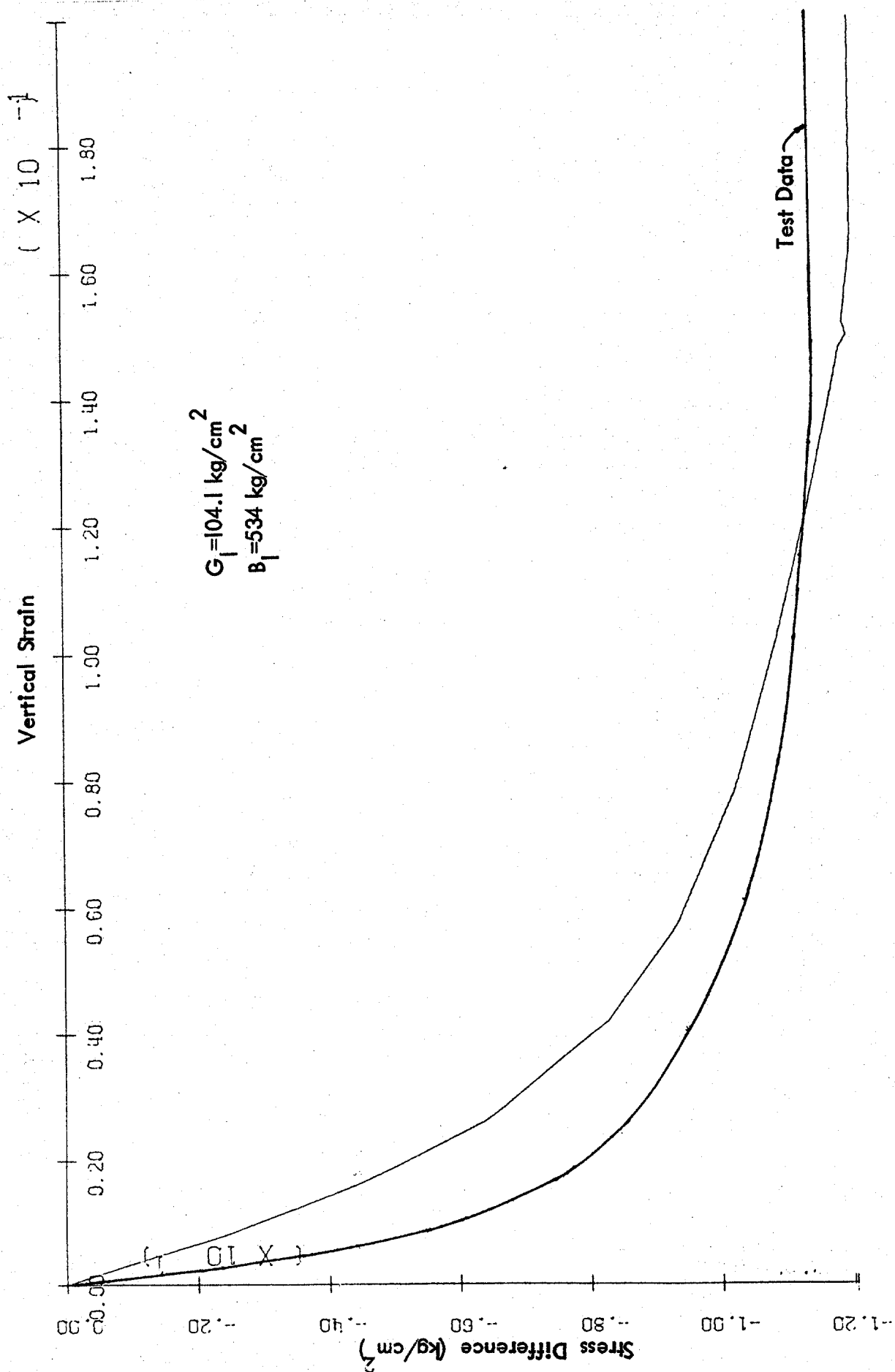


Figure 38a. Stress Difference - Vertical Strain, compression test, $\sigma_H = 5.0 \text{ kg/cm}^2$

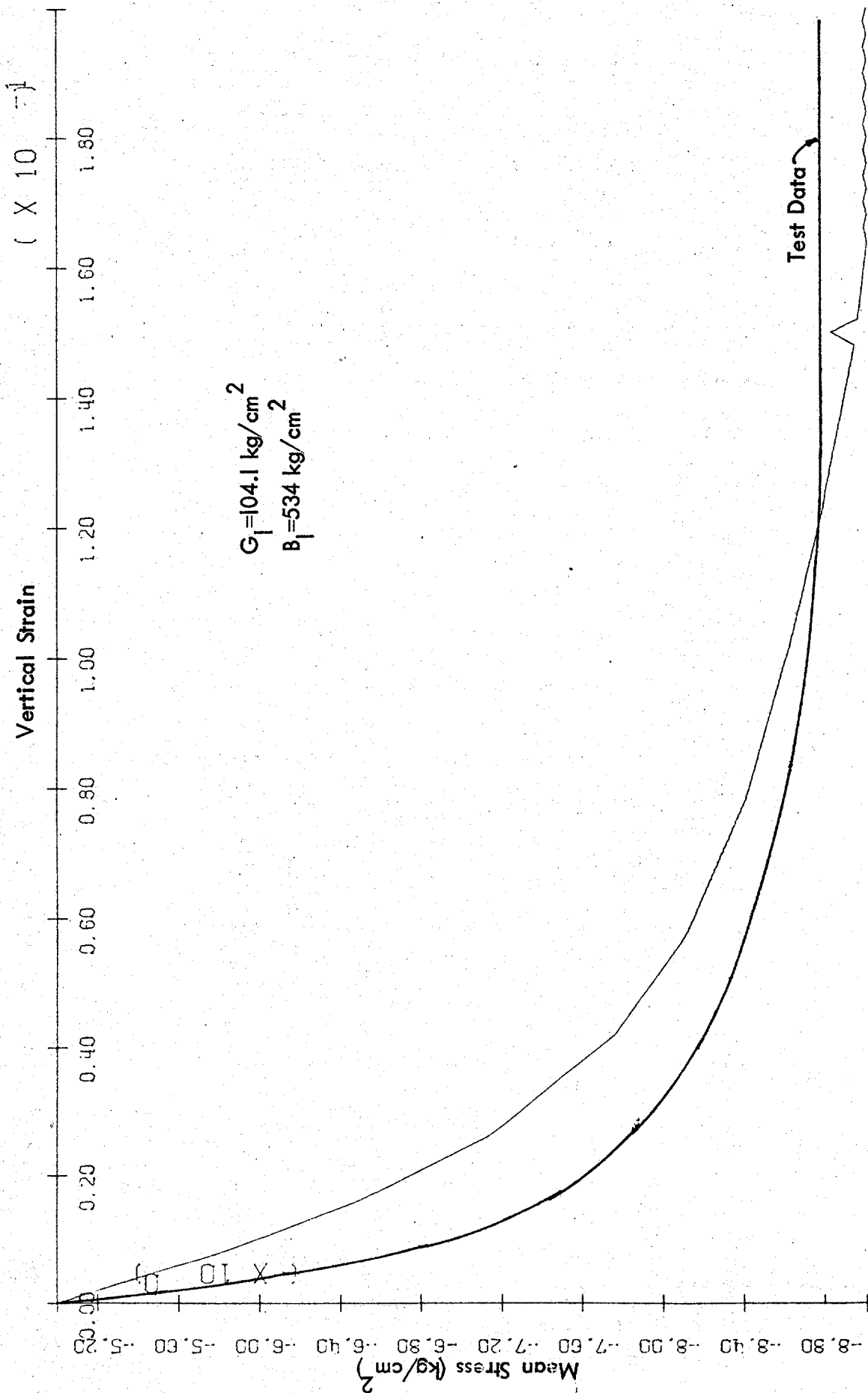


Figure 38b. Mean Stress - Vertical Strain, compression test, $\sigma_H = 5.0 \text{ kg/cm}^2$

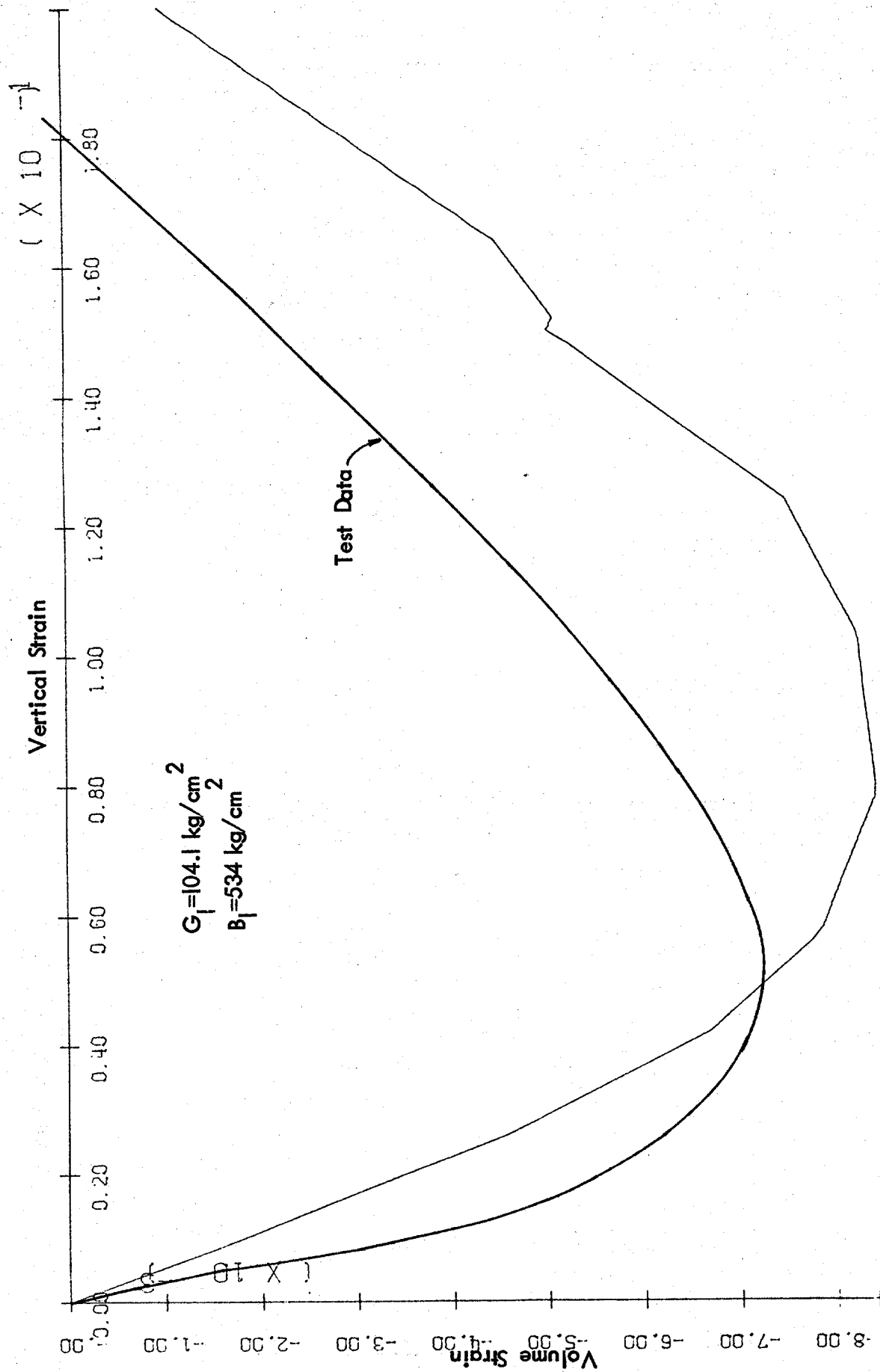


Figure 38c. Volume Strain - Vertical Strain, compression test, $\sigma_H = 5.0 \text{ kg/cm}^2$

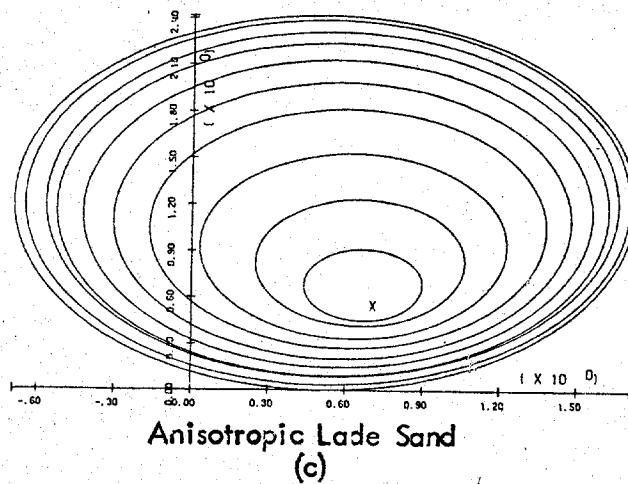
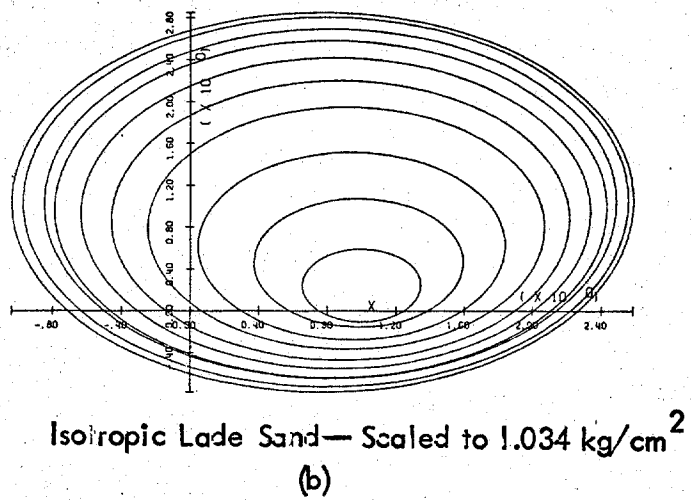
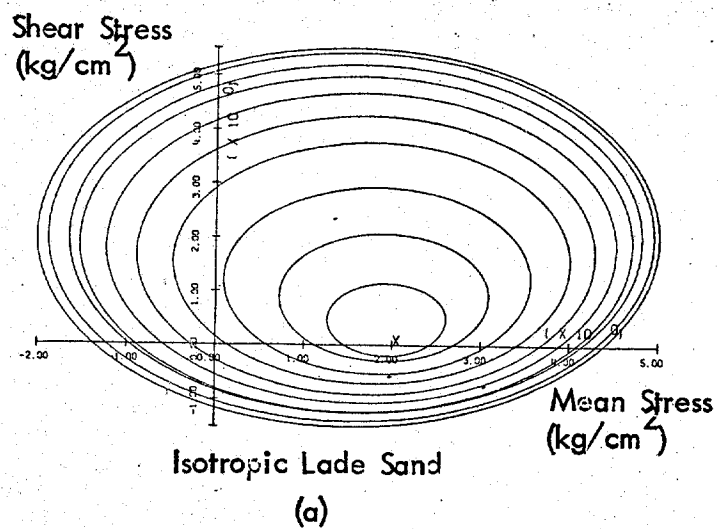


Figure 39 . Scaling of Yield Surfaces

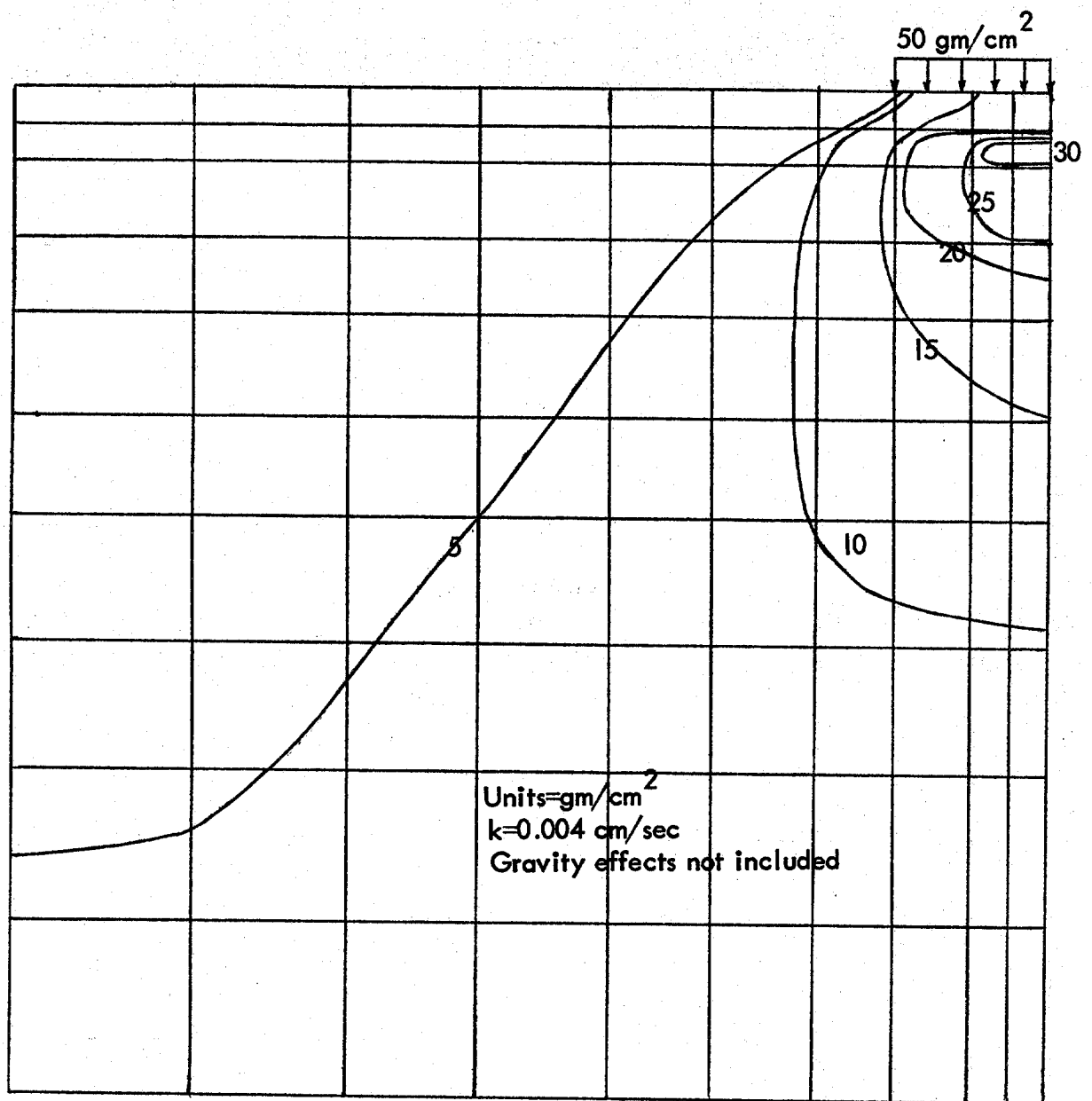


Figure 40 . Pore pressure contours — Prevost soil model (anisotropic)
 Step=14, time=24.8 sec

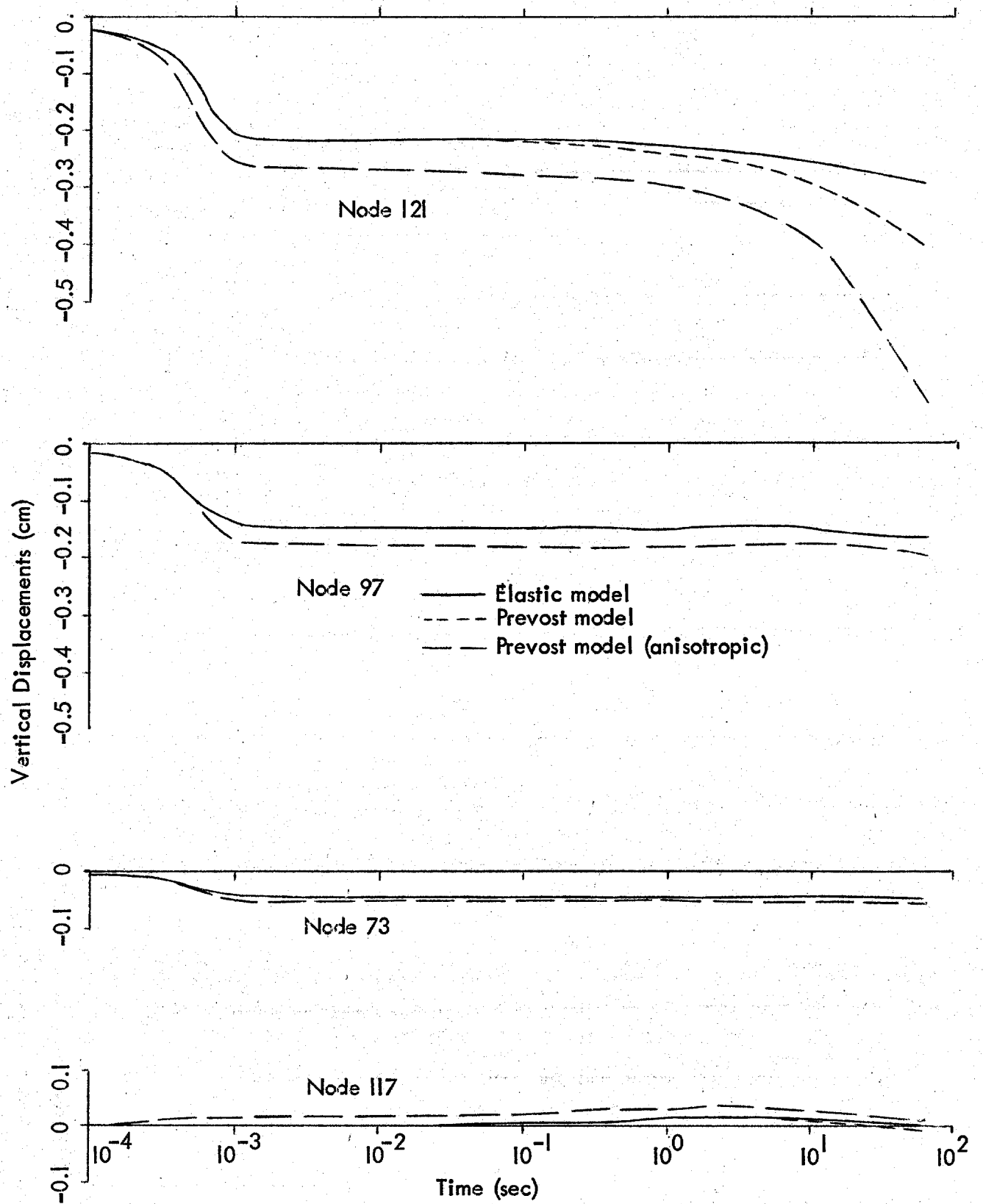


Figure 41. Vertical nodal displacements — 2D consolidation

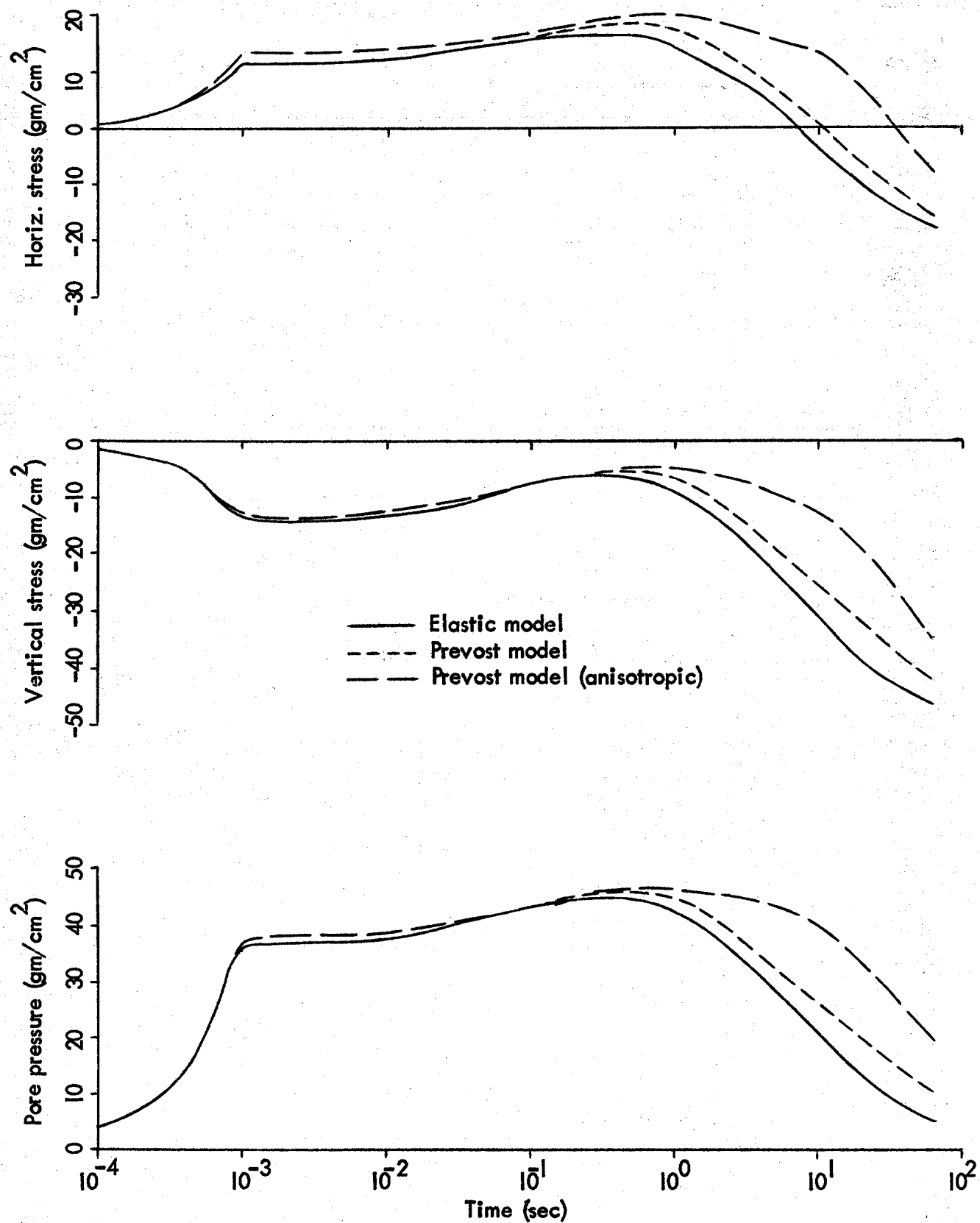


Figure 42. Stress time histories — 2D consolidation
(Element 89)

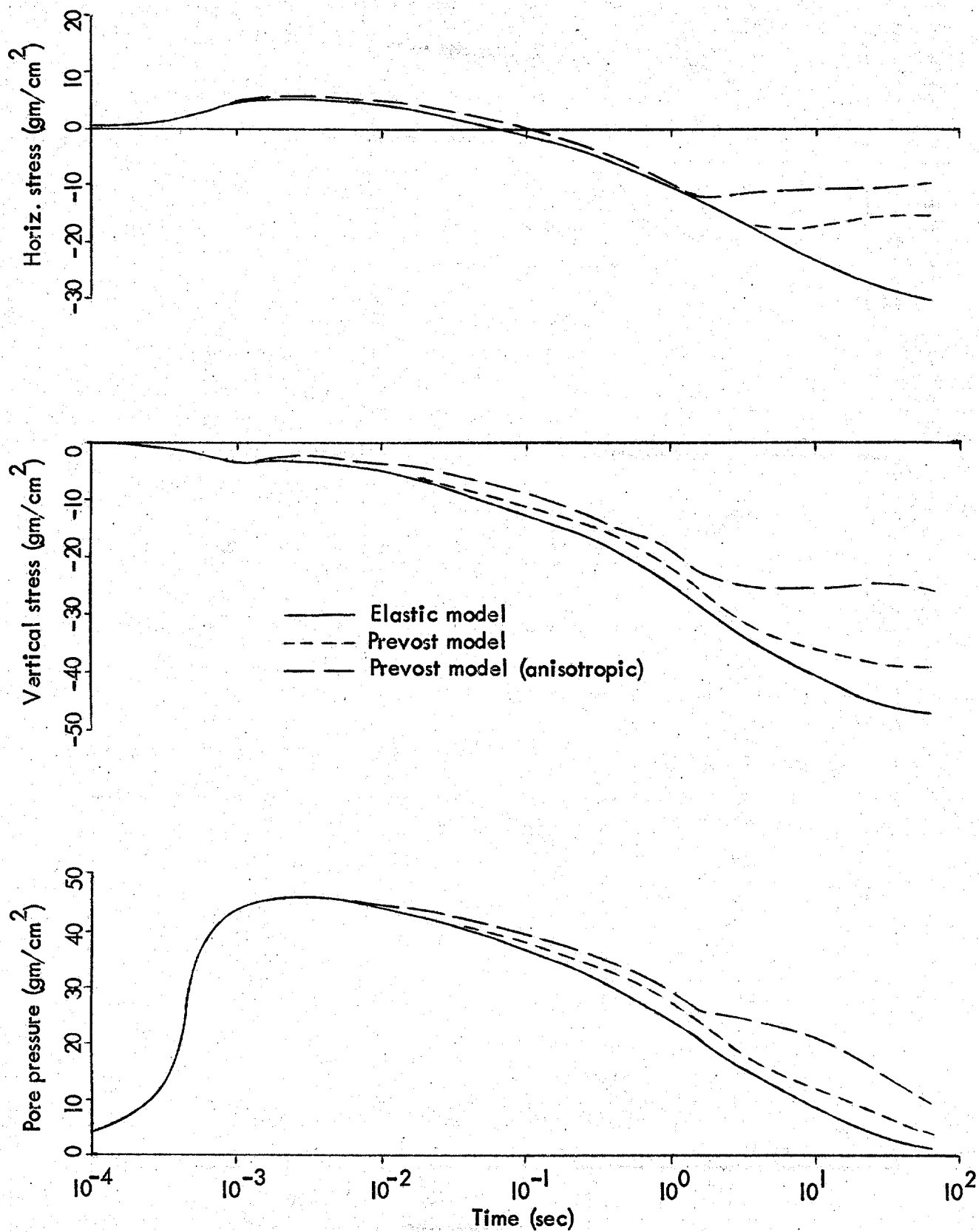


Figure 43. Stress time histories — 2D consolidation (Element 100)

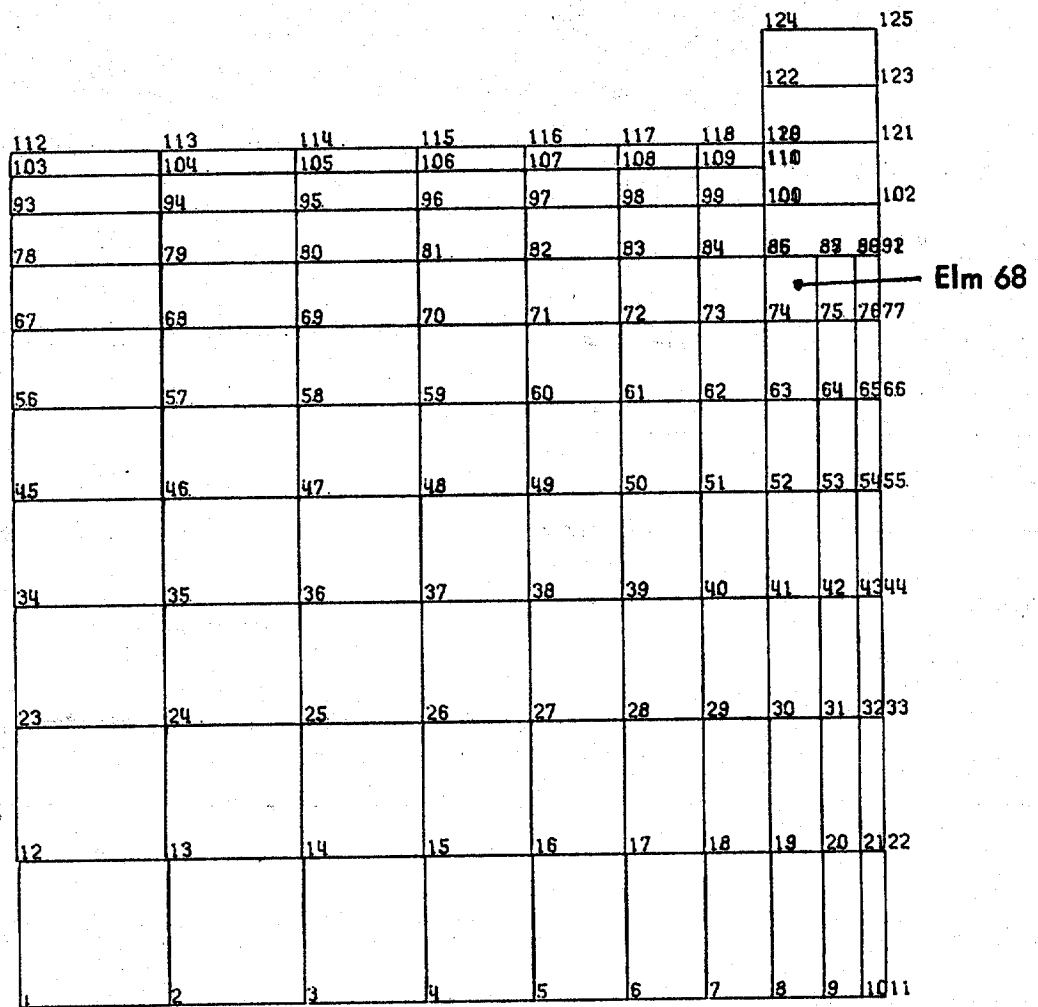


Figure 44. Undeformed mesh—2D Soil field with building

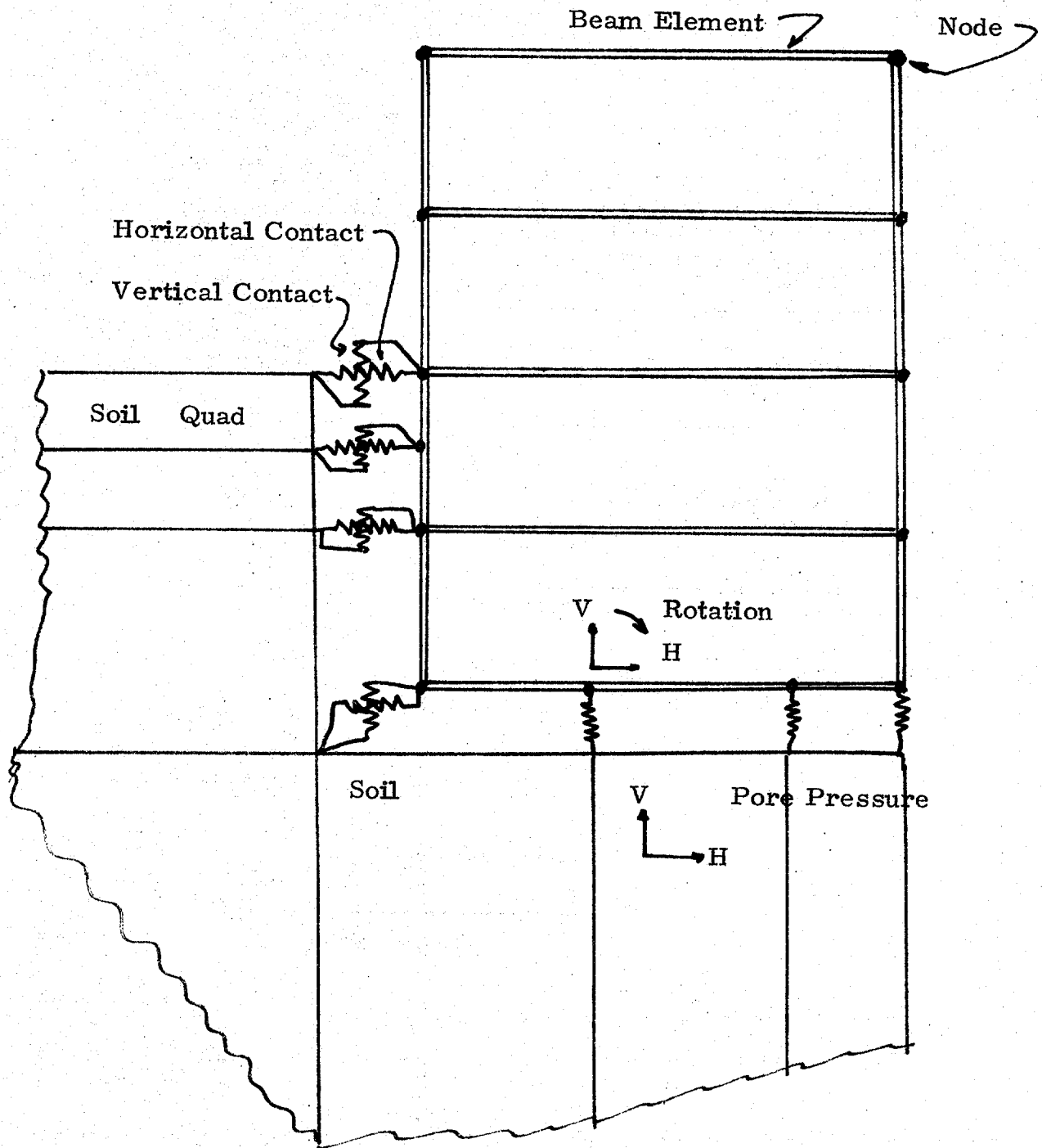


Figure 45. Contact elements at structure interface.

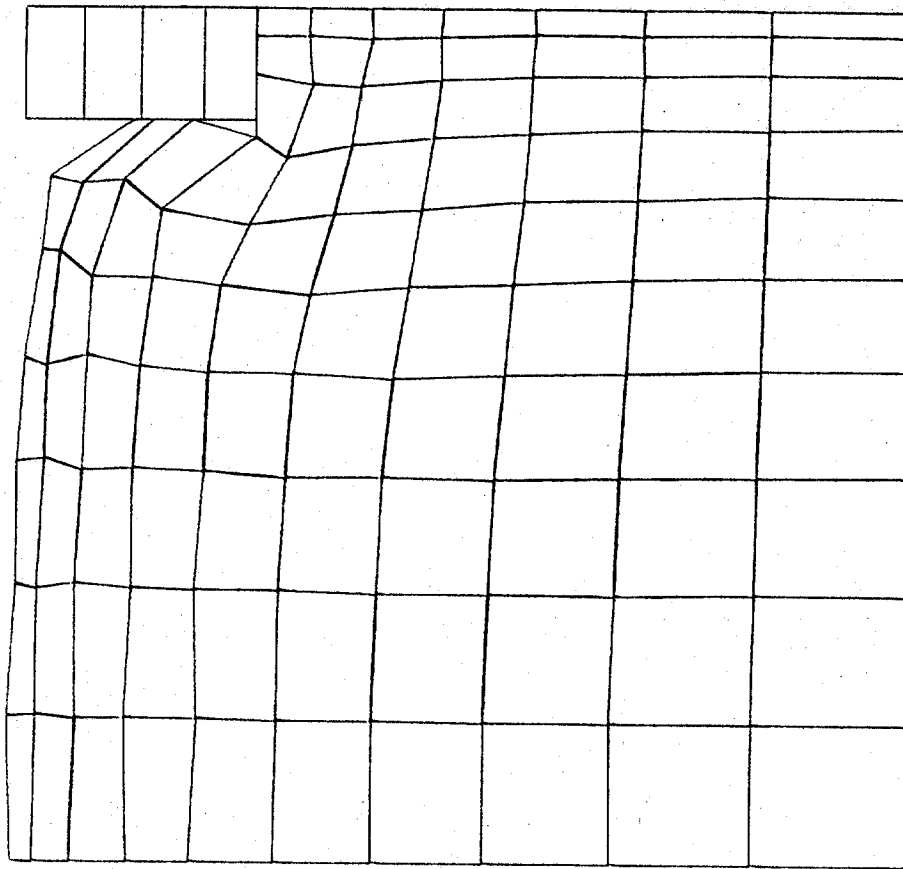


Figure 46 . Deformed mesh step 5.

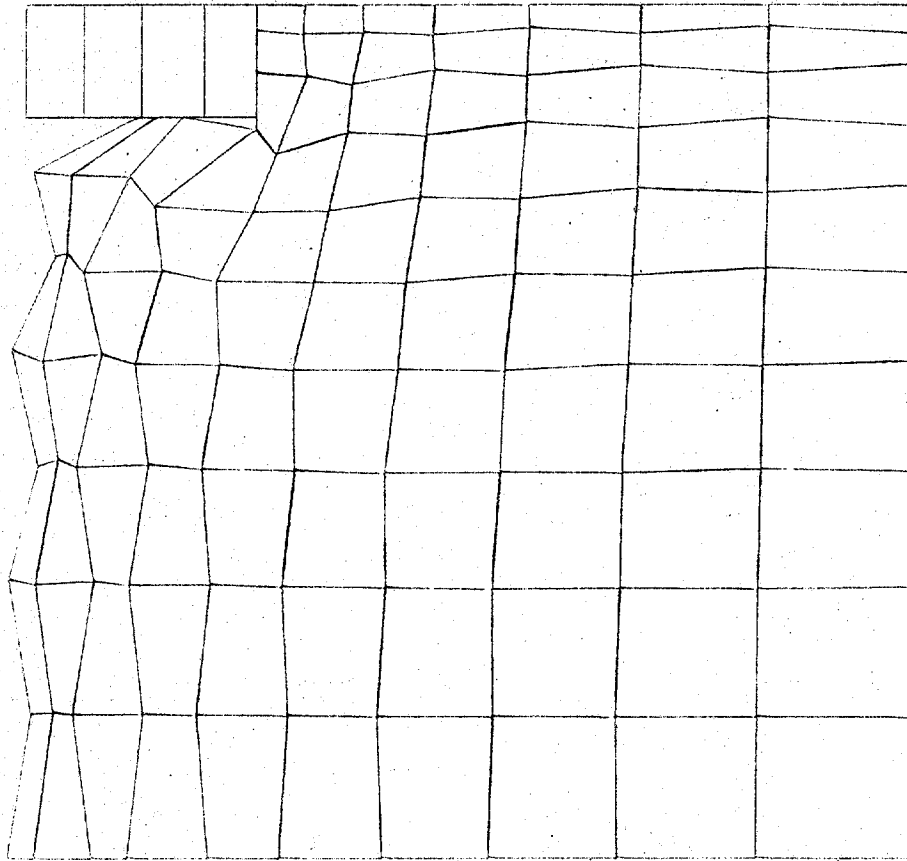


Figure 47. Deformed mesh step 15.

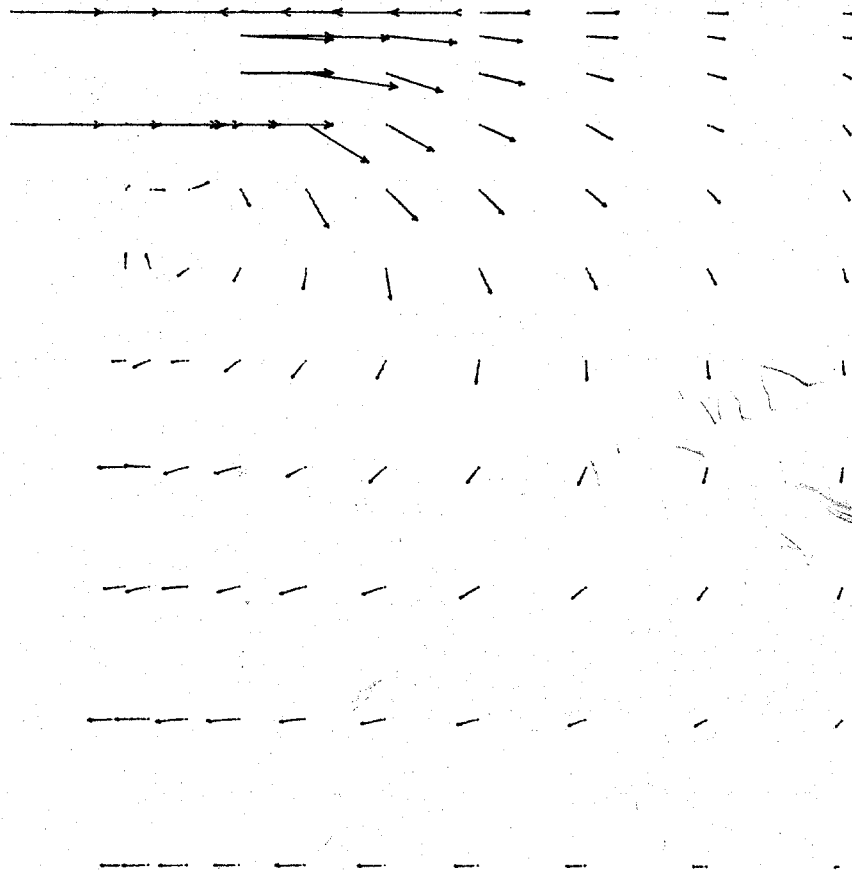


Figure 48. Vector Velocity step 5.

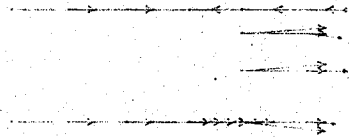


Figure 49. Vector velocity step 15.

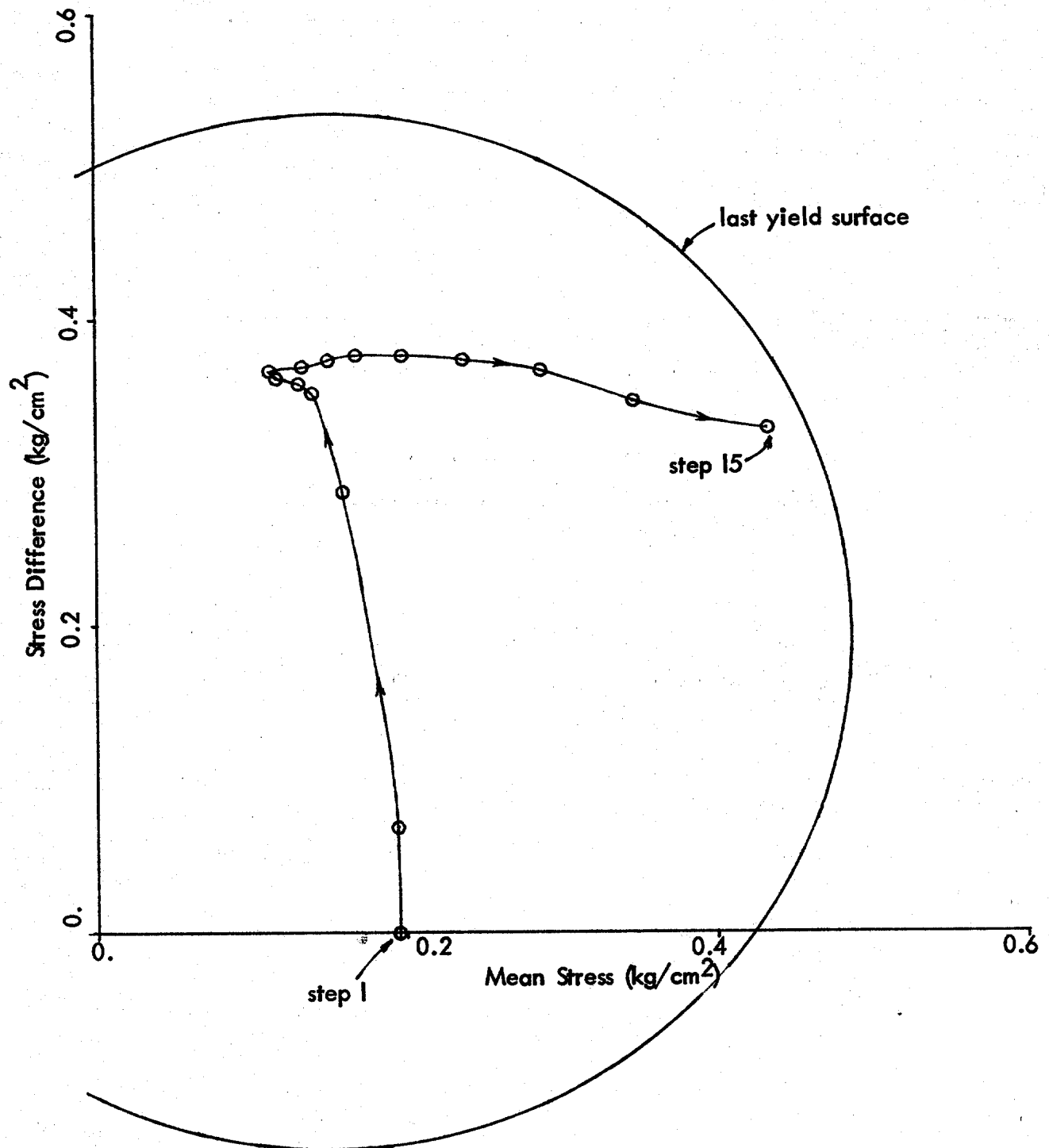


Figure 50 . Effective Stress Path—2D Soil field with building (Element 68)

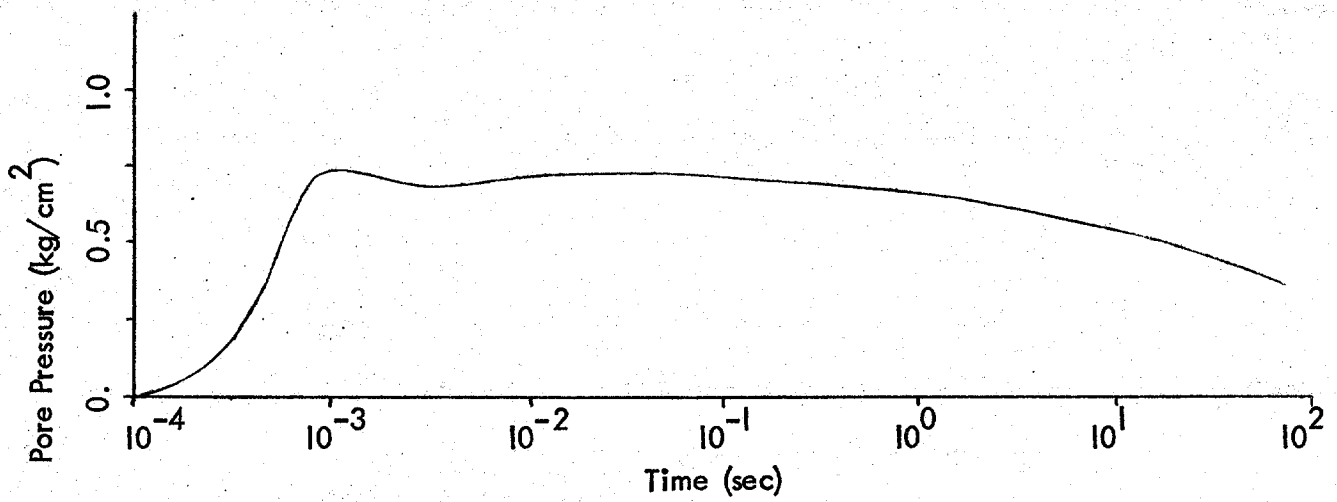


Figure 51. Pore Pressure History—2D Soil field with building (Element 68)

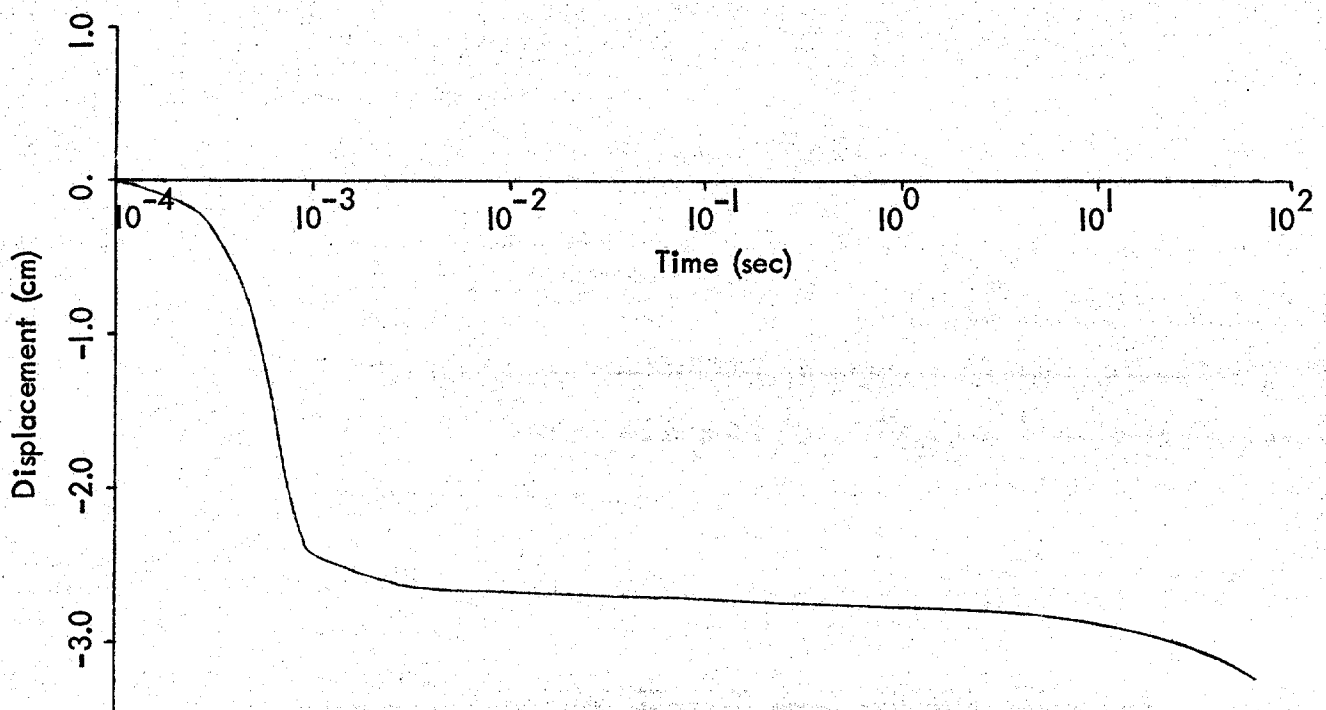


Figure 52. Displacement History—2D Soil field with building (Node 85)

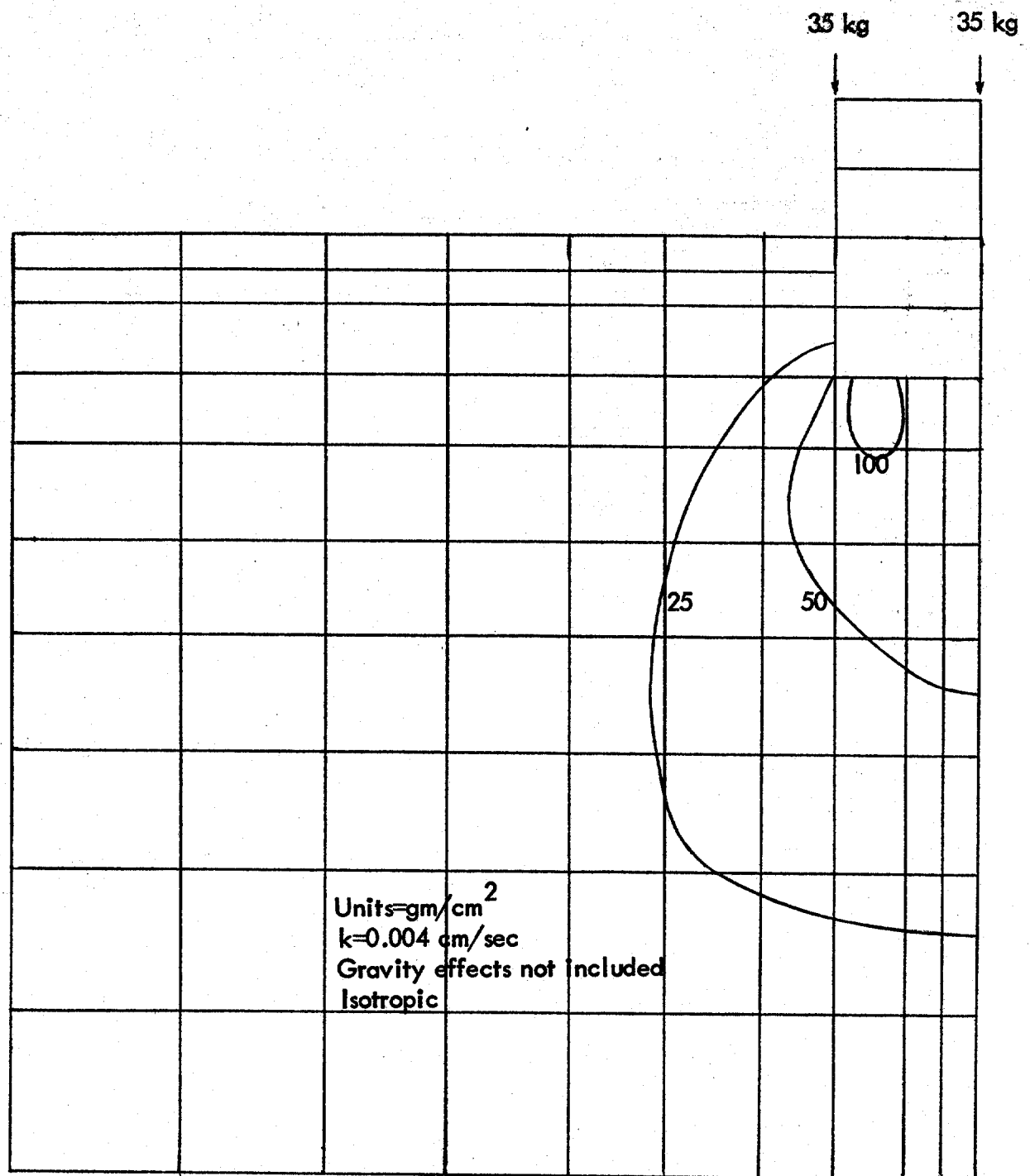


Figure 53. Pore pressure contours — Prevost soil model
 Step=2, time=0.00035 sec

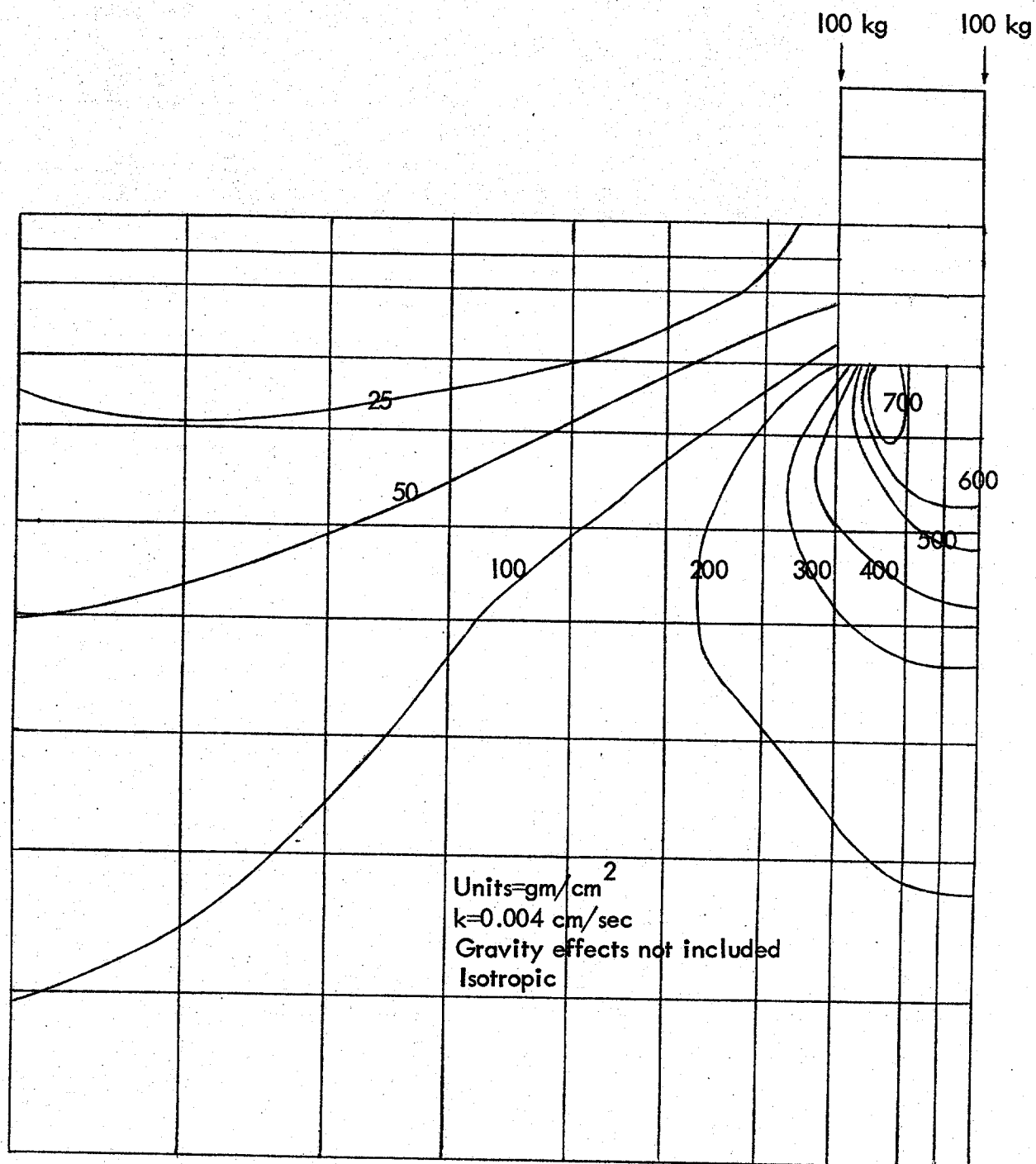


Figure 53. (Continued) Step=4, time=0.0025 sec

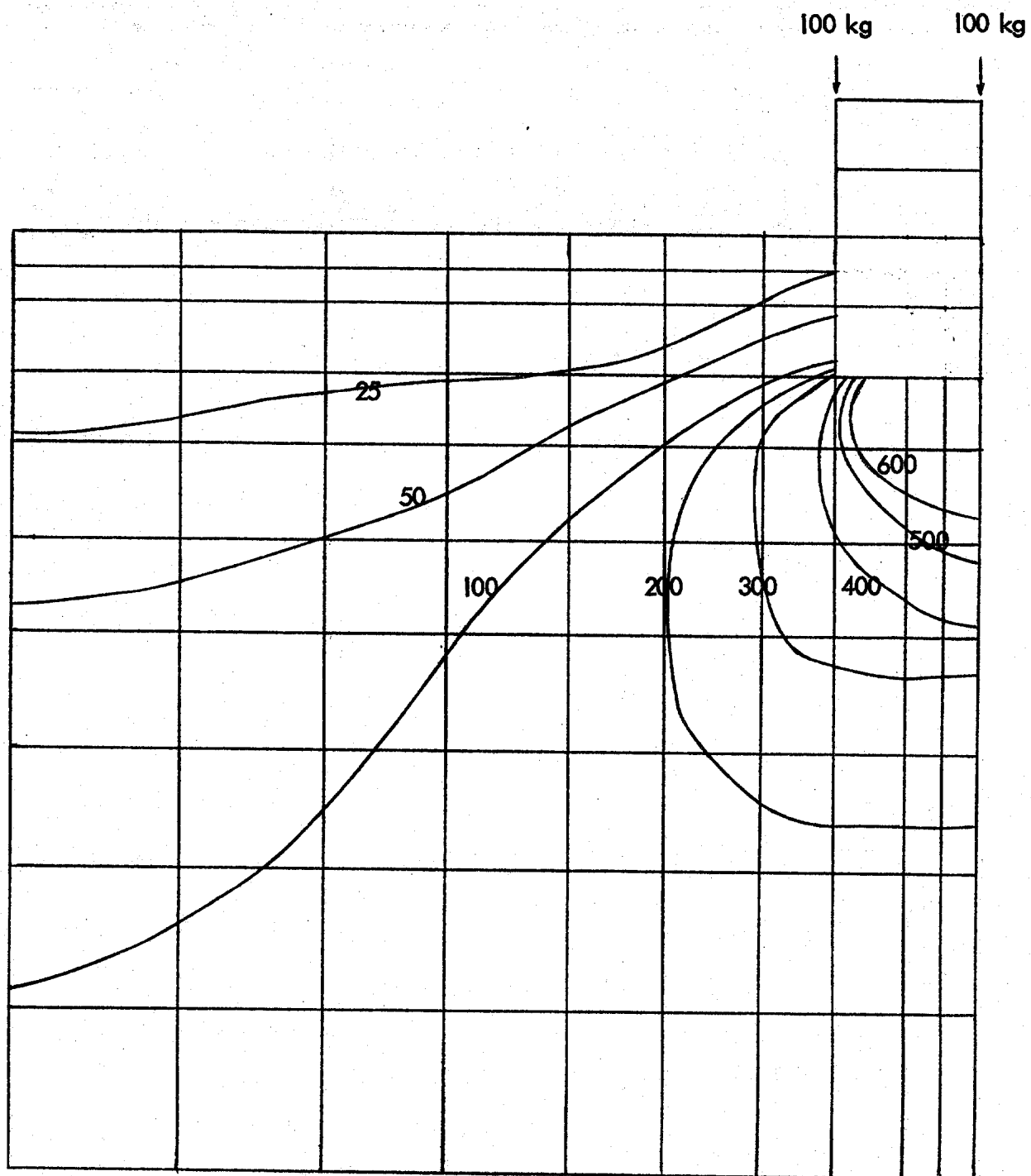


Figure 53. (Continued) Step=10, time=0.64 sec

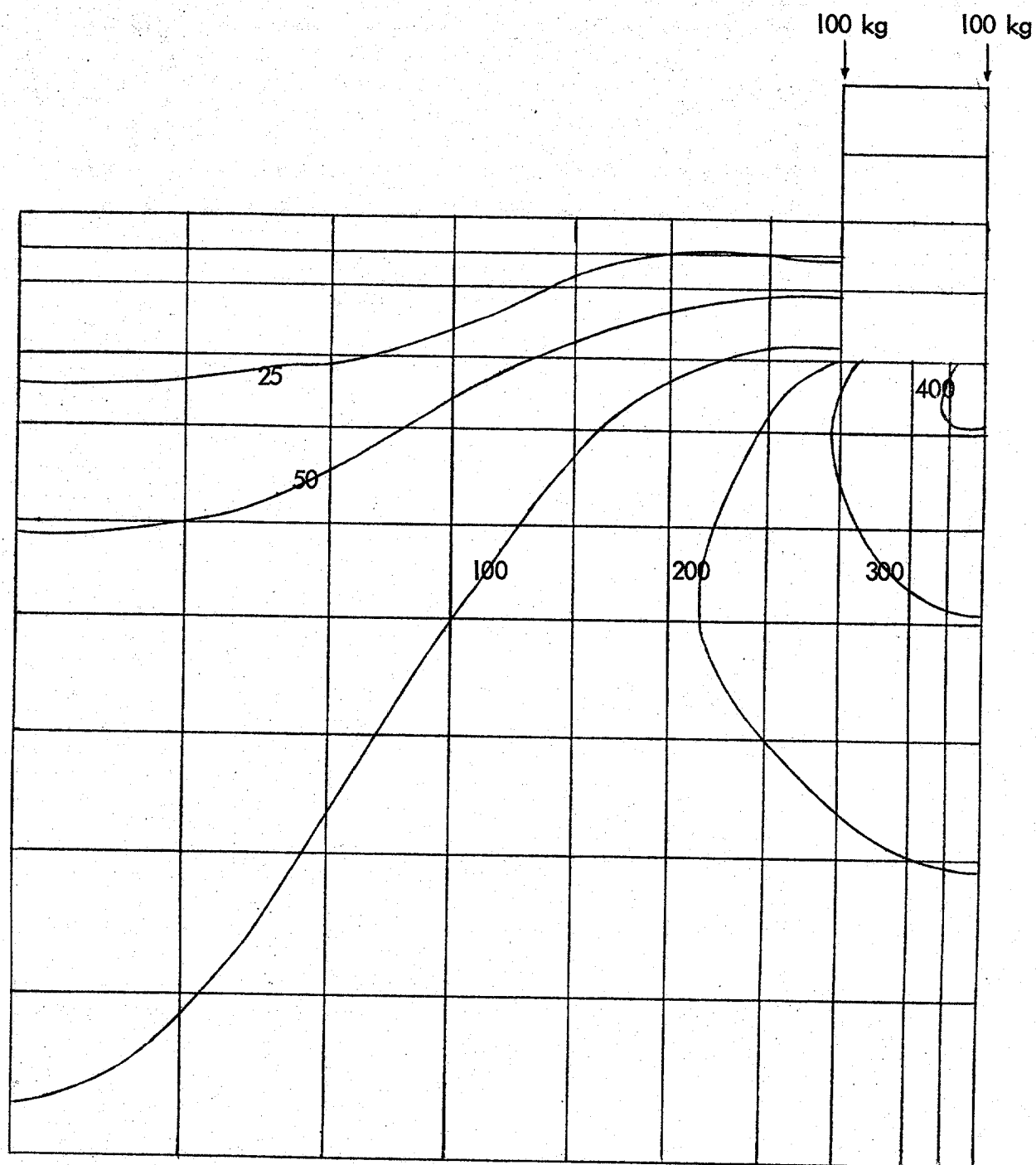


Figure 53. (Continued) Step=14, time=24.8 sec

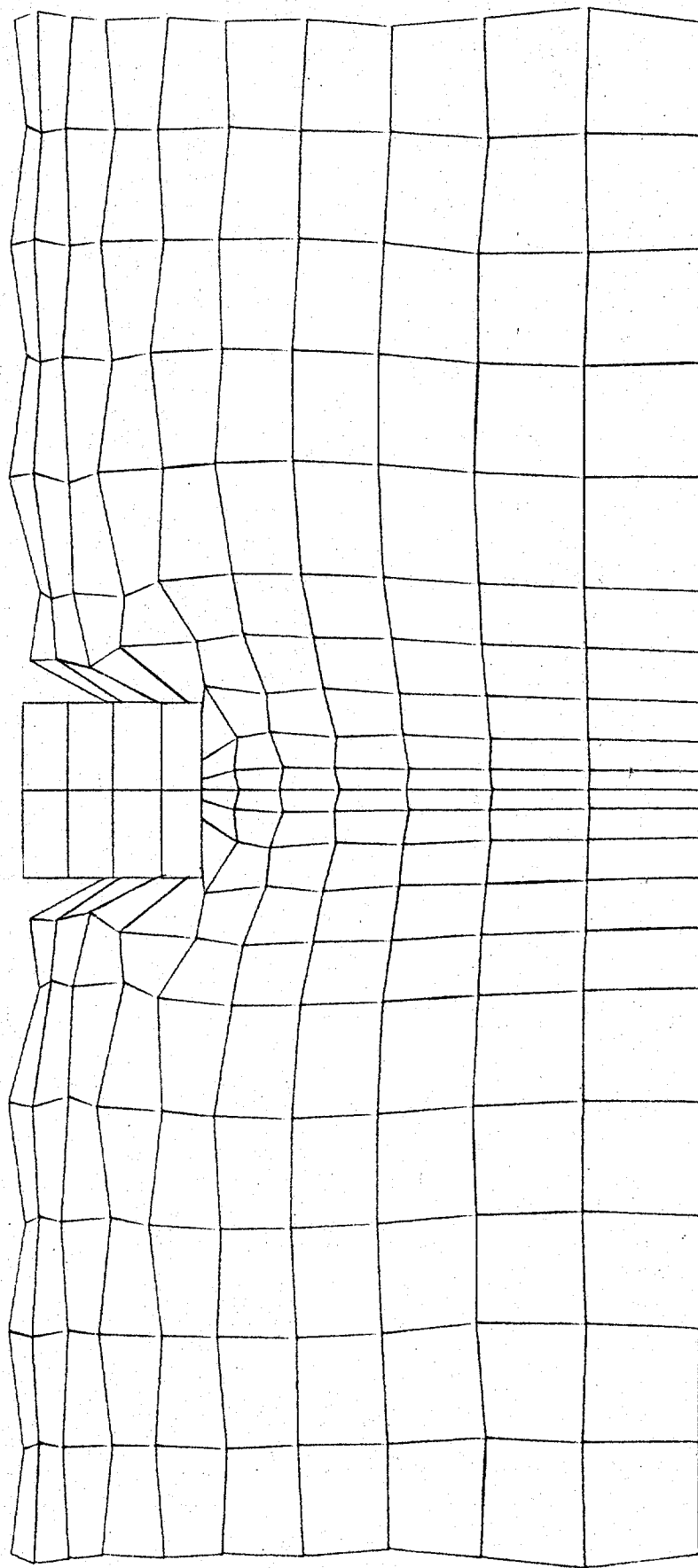


Figure 55. Deformed mesh — Static solution
Scale factor=1.143, time=63.57 sec

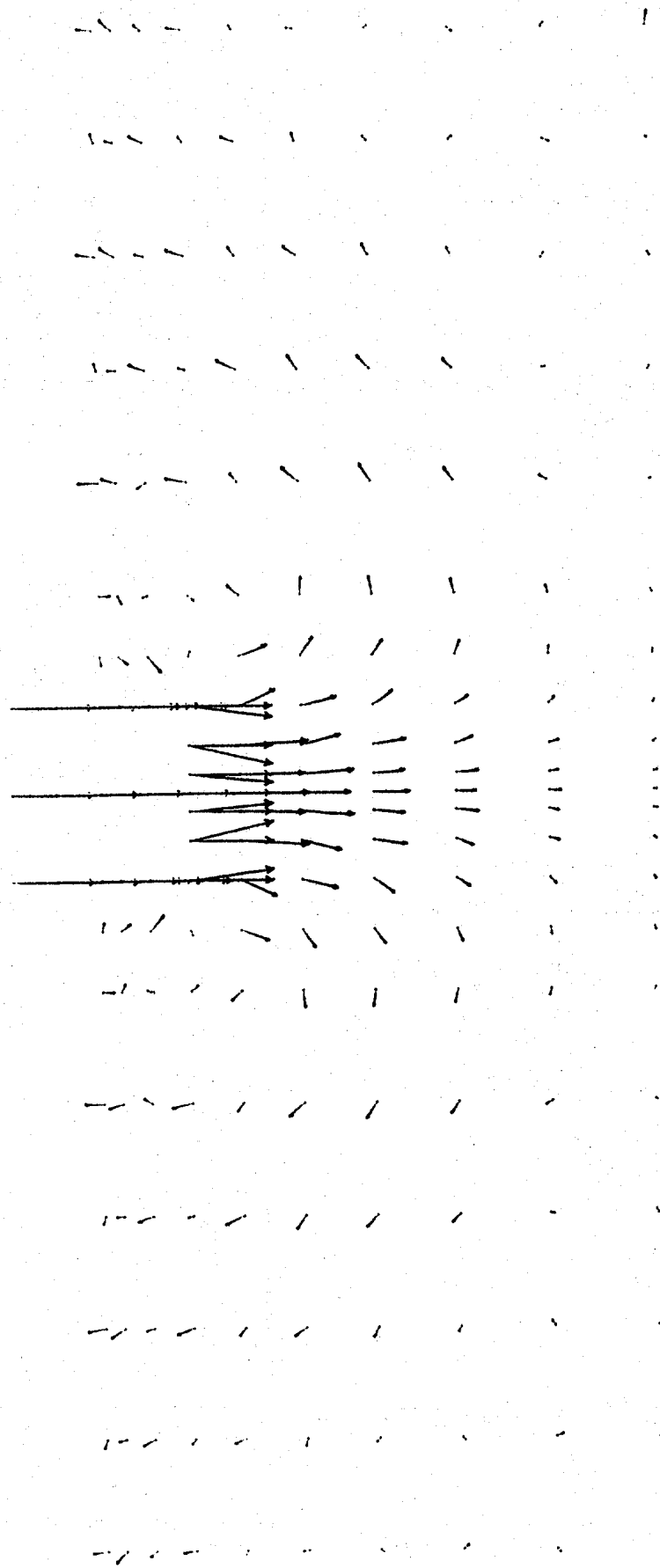


Figure 55. (Continued) Displacement vectors — Static solution
Scale factor=1.143

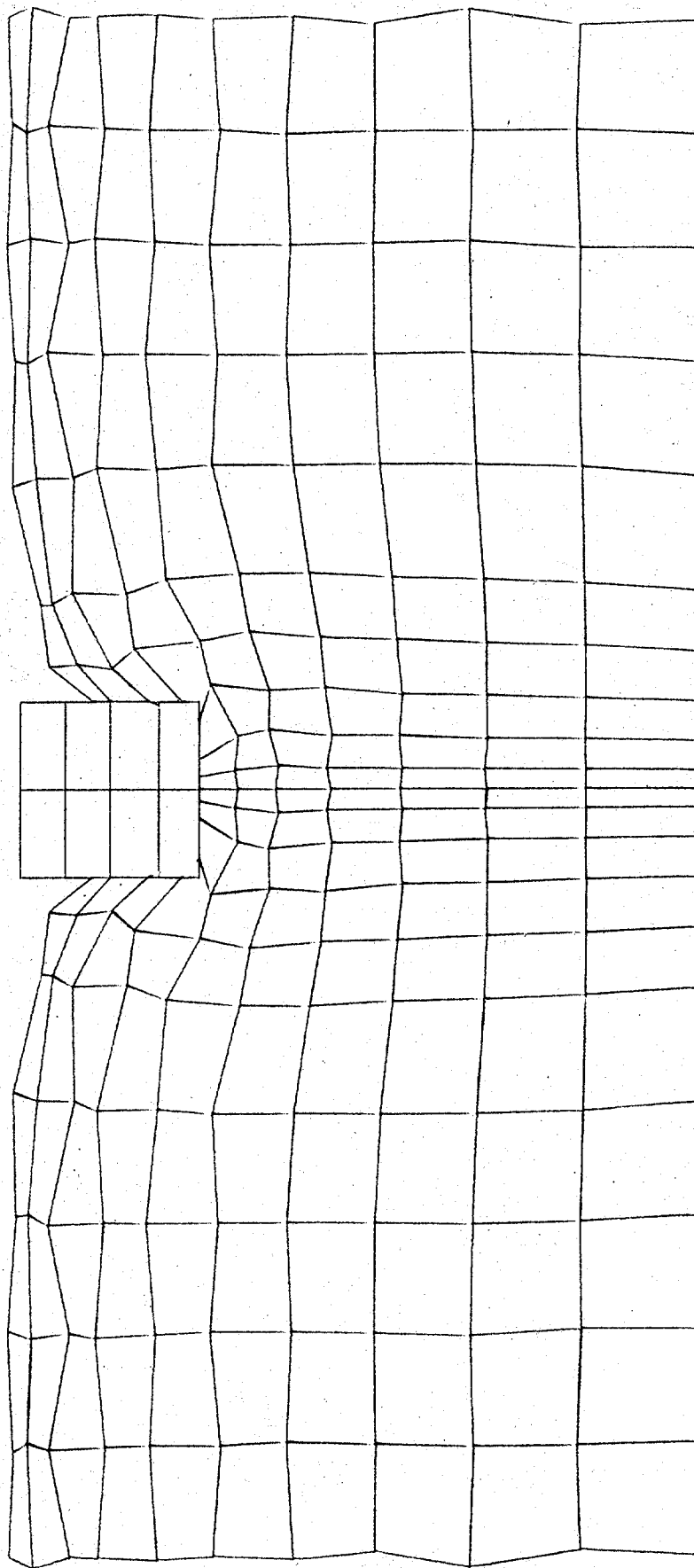


Figure 56. Deformed mesh — Dynamic solution
Scale factor=1.012, step=210, time=66.07 sec

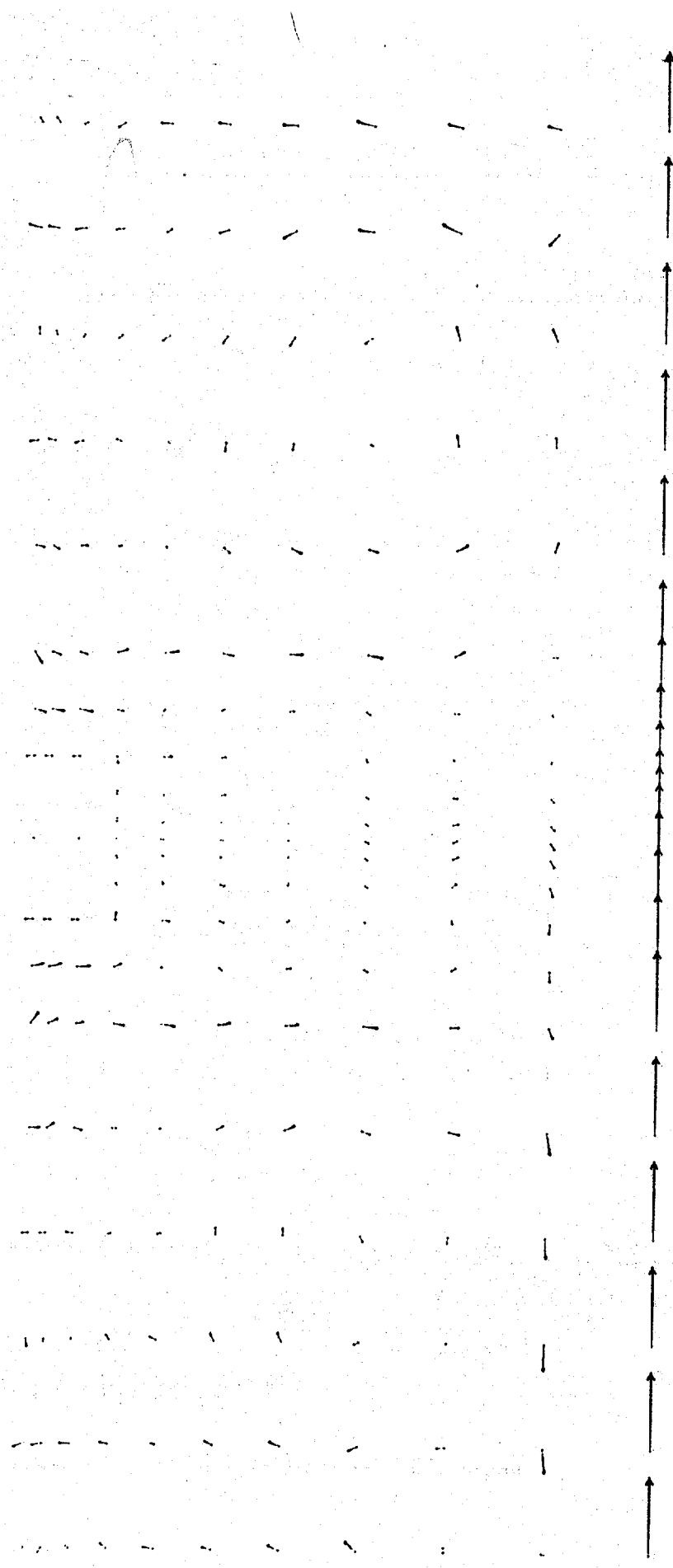


Figure 57. Velocity vectors — Dynamic solution
Scale factor: 1 in=0.503 cm/sec

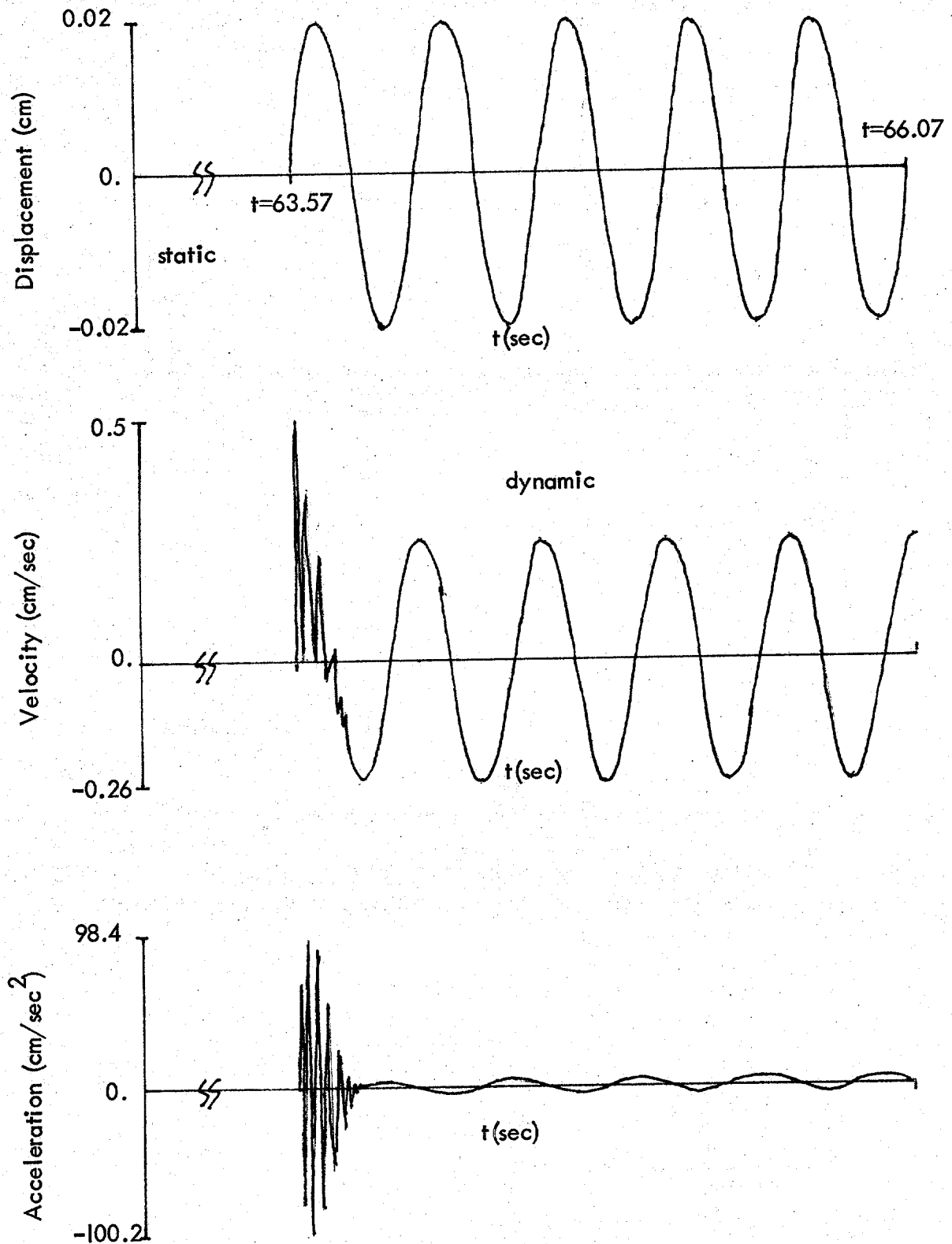


Figure 58a. Time histories — Node 10, horizontal
(Base of soil field)

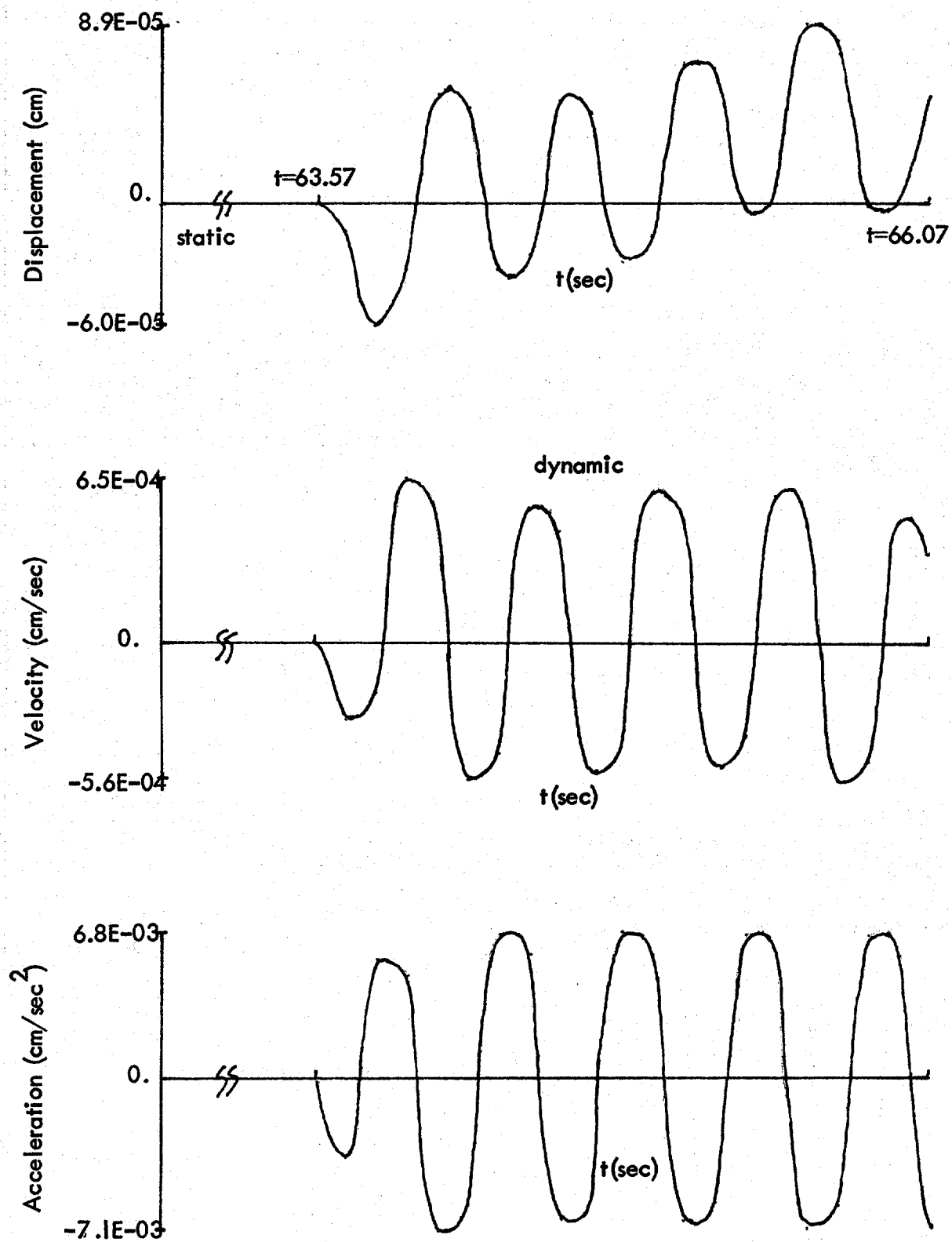


Figure 58b. Time histories — Node 168, horizontal
(Base of building)

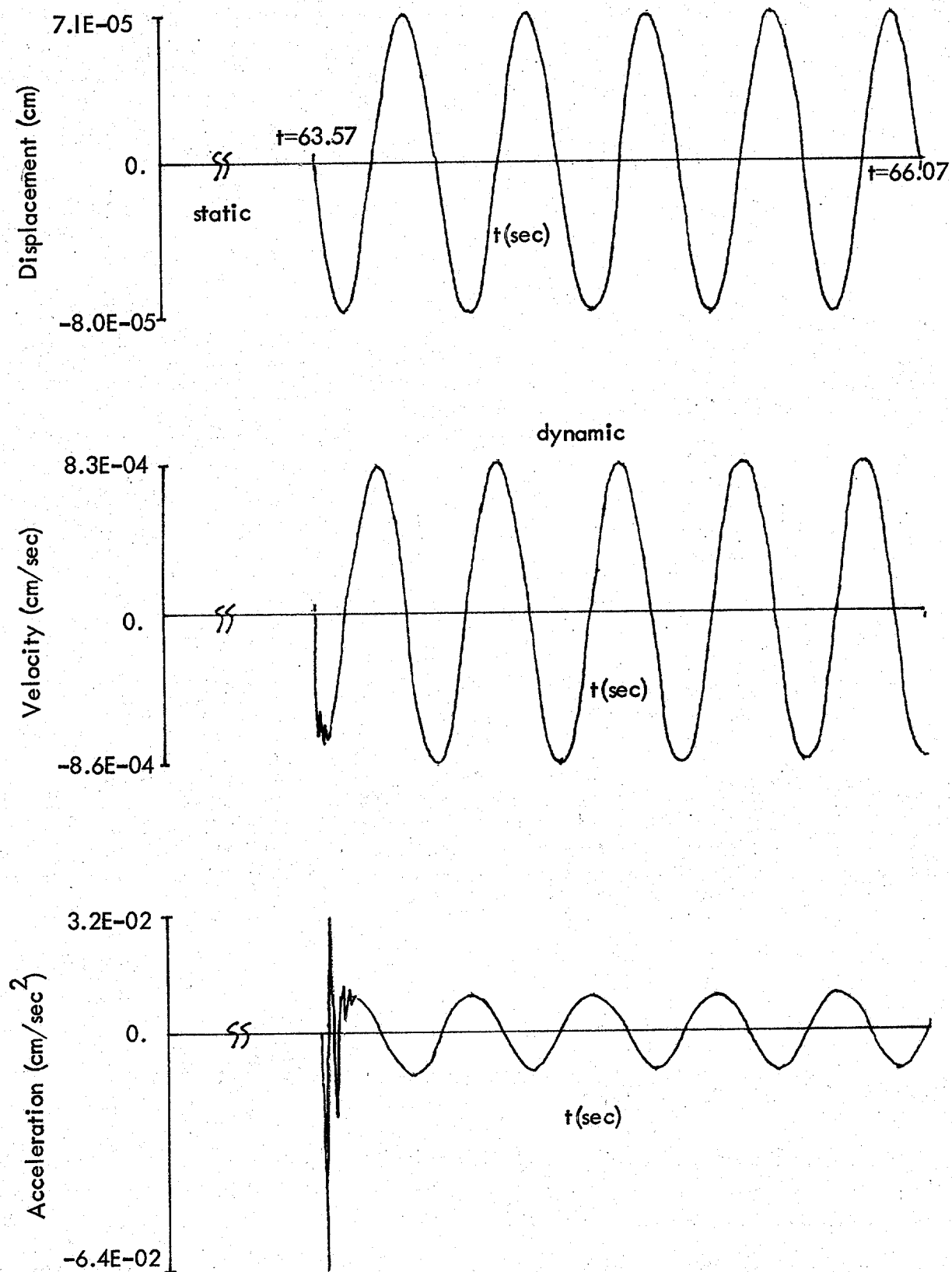


Figure 58c. Time histories — Node 237, horizontal (Top of building)

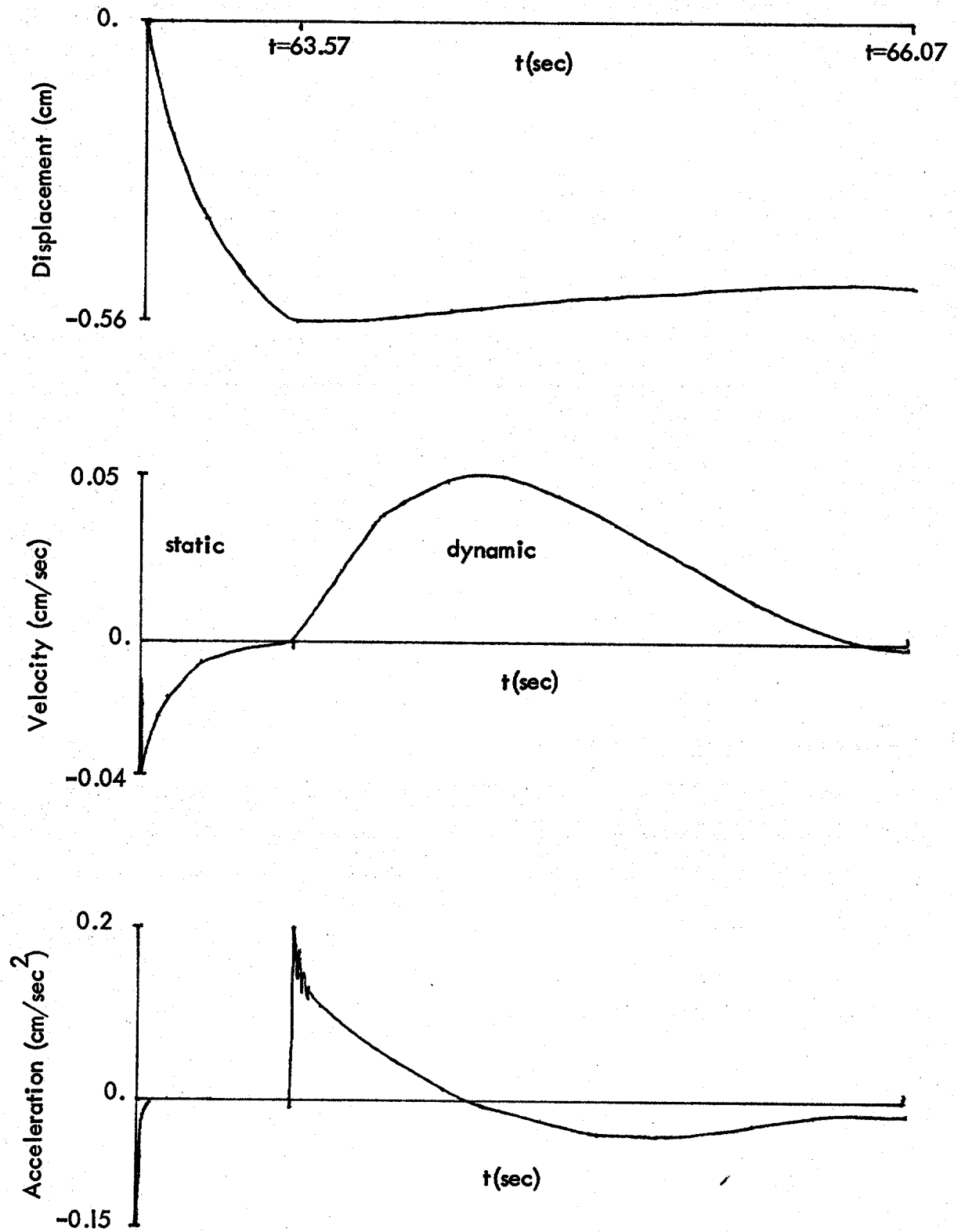


Figure 58d. Time histories — Node 237, vertical
(Top of building)

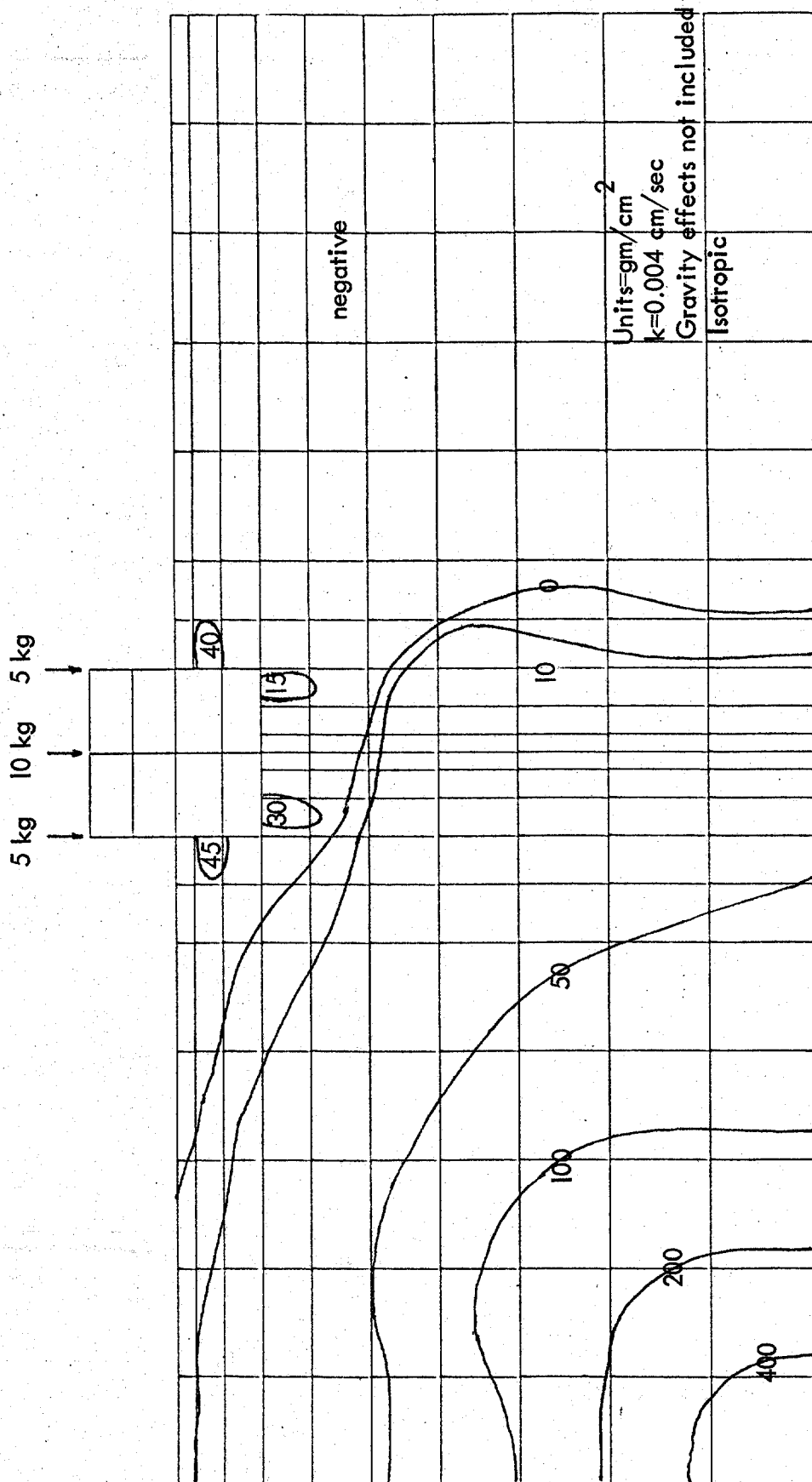


Figure 59. Pore pressure contours — Prevost soil model
 Step=20, time=63.70 sec

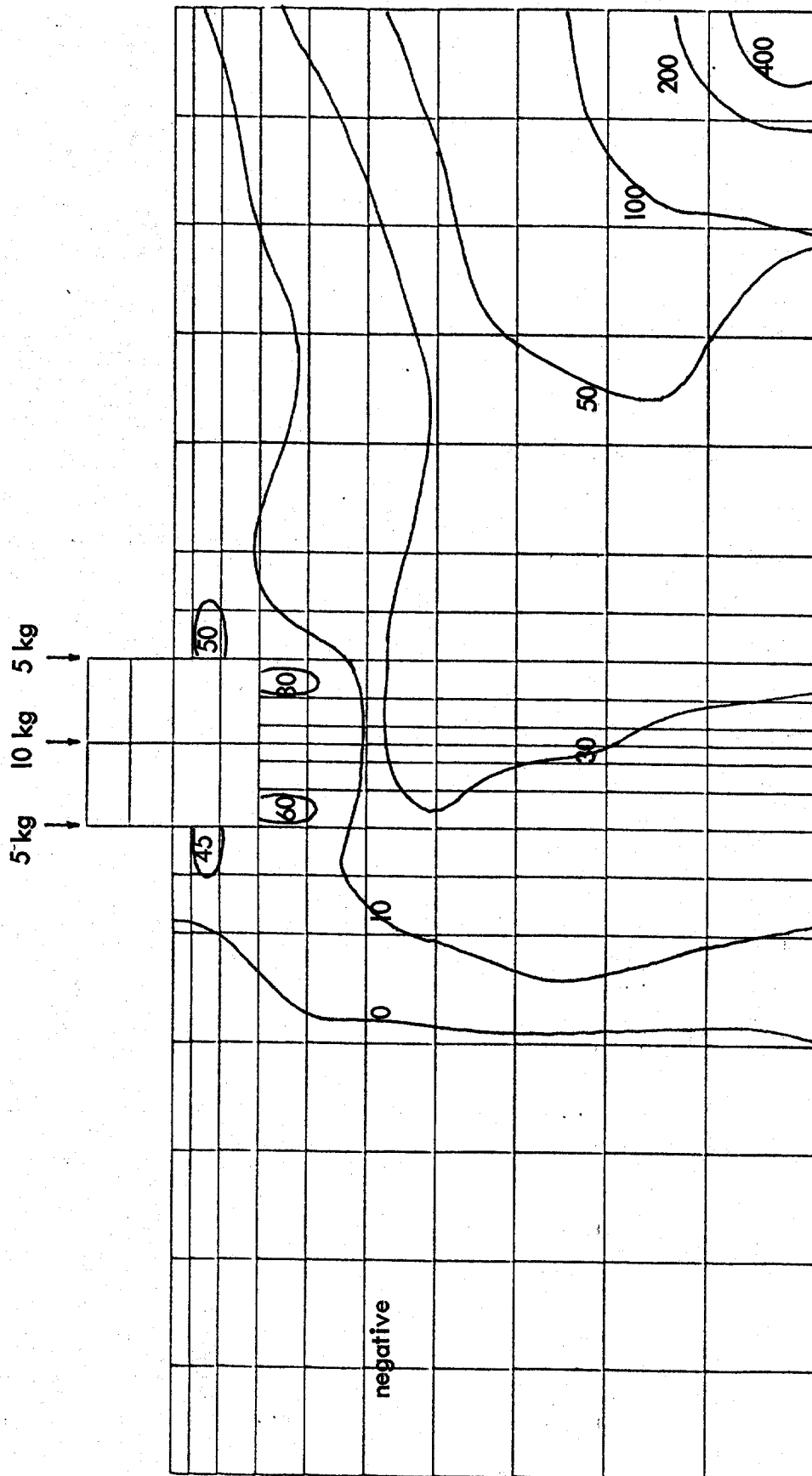


Figure 57. (Continued) $\Delta t=120$, time=64.95 sec

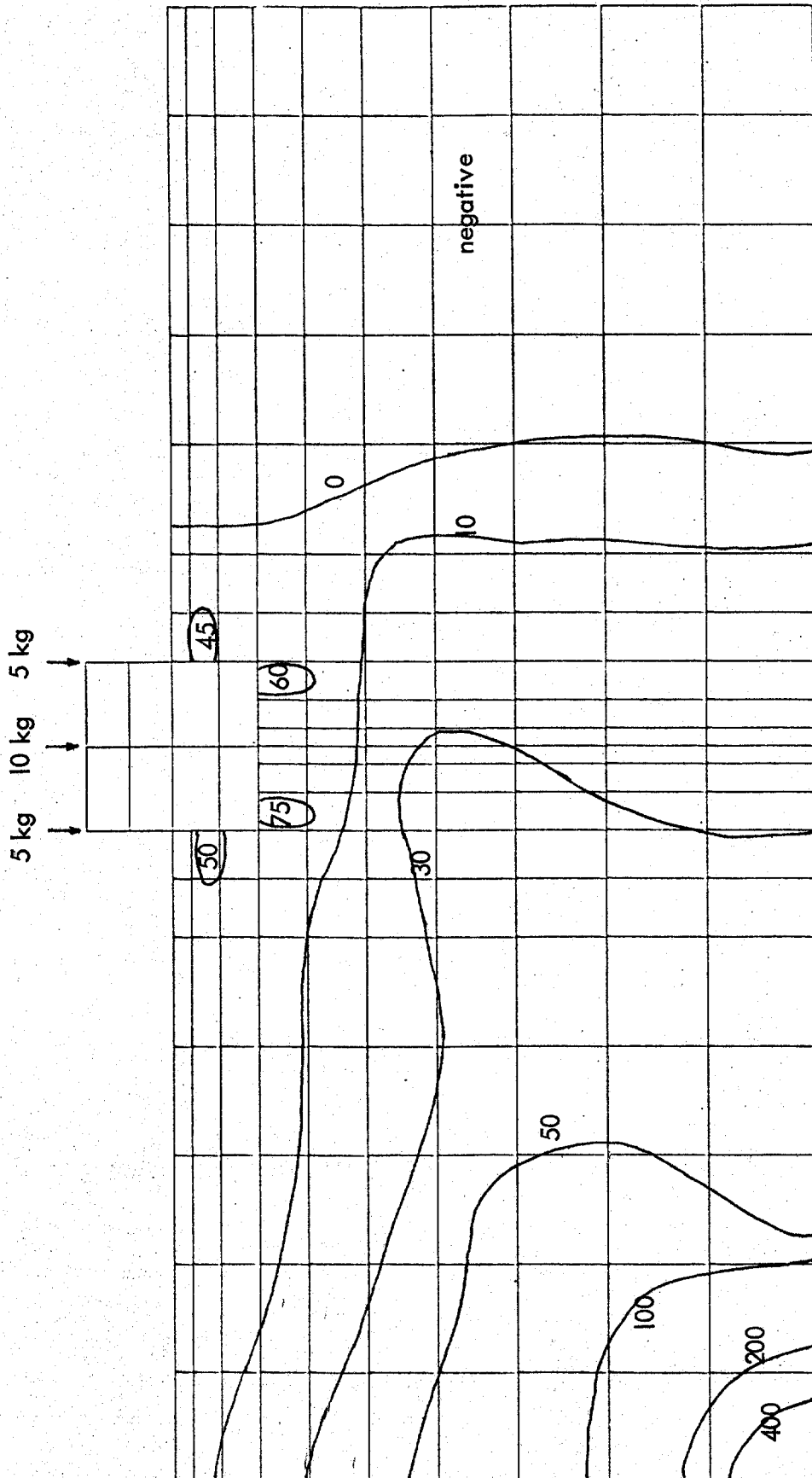


Figure 59. (Continued) Step=140, time=65.20 sec

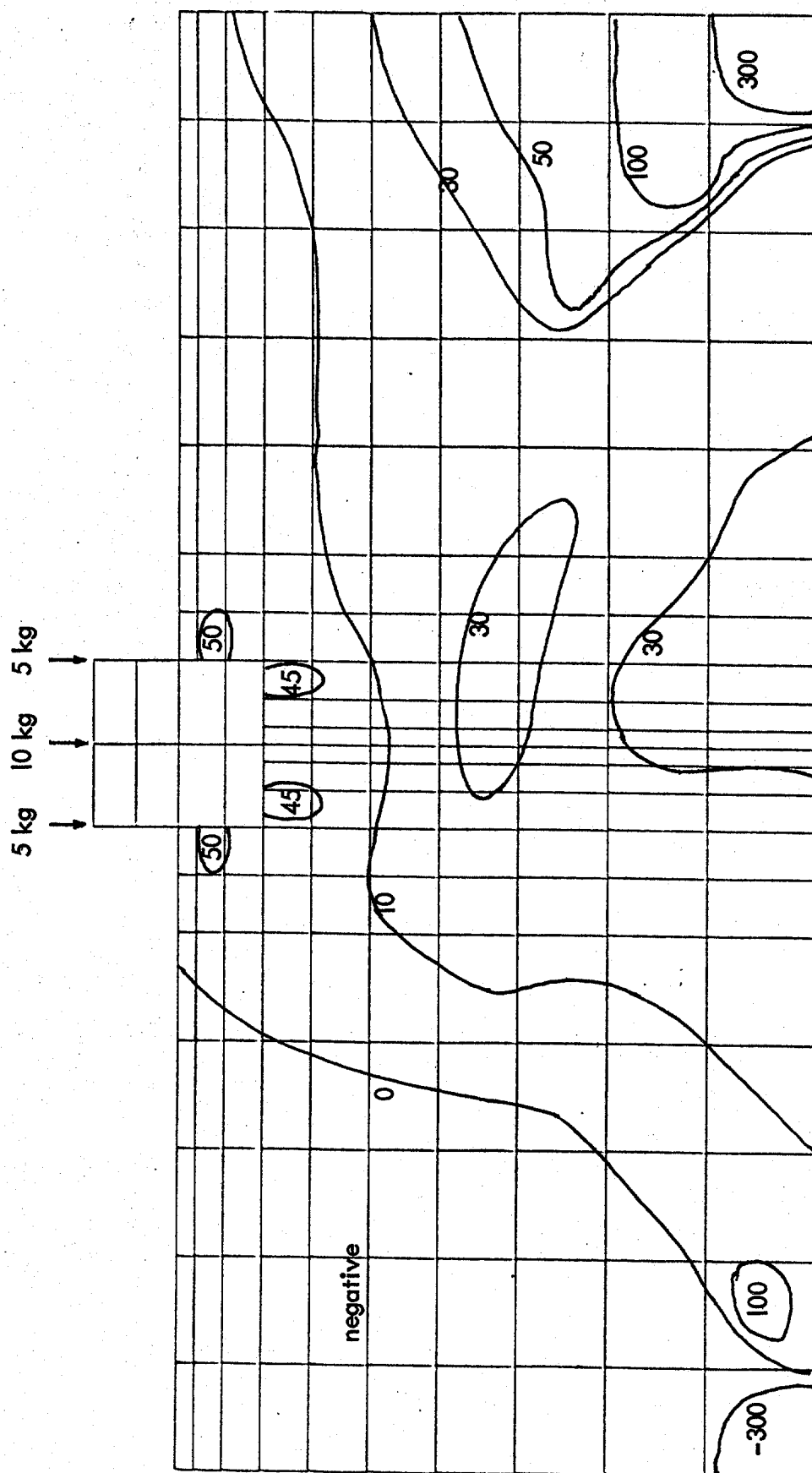


Figure 59 . (Continued) Step=210, time=66.07 sec

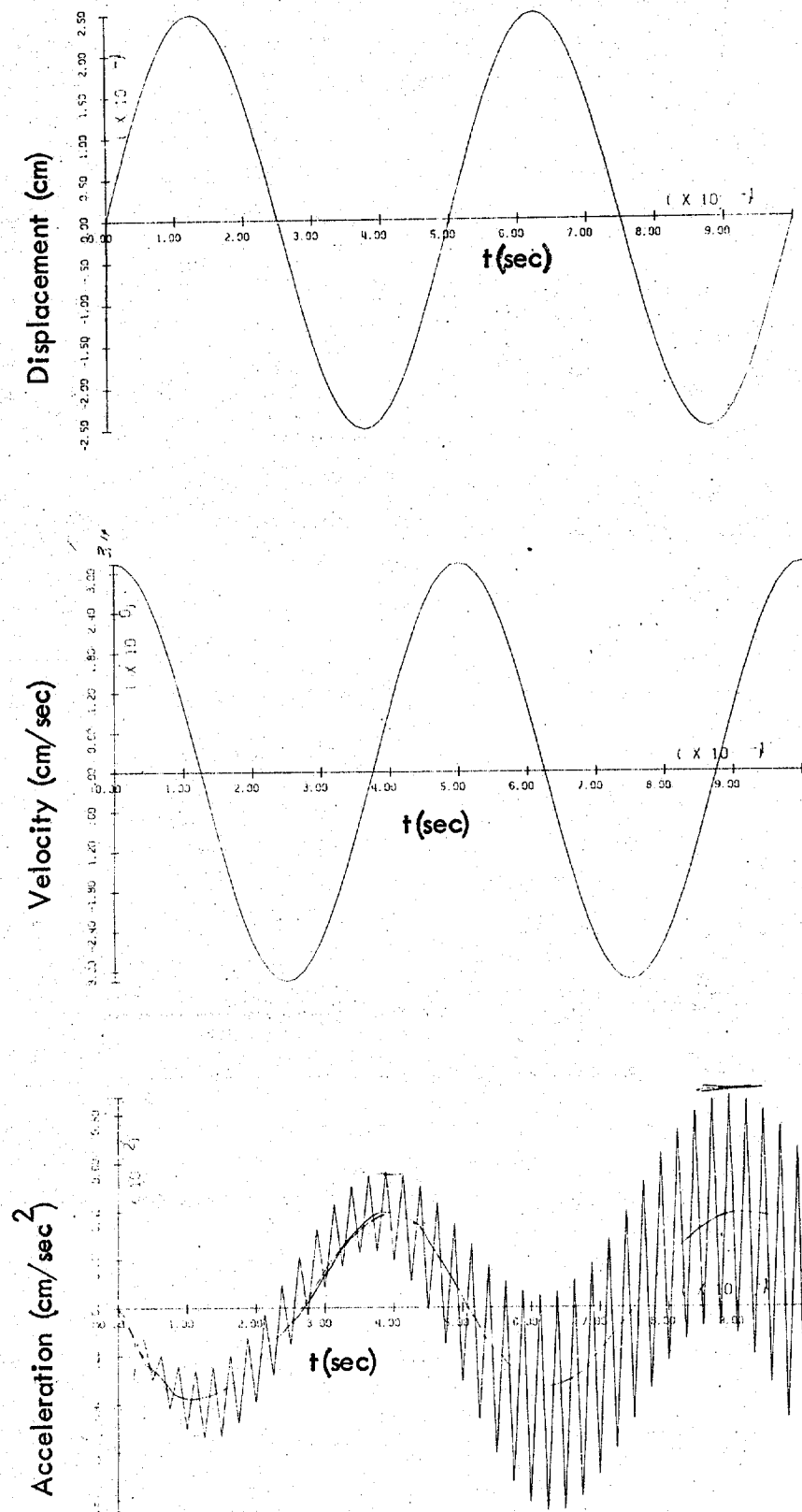


Figure 60a. Initial Conditions: $D = 0.25 \sin 4\pi t$
 $\Delta t = 0.0125$ sec, $\alpha = 0.50$, $\beta = 0.25$, $V_0 = 3.14$ cm/sec

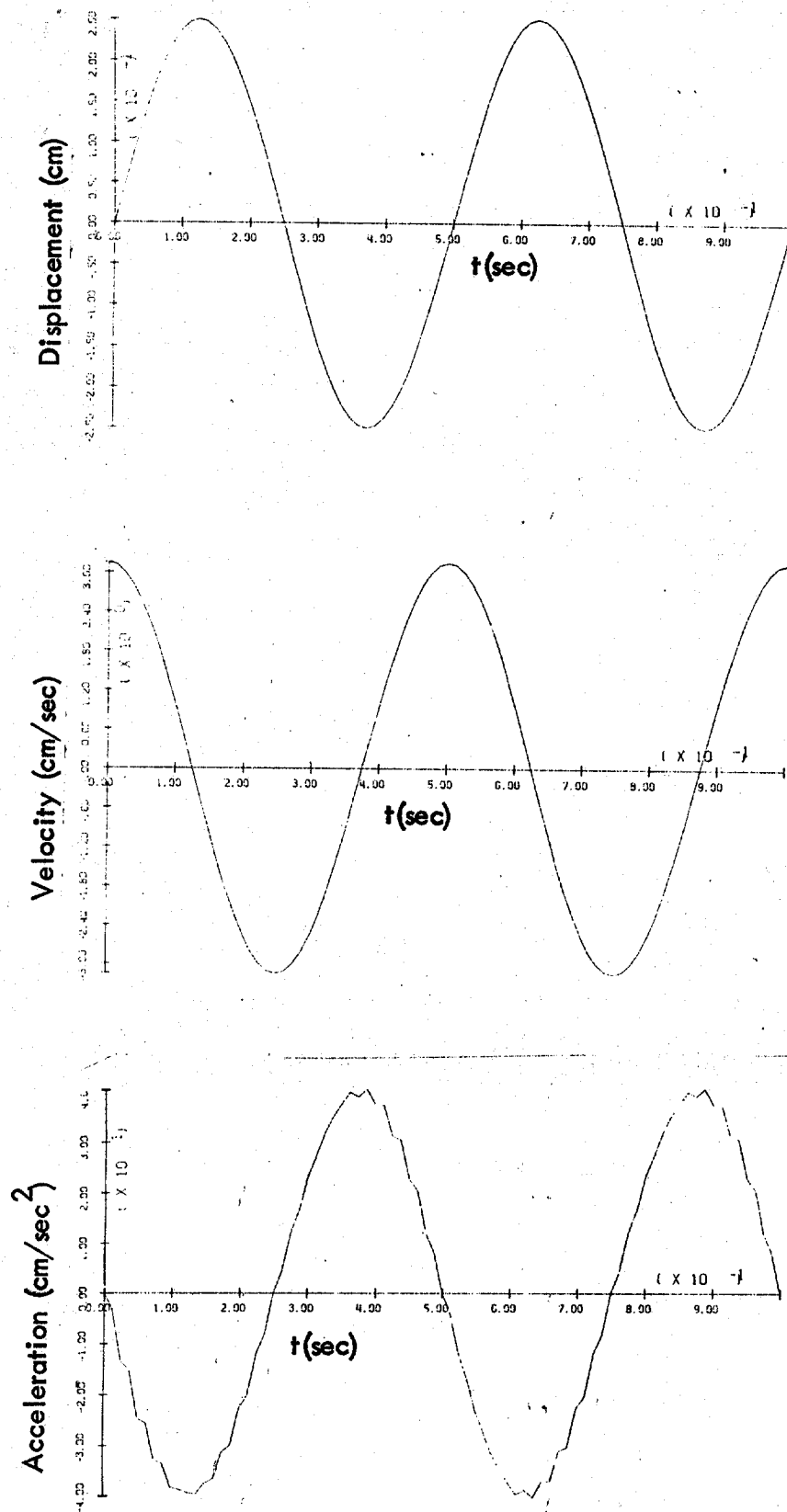


Figure 60b. Initial Conditions: $D = 0.25 \sin 4\pi t$
 $\Delta t = 0.0125 \text{ sec}$, $\alpha = 0.65$, $\beta = 0.33$, $V_0 = 3.14 \text{ cm/sec}$.

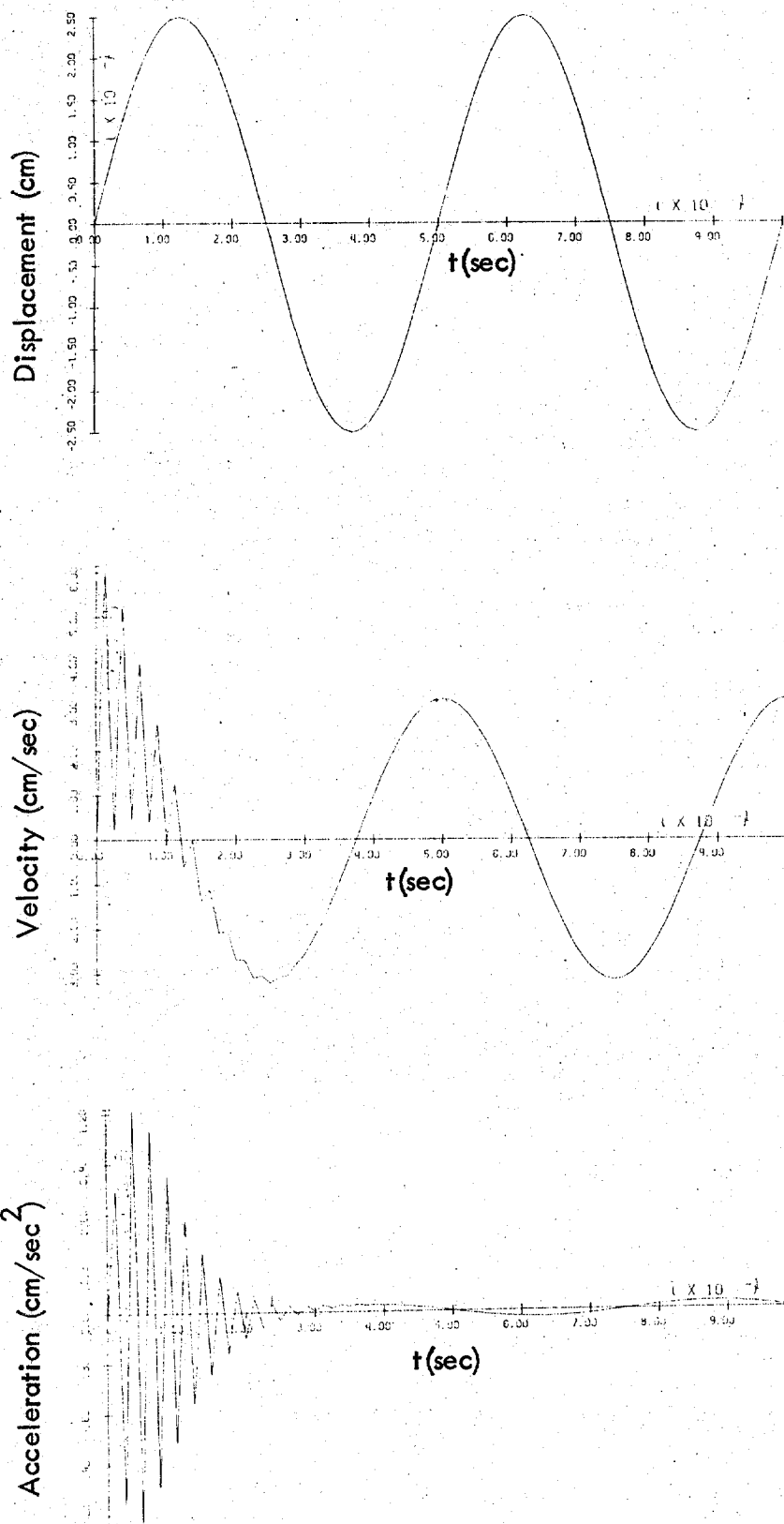


Figure 60c. No Initial Conditions: $D = 0.25 \sin 4\pi t$
 $\Delta t = 0.0125$ sec, $\alpha = 0.65$, $\beta = 0.33$, $V_0 = 0.0$

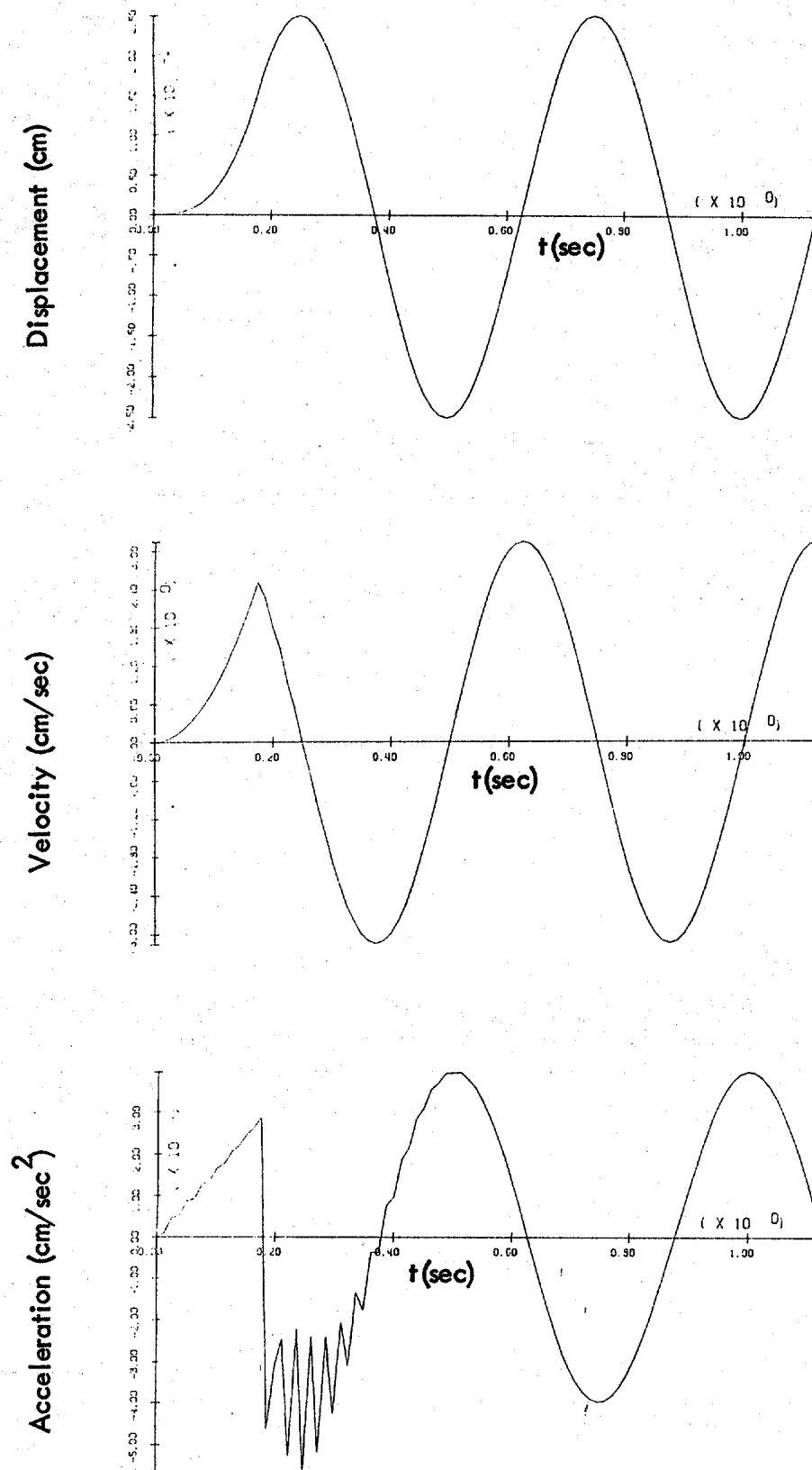
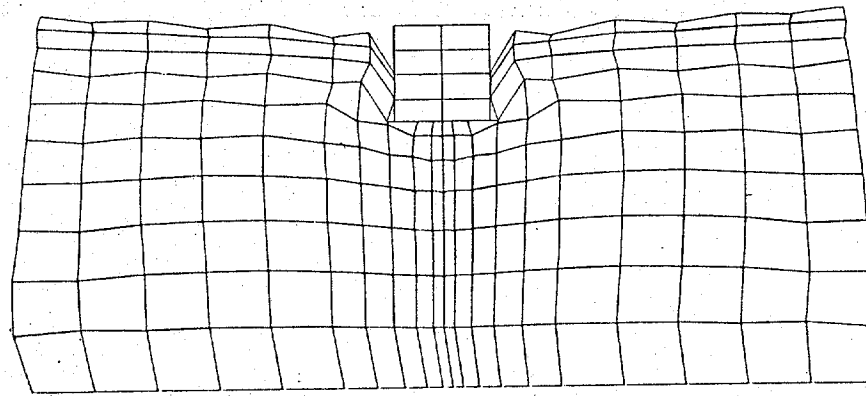
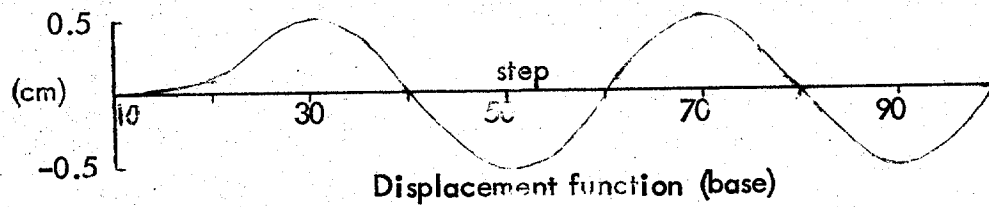
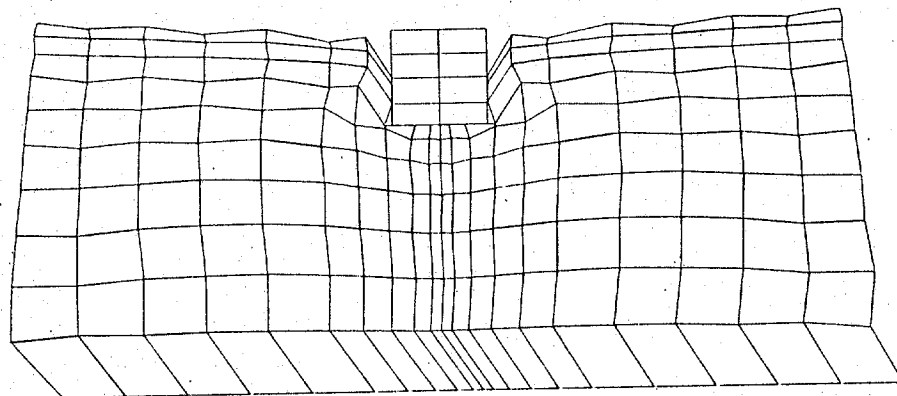


Figure 60d. $D=109.7t^3$, $0 \leq t \leq 0.175$, $D=0.25\sin 4\pi(t-0.125)$, $t \geq 0.175$
 $\Delta t=0.0125$ sec, $\alpha=0.65$, $\beta=0.33$, $V_0=0$.



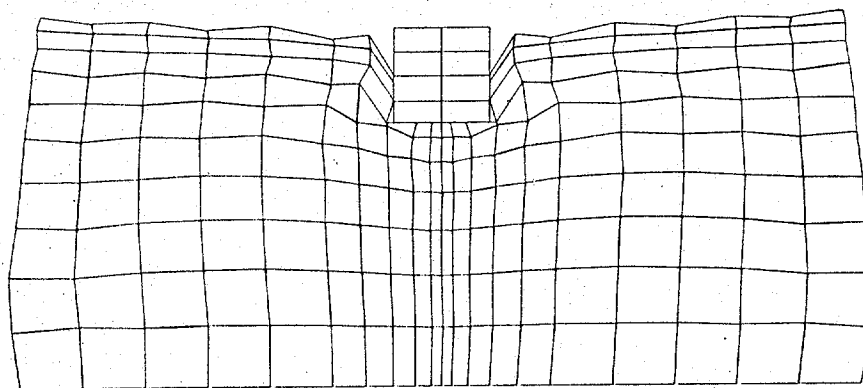
Step 20

Scale factor=1.18



Step 30

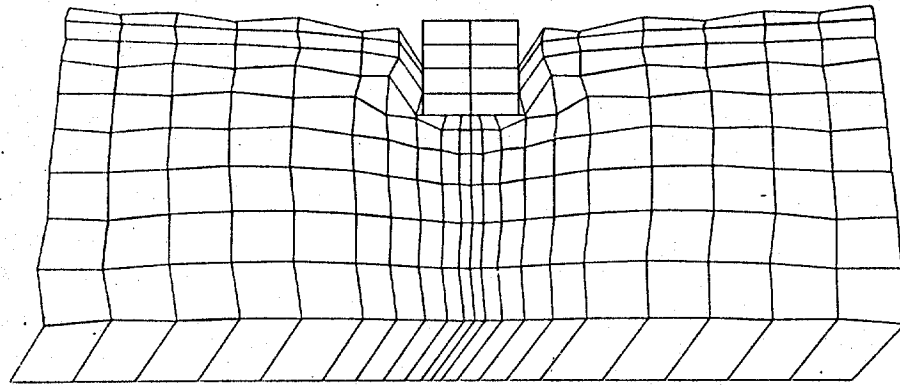
Scale factor=1.18



Step 40

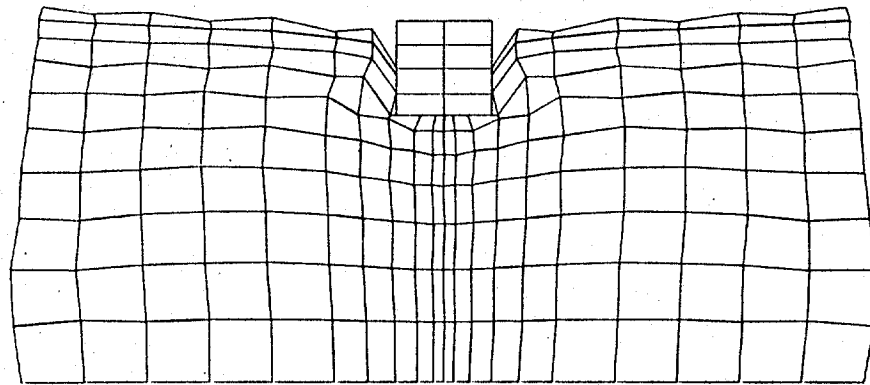
Scale factor=1.16

Figure 61. Deformed Mesh—Dynamic Solution



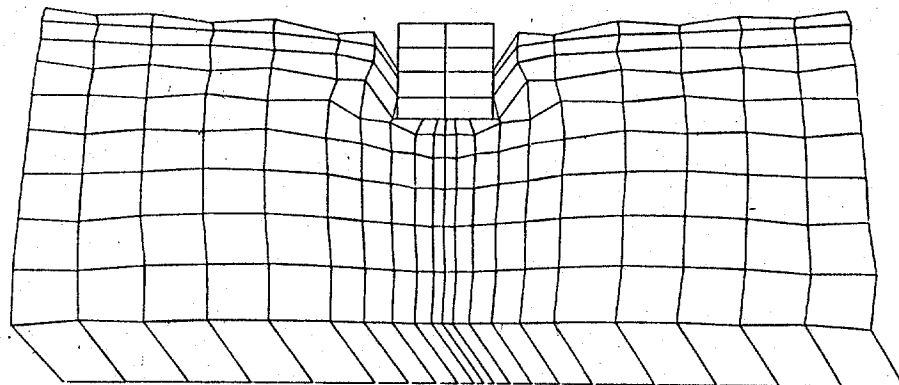
Step 50

Scale factor=1.15



Step 60

Scale factor=1.14



Step 70

Scale factor=1.12

Figure 61. (continued)

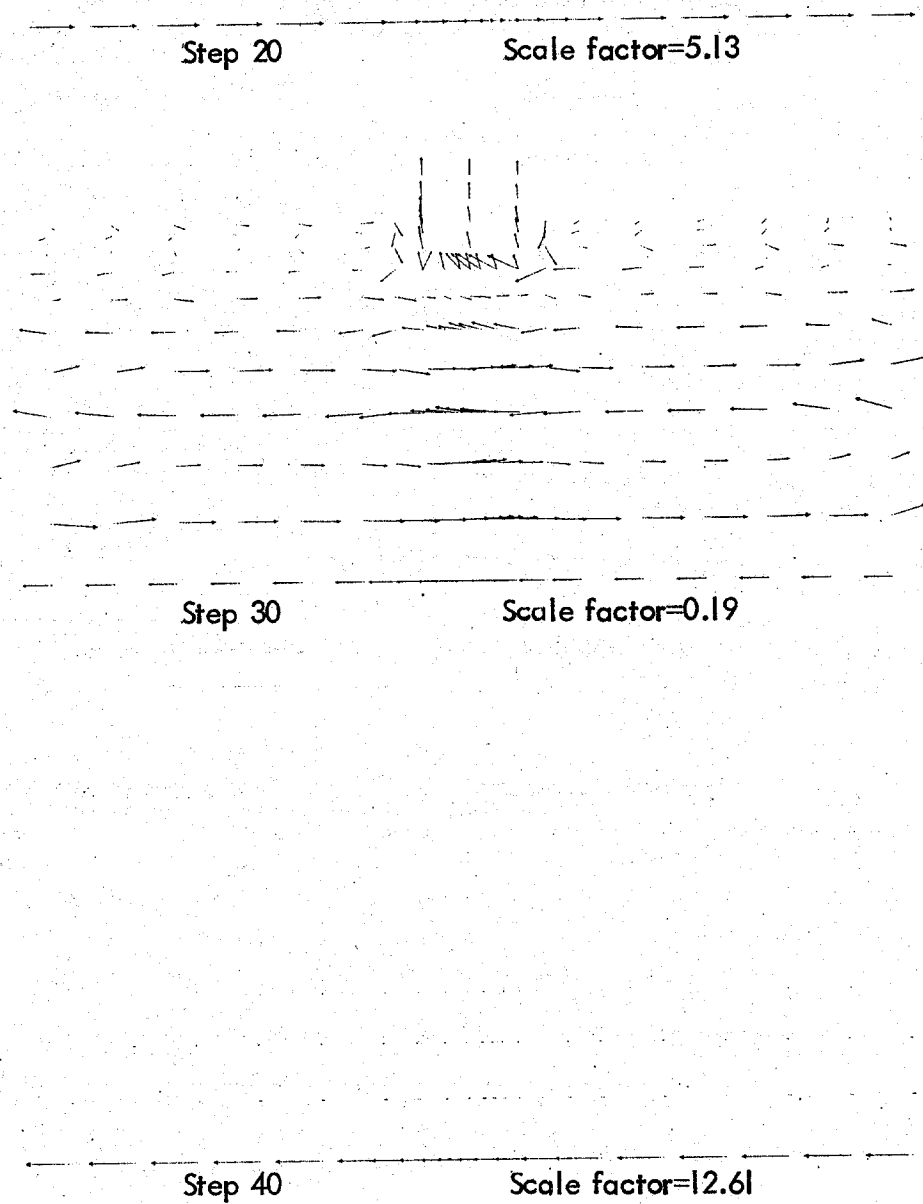


Figure 62. Velocity Vectors—Dynamic Solution

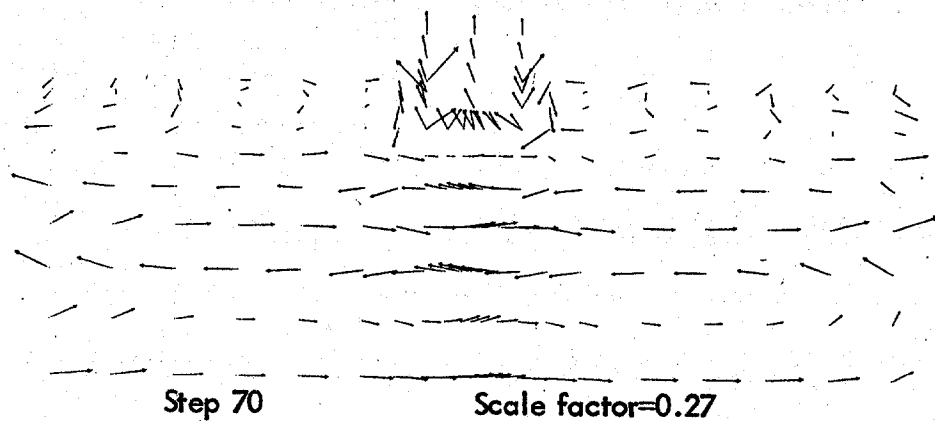
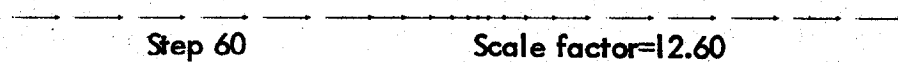
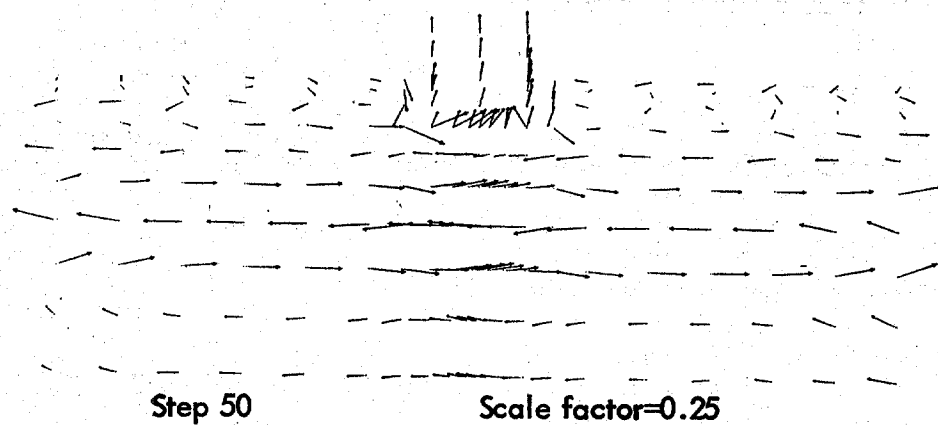


Figure 62 . (continued)

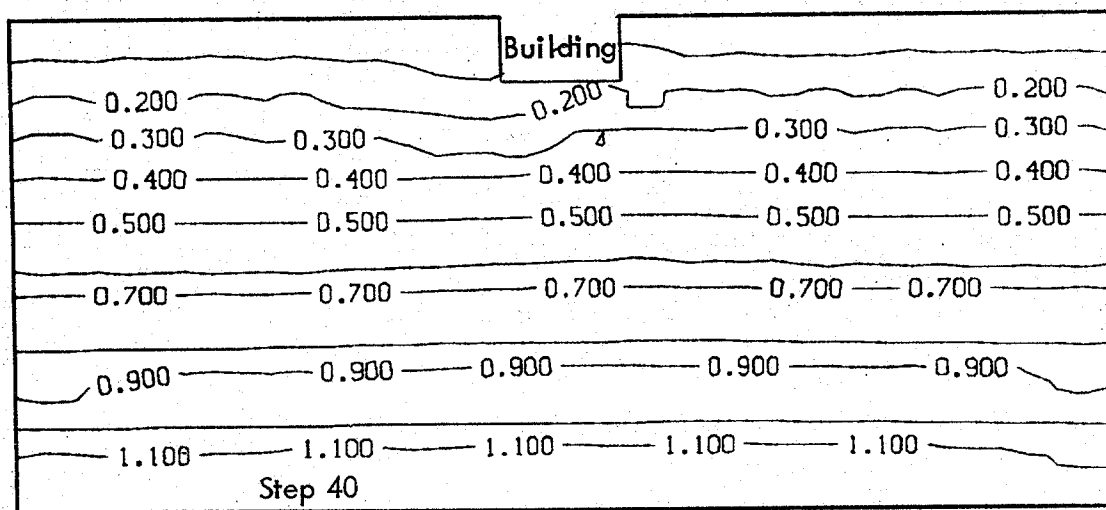
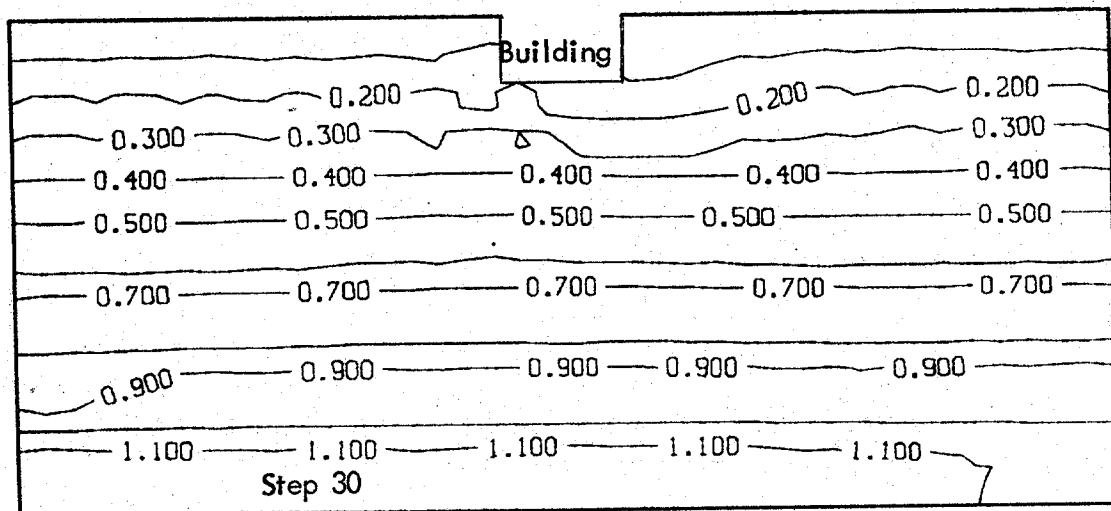
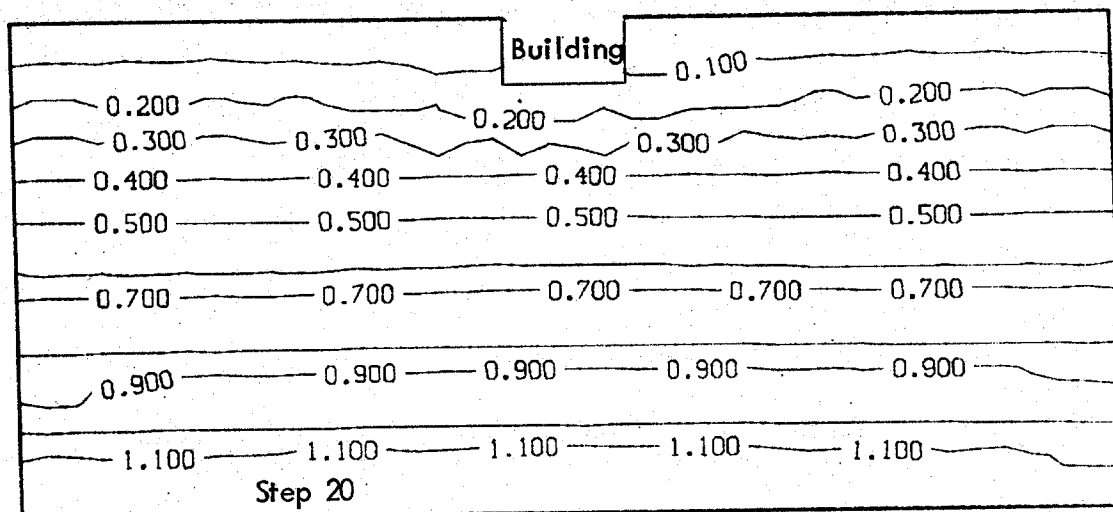


Figure 63. Pore Pressure Contours—Dynamic Solution
(Gravity included)

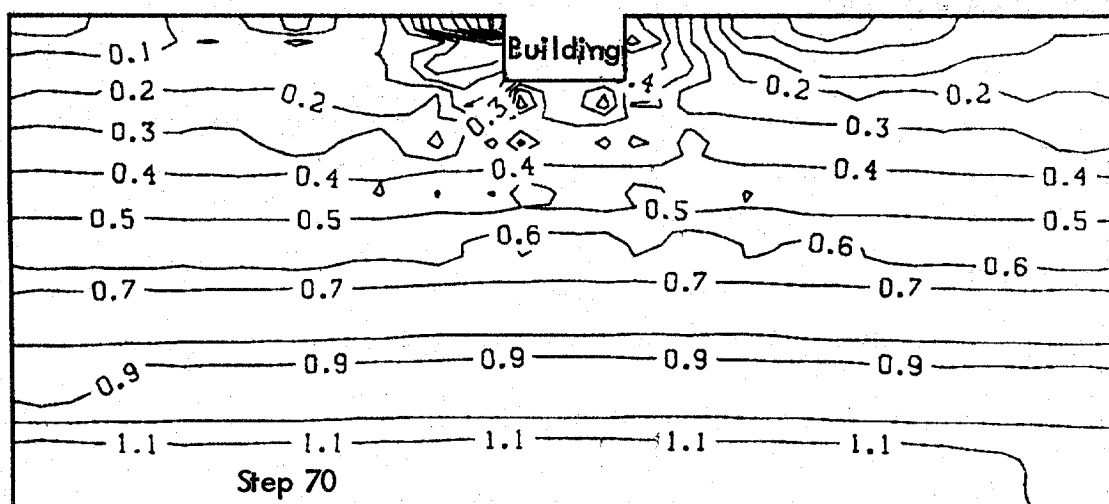
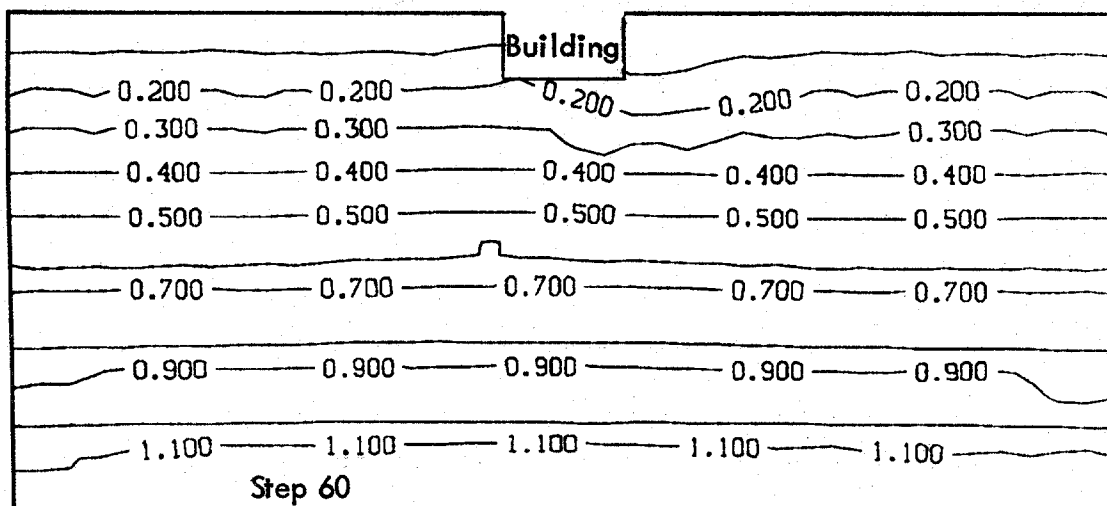
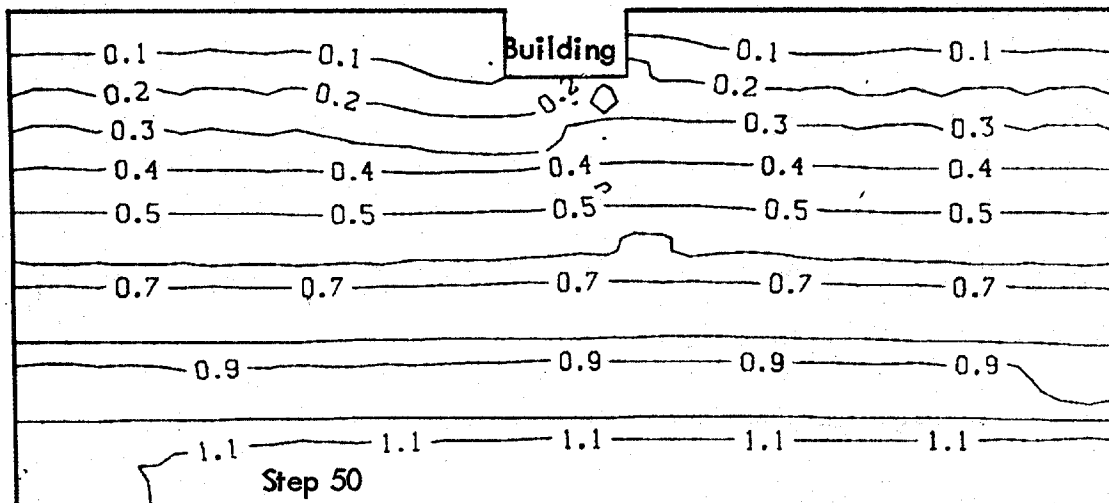
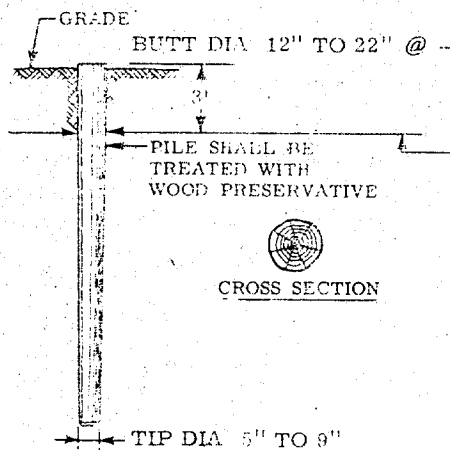
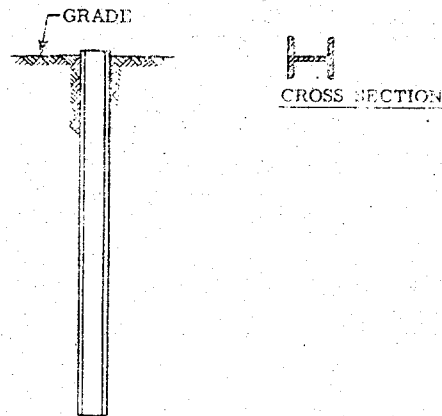


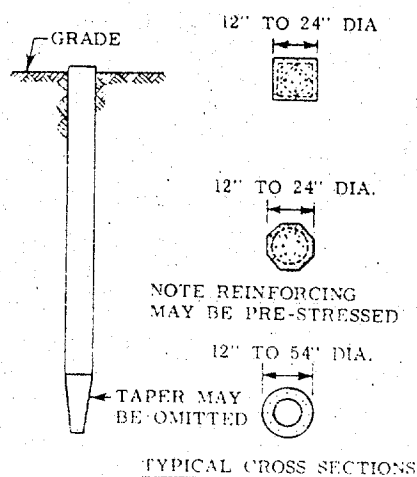
Figure 63 . (continued)



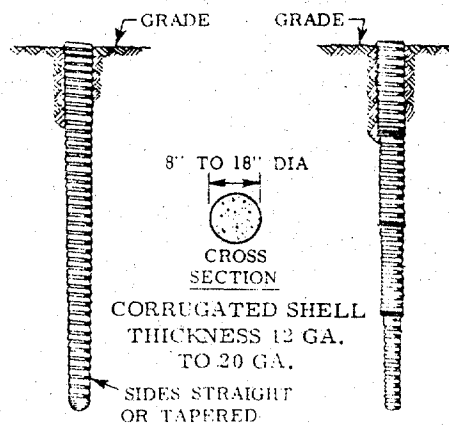
Timber



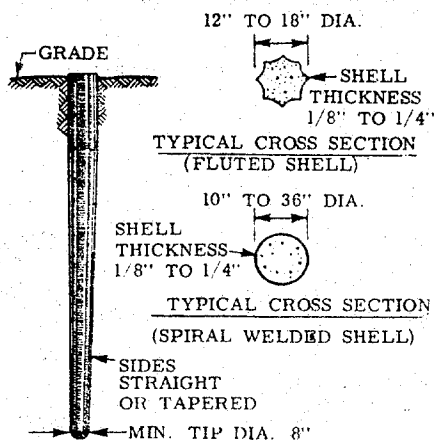
Steel



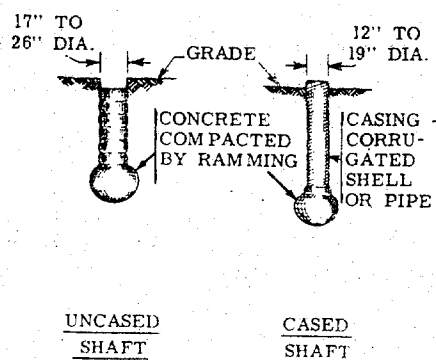
Precast Concrete



Cast-in-place Concrete & Mandrel

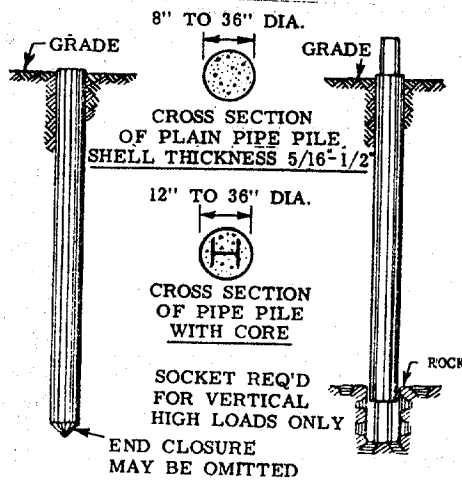


Cast-in-place Concrete

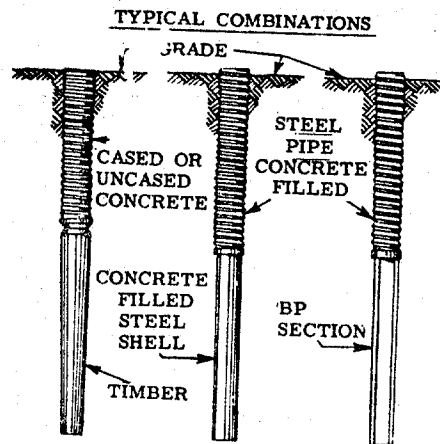


Pressure Injected Footings

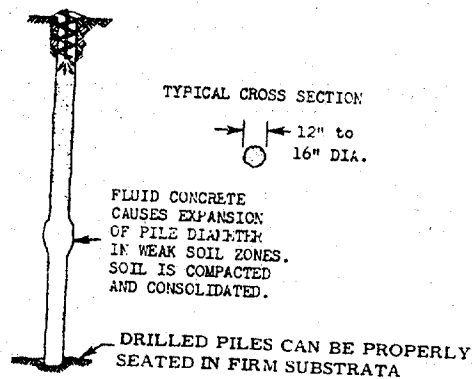
Figure 64. Typical pile types used.



Concrete Filled Steel Pipe Piles



Composite Piles

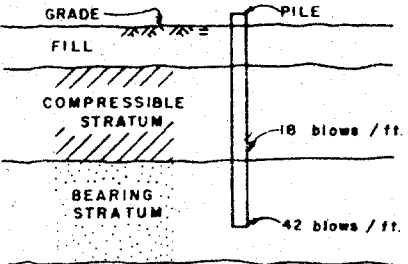
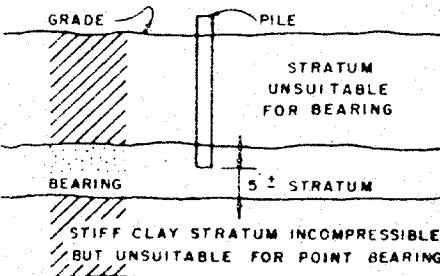


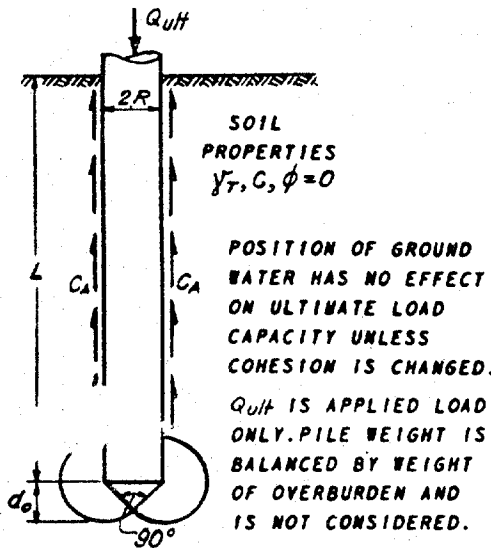
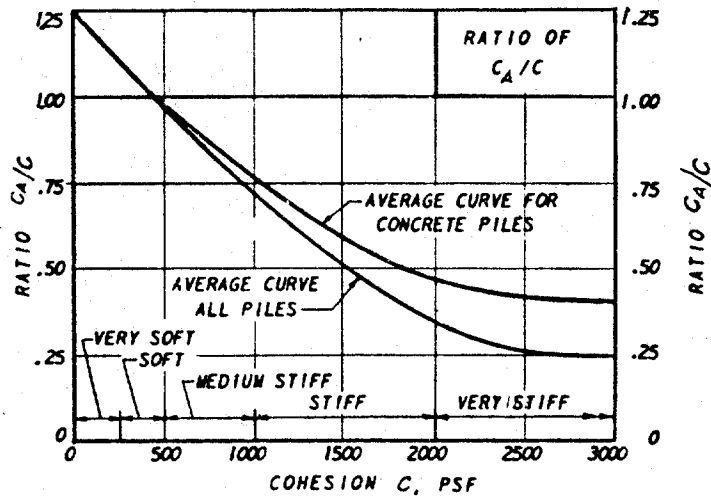
Auger-placed Pressure Injected Concrete Piles

Figure 64. Continued.

Figure 65
Application of Pile Driving Resistance Formulas

REF. NAVFAC DM-7

Basic pile driving formulas		
For drop hammer	For single-acting hammer	For double-acting differential hammer
$Q_{all} = \frac{2WH}{s+1}$	$Q_{all} = \frac{2WH}{s+0.1}$ {Use when driven weights are smaller than striking weights. $Q_{all} = \frac{2WH}{s+0.1} \frac{W_D}{W_S}$ {Use when driven weights are larger than striking weights.	$Q_{all} = \frac{2E}{s+0.1}$ {Use when driven weights are smaller than striking weights. $Q_{all} = \frac{2E}{s+0.1} \frac{W_D}{W_S}$ {Use when driven weights are larger than striking weights.
<p> Q_{all} = allowable pile load in pounds. W = weight of striking parts of hammer in pounds. H = the effective height of fall in feet. E = the actual energy delivered by hammer per blow in foot-pounds. s = average net penetration in inches per blow for the last 6 in. of driving. W_D = driven weights W_S = weights of striking parts } Note: Ratio of driven weights to striking weights should not exceed 3. </p>		
Modifications of basic pile driving formulas		
<p>A. For piles driven to and seated in rock as high capacity end-bearing piles: Drive to refusal (approximately 4 to 5 blows for the last quarter inch of driving). Redrive open end pipe piles repeatedly until resistance for refusal is reached within 1 in. of additional penetration.</p>		
<p>B. Piles driven through stiff compressible materials unsuitable for pile bearing to an underlying bearing stratum:</p> <p>Add blows attained before reaching bearing stratum to required blows attained in bearing stratum (see example).</p> <div style="display: flex; align-items: flex-start;"> <div style="flex: 1;">  </div> <div style="flex: 1; padding-left: 20px;"> <p>Example: required load capacity of pile $Q_{all} = 25$ tons hammer energy $E = 15,000$ ft-lb</p> $\frac{W_D}{W_S} < 1$ <p>Penetration(s) as per basic formula = $\frac{1}{2}$" or 2 blows per inch (24 blows/ft).</p> <p>Required blows for pile $24 + 18 = 42$ blows/ft.</p> </div> </div>		
<p>C. Piles driven into limited thin bearing stratum, drive to predetermined tip elevation. Determine allowable load by load test.</p> <div style="display: flex; align-items: center;">  </div>		



RECOMMENDED VALUES OF ADHESION

PILE TYPE	CONSISTENCY OF SOIL	COHESION, C PSF	ADHESION, C_A PSF
TIMBER AND CONCRETE	VERY SOFT	0 - 250	0 - 250
	SOFT	250 - 500	250 - 480
	MED. STIFF	500 - 1000	480 - 750
	STIFF	1000 - 2000	750 - 950
	VERY STIFF	2000 - 4000	950 - 1300
STEEL	VERY SOFT	0 - 250	0 - 250
	SOFT	250 - 500	250 - 460
	MED. STIFF	500 - 1000	460 - 700
	STIFF	1000 - 2000	700 - 720
	VERY STIFF	2000 - 4000	720 - 750

ULTIMATE LOAD CAPACITY

$$Q_{ult} = C N_{cs} \pi R^2 + C_A 2 \pi R L$$

PULLOUT CAPACITY

$$T_{ult} = C_A 2 \pi R L$$

T_{ult} UNDER SUSTAINED LOAD MAY BE LIMITED BY OTHER FACTORS.

ULTIMATE LOAD FOR BUCKLING OF STEEL PILES IN SOFT CLAY.

$$Q_{ult} = \lambda (CEI)^{1/2}$$

- $\lambda = 8$ FOR VERY SOFT CLAY, 10 FOR SOFT CLAY (DIMENSIONLESS)
 $C =$ SOIL SHEAR STRENGTH
 $I =$ MOMENT OF INERTIA OF CROSS SECTION
 $E =$ MODULUS OF ELASTICITY OF STEEL.

POUND AND
INCH UNITS

FORMULA APPLIES TO SLENDER STEEL PILES. GENERALLY HEAVY STEEL PILES OR TIMBER OR CONCRETE PILES ARE NOT SUBJECT TO BUCKLING IF EMBEDDED IN SOIL FOR THEIR ENTIRE LENGTH.

FIGURE 66
Ultimate Load Capacity of Piles in Cohesive Soils

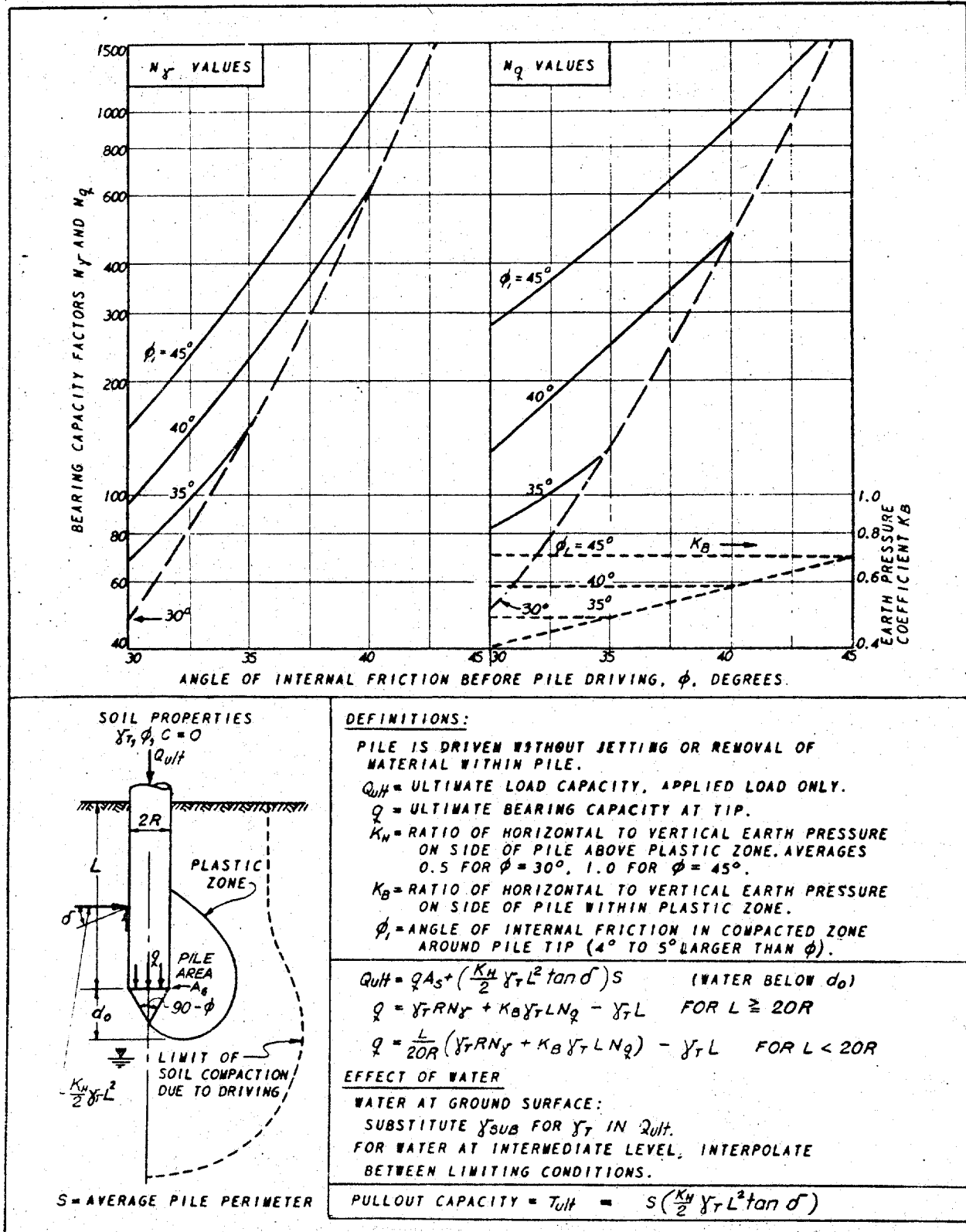


FIGURE 67

Ultimate Load Capacity of Piles in Cohesionless Soil (for Alternate Method, see Figure 68)

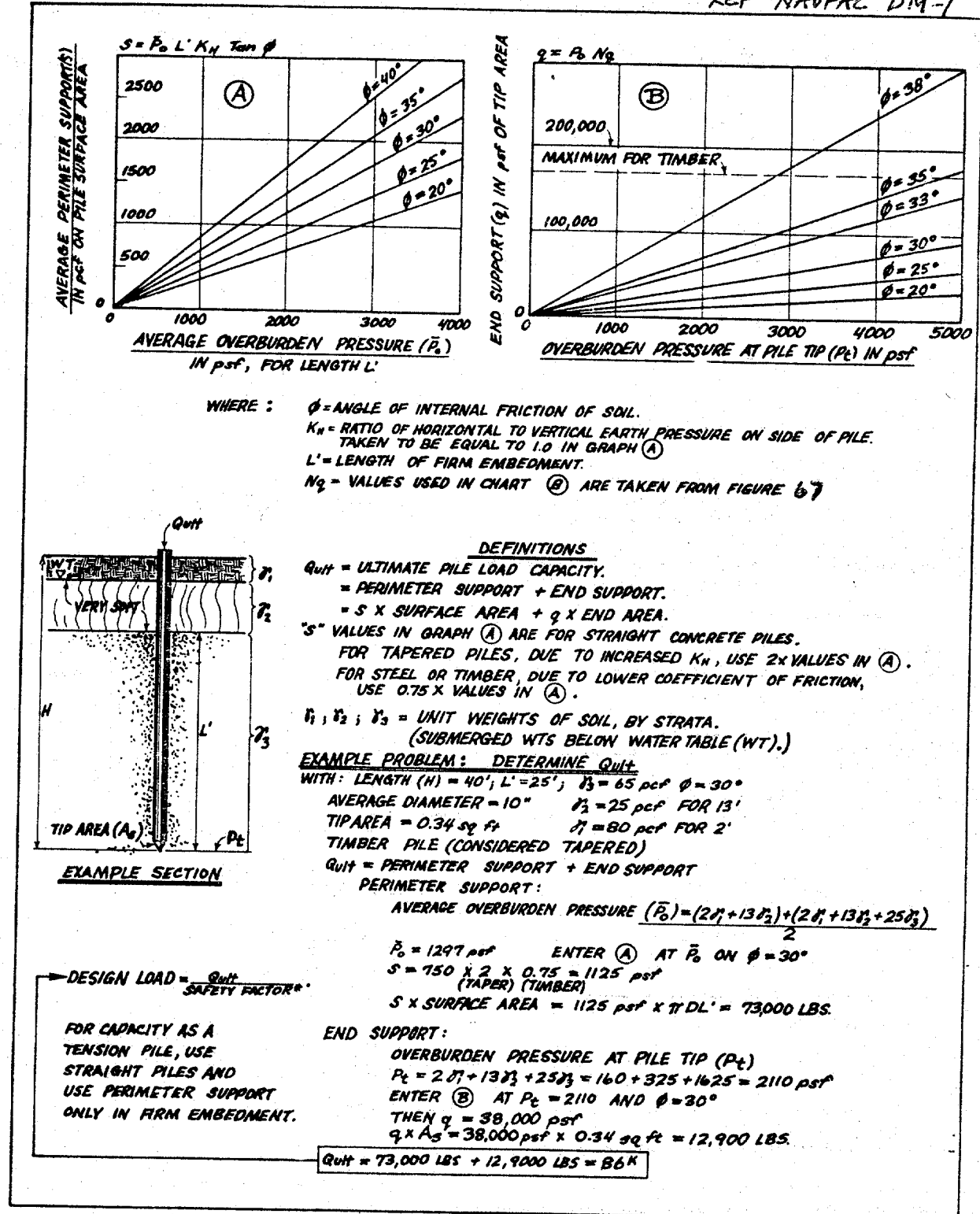


FIGURE 68
 Ultimate Load Capacity of Driven Piles in Cohesionless Soils
 (Alternate Method to Figure 67)

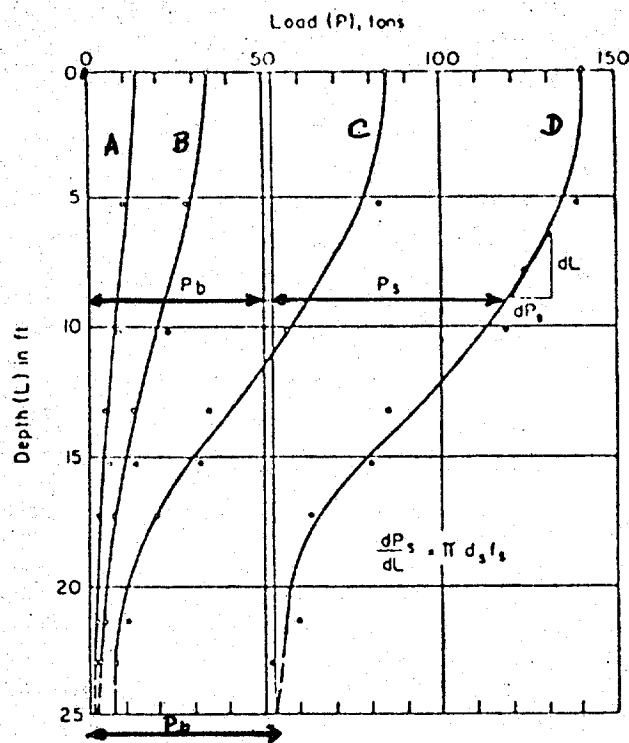


Figure 69. Load distribution in a 25-ft.-long straight-shaft pier drilled into stiff clay.

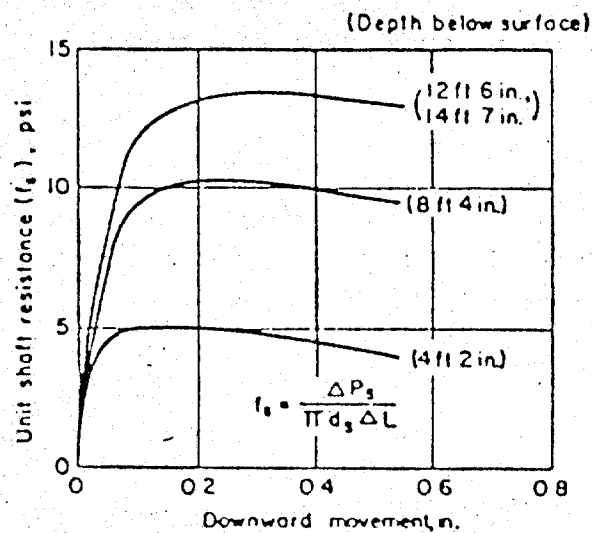


Figure 70. Load transfer to shaft segment (ΔL) vs. downward movement of segment.

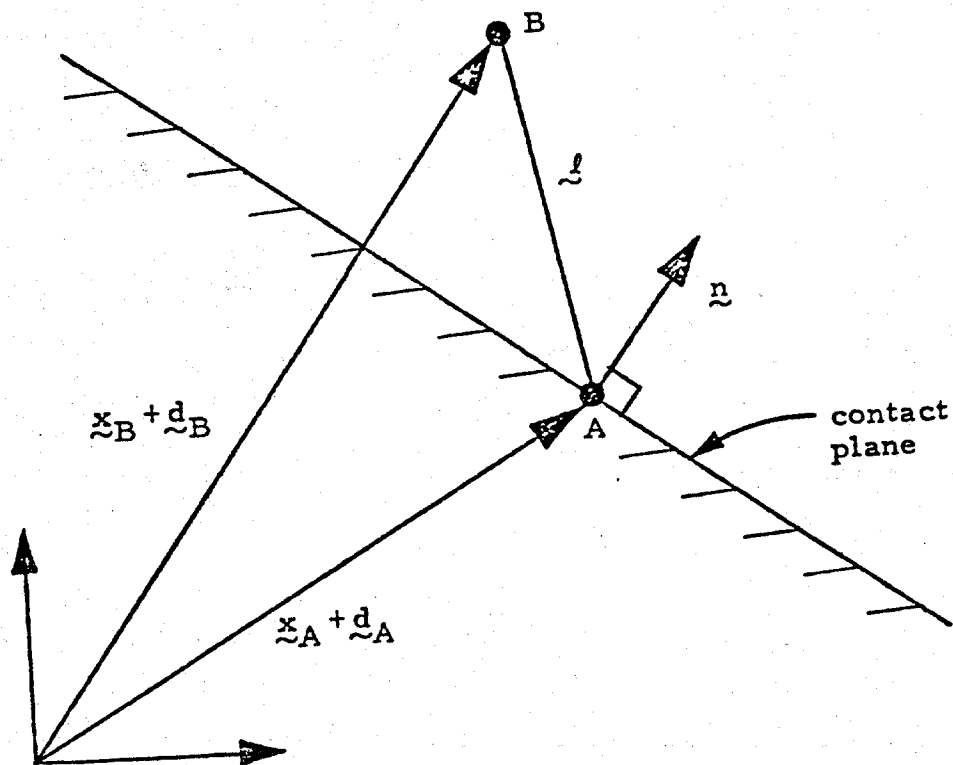


Figure 71. Contact element , Program DYNA-FLOW.

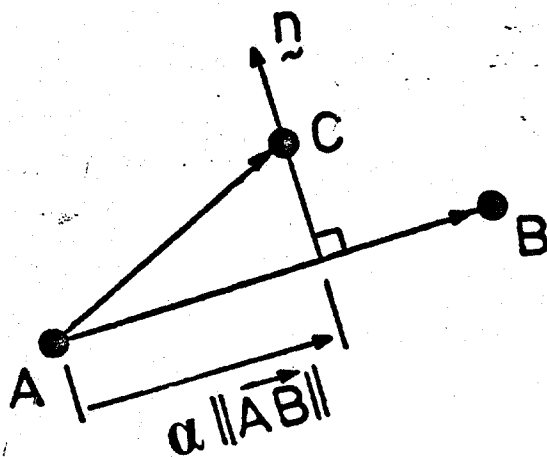
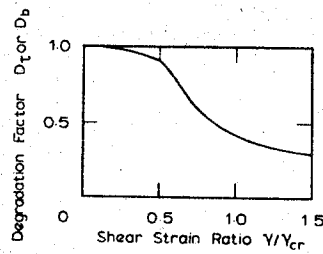


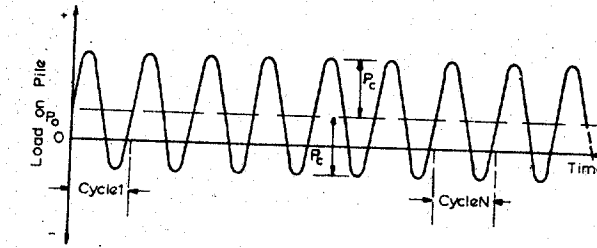
Figure 72. Slide element, Program DYNA-FLOW.



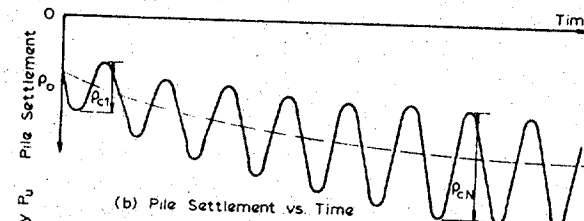
For skin friction (D_t) $\gamma_{cr} = \gamma_{ss}$ = critical shear strain for skin friction

For base resistance (D_b) $\gamma_{cr} = \gamma_{ss}$ = static failure strain for triaxial compression

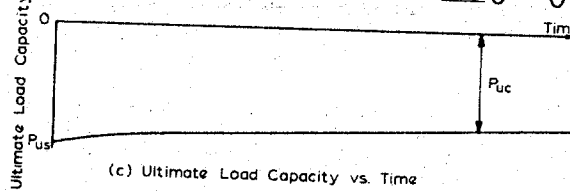
a. Degradation



(a) Load vs. Time



(b) Pile Settlement vs. Time



(c) Ultimate Load Capacity vs. Time

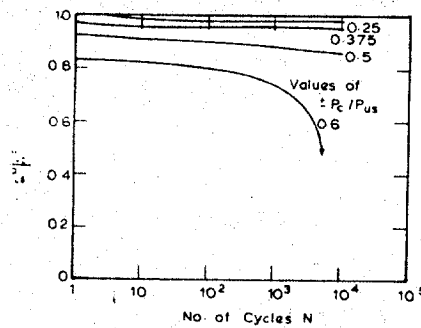
Pile Stiffness Definitions

$$K_s = P_0/P_0$$

$$K_{c1} = 2P_c/P_{c1}$$

$$K_c = 2P_c/P_{cN}$$

b. Cyclic Loading



c. Number of Cycles

Figure 73 . Pile degradation with cyclic loading.



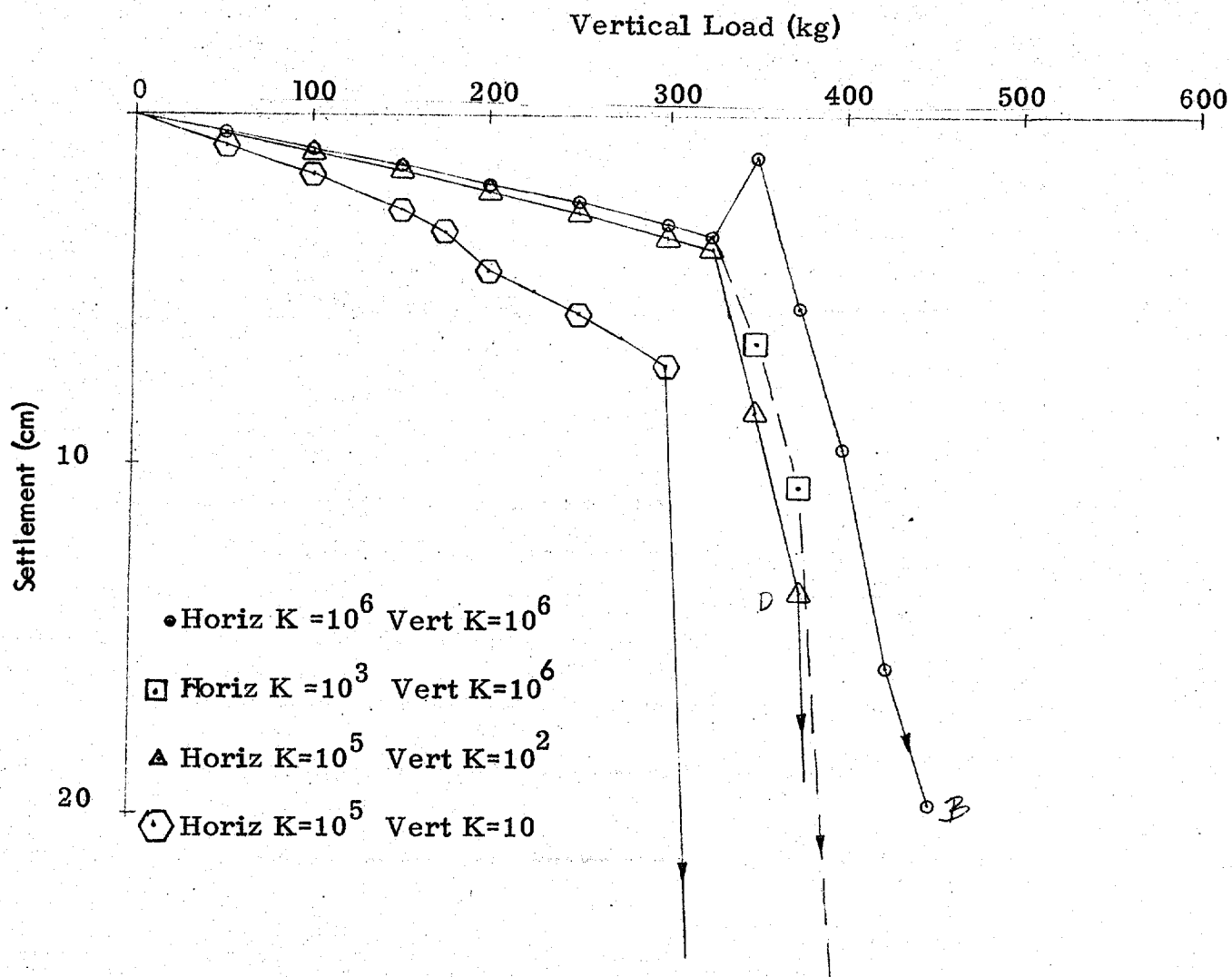


Figure 75 . Load - settlement of pile.

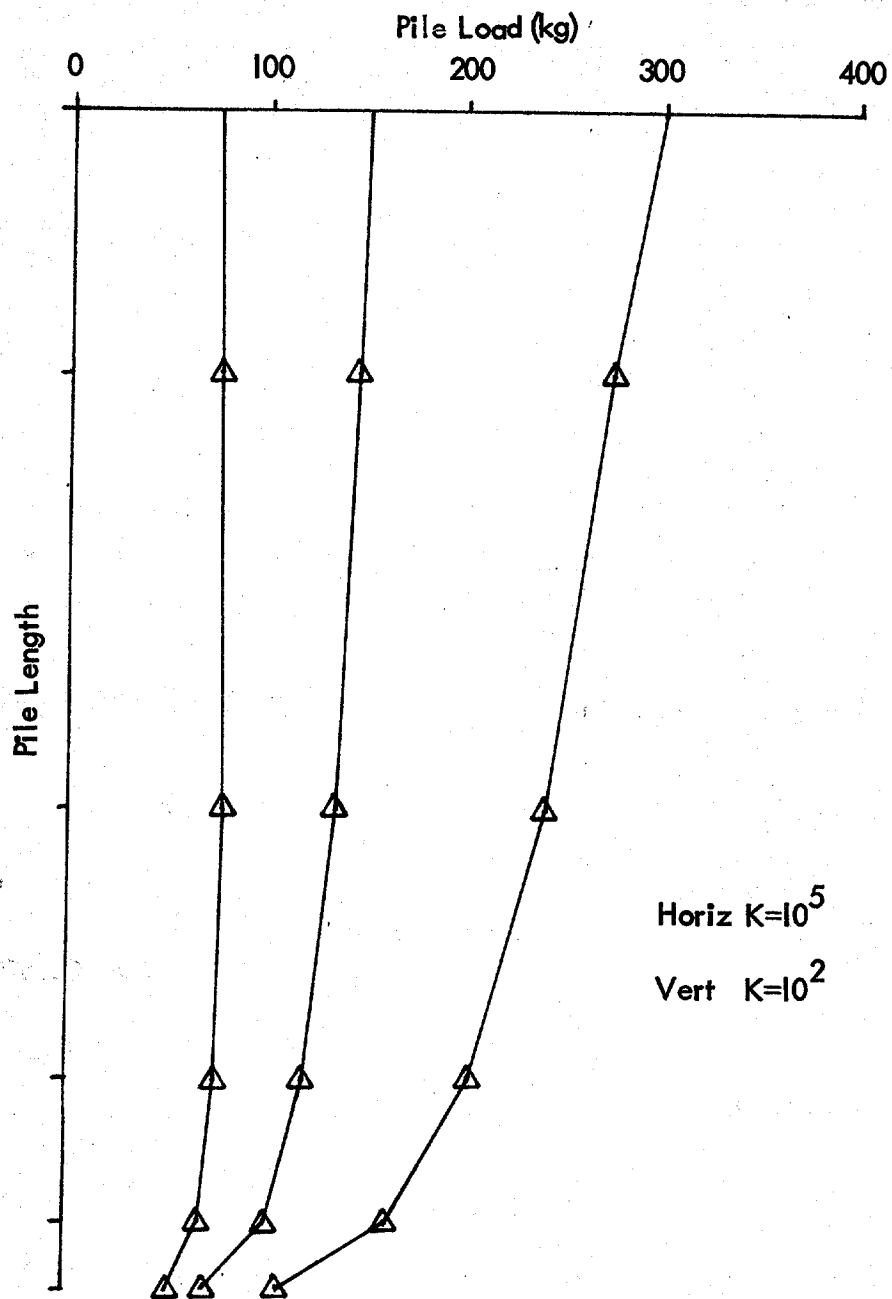


Figure 76. Distribution of force within pile,
75, 150 and 300 kg loads

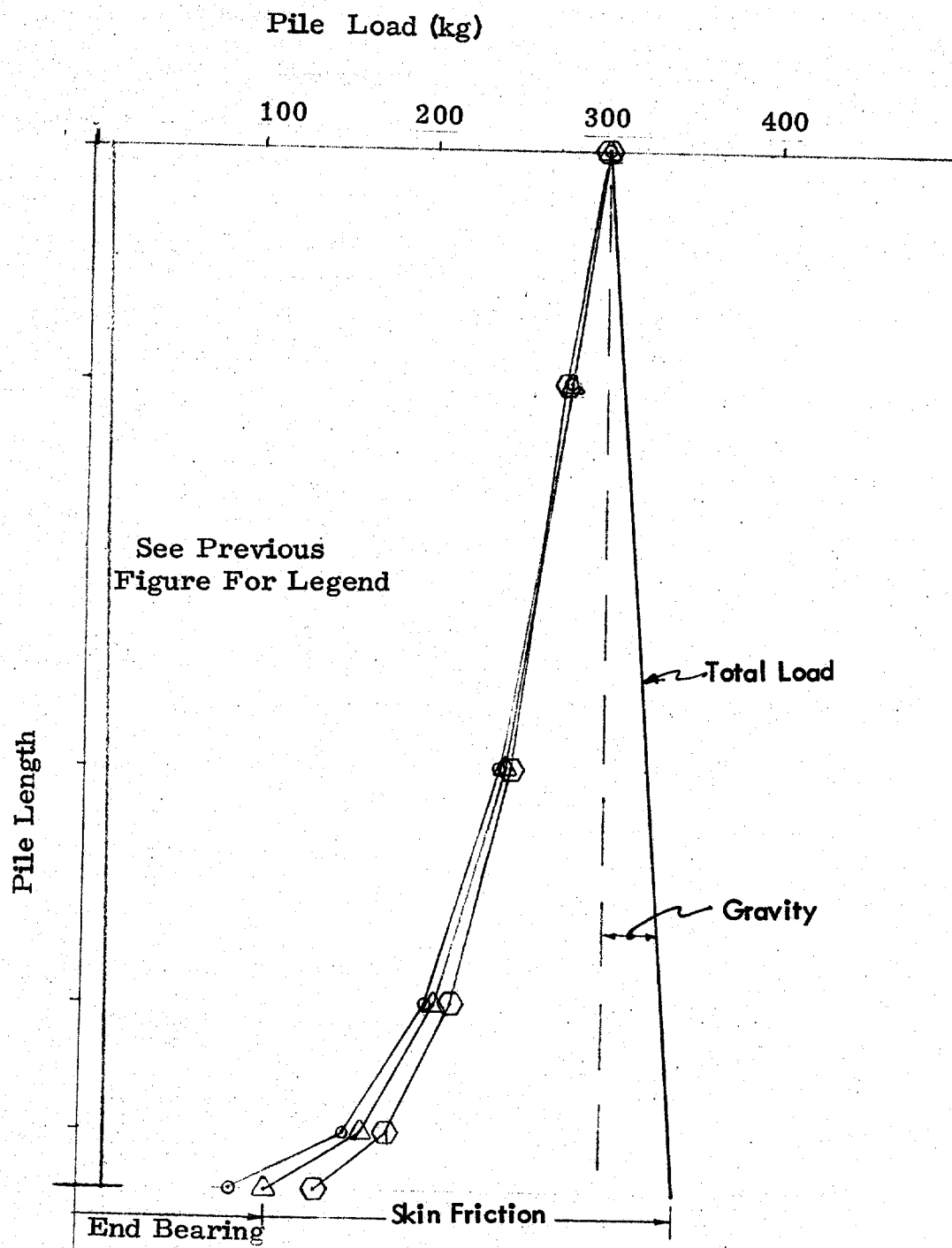


Figure 77 . Distribution of force within pile

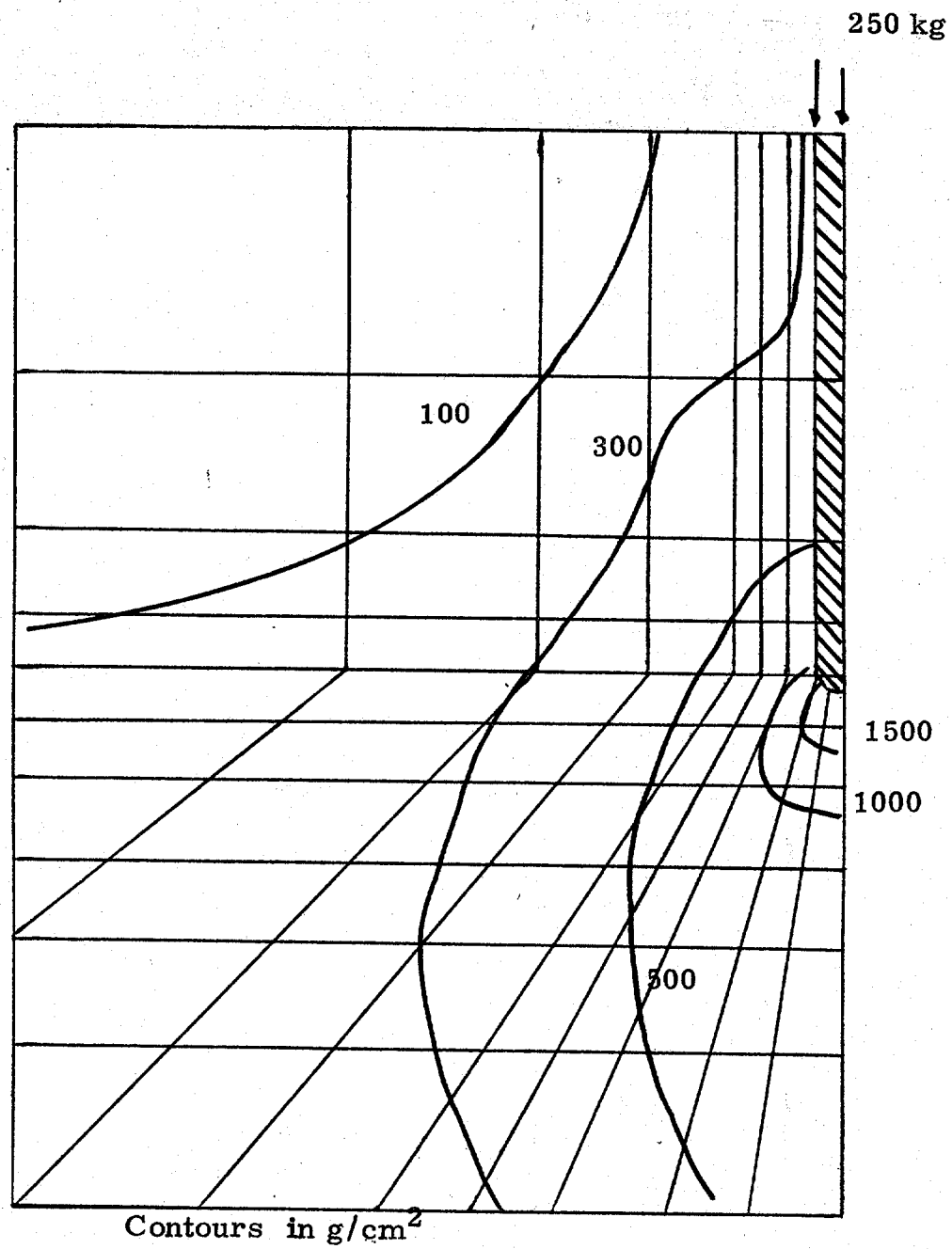


Figure 78. Contour of principle stress around pile.

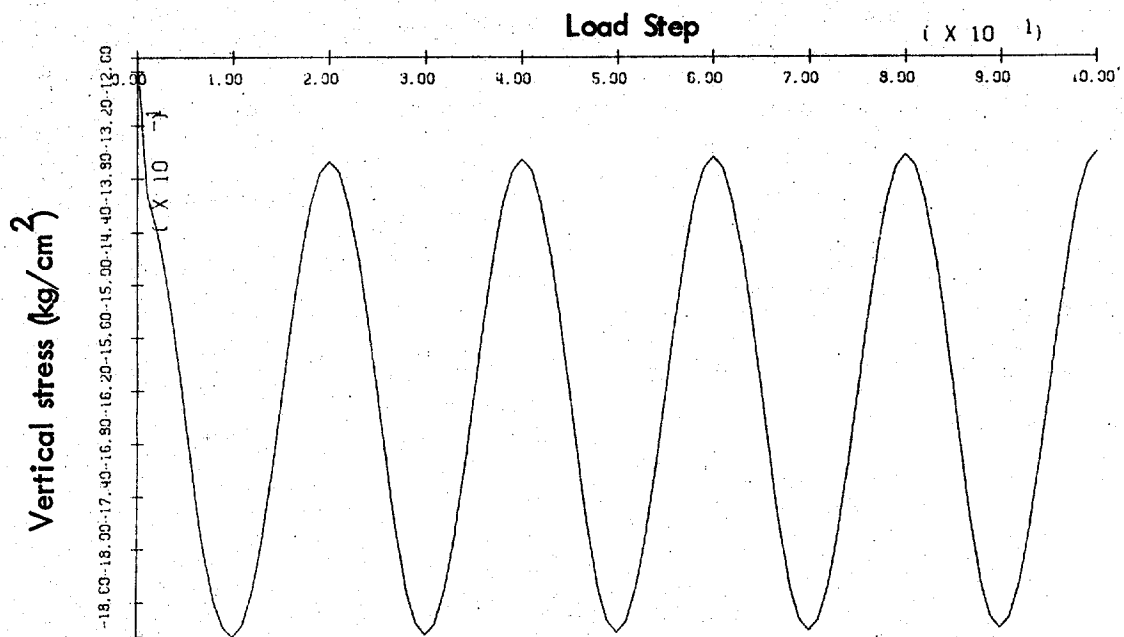
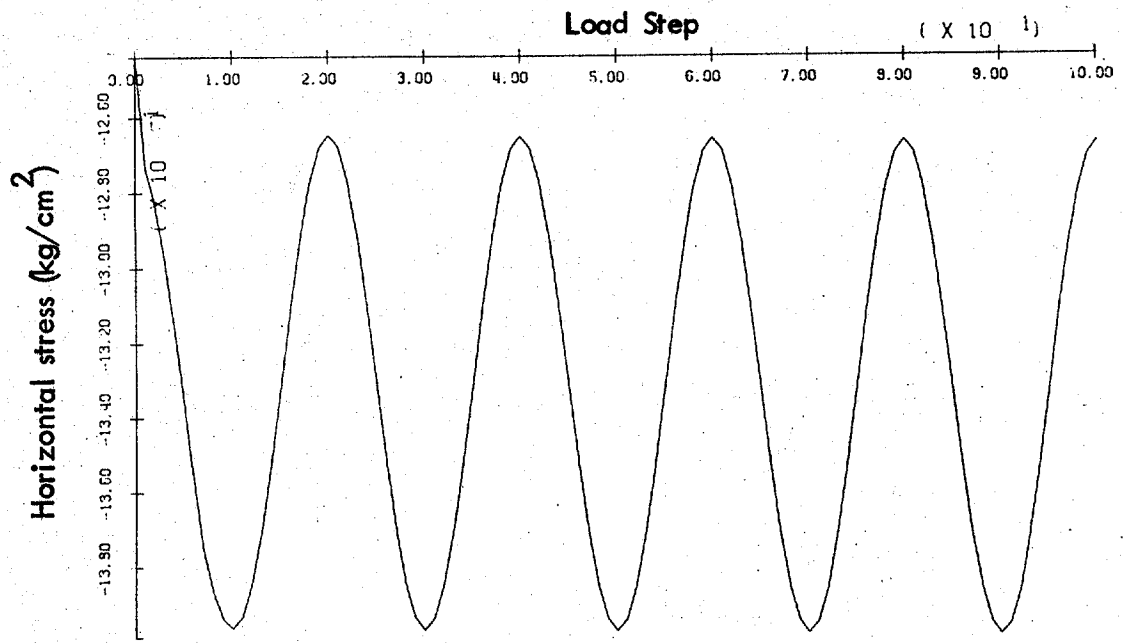


Figure 79. Pile in Soil Field—Cyclic load, 0 to 50 kg.
(Soil element beneath pile tip)

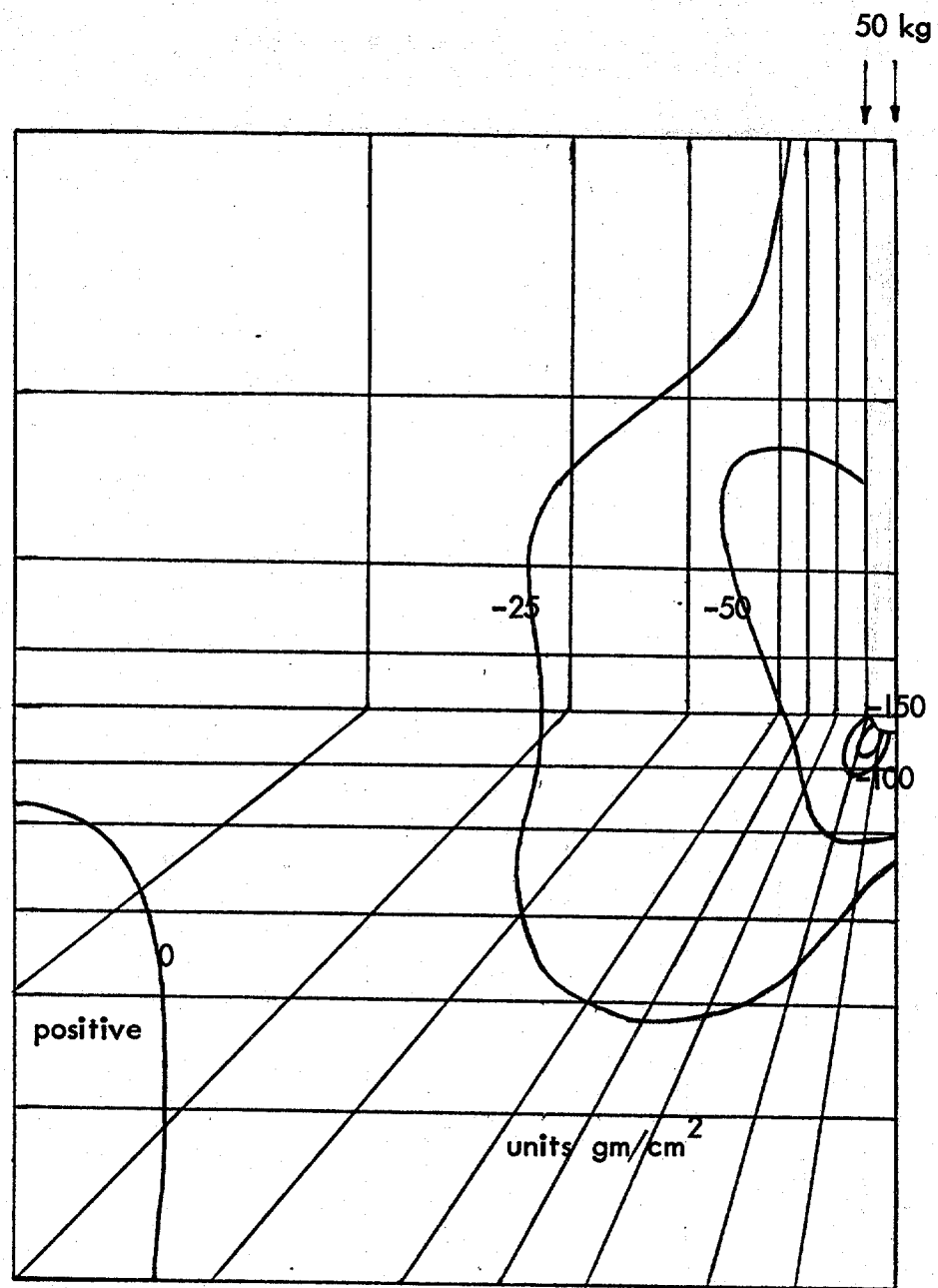


Figure 80. Pile in Soil Field—Cyclic load, 0 to 50 kg, Shear stress contours

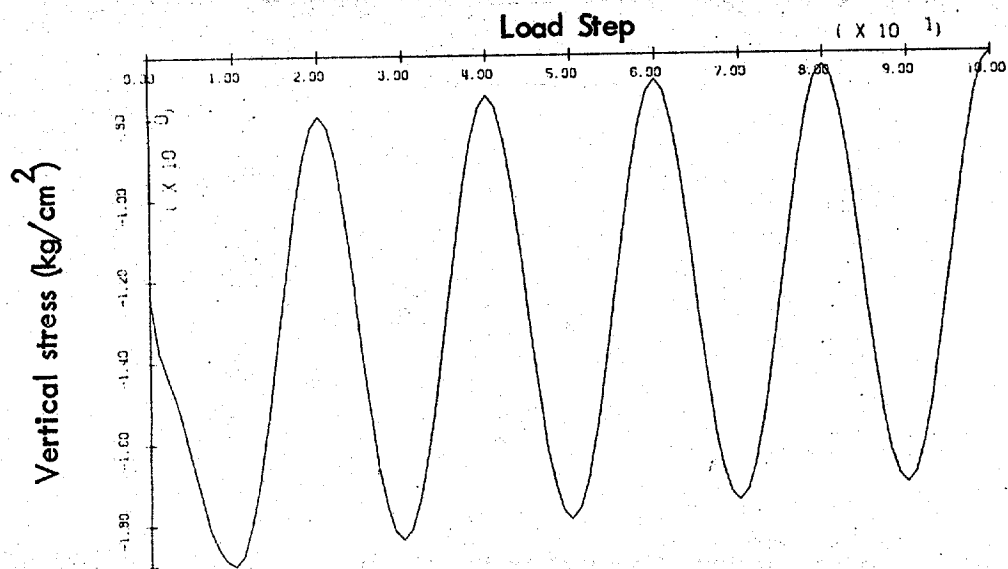
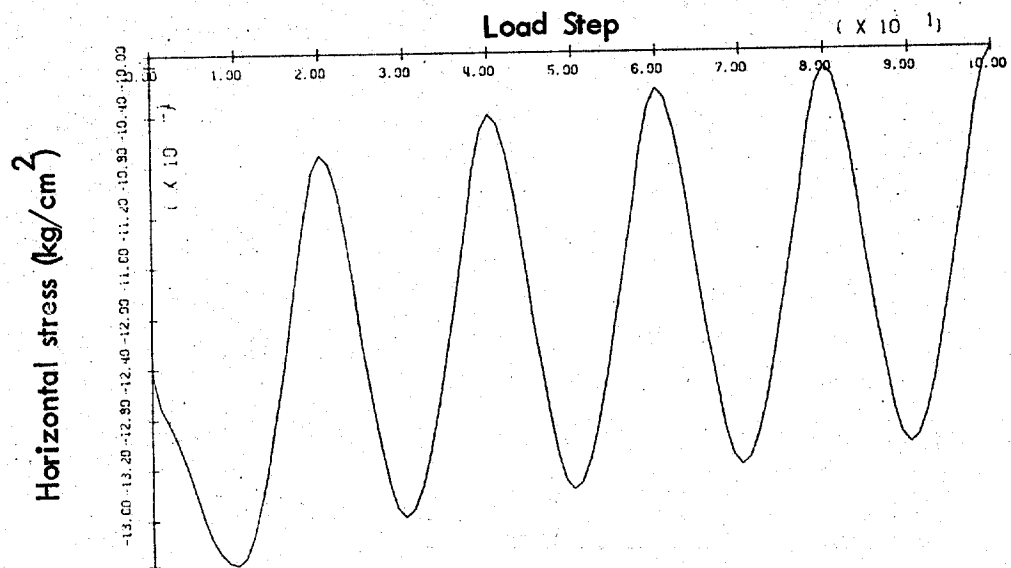


Figure 81 . Pile in Soil Field—Cyclic load, -50 to 50 kg.
(Soil element beneath pile tip)

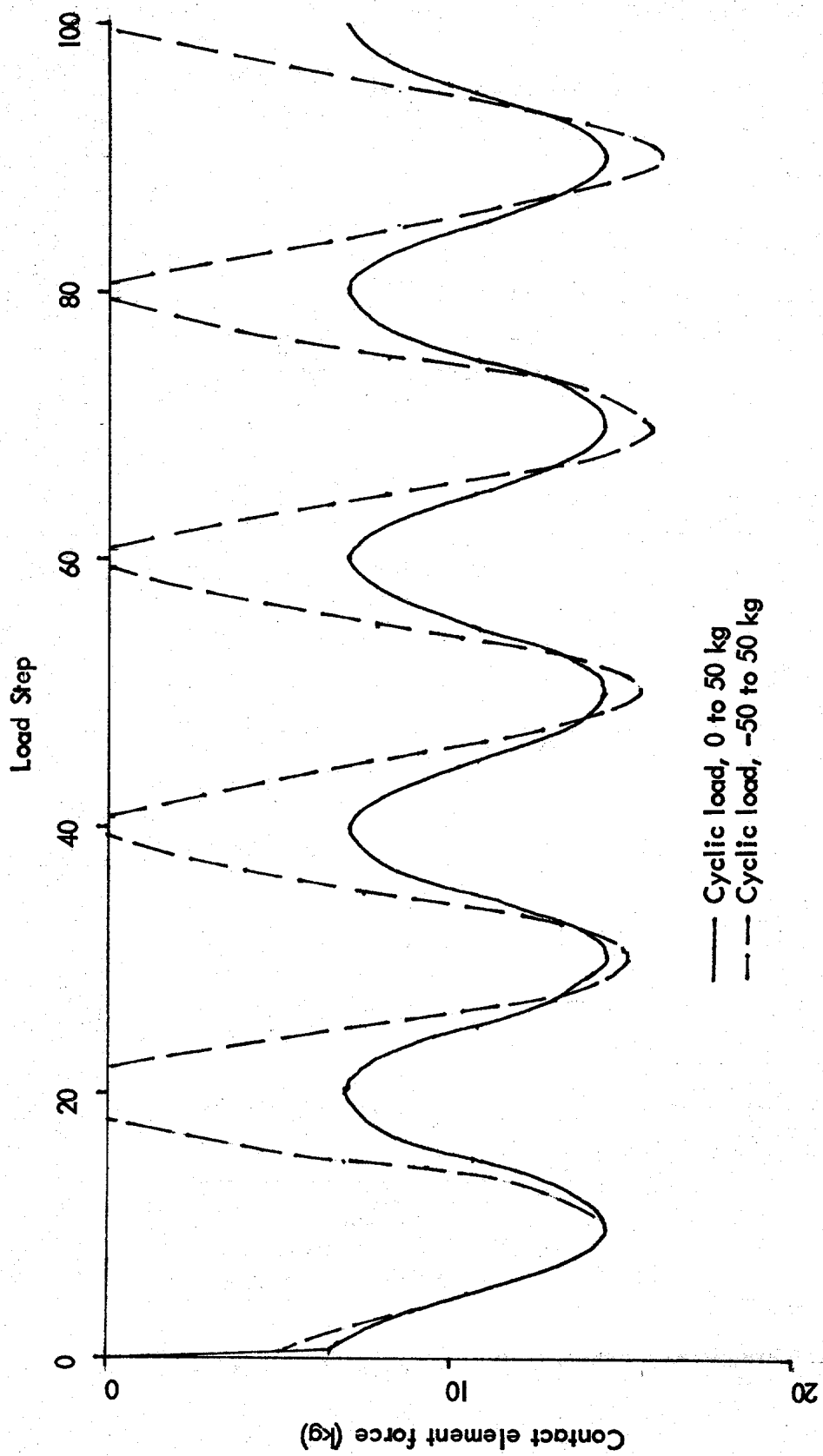


Figure 82. Pile in soil field, friction force in pile.

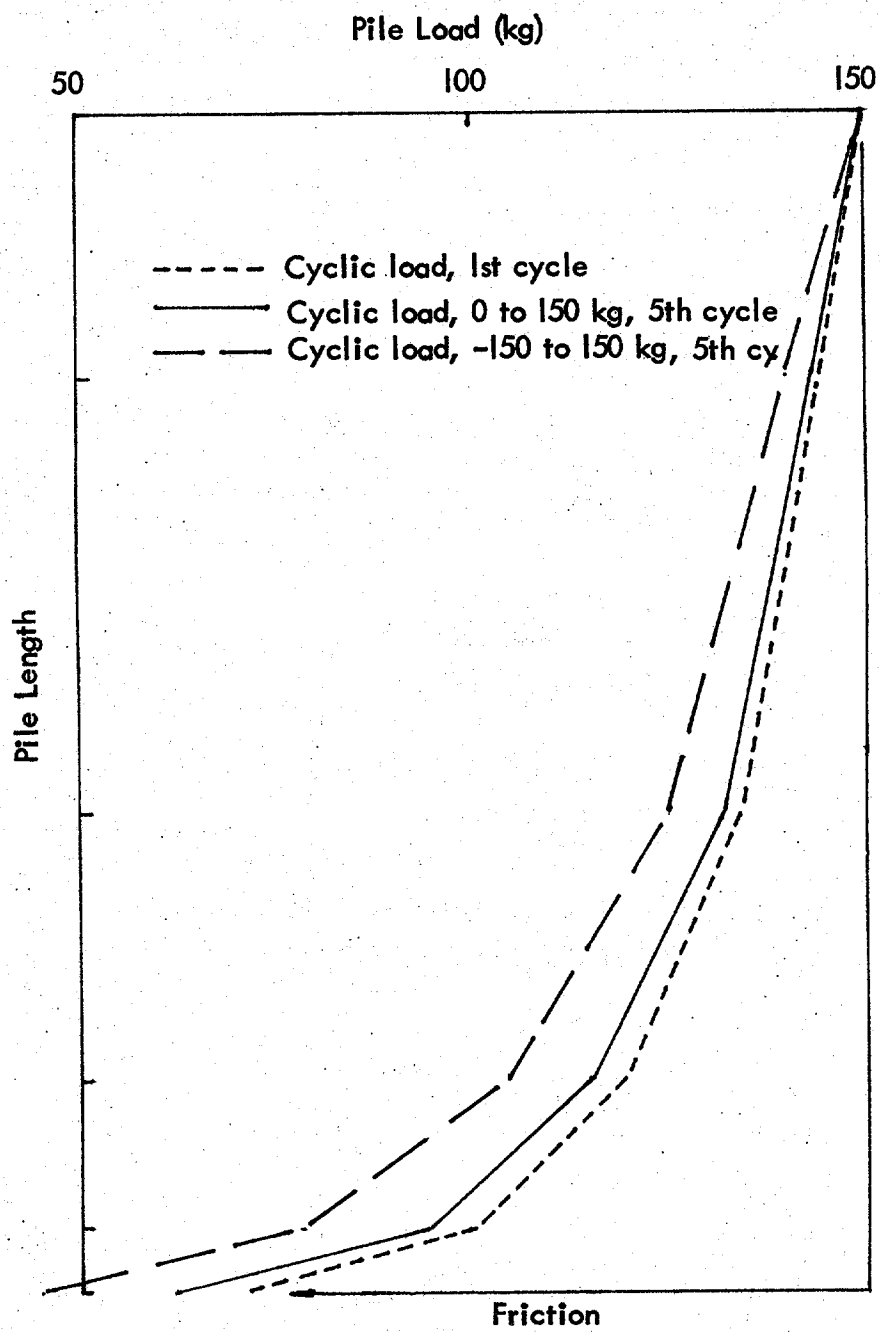


Figure 83. Distribution of force within pile, Cyclic load

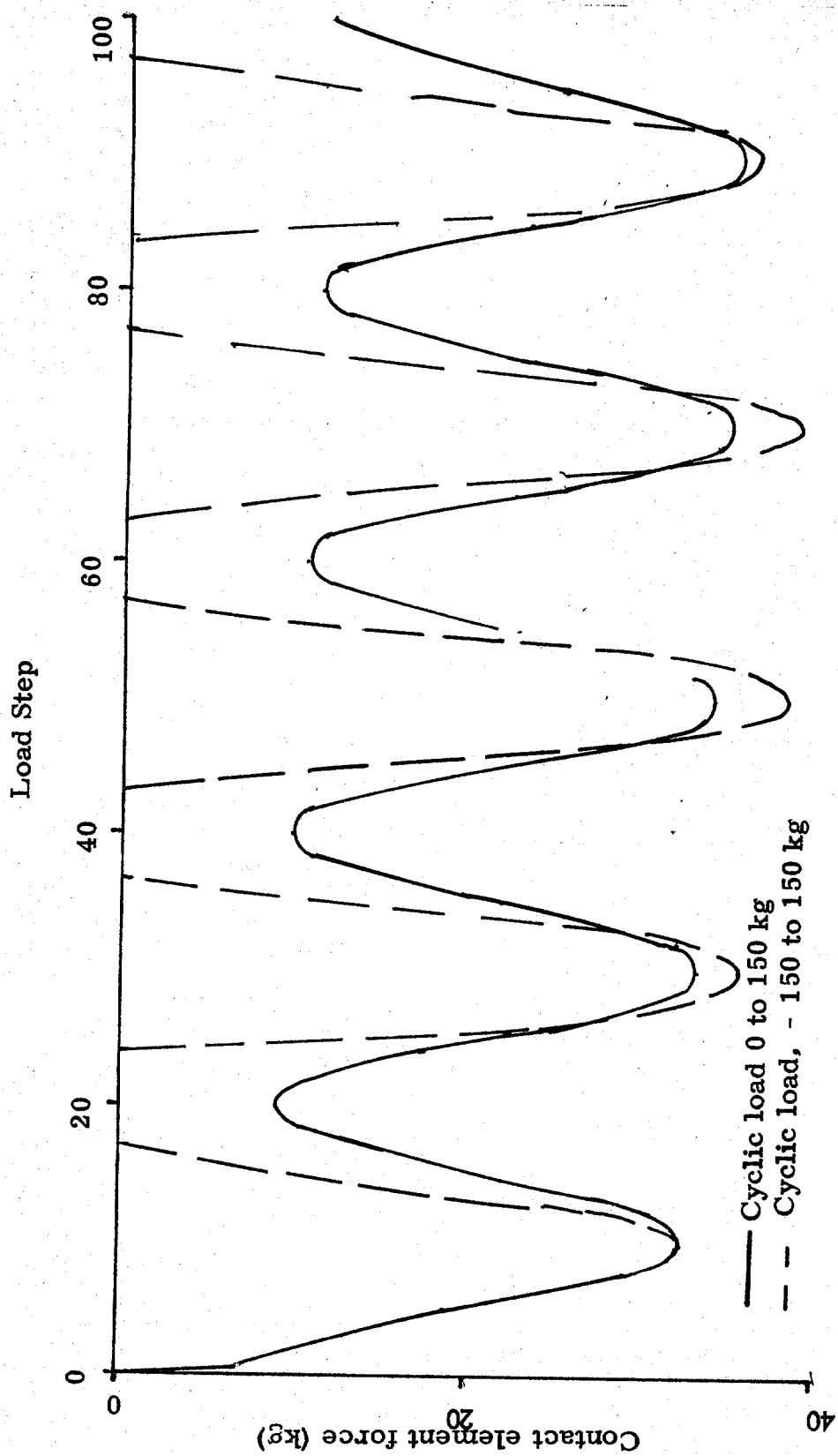


Figure 84 . Pile in soil field, friction force in pile.

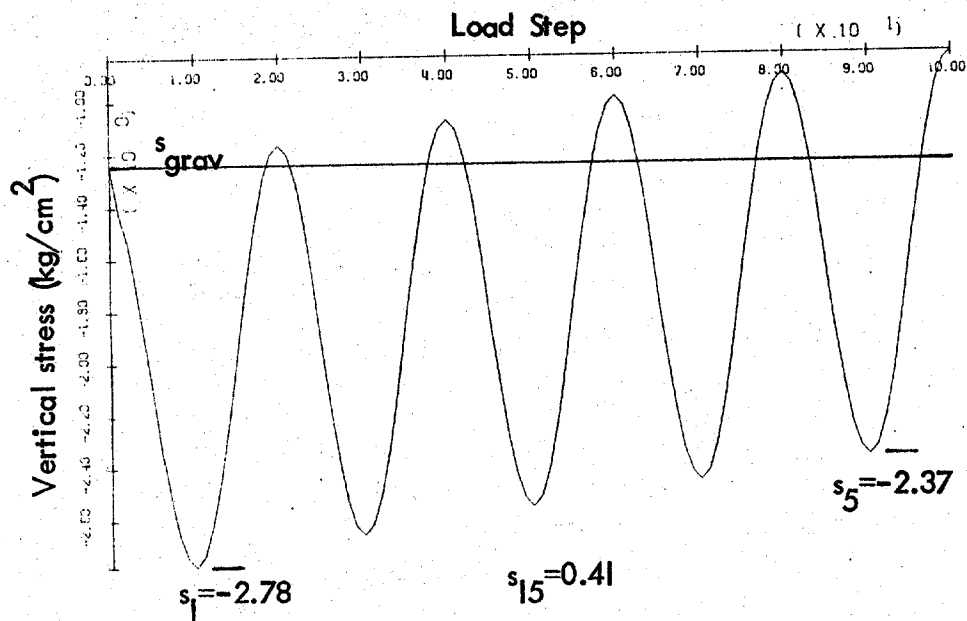
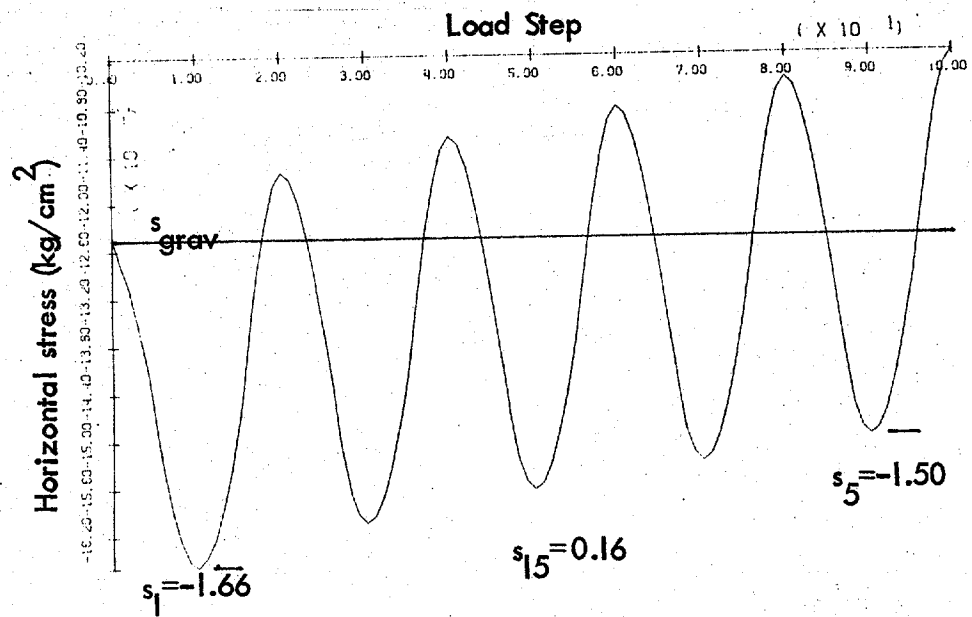


Figure 85. Pile in Soil Field—Cyclic load, 0 to 150 kg.
(Soil element beneath pile tip)

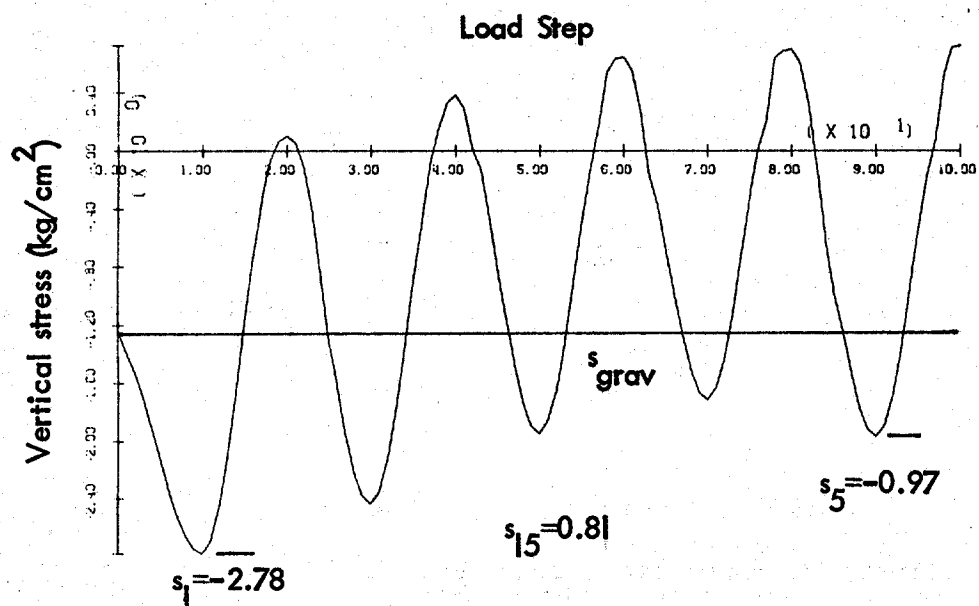
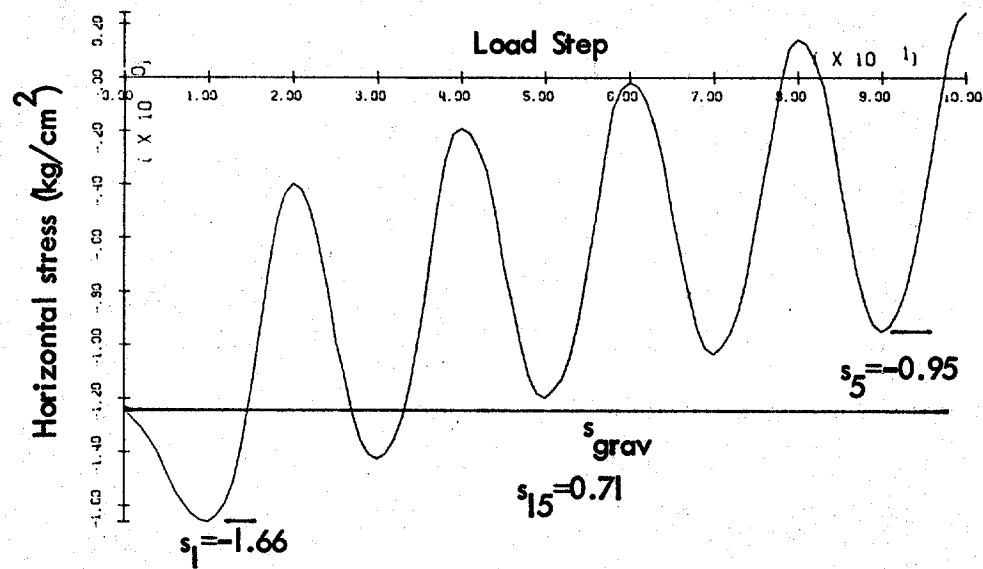


Figure 86. Pile in Soil Field—Cyclic load, -150 to 150 kg.
(Soil element beneath pile tip)

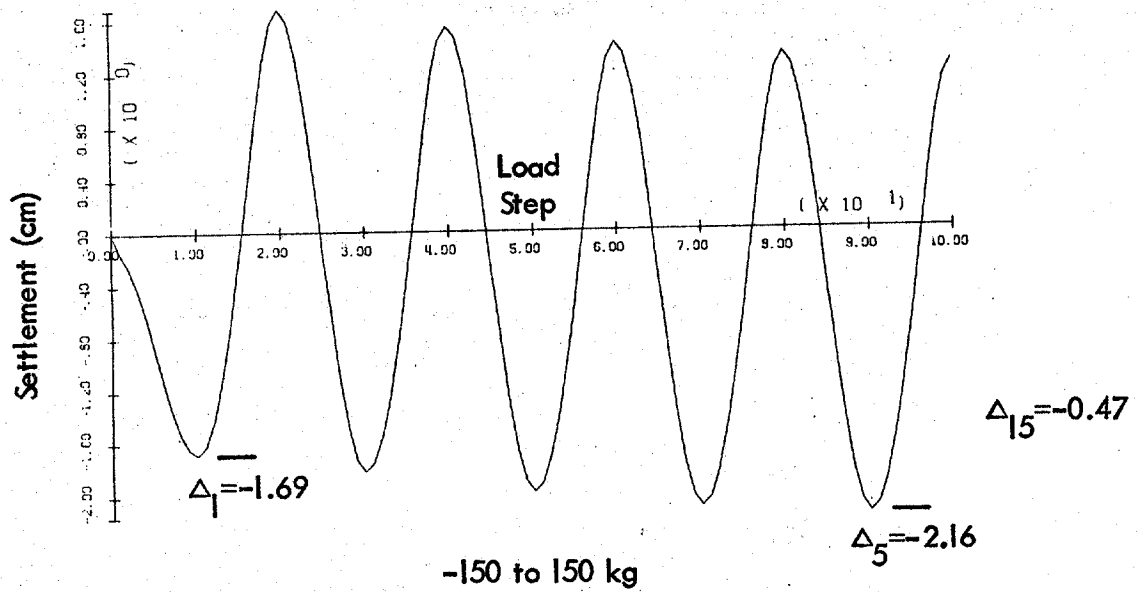
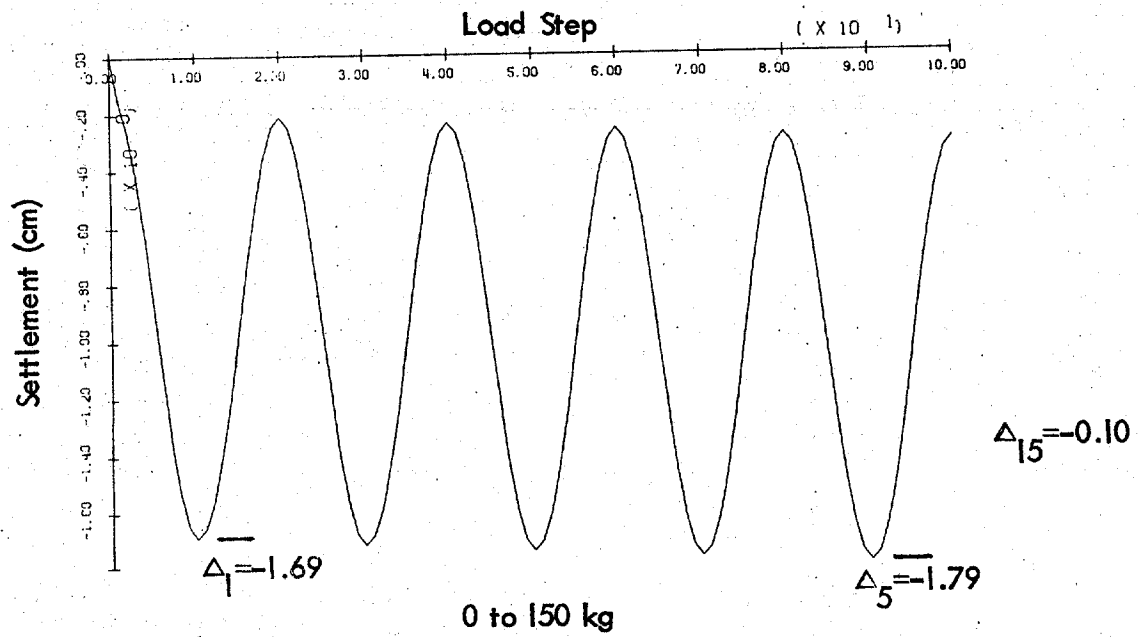
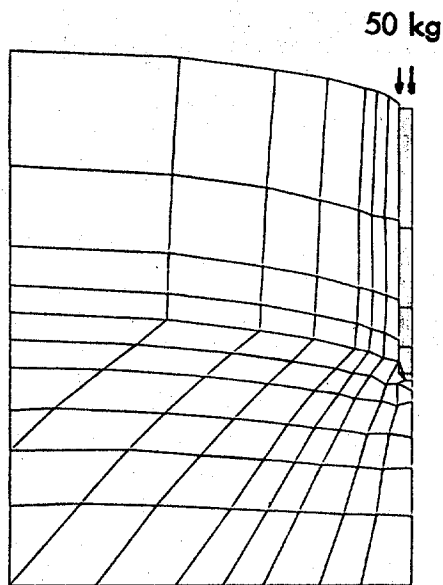
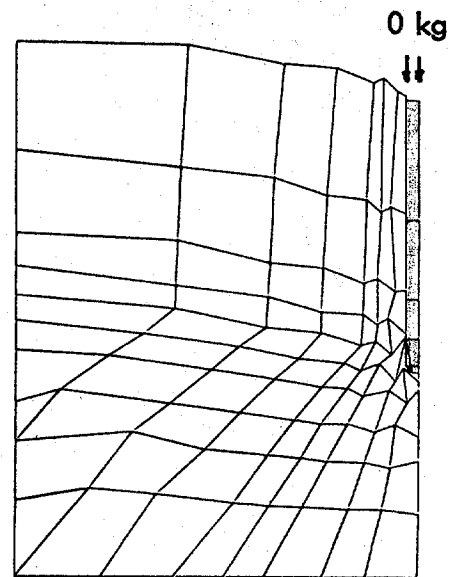


Figure 87. Pile in Soil Field—Cyclic load
(Pile settlement)



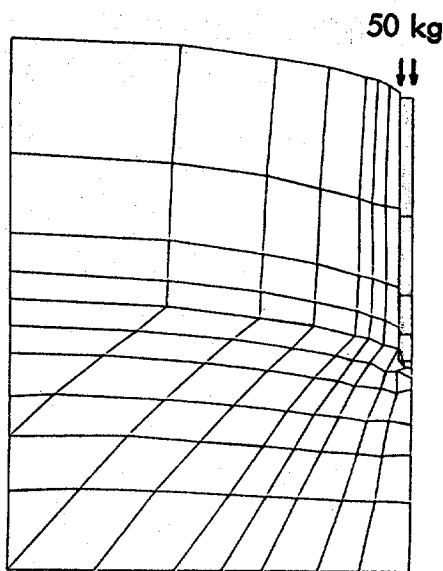
Scale factor = 1.25

Step 10



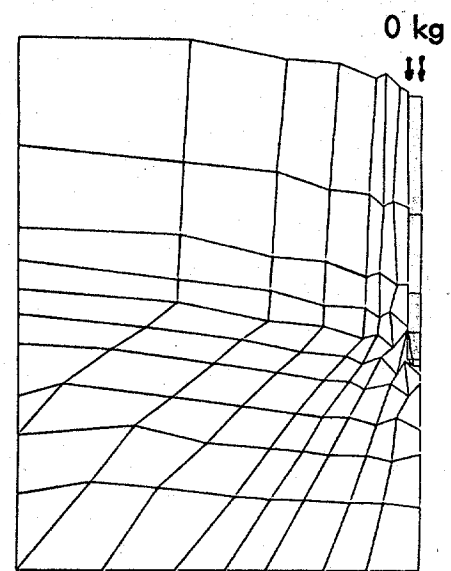
Scale factor = 0.25

Step 20



Scale factor = 1.25

Step 30



Scale factor = 0.25

Step 40

Figure 88. Deformed Mesh—Cyclic load, 0 to 50 kg.

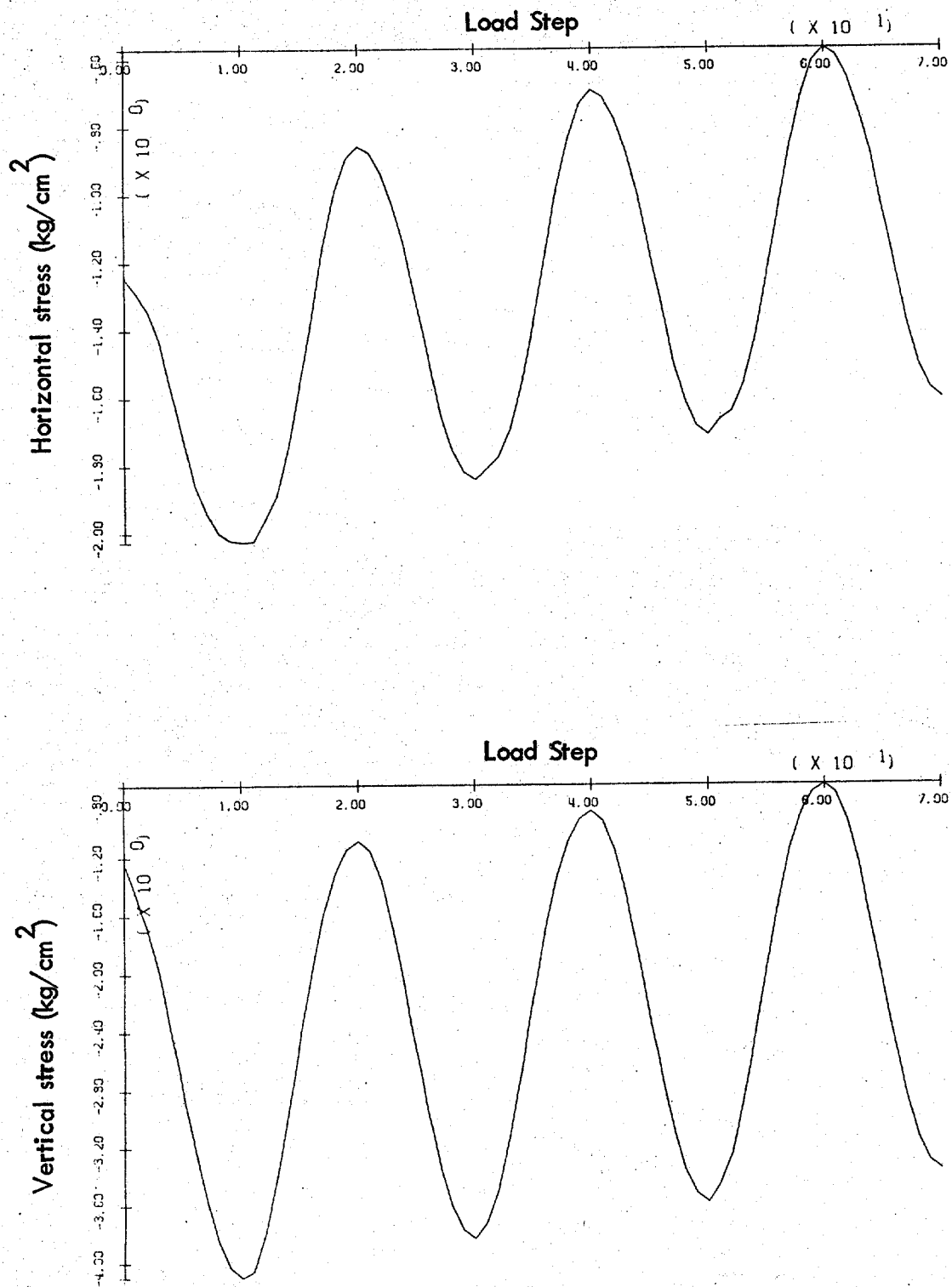
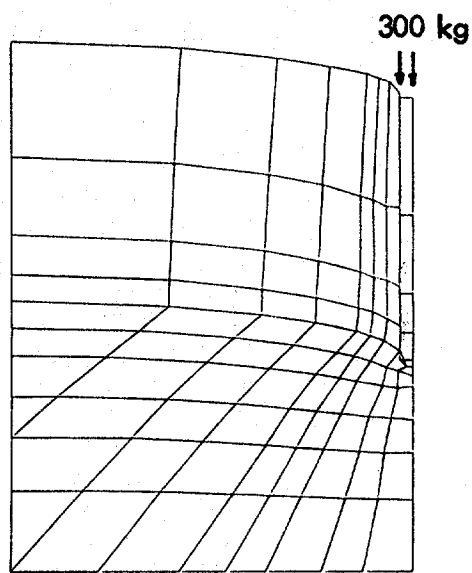
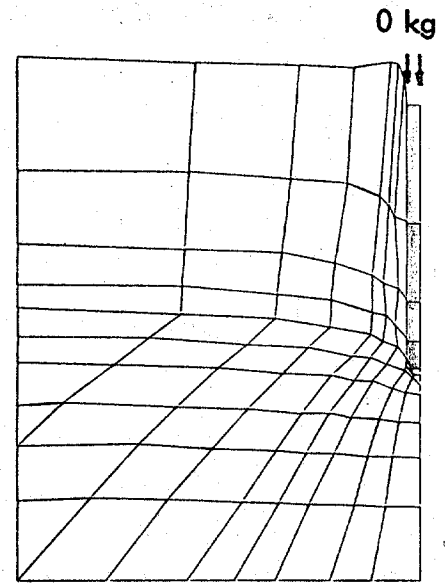


Figure 89. Pile in Soil Field—Cyclic load, 0 to 300 kg.
(Soil element beneath pile tip)



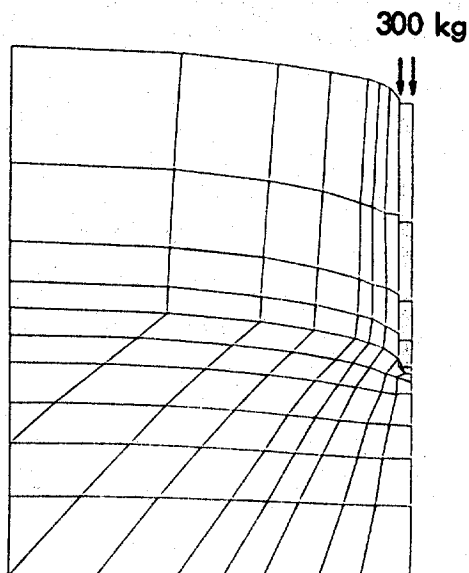
Scale factor = 7.05

Step 10



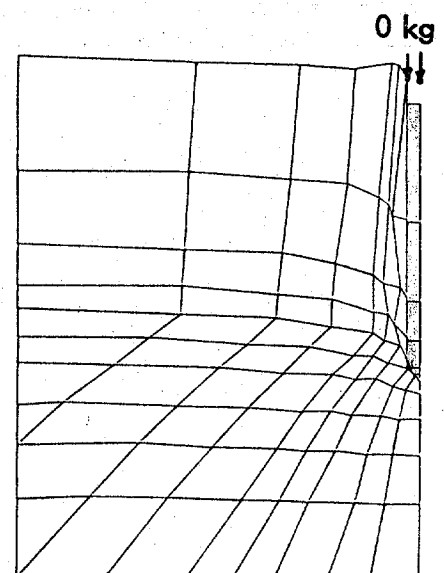
Scale factor = 1.13

Step 20



Scale factor = 7.36

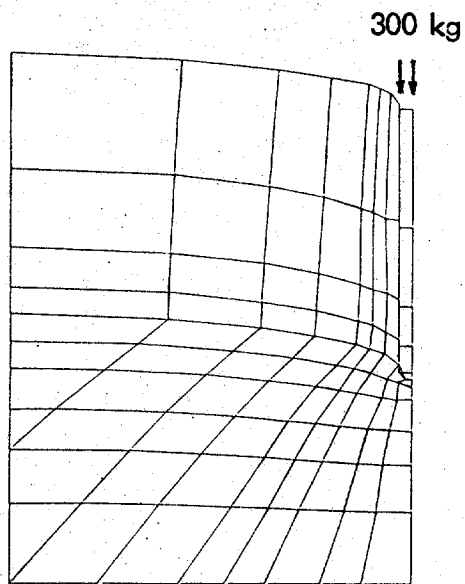
Step 30



Scale factor = 1.33

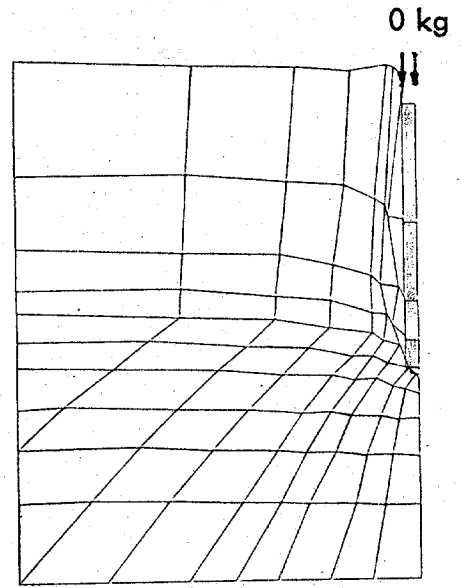
Step 40

Figure 90. Deformed mesh—Cyclic load, 0 to 300 kg.



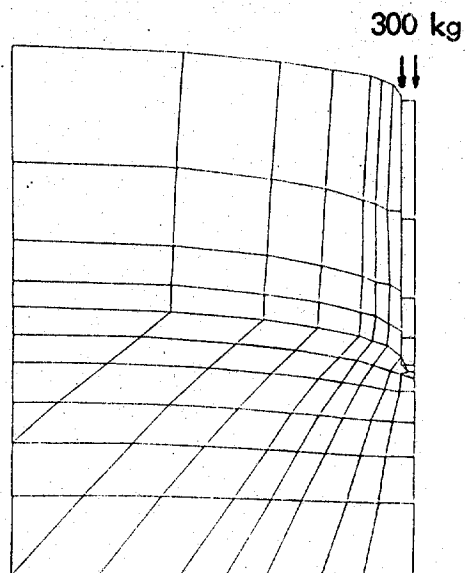
Scale factor = 7.58

Step 50



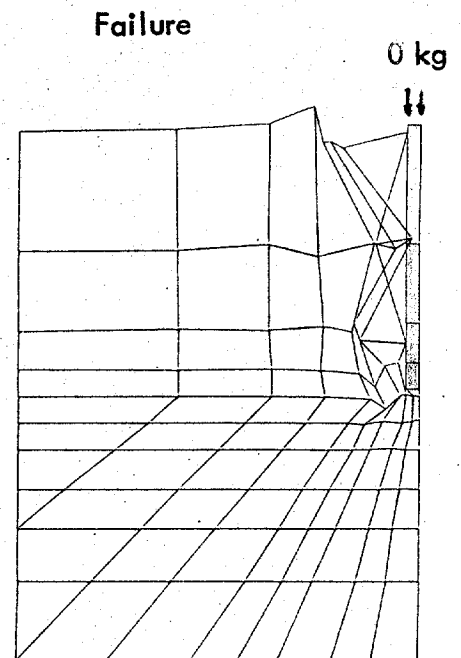
Scale factor = 1.52

Step 60



Scale factor = 7.79

Step 70



Scale factor = 1550

Step 80

Figure 90. Continued

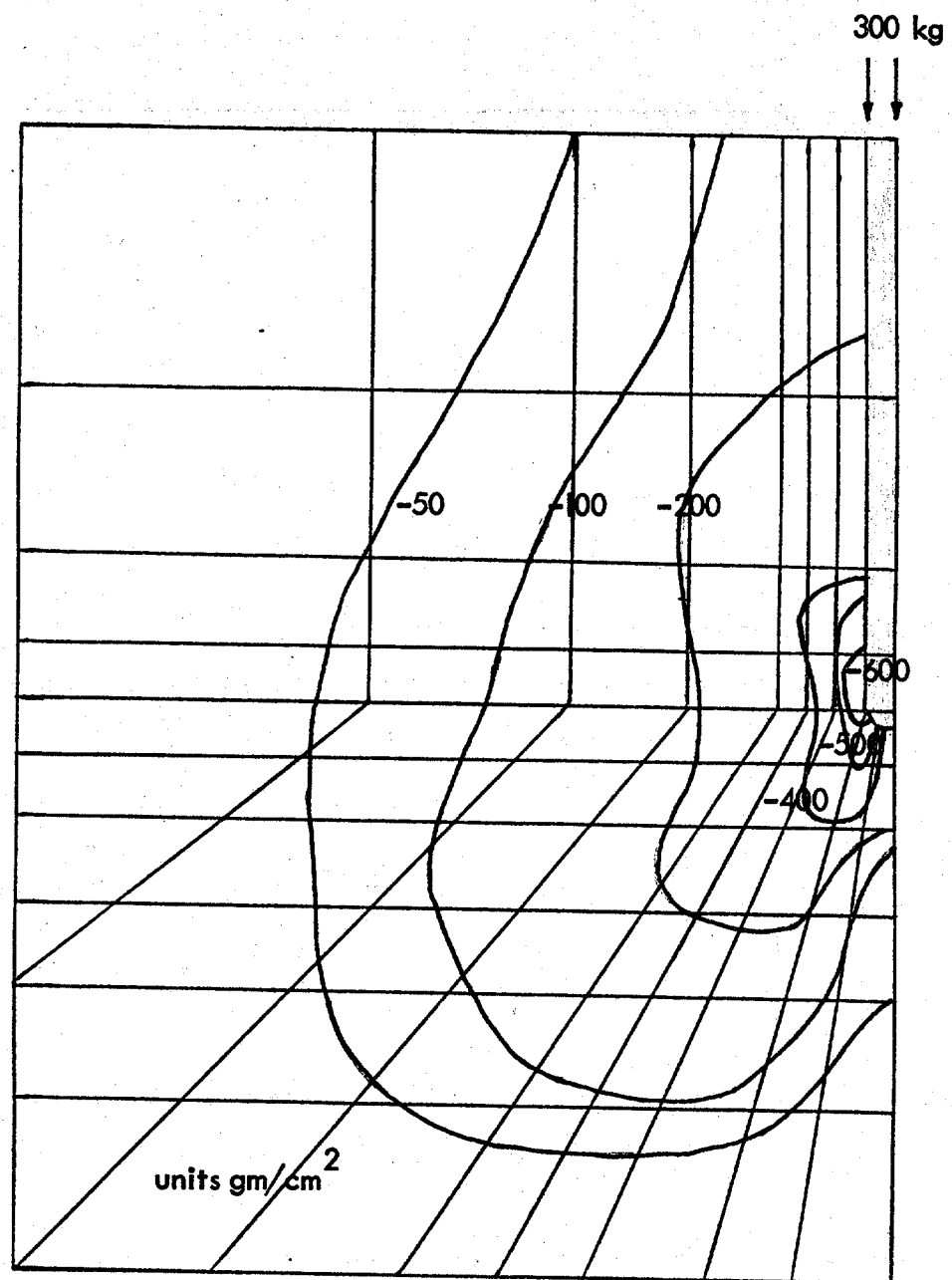


Figure 9l. Pile in Soil Field—Cyclic load, 0 to 300 kg,
Shear stress contours, step 10

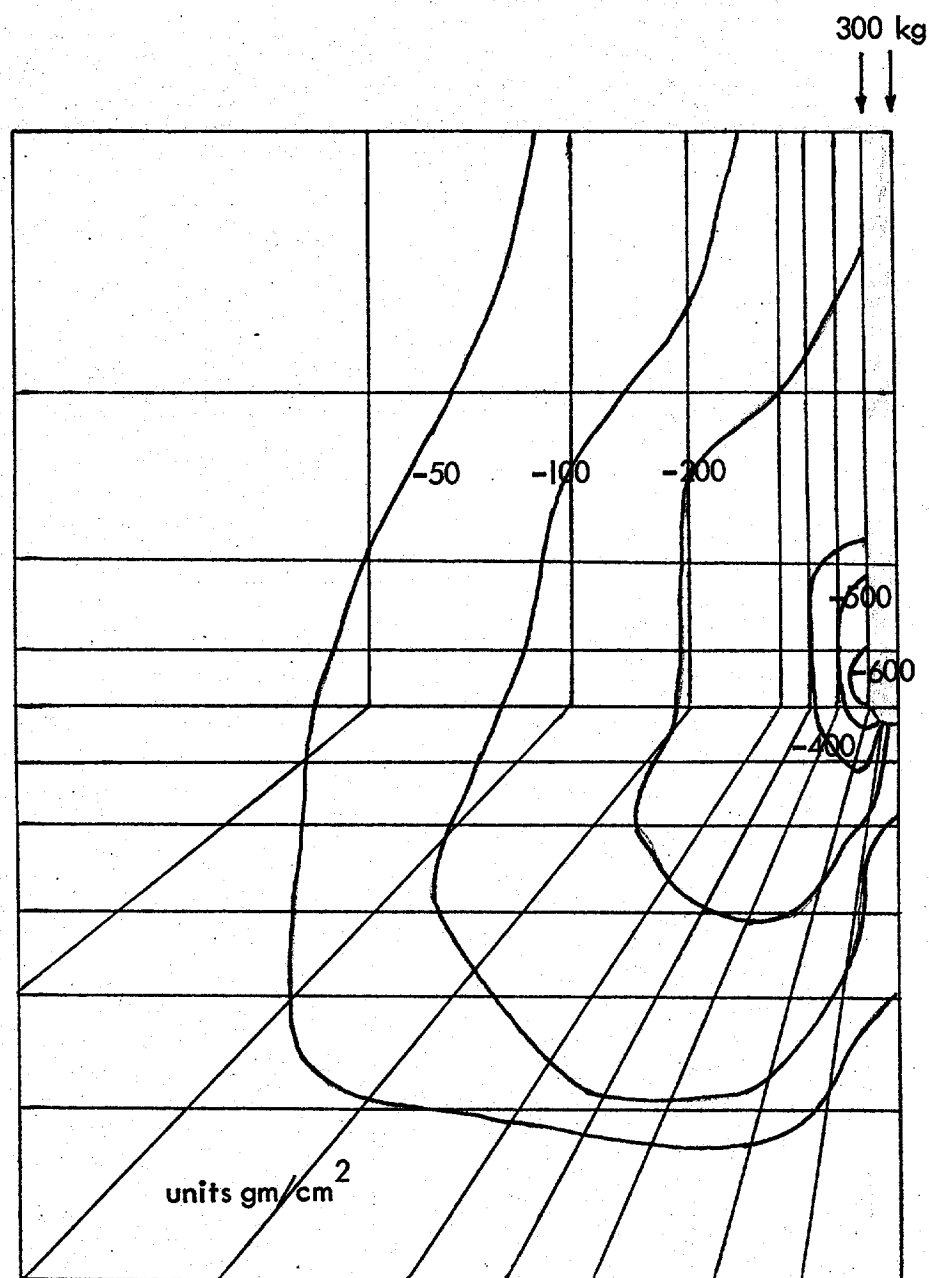


Figure 91. (Continued), step 70

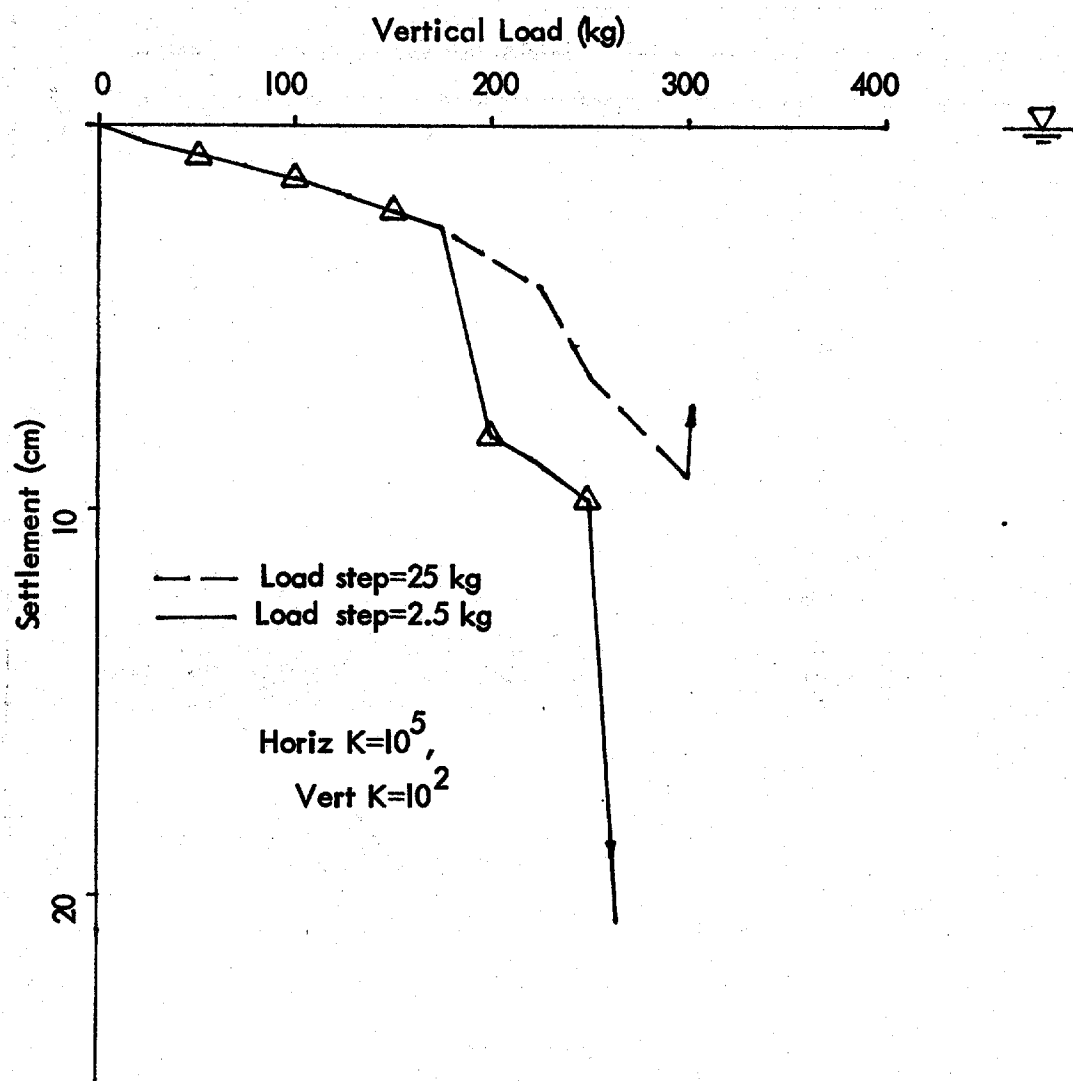


Figure 92. Load-Settlement of Pile
(with water table)

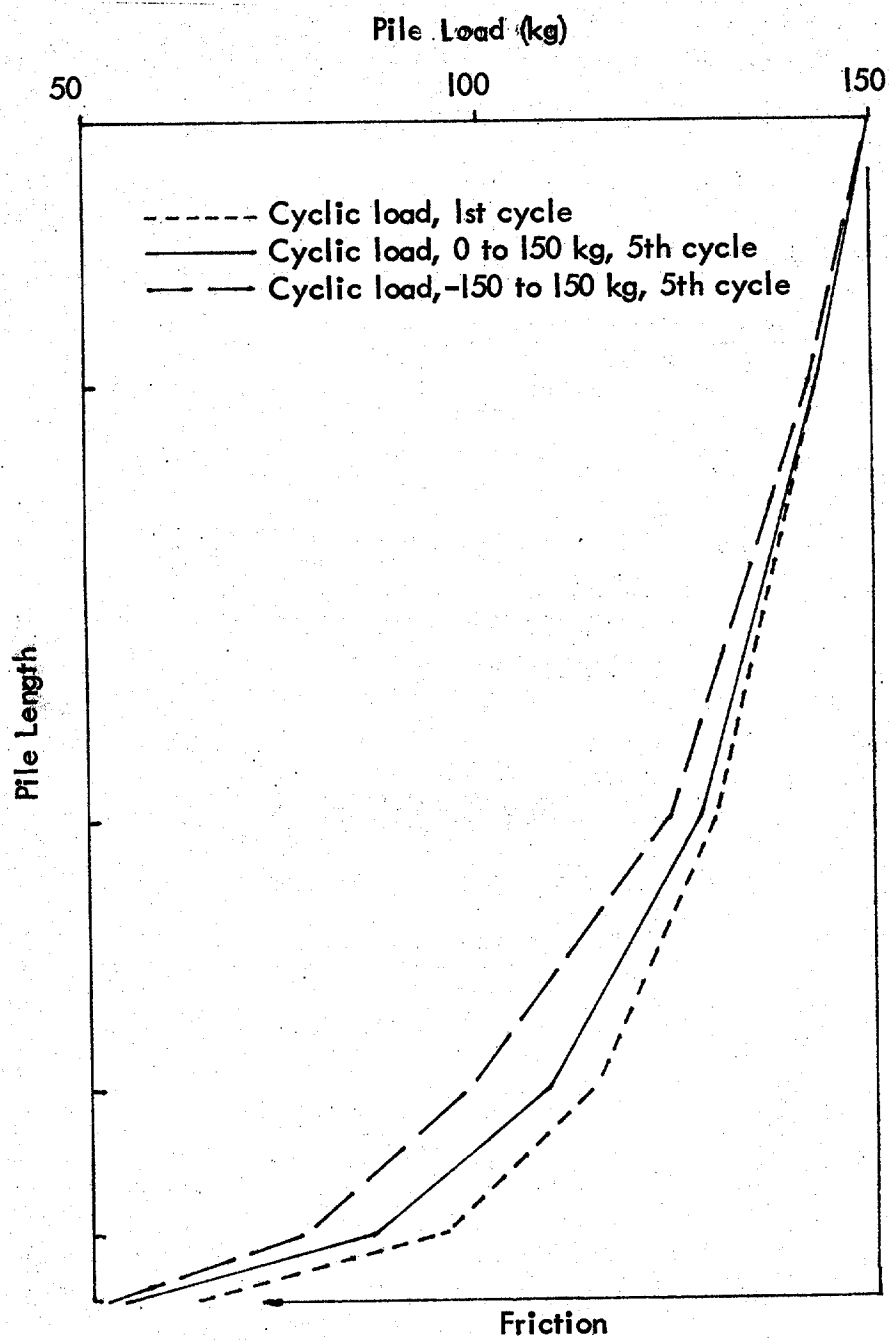


Figure 93 . Distribution of force within pile,
Cyclic load (with water table)

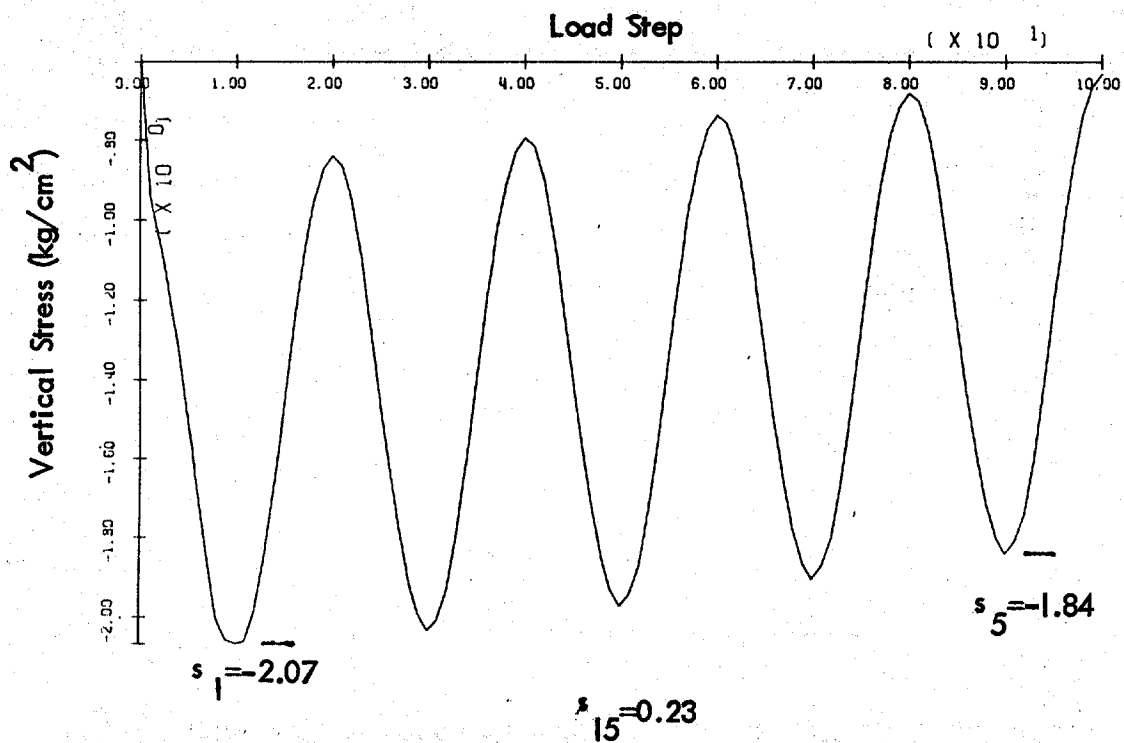
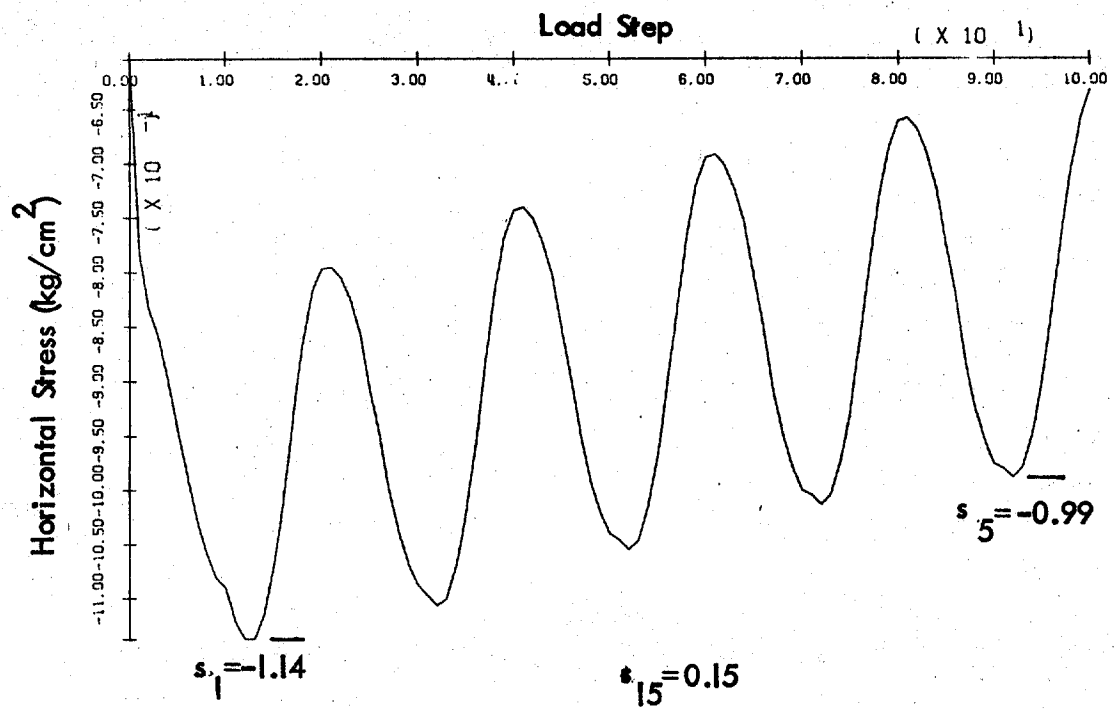


Figure 94. Pile in Soil Field—Cyclic load, 0 to 150 kg
(Soil element beneath pile tip)
(with water table)

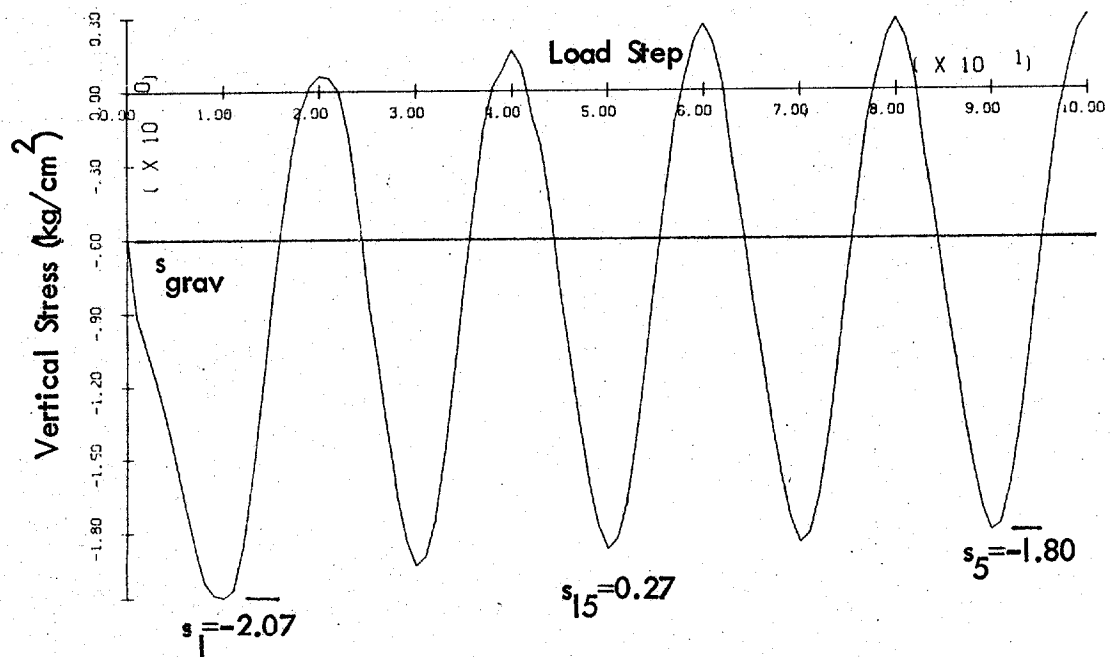
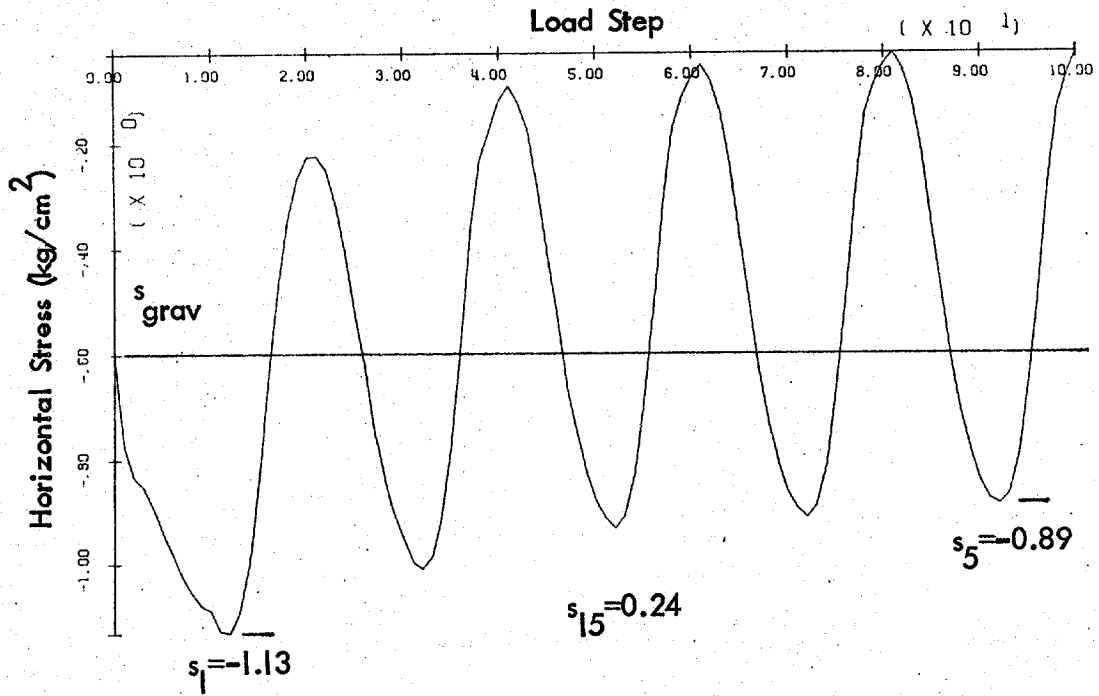


Figure 95. Pile in Soil Field—Cyclic load, -150 to 150 kg
(Soil element beneath pile tip)
(with water table)

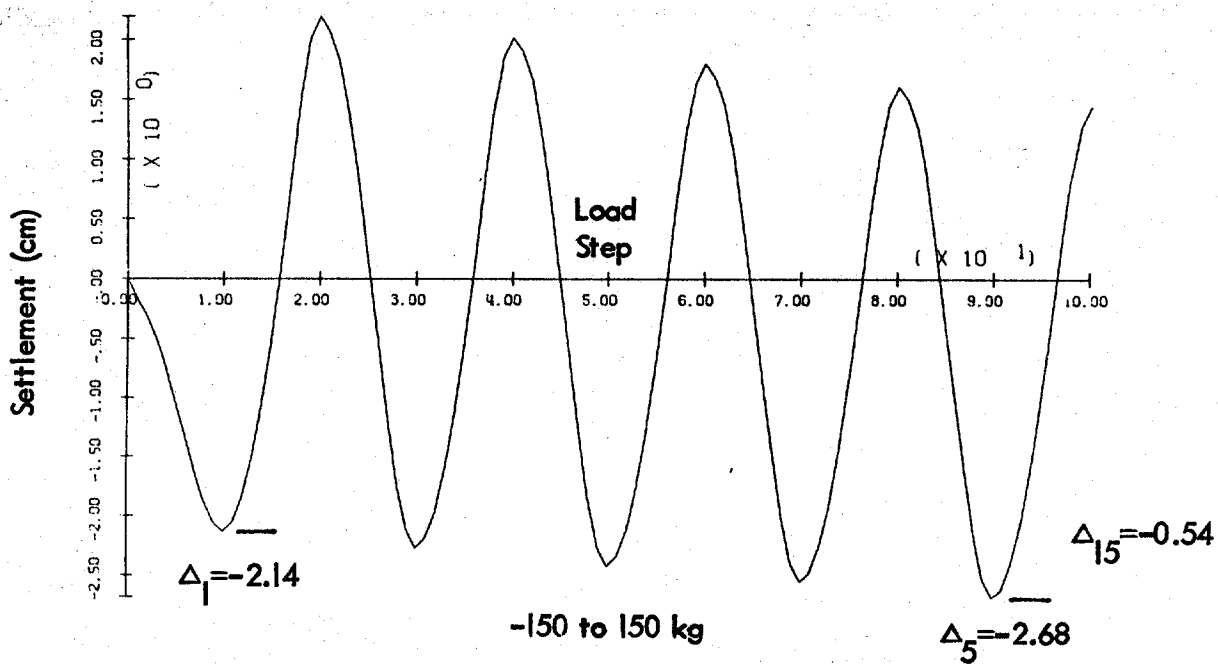
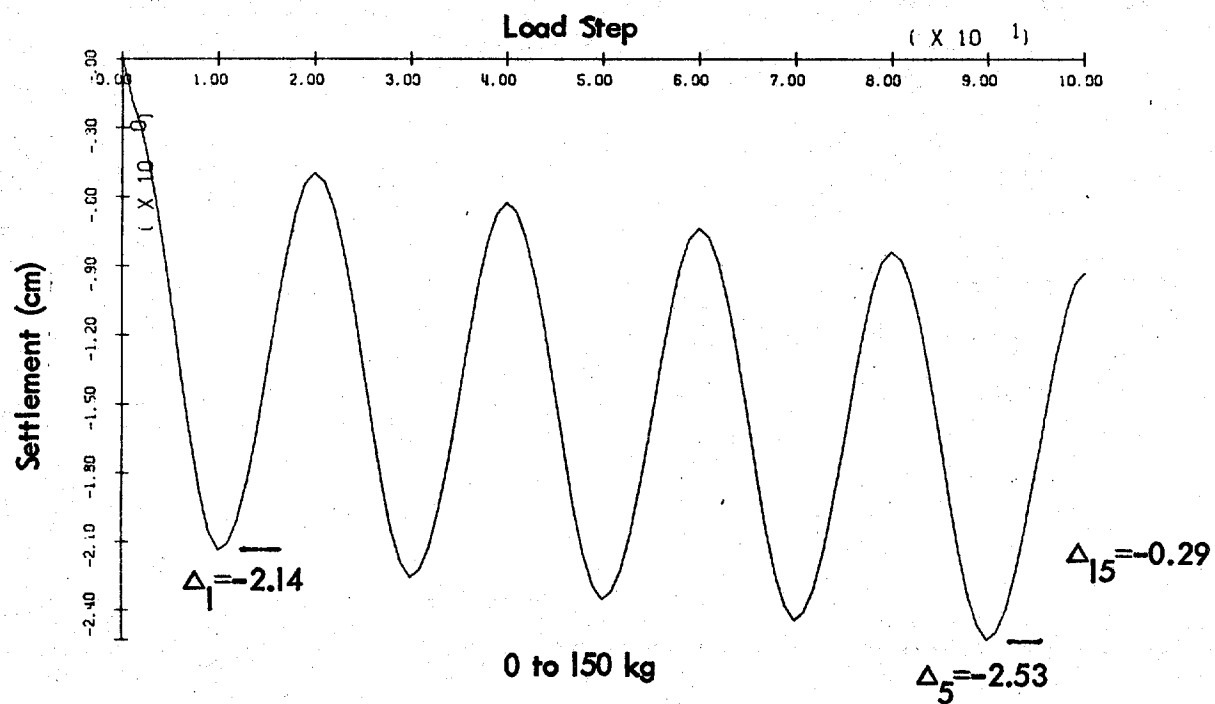


Figure 96. Pile in Soil Field—Cyclic Load
(Pile settlement) (with water table)

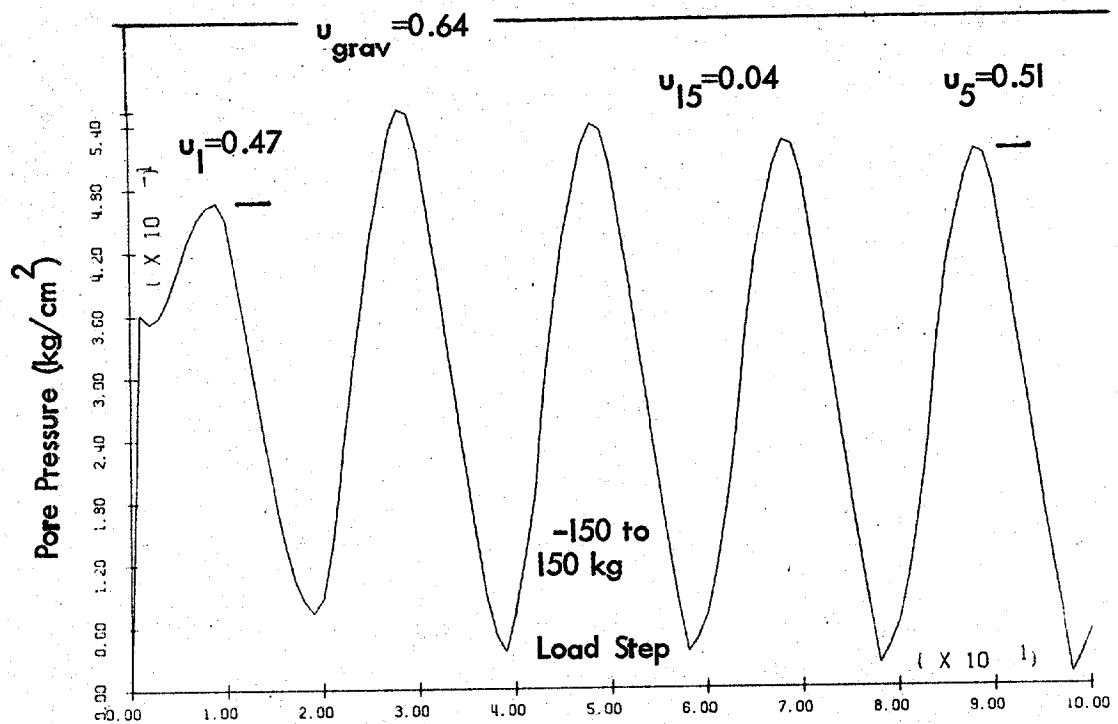
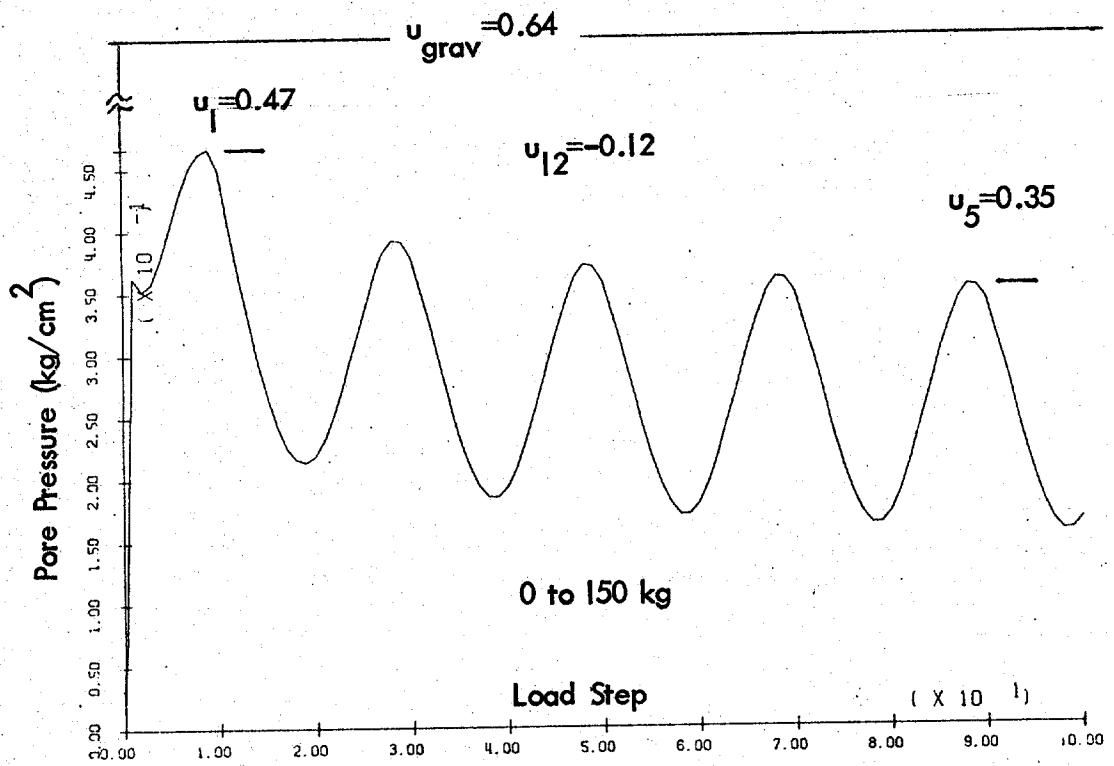


Figure 97. Pile in Soil Field—Cyclic Load
(soil element beneath pile tip)
(with water table)

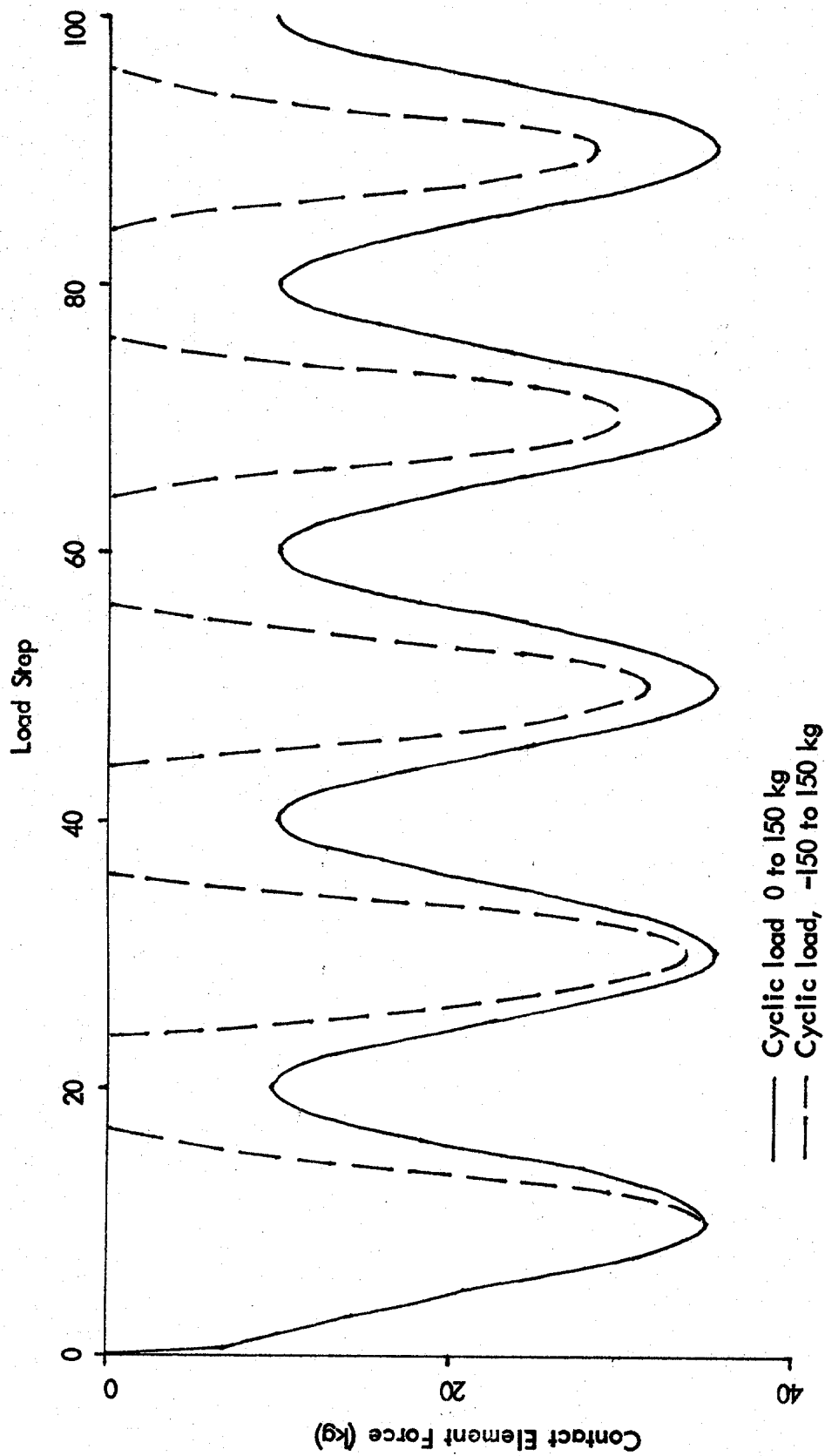


Figure 98. Pile in Soil Field—Friction force in pile
(with water table)

